Highly Filled Polymer Nanocomposite Films Derived from Novel Nanostructured Latexes

THÈSE N^{O} 4581 (2009)

PRÉSENTÉE LE 27 JANVIER 2010

À LA FACULTÉ SCIENCES ET TECHNIQUES DE L'INGÉNIEUR
LABORATOIRE DE TECHNOLOGIE DES COMPOSITES ET POLYMÈRES
PROGRAMME DOCTORAL EN SCIENCE ET GÉNIE DES MATÉRIAUX

ÉCOLE POLYTECHNIQUE FÉDÉRALE DE LAUSANNE

POUR L'OBTENTION DU GRADE DE DOCTEUR ÈS SCIENCES

PAR

Riccardo RUGGERONE

acceptée sur proposition du jury:

Prof. K. Scrivener, présidente du jury
Prof. J.-A. Månson, Dr J. C. Plummer, directeurs de thèse
Prof. J. M. Kenny, rapporteur
Prof. R. Mezzenga, rapporteur
Dr L. Weber, rapporteur

ÉCOLE POLYTECHNIQUE
FÉDÉRALE DE LAUSANNE
Suisse
2010

Abstract

The overall aim of this thesis has been to assess the potential of latex-based technologies for the preparation of polymer/clay nanocomposites. The key feature of latex-based technologies is that they offer the possibility of improved control of the final nanocomposite morphology at significantly higher clay loadings than can be obtained with more conventional processing techniques, such as melt blending or *in situ* polymerization. The idea is to exploit swelling of the clay in either the aqueous or the monomer phase of a water-based latex, depending on the clay surface functionalization, to produce hybrid polymer/clay latex particles with controlled diameters of the order of 100 nm, which may then be consolidated to produce solid nanocomposite films. The materials considered in this work were based on styrenic matrices, considered to be a model system, and acrylics, which are of more interest for commercial coating applications. Two different polymerization techniques were investigated, namely conventional emulsion polymerization and miniemulsion polymerization. The thermal and mechanical properties of films produced from the resulting latexes were then studied in detail. Conventional emulsion polymerization was found to be particularly suitable for the preparation of particles with a well-defined "armoured" morphology, in which the clay formed a more or less complete shell around a matrix core, providing the focus for the remainder of the project. Clay contents of up to about 50 wt % were obtained for both the styrenic and the acrylic latexes using this approach, with excellent degrees of dispersion, the average clay aggregate thickness not exceeding 10 nm. The armoured morphology of the latex particles resulted in a cellular arrangement of the clay in the consolidated films, which became better defined as the clay content increased.

The reinforcing effect of the clay on mechanical properties varied according to the physical state of the matrix. Increases in Young's modulus by a factor of 3 to 4 were observed in styrenic films with the cellular morphology in the glassy state, and the degree of exfoliation of the clay was found to be a critical parameter under these conditions, samples containing 5 to 7 wt % of clay showing increased moduli with respect to those obtained at somewhat higher clay contents, for which aggregation was more apparent. In the rubbery state, on the other hand, the Young's modulus increased by more than 2 orders of magnitude for clay contents above 20 wt % and was strongly correlated with the overall filler content. Thermal analysis showed that a significant proportion of the matrix remained immobilized in the rubbery state, i.e. did not contribute to the glass transition. This was argued to be due to strong physical confinement of regions of the matrix intercalated in the clay aggregates. While the increases in Young's modulus in the glassy state could be accounted for in terms of classical micromechanical models, such as those of Halpin-Tsai and Mori-Tanaka, the same models failed to predict the behaviour in the rubbery state. Models based on foam mechanics were therefore developed incorporating an immobilized matrix fraction in the cell walls, whose elastic properties were treated as fitting parameters. Although somewhat different values of the Young's modulus for this immobilized matrix fraction were required to fit the data, depending on the details of the model, they were consistently found to be two to three orders of magnitude greater than that of the neat matrix in the rubbery state (but not to exceed the Young's modulus of the matrix in the glassy state), providing direct evidence for the importance of this interphase for the overall nanocomposite properties. The importance of the cellular arrangement of the clay was also confirmed through comparison with nanocomposites containing non-cellular morphologies resulting from other preparation techniques or the use of mechanical deformation to break-up the initial cellular structure. Finally, it was demonstrated that the results obtained for the styrenic systems could be

extended to acrylic-based nanocomposites with comparable morphologies, underlining their broader significance for formulations of potential commercial interest.

A further goal of this thesis was to study the effect of the clay on the microdeformation and fracture mechanisms of the nanocomposites, and it was also of interest to compare these results with those obtained for conventional isotactic polypropylene (PP)/clay nanocomposites prepared by melt blending, whose macroscopic properties have been studied previously in our institute. *In situ* TEM investigation of deformation in glassy styrenic nanocomposite films of about 200 nm in thickness containing the cellular structure revealed a decrease in local matrix drawability at clay contents above 10 wt %, and extensive coarse cavitation, thought to be associated with the particle cores, which replaced crazing as the dominant deformation mechanism, accounting for the observed decrease in macroscopic tensile strength at intermediate clay contents. Moreover, at the highest clay contents, these mechanisms were replaced by failure of the particle-particle interfaces, leading to an extremely brittle macroscopic response. Above T_g, localized deformation zones were also observed, indicating the network formed by the clay and the immobilized regions of matrix to show yielding behaviour, again consistent with the macroscopic response. The conventional PP/clay nanocomposites also showed a decrease in matrix ductility and an increase in coarse cavitation with increasing clay content. In this latter case, however, the zones of cavitation were clearly identified with breakdown of the clay aggregates or the interfaces between the clay and the matrix, underlining the important role of the clay-matrix interface for the properties of the styrenics, and by inference, those of the acrylics. To provide further insight into the role of the cellular structure of the styrenics, finite element (FE) simulations were used to investigate the distribution in hydrostatic stress in the nanocomposite films under finite deformations. These showed the principal stress concentrations to appear in the clay aggregates aligned in the direction of the applied deformation, while the hydrostatic stress in the matrix remained relatively uniform, suggesting that as long as the interface and clay aggregates remain stable, cavitation may initiate anywhere within the matrix, as in the unmodified polymer. The FE simulations were also used to model the elastic properties in the rubbery state, confirming the need to assume the presence of an immobilized matrix fraction in order to account for the observed Young's moduli. The results of these calculations were found to be consistent with those obtained from the foam-based micromechanical models, confirming the applicability of these latter, and suggesting the local anisotropy of the clay aggregates to play a limited role in the overall low strain elastic properties.

The main outcome of this thesis has been the establishment of a general physical basis for predicting structure-mechanical property relationships in a new range of latex-based nanocomposite materials with exceptional properties, thanks to the possibility of incorporating very high clay loadings without compromising processability, and vast potential for fine tuning of stiffness and stiffness related properties. Moreover, the work has highlighted the important role of the "nano" effect, particularly at temperatures above the glass transition of the matrix, where matrix immobilization at the clay-matrix interface is clearly demonstrated to contribute to both thermal and mechanical properties. It is consequently expected to provide solid guidelines for the choice of morphological and materials parameters for the optimization of basic mechanical properties in such materials via controlled synthesis. Moreover, with further advances in synthesis and processing and hence in film quality, it should ultimately be possible to extend the basic physical model developed here to account for the structure dependence of other important applicative properties, such as permeability and fire resistance.

Keywords: laponite, clay nanocomposites, emulsion polymerization, miniemulsion polymerization, latexes, foam, foam mechanics, mechanical properties.

Version abrégée

Le but principal de cette thèse a été d'évaluer le potentiel des technologies latex pour la préparation de nanocomposites polymère/argile. La principale caractéristique des technologies latex est qu'elles offrent la possibilité d'un meilleur contrôle de la morphologie du nanocomposite final avec une fraction volumique d'argile sensiblement plus élevée que celles obtenue avec les techniques de transformation plus classiques, comme le mélange à l'état fondu ou la polymérisation *in situ*. L'idée a été d'exploiter le gonflement de l'argile soit dans la phase aqueuse soit dans le monomère, selon la fonctionnalisation de la surface de l' argile, pour produire des particules hybrides de latex polymère/argile avec un diamètre contrôlé de l'ordre de 100 nm, qui ont pu être finalement consolidées pour produire des couches minces nanocomposites. Les matériaux pris en compte dans ce travail ont été d'une part des systèmes modèles à base de styrène et d'autre part des acryliques, plus intéressants pour des applications de revêtements commerciaux. Deux techniques de polymérisation différentes ont été examinées, à savoir la polymérisation en émulsion classique et la polymérisation en miniémulsion. Les propriétés thermiques et mécaniques des films produits à partir des latex ont ensuite été étudiées en détail. La polymérisation en émulsion classique a été jugée particulièrement appropriée pour la préparation de particules avec une morphologie particulière, dans lesquelles l'argile forme une coquille plus ou moins complète autour d'un noyau de matrice. Des teneurs en argile, jusqu'à environ 50 % en poids ont été obtenues tant pour le styrène que pour les latex acryliques en utilisant cette approche, avec d'excellents niveaux de dispersion, l'épaisseur d'argile moyenne globale ne dépassant pas 10 nm. La morphologie cœur-écorce des particules de latex a abouti à un arrangement cellulaire de l'argile dans les films, mieux défini aux teneurs en argile élevées.

L'effet de renfort de l'argile sur les propriétés mécaniques dépendait de l'état physique de la matrice. A l'état vitreux des augmentations du module de Young d'un facteur 3 à 4 ont été observés dans les films de styrène avec la morphologie cellulaire. Le degré d'exfoliation de l'argile s'est révélé être un paramètre critique dans ces conditions. Le module d'échantillons contenant de 5 à 7 % en poids d'argile exfoliée était en effet supérieur à celui obtenu à des teneurs en argile plus élevées, mais pour lesquelles l'agrégation était plus manifeste. A l'état caoutchoutique, d'autre part, le module de Young augmentait de plus de 2 ordres de grandeur pour des teneurs en argile supérieures à 20 % en poids et était fortement corrélé à la teneur en argile globale. L'analyse thermique a montré qu'une portion importante de la matrice restait immobilisée à l'état caoutchoutique, soit ne contribuait pas à la transition vitreuse. Ceci a été considéré comme la conséquence du confinement physique de portions de matrice intercalées dans les agrégats d'argile. Alors que l'augmentation du module d'Young à l'état vitreux pouvait être expliquée en termes de modèles classiques micromécaniques, telles que ceux de Halpin-Tsai et Mori-Tanaka, ces mêmes modèles n'ont pas réussi à prédire le comportement à l'état caoutchoutique. Des modèles fondés sur la mécanique des mousses ont donc été développés, intégrant une fraction immobilisée de matrice dans les parois cellulaires, dont les propriétés élastiques étaient traitées comme des paramètres d'ajustement. Bien que des valeurs différentes du module de Young de cette fraction immobilisée de matrice ont été nécessaires pour obtenir un bon accord avec les données expérimentales, ceux-ci étaient systématiquement deux à trois ordres de grandeur supérieurs au module de la matrice à l'état caoutchoutique (mais ne dépassant pas le module de Young de la matrice à l'état vitreux), fournissant donc des preuves directes de l'importance de cette interphase pour l'ensemble des propriétés des nanocomposites. L'importance de l'arrangement cellulaire de l'argile a également été confirmée par comparaison avec des nanocomposites contenant une morphologie non cellulaire obtenus avec différentes techniques de préparation ou en déformant mécaniquement jusqu'à rupture la structure initiale. Enfin, il a été démontré que les résultats obtenus pour les systèmes à base de styrène pourraient être étendus aussi aux nanocomposites acryliques avec des morphologies comparables, en soulignant leur intérêt plus large pour des formulations d'intérêt commercial potentiel.

Un autre objectif de cette thèse était d'étudier l'effet de l'argile sur la microdéformation et les mécanismes de rupture des nanocomposites. Il était également intéressant de comparer ces résultats avec ceux obtenus pour des nanocomposites polypropylène isotactique (PP)/argile classiques préparés

par mélange à l'état fondu, et dont les propriétés macroscopiques avaient été étudiés précédemment dans notre institut. Investigations MET in situ de la déformation dans des couches nanocomposites à base de styrène d'environ 200 nm d'épaisseur contenant la structure cellulaire ont révélé une diminution de la plasticité locale pour des teneurs en argile supérieure à 10 % en poids, et la présence de cavitation importante, supposée être associée avec les noyaux des particules. Ce mécanisme se substitue au mécanisme de déformation dominant par craquelures, et contrôle la diminution de la résistance en traction macroscopique à des teneurs intermédiaires en argile. En outre, à une teneur plus élevée en argile, ces mécanismes étaient remplacés par la rupture des interfaces particule-particule, conduisant à une réponse macroscopique extrêmement fragile. Au-dessus de Tg, des zones de déformation localisées ont aussi été observées, indiquant que le réseau formé par l'argile et les régions immobilisées de la matrice pouvait se déformer, résultat compatible avec la réponse macroscopique. Les nanocomposites PP/argile conventionnels ont également montré une diminution de la ductilité de la matrice et la présence de cavitation quand la teneur en argile augmentait. Dans ce dernier cas, toutefois, les zones de cavitation ont été clairement identifiées avec une rupture des agrégats d'argile ou des interfaces entre l'argile et la matrice, soulignant le rôle important de l'interface argile-matrice pour les propriétés des styréniques et, par extension, celles des acryliques. Pour donner un aperçu du rôle de la structure cellulaire, des simulations par éléments finis (EF) ont été utilisées pour étudier la distribution en contrainte hydrostatique dans les films styréniques nanocomposites sous déformation. Ces simulations ont montré des concentrations de contrainte principale dans les agrégats d'argile alignées dans le sens de la déformation appliquée, tandis que la contrainte hydrostatique dans la matrice restait relativement uniforme. Ces résultats suggèrent que tant que l'interface et les granulats d'argile restent stables, la cavitation peut commencer partout au sein la matrice, comme dans le polymère non modifié. Les simulations EF ont également été utilisées pour modéliser les propriétés élastiques à l'état caoutchoutique, et ont confirmé la nécessité de prendre en compte la présence d'une fraction immobilisée de matrice afin d'obtenir les modules de Young observés expérimentalement. Les résultats de ces calculs ont été jugés conformes à ceux obtenus à partir des modèles micromécaniques développés pour les mousses, confirmant la pertinence de ces derniers et suggérant que l'anisotropie locale des agrégats d'argile joue un rôle limité dans l'ensemble des propriétés élastiques.

Le résultat global de cette thèse a été la création d'une base physique générale pour prédire les relations structure-propriétés mécaniques d'une nouvelle gamme de matériaux à base de latex nanocomposites aux propriétés exceptionnelles, grâce à la possibilité d'incorporer des charges d'argile en quantités très élevées sans compromettre la mise en œuvre, et le vaste potentiel pour ajuster précisément la rigidité et les propriétés associées. En outre, les travaux ont souligné le rôle important d'un effet "nano", notamment aux températures supérieures à la transition vitreuse de la matrice, en dèmonstrant clairement que l'immobilisation de cette dernière à l'interface argile/matrice contribue aux propriétés thermiques et mécaniques. Ce travail devrait permettre de fournir des orientations solides pour le choix des paramètres morphologiques et des matériaux afin d'optimiser les propriétés mécaniques de base de ces latex nanocomposites par une synthèse contrôlée. De plus, avec de nouveaux développements dans la synthèse et dans la mise en œuvre et donc dans la qualité du film, il devrait finalement être possible d'étendre le modèle physique de base pour prendre en compte l'influence de la structure sur d'autres importantes propriétés pratiques, telles que la perméabilité et la résistance au feu.

Mots clés : laponite, nanocomposites avec argile, polymérisation en émulsion, polymérisation en miniémulsion, latex, mousse, mécanique des mousses, propriétés mécaniques.

Acknowledgements

This thesis is the result of a co-operation with many persons. I would like to thank them all.

First I would like to thank Prof. Jan-Anders E. Månson, my thesis director and head of the Laboratory of Composites and Polymers Technology (LTC), for trusting in me and for the excellent working conditions I found in his laboratory.

A large part of the credits for this work go to Dr. Christopher J.G. Plummer, my direct supervisor and co-director of my thesis. I would like to thank him for his rigorous approach to science he tried to teach me, for the many discussions we had and for his never-ending patience in correcting reports, papers and of course this manuscript.

Prof. Karen Scrivener of LMC (EPFL), Dr. Ludger Weber of LMM (EPFL), Prof. Raffaele Mezzenga (ETHZ) and Prof. José M. Kenny (University of Perugia) are kindly acknowledged for accepting to be part of the jury of my thesis exam.

Dr. Elodie Bourgeat-Lami, Dr. Véronique Mellon and Dr. Françis Pardal of LCPP (University of Lyon I, CPE) are kindly acknowledged for their kindness during my many visits in their lab, for teaching me about emulsions and for many practical advices about synthesis. I really appreciated our collaboration during my thesis, thank you very much. Dr. Emanuel Beyou of ISTIL (University of Lyon I) is also acknowledged for the NMP samples. This thesis had a lot to deal with electron microscopy. I would like to thank some members of CIME at EPFL: Dr. Marco Cantoni, Daniel Laub, Grégoire Baroz, Fabienne Bobard Dr. Graham Knott and Prof. Pierre Stadelmann. Thank you for your ready help and advices with the microscopes. Dr. Igor Stolitchnov of LC (EPFL) is warmly acknowledged for the access to XRD facilities.
I would like to thank some people of the Napoleon consortium for many discussions during our official meetings and in margin to them: Dr. Costantino Creton (ESPCI Paris), Prof. Catherine Gauthier, Dr. Laurent Chazeau and Dr. Jenny Faucheux (INSA Lyon), Prof. Yves Holl (ICS Strasbourg).

Of course I have to thank all the past and present members of LTC for the very good work environment they created. I think the mood of cooperation and the will of sharing and solving problems related to machines and measures make of LTC a very nice place to work. Special mentions are given to Prof. Véronique Michaud for accepting me as her office mate and also to Dr. Yves Leterrier for being both members of my PEX committee. Dr. Cristian Neagu is warmly acknowledged for the many discussions on modelling and FE calculations. Dr. Pierre-Etienne Bourban, Maria Delaloye and Chiara Donini are acknowledged for their administrative help, especially for the many problems related to Napoleon financial

affairs. François Bonjour and Sebastien Lavanchy are acknowledged for their technical help with machines, reparations and many practical advices. Not least I would like to say thank you to my semester or summer students for the great job they did: Christophe Mondoux, Valentin Chapuis, Elvis Fornasiere.

I would also like to thank my Italian friends who accompanied me along all these years: Pav, Matteo & Daniela, I Kosi, Laura C., Marco B., Murizio, Marta & Luca. Thank you for your friendship, for the many late night discussions and laughs and for your support even on the day of my exam.

Finally, thank you to my parents Elisa and Massimo for their trust and love, to my sister Arianna and most important to Laura for the love, comprehension and patience through these long years of study and sacrifices.

This work has been possible with the financial help of the European Framework 6 Project Napoleon, IP 011844-2 contract.

List of symbols

Greek Letters

Symbol	Unity	Definition
α	-	Filler aspect ratio
ϕ_{AM}	-	Weight fraction of the mobile amorphous fraction
ϕ_C	-	Weight fraction of crystalline phase
ϕ_c	-	Optical density of a TEM image in correspondence of a craze
ϕ_f	-	Volume fraction of the filler
ϕ_f	-	Optical density of a TEM image in correspondence of the film
ϕ_h	-	Optical density of a TEM image in correspondence of a hole
ϕ_m	-	Volume fraction of the matrix
ϕ_{Part}	-	Clay particle volume fraction
ϕ_{RAF}	-	Weight fraction of the rigid amorphous fraction
ν	-	Poisson's ratio
ν_0	-	Poisson's ratio of the matrix
ν_1	-	Poisson's ratio of the filler
ν_e	m^{-3}	Entanglement network density
ρ	g/m^3	Foam density
ρ	g/m^3	Mass density per unit volume
ρ_s	g/m^3	Density of the matrix in a foam
λ	Å	Wavelength
λ_{max}	-	Extension ratio
θ	°	Diffraction angle
Γ_0	N/m	Van der Waals surface tension in a craze
σ_f	Pa	Maximum fibril stress
σ	Pa	Stress
σ_{ij}	Pa	Stress components
$\langle\sigma_{ij}\rangle$	Pa	Homogenized stress
ε_{kl}	-	Strain components
$\langle\varepsilon_{ij}\rangle$	-	Homogenized strain
u_{lk}	m	Displacement
χ	-	Silicate volume fraction in the effective particle
η^*	Pa*sec	Complex viscosity
Ω	m^3	Total volume
$\Phi_{lap,aggr}$	-	Surface fraction of the clay in the aggregate in the RVE

Latin letters

Symbol	Unity	Definition
ΔC_p	J/g*K	Heat capacity step at T_g for the nanocomposite
$\Delta C_{p,pure}$	J/g*K	Heat capacity step at T_g for the matrix
a	m	Half of the RVE width
A	m^2	Surface area
A_k	m^2	Surface area of the k-th element in FE
A_{RVE}	m^2	Area of the RVE
A_{aggr}	m^2	Area occupied by all the clay aggregates in the RVE
b	m	Length of the clay aggregates
C_{ijkl}	Pa	Stiffness tensor components
d	m	Clay platelets distance
d	m	Size of the clay scattering unit
d_e	m	Root mean square distance between two entanglement points
d_{001}	m	Basal spacing of the clay
D	m	Fibrill diameter
D	m	Latex particle diameter
E	Pa	Tensile modulus
E_c	Pa	Composite Tensile modulus
E_f	Pa	Filler Tensile modulus
E_m	Pa	Matrix Tensile modulus
E_s	Pa	Tensile modulus of the matrix in a foam
E'	Pa	Tensile modulus of the foam
E'	Pa	Storage modulus
E''	Pa	Loss modulus
E_1	Pa	Tensile modulus normal to craze fibrils
E_1	Pa	Cell wall tensile modulus
E_2	Pa	Tensile modulus parallel to craze fibrils
E_{11}	Pa	Longitudinal tensile modulus
E_{33}	Pa	Transverse tensile modulus
$E_{H\text{-}T}$	Pa	Tensile modulus obtained by Halpin-Tsai model
$E_{M\text{-}T}$	Pa	Tensile modulus obtained by Mori-Tanaka model
$E_{m,wall}$	Pa	Matrix tensile modulus in the cell walls
F	N	Force
F_g	N	Gravitational force
F_d	N	Deformation force
g	m/sec^2	Gravitational acceleration
G	Pa	Shear modulus of the composite
G_0	Pa	Shear modulus of the matrix
G_1	Pa	Shear modulus of the filler
G'	Pa	Storage shear modulus
G''	Pa	Loss shear modulus
G_{ij}	Pa	Shear modulus components
K	Pa	Bulk modulus of the composite
K_0	Pa	Bulk modulus of the matrix
K_{IC}	$Pa*m^{0.5}$	Fracture toughness

l	m	Ligament length
l_e	m	Chain contour length
L	m	Contour length of an element in FE
M_e	g/mol	Mean molecular weight between two entanglement points
n	m	Half of the laponite layers per aggregate
P	Pa	Hydrostatic pressure
S	Pa	Stress required for scission chain crazing
S	Pa	Stress at the craze bulk interface
t	m	Tensile sample thickness
t	m	Laponite aggregate thickness
t_m	m	Thickness of the intercalated matrix layer
T_α	K	α Transition Temperature
T_g	K	Glass Transition Temperature
$Tg\delta$	-	Loss factor
U	J	Energy for chain scission
V	m^3	Volume
W_e	kJ/m^2	Essential work of fracture
W_p	kJ/m^2	Non Essential Work of Fracture
W_f	kJ/m^2	Total energy absorbed during fracture
x_i	m	Position

List of abbreviations

ABS	Acrylonitrile Butadiene Styrene
AFM	Atomic Force microscopy
AsAc	Ascorbic Acid
BA	Butyl Acrylate
CEC	Cation Exchange Capacity
CRR	Cooperative Rearranging Region
DDAB	Didodecyldimethylammonium Bromide
DENT	Double Edge Notched Tensile specimen
DLS	Dynamic Light Scattering
DMA	Dynamic Mechanical Analysis
DSC	Differential Scanning Calorimetry
EPFL	Ecole Polytechnique Fédérale de Lausanne
Et2O	Diethyl Ether
EWF	Essential Work of Fracture
FE	Finite Element
FEM	Finite Element Modeling
FTIR	Fourier Transform Infrared Spectroscopy
GMT	Glass Mat Thermoplastic
GPC	Gel Permeation Chromatography
HBP	Hyperbranched polymer
HCL	Hydrochloric acid
HDT	Heat Deflection Temperature
HIPE	High internal phase emulsion
HRR	Heat Release Rate
HT	Halpin-Tsai model
IFPZ	Inner Fracture Process Zone
i-PP	Isotactic polypropylene
KPS	Potassium Persulfate
LBL	Layer by layer
LCPP	Laboratoire de Chimie et Procédés de Polymérisation
LEFM	Linear Elastic Fracture Mechanics
LTC	Laboratory of composites and polymers technology
MA	Maleic Anhydride
MAF	Mobile Amorphous Fraction
MD	Melt flow direction
MDSC	Modulated Differential Scanning Calorimetry
MLR	Mass Loss Rate
MMA	Methyl methacrylate
MMT	Montmorillonite
MT	Mori-Tanaka model
Na^+MMT	Sodium Montmorillonite
NAPOLEON	NAnostructured POLymEr films with OutstaNding properties
NMP	Nitroxide Mediated Polymerization
NMR	Nuclear Magnetic Resonance

MPTMS	γ-methacryloxy propyl trimethoxysilane
N_d	Number of monomer droplets
N_p	Number of latex particle
OPDZ	Outer Plastic Deformation Zone
PA6	Polyamide 6
PA66	Polyamide 66
PA12	Polyamide 12
PDMS	Polydimethylsiloxane
PC	Polycarbonate
PE	Polyethylene
PEG	Polyethylene Glycol
PEO	Polyethylene oxide
PEO-MA	Poly(ethylene oxyde) 1000 monomethyl ether methacrylate
PES	Polyethylene sulphide
PLA	Polylactic aacid
PMMA	Polymethylmethacrylate
PP	Polypropylene
PS	Polystyrene
PTA	Phospotungstic Acid
PVA	Polyvinyl Alcohol
PU	Polyurethane
RAF	Rigid Amorphous Fraction
RVE	Representative Volume Element
SA	Stearyl Acrylate
SAXS	Small Angle X-ray Scattering
SBR	Styrene Butadiene Rubbers
SDS	Sodium Dodecyl Sulphate
SEN	Single Edge Notched geometry
SLS	Sodium Lauryl Sulfate
SEM	Scanning Electron Microscope
TEM	Transmission Electron Microscope
TBHP	Tert-butyl Hydroperoxide
TD	Transverse flow direction
TGA	Thermogravimetric Analysis
UPV	University of the Bask Country
VOC	Volatile Organic Compounds
WAXS	Wide angle X-ray Scattering
WP	Work Package
XRD	X-Ray Diffraction

Table of contents

Chapter 1

Introduction

1.1 Polymer nanocomposites

Polymeric materials have applications in many different fields, including aeronautics [1,2], automotive [3,4], textiles [5-9] and electronics [10, 11]. In recent years, polymer-based nanocomposites have received particular attention in both industry and academia. Layered silicates [12, 13], ceramic nanoparticles, such as silica or titania [14], and carbon [15,16] are among the most widely studied nanofillers. It is generally thought that the improved properties of nanocomposites with respect to conventional macro- and micro-composites are related to the modification of the structure and dynamics of the polymer matrix near the particle surface. Because of the very large specific surface area of nanoparticles, this fraction of the polymer may contribute significantly to bulk properties even at filler contents as low as a few wt %. Indeed, it has been demonstrated that it is possible to tailor the mechanical properties of the resulting nanocomposites by controlling the interphase properties [17]. On the other hand, when the filler consists of micron-sized particles, a high degree of loading (generally more than 20 % by volume) is required to obtain a substantial improvement in mechanical properties, and this may compromise processability, appearance and density, for example.

Nanofillers and nanoparticles have been combined with a range of polymer matrices in order to explore their potential for different applications. In the Laboratory of Composites and Polymer Technology (LTC) at the Ecole Polytechnique Fédérale de Lausanne (EPFL), for example, their compatibility with conventional polyurethane thermoset technology has been assessed through studies of the changes in rheological and mechanical properties of the resulting nanocomposites [18-21]. Other examples are the incorporation of layered silicates into melt spun

fibres and the processing of nanocomposite-based hybrid glass mat thermoplastic (GMT) materials [22-24]. The use of hybrid organic/inorganic nanomaterials to improve oxygen barrier properties was also studied by Singh et al. [25, 26]. Many other reports of the use of nanofillers may be found elsewhere in the literature. For example, the US Army research laboratory studied the ballistic impact strength of polycarbonate/layered silicate nanocomposites [27], Koo and Pilato investigated polymer nanocomposites for high temperature applications, e.g. fire retardant coatings [28], Nylon 6/clay nanocomposites were used by researchers of Toyota Company to produce timing belt covers [29] and these latter materials have also been used in covers for Mitsubishi engines [30]. A review of preparation techniques for different matrices and property improvements achieved with nanoparticles has been given by Alexandre et al. [12], while Jordan et al. focused mainly on the effects of nanofillers on viscoelasticity, crystallinity and density [31]. An extensive review of the processing, manufacturing and applications of polymer-based nanocomposites from the industrial point of view has also been given by Hussein et al. [32].

1.2 Background of this thesis.

The market demand for new products in the field of coatings, adhesives, paints and pigments is constantly increasing worldwide, as reflected by a global production growth of 6 % in 2007 and a forecast growth of 29 % for 2011. This drives research activity into the development of new materials with well defined and controlled properties. One of the greatest problems with the technology used to obtain such products is the use of organic solvents. Over the last few years, environmental considerations have brought about a radical change in the coatings and suspensions market. The production of waterborne coatings has doubled in the last ten years and today water based materials represent 55 % of the total paint and coatings consumption in Europe. According to new government regulations in Europe (EU directive 2004/42/CE), the emissions of volatile organic compounds (VOC) and air pollutants must be drastically reduced for this class of materials in two phases, with the second phase to be completed by January 1st 2010. This makes solvent based products less viable from an industrial point of view, but alternative water based products are still unable to match their performance. Properties such as scratch resistance, stiffness, solvent resistance and mechanical response in hot and humid environments still need to be improved [33].

In 2005 the European Community funded a project with the Sixth Framework Priority Programme called NAPOLEON (NAnostructured POLymEr films with OutstaNding properties),

whose objective is the development of new polymer coatings and adhesives using emulsion techniques. The basic idea is to use environmentally sustainable technology to produce latex materials with improved properties by controlling the structure of the individual latex particles. The project covers the study of these materials from the very fundamental level up to the development of a technology platform for industrial applications, and, for this reason, the research consortium comprises both academic and industrial partners. The milestones of the project may be summarized as follows:

1) Synthesis of stable dispersions of composite latex particles (either polymer/polymer or polymer/inorganic) with a diameter of 100 nm or less, solids contents of at least 50 wt % and controlled morphology. The focus has been on miniemulsion polymerization, whose characteristics will be reviewed in chapter 2.

2) Study of film formation and process optimization for the production of thin films with controlled morphologies.

3) Understanding of the relationships between the microscopic structure of their films and their macroscopic properties.

4) Scaling-up of production for industrial implementation of synthesis through the creation of pilot plants.

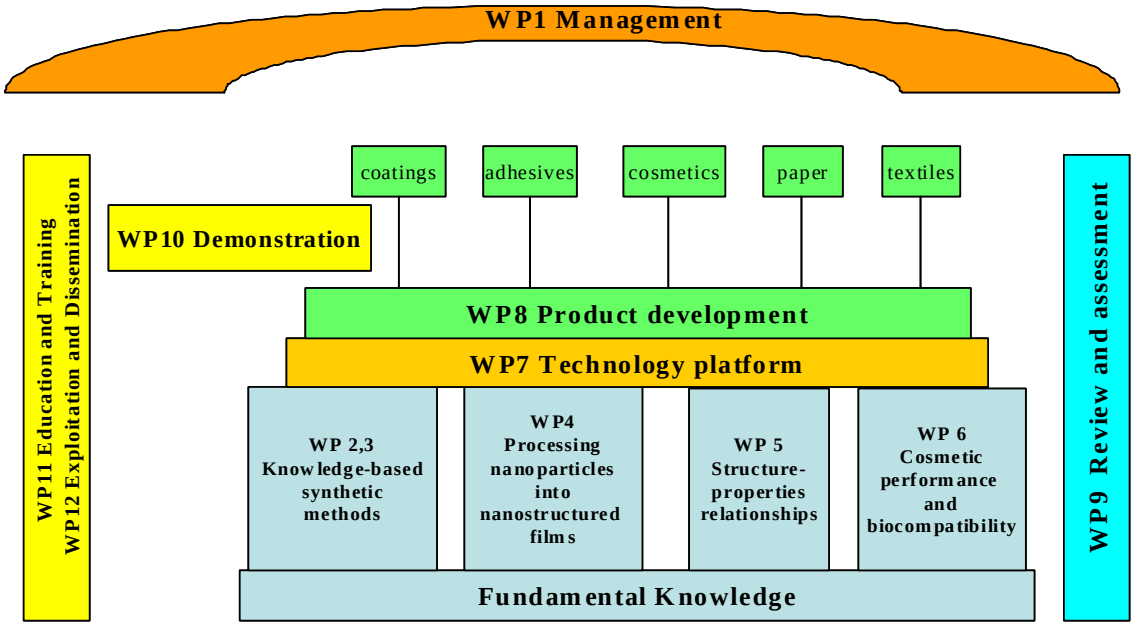

Fig.1 Structure of the Napoleon project.

The project consists of several work packages, with the overall structure shown in Fig. 1. The LTC at EPFL has been involved principally in work package 5 (WP5), focusing attention on the study of the structure-property relationships. The final goal of WP5 is the determination of the links between the film microstructures and their macroscopic properties.

The activity of the consortium was divided according to three main classes of material:

1) acrylic/alkyd resin latexes for coatings applications
2) acrylic copolymer/clay latexes for coatings applications
3) polyurethane latexes for adhesives applications.

The present work concerns the second family of materials, but particular attention has been given to styrenic/laponite systems, which are considered to represent a model for other more complex systems, as will be described in the following chapters.

1.3 Goal of this thesis

Polymer/clay nanocomposites offer a number of potential improvements in the field of coating materials. For example, increases not only in Young's modulus but also in tensile strength may be obtained for sufficiently good dispersions, without a loss in transparency, which is substantially maintained in the visible range of wavelengths at relatively low clay concentrations (<10 wt %). Fire resistance and barrier properties are also typically improved, the layered structure of the clay slowing down the diffusion of volatile products owing to the relative impermeability of the clay platelets. Again, good dispersion and high platelet aspect ratios are preferable in order to increase diffusion paths.

There has consequently been extensive work on polymer/clay nanocomposites in recent years (see for example [12] for a detailed review). However the full potential of nanoclays is yet to be achieved because of the difficulty in obtaining a sufficient degree of exfoliation and dispersion and because of a lack of knowledge of the effect of the clay on the microdeformation mechanisms and the properties of the interphase. With regard to the problem of clay dispersion, the latex route is known to be particularly promising. The advantage of the emulsion techniques used to obtain polymer/clay nanocomposite latexes is that the clay swells naturally in an aqueous medium, providing an efficient means of obtaining a high degree of exfoliation. The coupling between the clay and the polymer matrix may be assured by clay functionalization. Several reports of

polymer/clay nanocomposites obtained by emulsion polymerization are to be found in literature [34-38]. Moreover the synthetic techniques employed in the present work offer the potential for greatly improved control of the clay dispersion and orientation with respect to conventional techniques, such as melt blending or *in situ* polymerization. This may be achieved by the attachment of the clay to the latex particle surfaces or by encapsulating the clay within the particles. Attaching the clay to the latex particle surfaces is found to create a percolating clay-rich network, leading to remarkable mechanical property improvements, which will be analyzed in depth in the following chapters.

The synthetic techniques used for the production of the materials studied in this thesis were developed at the Laboratory of chemistry and polymerization processing (LCPP) of the University of Lyon I, France. Both conventional emulsion polymerization and miniemulsion polymerization were explored, this latter being the synthetic technique chosen for development within the Napoleon consortium. However the current limitations of miniemulsion polymerization, linked to the need to optimize its many steps, mean that conventional emulsion polymerization remains a more robust technique for clay nanocomposite production for coating applications at the present time.

Another important achievement of this work has been the incorporation of up to 50 wt % of clay with respect to the monomer in the latex without increasing the degree of filler aggregation at the macroscopic scale. This compares with maximum loadings of about 5 to 10 wt % generally reported for nanocomposites produced by conventional techniques. The introduction of such large amounts of filler has opened up new possibilities for the investigation of the origin and the effect of matrix immobilization in the interphase between the polymer and the clay. As mentioned previously, the enhancement of mechanical properties in nanocomposites has often been ascribed to the presence of an immobilized layer of matrix, but few attempts have been made to characterize or quantify this effect.

A third important aspect of the present work has been the effort to understand the relationship between the morphology at the meso- and nanoscale and the large strain mechanical behaviour of the latex based materials. Although a large number of papers can be found in literature describing the mechanical response of different nanocomposite systems, few analyze the effect of nanofillers on the deformation and fracture behaviour of the nanocomposites. Based on the results of mechanical tests and *in-situ* microdeformation experiments, it will be shown that material morphology plays a very important role on the macroscopic properties.

Although not considered a material of strategic interest for the Napoleon project, the main part of the present work has focused on latex-based polystyrene (PS)/laponite clay

nanocomposites, which represents a model system for fundamental studies. Nevertheless acrylic latexes with a similar morphology were also considered in an effort to establish the generality of the conclusions.

The experimental work on the latex-based materials may be summarized as follows:

1) Development of techniques to investigate single latex particle morphology. SEM and TEM related techniques have been extensively used in order to determine the morphology of the latex particles. This is a very important step in understanding and predicting the final film morphology.
2) Optimization of the conditions of film formation for different polymeric systems. The aim here is to obtain homogeneous, transparent and crack free films in a reproducible way.
3) Studies of the film properties. Several types of mechanical test have been performed under different conditions in order to study the effect of clay loading on the matrix. The results have been interpreted in terms of final film microstructures and relationships have been established. Mechanical models have been proposed based on composite theory modified *ad hoc*.
4) Study of the microdeformation mechanisms. The results of fracture experiments are combined with *in-situ* observations of the deformation by TEM.

To put the results from this last task into perspective, the microdeformation mechanisms in conventional clay nanocomposites obtained by melt blending and extrusion were also studied. Attention was focused on polypropylene (PP)/montmorillonite (MMT) nanocomposites. These systems differ from latex based materials in that relatively little control of the final morphology can be achieved and MMT contents are limited. Such studies allowed not only the direct comparison of two production techniques for clay nanocomposite materials but also the effect of the clay on two different classes of thermoplastic matrices (amorphous PS and semicrystalline PP), and hence to draw more general conclusions concerning the microdeformation of clay nanocomposites.

1.4 Outline

The report is organized as follows. In chapter 2 a review of the synthesis and properties of polymer clay nanocomposites is given. Particular attention is devoted to current knowledge in the field of interphase characterization. A brief description of the microdeformation mechanisms in amorphous and semicrystalline polymers is also given. Chapter 3 describes the synthesis and characteristics of the materials studied, together with experimental techniques and sample preparation methods. Chapter 4 describes the results of the investigation of PS/laponite nanocomposites obtained by emulsion and miniemulsion polymerization. Mechanical and thermal properties are discussed and models proposed to fit the experimental results. The swelling of laponite clay in water and results for PS/laponite nanocomposites obtained by conventional in-situ polymerization are also analyzed. Chapter 5 describes results for acrylic latex based nanocomposites in the light of the results for the styrenics. Chapter 6 describes studies of the microdeformation and fracture mechanisms in styrenic/laponite nanocomposites along with the results of macroscopic tests. Investigations of microdeformation and fracture in PP/MMT nanocomposites are also presented and general conclusions on the effect of the MMT on mechanical properties and fracture are drawn. Chapter 7 describes the results of simulations by finite element modeling (FEM) of the hydrostatic stress field in deformed PS/laponite nanocomposites and their implications for the microdeformation mechanisms discussed in Chapter 6. The tensile modulus of the same nanocomposites is also calculated in order to verify the conclusions of Chapter 4. Finally Chapter 8 gives the overall conclusions, and perspectives for future work.

1.5 Bibliography

[1] N. Bernet, M.D. Wakeman, P.-E- Bourban, J.-A.E. Månson, *An integrated cost and consolidation model for commingled yarn based composites.* Composites Part A **33** (2002) 495.

[2] J.A. Balta, J. Simpson, V. Michaud, , J.-A.E. Månson, J. Schrooten, *Embedded shape memory alloys confer aerodynamic profile adaptivity.* Smart. Mat. Bull. **12** (2001) 8.

[3] M.D. Wakeman, E. Eble, C. Norrey, T. Hemnann, J.-A.E. Månson, *Overinjection molding of stamped thermoplastic composite textile inserts - A process and property comparison of PP and PET based materials*. in *International SAMPE Symposium and Exhibition (Proceedings)*. 2005.

[4] N. Jansson, M.D. Wakeman, J.-A.E. Månson, *Optimization of hybrid thermoplastic composite structures using surrogate models and genetic algorithms.* Comp. Struct. **80** (2007) 21.

[5] M.D. Wakeman, L. Zingraff, P.-E. Bourban, J.-A.E. Månson, P. Blanchard, *Stamp forming of carbon fibre/PA12 composites - A comparison of a reactive impregnation process and a commingled yarn system.* Comp. Sci. Tech. **66** (2006) 19.

[6] S. Clifford, N. Jansson, W. Yu, V. Michaud, J.-A.E. Månson, *Thermoviscoelastic anisotropic analysis of process induced residual stresses and dimensional stability in real polymer matrix composite components.* Composites Part A **37** (2006) 538.

[7] D. Falconnet, P.-E. Bourban, S. Pandita, J.-A.E. Månson, I. Verpoest, I., *Fracture toughness of weft-knitted fabric composites.* Composites Part B **33** (2002) 579.

[8] J. Verrey, Y. Winkler, V. Michaud, J.-A.E. Månson *Interlaminar fracture toughness improvement in composites with hyperbranched polymer modified resins.* Comp. Sci. Tech. **65** (2005) 1527.

[9] J. Verrey, V. Michaud, J.-A.E. Månson, *Dynamic capillary effects in liquid composite moulding with non-crimp fabrics.* Composites Part A **37** (2006) 92.

[10] M.A. Doyle, P.O. Hagstrand, J.-A.E. Månson, *Process-induced internal stresses in phenol-formaldehyde cellulose composites.* Polym. Comp. **25** (2004) 214.

[11] Y. Leterrier, L. Medico, F. Demarco, J.-A.E. Månson, U. Betz, M.F. Escola, M.K. Olsson, F. Atamny, *Mechanical integrity of transparent conductive oxide films for flexible polymer-based displays.* Thin Solid Films **460** (2004) 156.

[12] M. Alexandre, P. Dubois, *Polymer-layered silicate nanocomposites: preparation, properties and uses of a new class of materials.* Mater. Sci. Eng. Report **28** (2000) 1.

[13] E.P Giannelis, *Polymer layered silicate nanocomposites.* Adv. Mater. **8** (1996) 29.

[14] J.E. Mark, *Ceramic-reinforced polymers and polymer-modified ceramics.* Polym. Eng. Sci. **36** (1996) 2905.

[15] G. Chen, C. Wu, W. Weng, D. Wu, W. Yan, *Preparation of polystyrene/graphite nanosheet composites.* Polymer **44** (2003) 1781.

[16] E.T. Thostenson, Z. Ren, T-W. Chou, *Advances in the science and technology of carbon nanotubes and composites: a review.* Comp. Sci. Tech. **61** (2001) 1899.

[17] C.L.Wu, Q. Zhang, M.Z. Rong, K. Friedrich, *Tensile performance improvement of low nanoparticles filled-polypropylene nanocomposites.* Comp. Sci. Tech. **62** (2002) 1327.

[18] C.J.G. Plummer, M. Rodlert, J.-L. Bucaille, H.J.M. Grűnbauer, J.-A.E. Månson, *Correlating the rheological and mechanical response of polyurethane nanocomposites containing hyperbranched polymers.* Polymer **46** (2005) 6543

[19] M. Rodlert, C.J.G. Plummer, Y. Leterrier, J.-A.E. Månson, *Rheological behaviour of hyperbranched polymer/montmorillonite clay nanocomposites.* Journ. Of Rheology *48* (2004) 1049

[20] M. Rodlert, C.J.G. Plummer, H.J.M. Grűnbauer, J.-A.E. Månson, *Hyperbranched polymer/clay nanocomposites.* Adv. Eng. Mat. **6** (2004) 715

[21] M. Rodlert, C.J.G. Plummer, L. Garamszegi, Y. Leterrier, H.J.M. Grűnbauer, J.-A.E. Månson, *Hyperbranched polymer/montmorillonite clay nanocomposites*. Polymer **45** (2004) 949

[22] C. Houphouet-Boigny, Ph.D. Thesis N° 3851 Ecole Polytechnique Fédérale de Lausanne (2007)

[23] C. Houphouet-Boigny, C.J.G. Plummer, M.D. Wakeman, J.-A.E. Månson, *Towards textiles-based fiber-reinforced thermoplastic nanocomposites : melt spun polypropylene-montmorillonite nanocomposite fibers.* Polym. Eng. Sci. **47** (2007) 1122

[24] C. Houphouet-Boigny, C.J.G. Plummer, M.D. Wakeman, J.-A.E. Månson, *Hybrid glass fiber-reinforced thermoplastic nanocomposites.* Journ Thermopl. Comp. Mat. **21** (2008) 103

[25] B. Singh, J. Bouchet, G. Rochat, Y. Leterrier, J.-A.E. Månson, P. Fayet, *Ultra-thin hybrid Organic/inorganic gas barrier coatings on polymers.* Surf. Coat. Tech. **201** (2007) 7107

[26] B. Singh, J. Bouchet, Y. Leterrier, J.-A.E. Månson, G. Rochat, P. Fayet, *Durability of aminosilane-silica hybrids gas barrier coatings on polymers.* Surf. Coat. Tech. **202** (2007) 208

[27] A.J. Hsieh, *Ballistic impact strength measurements of polycarbonate layered silicate nanocomposites,* ANTEC (2001)

[28] J. Koo, L. Pilato, *Polymer nanostructures materials for high temperature applications,* SAMPE Journal **41** (2005) 2

[29] F. Gao, *Clay/Polymer composites: the story,* Materials Today **7** (2004) 50

[30] H. Cox, *Nanocomposite systems for automotive applications,* proceedings of the 4th World Congress in Nanocomposites, EMC, San Francisco, 1-3 September 2004

[31] J. Jordan, K.I. Jacob, R. Tannenbaum, M.A. Sharaf, I. Jasiuk, *Experimental trends in polymer nanocomposites-a review.* Mat. Sci. Eng. Part A **393** (2005) 1

[32] F. Hussain, M. Hojiati, M. Okamoto, R.E. Gorga, *Review article: polymer-matrix nanocomposites, processing, manufacturing and application: an overview.* Journ. Comp. Mat. **40** (2006) 1511.

[33] J.-C- Daniel, C. Pichot, *Les latex Synthétiques: élaboration, propriétés, applications* (2006) 527 Lavoisier, Tec & Doc ed.

[34] M.W. Noh, D.C. Lee, *Synthesis and characterization of PS-clay nanocomposites by emulsion polymerization.* Polym. Bull. **42** (1999) 619.

[35] H. Li, Y. Yu, Y. Yang, *Synthesis of exfoliated polystyrene/montmorillonite nanocomposite by emulsion polymerization using a zwitterion as clay modifier*. Eur. Polym. Journ. **41** (2005) 2016.

[36]Y.K. Kim, Y.S. Choi, K.H. Wang, I.J. Chung, *Synthesis of exfoliated PS/Na−MMT nanocomposites via emulsion polymerization*. Chem. Mater. **14** (2002) 4990.

[37] D.C Lee, L.W. Jang, *Preparation and characterization of PMMA-Clay hybrid composite by emulsion polymerization.* Journ. Appl. Polym. Sci. **61** (1996) 1117.

[38] Y.S. Choi, M.H. Choi, K.H. Wang, S.O. Kim, Y.K. Kim, I.J. Chung, *Synthesis of exfoliated PMMA/Na-MMT nanocomposites via soap-free emulsion polymerization*. Macromolecules **34** (2001) 8978.

Chapter 2

Literature review of polymer/clay nanocomposites

The following chapter describes the state of the art relative to the synthesis and characterization of polymer/clay nanocomposites. In section 2.1 the different methods for the production of polymer/clay nanocomposites are reviewed, with particular emphasis on the advantages of emulsion-based technologies. Section 2.2 will be dedicated to a review of the property improvements reported for clay addition to polymer matrices. Not only the effect on the macroscopic mechanical response, but also the effect on thermal, barrier and rheological properties will be described. In section 2.3, the importance of filler size and dispersion in the polymeric matrix for obtaining the best property improvements is discussed. In this section the advantages of nanoscale fillers are presented together with the benefits arising from an efficient filler dispersion within the matrix. Section 2.4 describes the reinforcing mechanisms of clay and the causes of mechanical failure. The possibility of an immobilized interphase is addressed and techniques for its characterization and quantification are presented. Section 2.5 describes recent developments in the techniques used to investigate nanocomposite morphologies. Finally section 2.6 is a review of the deformation mechanisms in both amorphous and semicrystalline polymers, which provides the background for the discussion of microdeformation in the nanocomposites.

2.1 Synthesis of polymer/clay nanocomposites

2.1.1 Clay structure

Different clay fillers have been used for polymer nanocomposites, including montmorillonite, hectorite and laponite. They are all smectite type layered silicates with large specific surface areas and surface reactivities. Each silicate layer is approximately 1 nm thick and its lateral dimensions can vary from 30 nm to several microns. These sheets are held together by

electrostatic and van der Waals forces, forming particles called tactoids (Fig.2.1). The most critical requirement for preparing true nanocomposites is to break down these particles and disperse the single clay layers in the polymeric matrix [1-8]. Three different types of morphology, shown in Fig. 2.2, are generally possible with polymer/layered silicate composites: phase separated systems, intercalated systems in which the polymer infiltrates the clay layers and exfoliated systems, in which the single layers of the clay are dispersed in the polymer matrix.

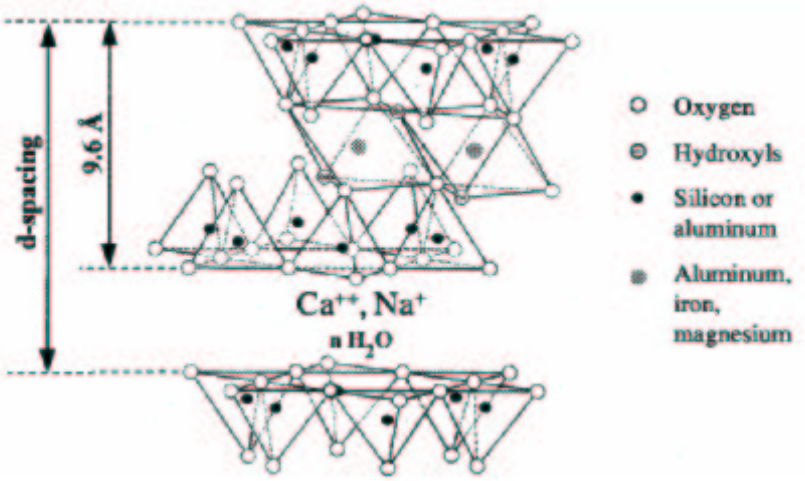

Fig.2.1 Montmorillonite structure.

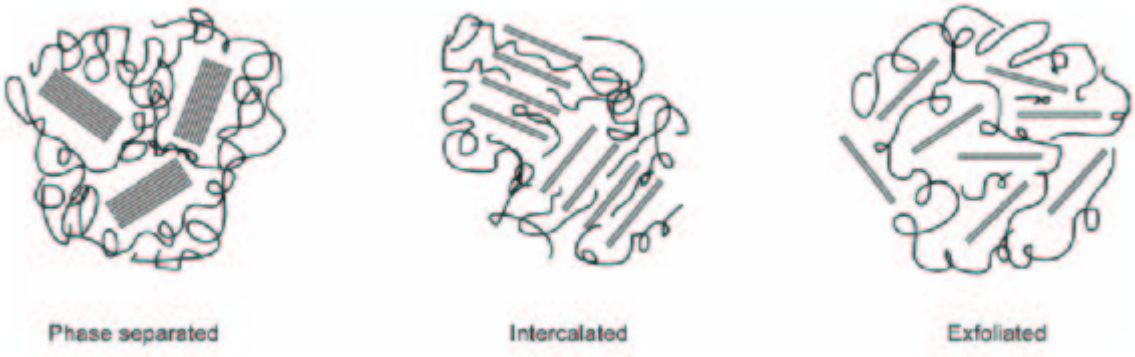

Fig. 2.2 Typical morphologies of layered silicate clays in polymer matrices [1].

2.1.2 Clay modification

Very weak physical interactions are generally present between the organic and inorganic phases, and in order to render the layered silicates compatible with a polymeric matrix, the clay surface is often modified. Clay surface modification through silane reactions [9] and cation exchange processes [10-14] have been extensively investigated. The strategy of silylation is based on the

creation of covalent bonds between an organosilane and the clay surface. In general the edges of the clay platelets contain hydroxyl groups that can react with silanols and form siloxane bonds [15]. If a silanol is chosen with a functional group able to react with the polymer, a covalent bond may be created between the clay filler and the polymer matrix [16].

The cation exchange modification involves the substitution of the structural clay cations by organic cations that can react with the polymer matrix or initiate polymerization of the monomers. For example, Yang at al. reported the synthesis of a cationic free radical initiator and its intercalation in montmorillonite galleries [17]. The total amount of exchangeable cations depends on the structure of the clay and on the total amount of available sites through a parameter called the cation exchange capacity (CEC). Some cations are highly hydrated in water, increasing the interlayer spacing and favouring the cation exchange. They are in general small cations such as Na^+, Li^+, Ca^{2+}, Mg^{2+}.

A third method of clay functionalization is the absorption of polar and hydrophilic oligomers such as Polyethylene oxide (PEO). Rubio and then Shen found that the mechanism of PEO adsorption onto silica is hydrogen bonding between the surface silanol groups of silica and the ether oxygen of the polymer [18, 19]. PEO hence naturally adsorbs onto clay platelets in aqueous solution [20]. This technique has been used for the functionalization of the clay materials studied in the present thesis.

2.1.3 Preparation of polymer/clay nanocomposites

Three main techniques have been used to obtain polymer/clay nanocomposites: *in situ* intercalative polymerization, melt blending and exfoliation adsorption by solution processing. Emulsion related techniques are a particular case of solution processing. These techniques will be described in the following sections.

2.1.3.1 *In situ* intercalative polymerization

In this approach, a modified silicate is swollen in the liquid monomer and polymerization is then initiated [21-24]. This is a particularly convenient method for preparing thermoset clay nanocomposites [7] but has also been used for thermoplastics [21,25-35]. The success of the method often depends on the tethering effect, which enables the surface modified clay to link with

the polymer chains during reaction. Many examples may be found in literature. The first system investigated by Toyota researchers was nylon 6 [21,26] (see Fig. 2.3), followed by polystyrene (PS) [27,28], polymethylmethacrylate (PMMA), [29,30], polyethylene (PE) [31-33] and also polypropylene (PP) [34,35].

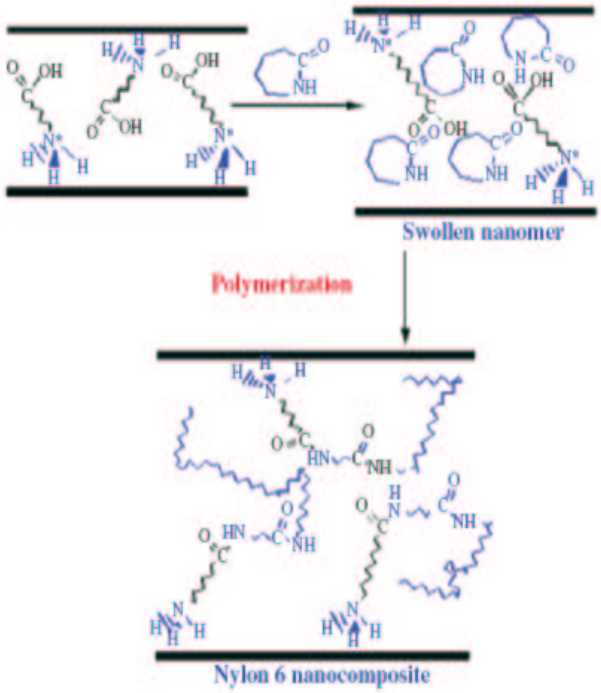

Fig. 2.3 Example of *in situ* polymerization of nylon 6 by using an ammonium salt modifier for the clay. The monomer is introduced after clay modification and then copolymerized with the clay modifier [26].

A recent development of *in situ* polymerization is the nitroxide-mediated polymerization of styrene from the surface of clay platelets. This has been used for montmorillonite clay (MMT) [36] and also for laponite [37]. In this case, controlled free radical polymerization takes place in the clay galleries with the advantage of strict control on the final polymer molecular weight. The main disadvantage of the *in situ* production of polymer/clay nanocomposites is that only a limited amount of clay may be incorporated. A large amount of clay implies a large number of nucleating sites for the matrix chains, leading to low molecular masses.

2.1.3.2 Melt blending

In melt blending, the clay is combined with the polymer matrix in the molten state and mixed mechanically e.g. by extrusion [5,22,38,39]. It is mainly used for thermoplastics and examples can be found in the literature of melt-blended nanocomposites based on polymeric systems such

as PS [40-42], PE [43,44], Nylon-6 [45-47], PP [25,48-53]. Melt blending can provide exfoliated structures in relatively polar polymers (e.g. Nylons), but it is harder to disperse the clay in apolar materials such as PS, PE or PP. In the case of PP, the usual approach has been to modify the matrix in order to make the polymer/clay interactions more favourable. PP was modified with hydroxyl groups (OH) or maleic anhydride (MA), then mixed with MMT to create a master-batch that is finally blended with pure PP [25,54]. If the MA content is too low, nanocomposites are not formed, but when the MA content is too high, the master-batch is immiscible with neat PP. Two improvements were proposed by Manias [55]. In the first, copolymers of PP with about 1 mol % of functionalized monomers such as MA, alcohol and methylstyrene were used. In the second an organic modifier was chosen for the MMT whose interactions with the clay were less favorable than the PP-MMT interactions. PP blends with organo modified clay for high volume clay nanocomposites preparation are commercially available as concentrates [50-53]. They have been extensively used in our institute to produce hybrid PP fibres or films by extrusion calendering. The clay content in the concentrates generally exceeds 30 wt % and neat PP matrix must be added to facilitate processing by melt blending. However, while this approach is appropriate for large-scale preparation, it does not necessarily lead to optimal clay dispersions.

The same dispersion problems reported above were also encountered for PE, where a high degree of exfoliation was only obtained in presence of large amounts of MA [56]. The composite morphology is also strongly influenced by processing, leading e.g. to orientation of the clay platelets along the direction of the extrusion flow [51]. In general, the longer the mixing time the better clay dispersion. A disadvantage of the long mixing times is that polymer chains may experience degradation due to the high shear forces and high temperatures in the screw extruder chamber. Mechanical mixing is also difficult at relatively high clay contents (more than 5 wt %) owing to the high melt viscosity.

2.1.3.3 Solution processing

In solution processing, a suitably modified clay is swollen in a solvent together with the polymer matrix. The clay stacks may be dispersed in media such as water, acetone, chloroform or toluene and the polymer adsorbs onto the delaminated sheets. By evaporating the solvent the system rearranges to produce the composite [57]. Examples are nanocomposites based on polyvinyl alcohol (PVA) in water [20,58], PS and PMMA in toluene [59] and polyethylene glycol (PEG) in chloroform [60]. An example of the application of solution processing in our institute is the

dispersion of MMT platelets using hyperbranched polymers (HBP) in water [61, 62]. The HBP contains a high density of hydrophilic end groups that can interact with the MMT platelets, stabilizing their dispersion in the final composite. It was shown to be possible to prepare MMT//HBP mixtures containing up to 20 wt % of exfoliated MMT using this technique. The MMT/HBP mixtures could then be further processed with an organic solvent and hardener to produce highly exfoliated polyurethane nanocomposites.

However, while good exfoliation is obtained with solution techniques, they are generally not considered of wider commercial interest because of the large amount of solvent required, making it expensive and environmentally unfriendly. The main difficulty is in overcoming the strong tendency of the clay to form aggregates on drying, although this may be reduced or avoided by intense stirring and/or sonication of the solution.

2.1.3.4 Emulsion and miniemulsion polymerization

Emulsion polymerization is a well known technique for obtaining polymer composite materials and it has already been widely developed in both academia and industry [63]. The monomer is dispersed in an aqueous medium that contains the initiator and surfactant. In the aqueous phase, most of the monomer is present in form of droplets of a few microns in diameter stabilized by surfactant, although small amounts are also present in the aqueous phase, depending on the monomer solubility, and in surfactant micelles. The initiator radicals are generally thermally activated and they start to react with the small amount of soluble monomer, generating oligoradicals. As these become bigger, they enter the micelles. The reaction proceeds by migration of the monomer from the droplets to the micelles through the aqueous phase. The surfactant associated with the original droplets and with empty micelles redistributes to stabilize the growing particles. Micellar nucleation and growth is typical of monomers with low solubility in water (e.g. styrene). A sketch of this mechanism is given in Fig. 2.4. More soluble monomers undergo homogeneous nucleation so that after formation of the oligoradicals, the particles precipitate and continue to grow by monomer addition or coagulation.

As already discussed in paragraph 1.3, the advantage of emulsion techniques for obtaining polymer/clay nanocomposites is that the clay may undergo natural swelling in an aqueous medium and this provides a very efficient way to obtain a high degree of exfoliation. The interaction between the modified organophilic clay and the polymer matrix is mainly ensured by functionalization of the clay as described in section 2.1.2. To date mainly PS and PMMA matrices have been used to prepare clay nanocomposites from latex dispersions [64-68].

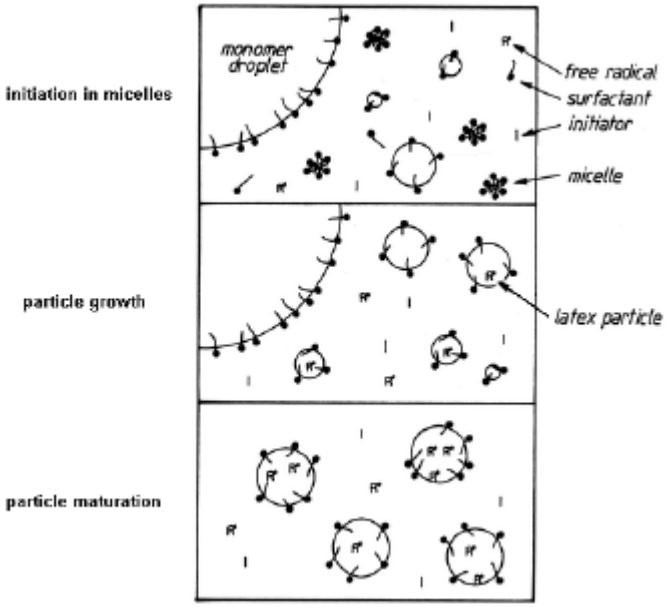

Fig. 2.4 Schematic of emulsion polymerization via micellar growth (from http://www.rsc.org).

To our knowledge, Lee at al. were the first to prepare a polymer clay nanocomposite system by emulsion polymerization [67]. MMA was dispersed in water and polymerized in presence of Na^+MMT. The PMMA obtained in this way possessed a similar molecular weight to commercial PMMA. These preliminary results drove further development of the technique, but dispersion of clay in water was consistently found to give better results than in organic solvents [69].

In the initial reports on polymer/clay nanocomposites obtained by emulsion polymerization, no analysis of the single latex particle morphology was provided. In more recent papers, however, cryo-transmission electron microscopy (TEM) has been used to study the location of clay with respect to the matrix particles. In most cases the clay is attached at the particle surfaces so as to form a shell around the particles [9, 11, 16, 70, 71].

For clay encapsulation in the particles, the technique of miniemulsion polymerization appears more attractive than conventional emulsion polymerization [72-80]. The general mechanism of miniemulsion polymerization is shown in Fig. 2.5. The organic phase containing the monomer(s) (phase I) is mixed by ultrasonication or high pression homogeneizers with an aqueous phase (phase II) containing surfactant and a co-emulsifier (usually hexadecane or hexadecanol) and nanodroplets are formed.

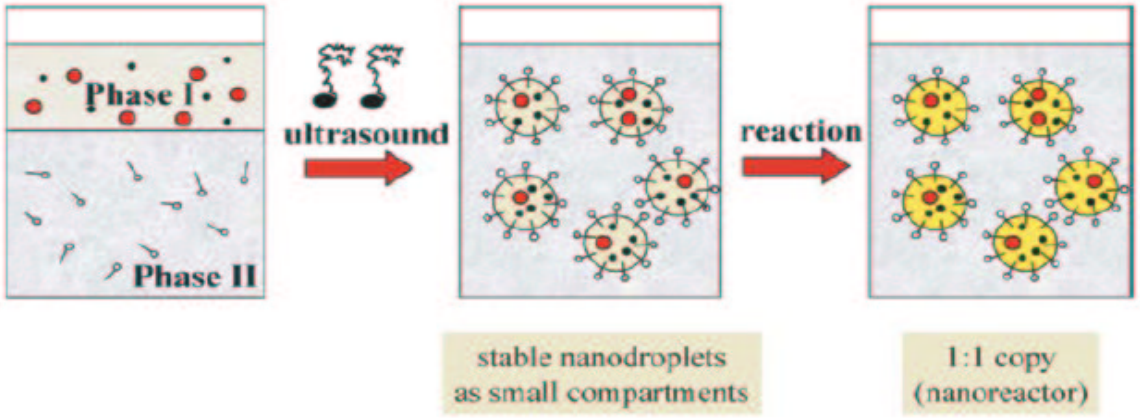

Fig. 2.5 Mechanism of miniemulsion polymerization [63].

The role of the co-emulsifier is to prevent droplet coalescence by segregating to the water/oil interface and/or to limit the diffusion of the oil phase from smaller to larger droplets. The main difference between conventional emulsion polymerization and miniemulsion polymerization is that the monomer is directly incorporated into the nanodroplets in this latter, so that no monomer migration through the aqueous phase takes place during the reaction. The size of the droplets remains in principle very small (between 50 and 500 nm) and there is a one to one conversion of droplets into polymer particles. Thus coalescence and secondary nucleation are avoided. The morphology of clay-based nanocomposites obtained by miniemulsion polymerization depends on the medium in which the clay is dispersed after modification. If the clay is dispersed in water then it will tend to attach to the surface of the polymer particles, but if it is dispersed in the monomer, it will be encapsulated. Examples of the two kinds of morphology are shown in Fig. 2.6.

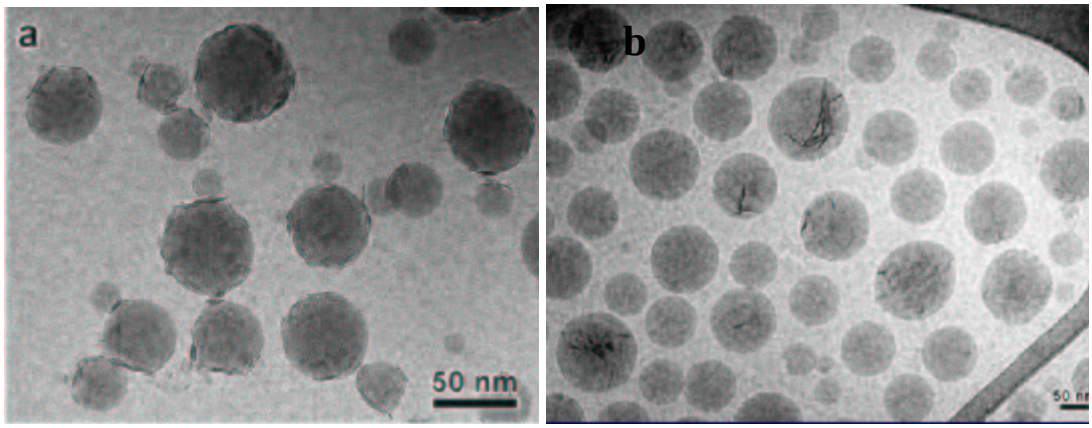

Fig. 2.6 Cryo-TEM images of latex particles with (a) clay on the surface and (b) with encapsulated clay [81].

Relatively little work in the field of polymer/clay nanocomposites has involved miniemulsions [82-85] and this remains a relatively unexplored research area. However, it has been established that encapsulation by miniemulsions is more effective with spherical particles such as silica or titania with a narrow size distribution [see 78 and its references], than with high aspect ratio particles such as clay platelets.

Within the Napoleon project, miniemulsion polymerization has shown two other main limitations for the synthesis of polymer/clay nanocomposites. The first is monomer conversion that is far from being complete, leaving about 20 wt. % of unreacted monomer. This could have drawbacks for film properties, the monomer acting as a plasticizing agent, and means that a stripping process is needed. It has also been suggested that in systems in which the clay is located at the particle surface, the same platelets may act as a barrier to radical entry and in the encapsulation process, it appears that some monomer molecules remain trapped within the clay layers and are inaccessible to the growing radicals. A second problem with encapsulation is the difficulty of dispersing the clay in all the polymer particles. Only about 25% of latex particles are typically found to contain clay platelets, the others remaining empty [81]. These two problems must be solved before envisaging a systematic study of the mechanical properties of the miniemulsion based systems, as will be discussed in the next chapters.

2.2 Properties of polymer/clay nanocomposites

In general polymer/clay materials show improved stiffness, strength and heat resistance and decreased gas permeability with respect to the neat matrix. All these improvements may in principle be obtained at much lower filler contents than for conventional composite materials (less than 5 wt %), representing an advantage in terms of weight and processability. In the following sections, current knowledge of the properties of polymer/clay nanocomposites is reviewed.

2.2.1 Mechanical properties of polymer/clay nanocomposites

The first class of polymer/clay nanocomposites to be systematically studied was nylon-6/MMT. For clay contents around 4-5 wt % the elastic modulus almost doubles and the tensile strength increases by about 50 % [86-88]. These nanocomposites were all obtained by *in situ* reactions (see section 2.1.3.1). A representative commercial nylon-6 with organically modified MMT,

obtained by *in-situ* polymerization, showed an 88 % increase in elastic modulus for a clay loading of 6 wt % [89]. The importance of the clay dispersion was confirmed by two distinct studies. Liu at al. obtained an intercalated nylon-6/MMT nanocomposite containing 4.2 wt % of clay by melt blending and showed an increase of only 25 % in modulus [46]. Fornes at al. prepared exfoliated nylon-6/MMT systems by melt processing that showed an almost 100 % increase in elastic modulus [45]. In all cases the increases in elastic modulus and tensile strength were accompanied by significant decreases in elongation at break.

PP/Clay nanocomposites are characterized by a sharp increase of tensile modulus at low clay loadings (below 4 wt %) followed by a decrease for higher clay contents [90,91]. The reinforcement effect depends on the processing method and on the nature of the PP and MMT. Improvements in tensile modulus ranging from 28 to 50 % can be observed [92]. It has been shown that for a given PP matrix, the reinforcement strongly depends on processing technique [51]. A nearly two-fold increase in tensile modulus was observed for extrusion calendered PP-MMT films tested in the flow direction MMT contents of 6 wt %. The tensile modulus decreased slightly for the same films tested in the transverse direction, while only limited reinforcement was found in injection moulded specimens. Also, the addition of maleic anhydride (MA) groups to the polymer chains can be beneficial for stiffness, allowing an increase in clay contents. PP-MA/MMT nanocomposites containing 7.2wt % of MMT showed an increase in tensile modulus of about 30 % [93] and PP-MA/fluoromica nanocomposites showed a twofold tensile modulus increase at 10 wt % loading [94]. However, the addition of compatibilizers such as MA may depress the fracture toughness of the nanocomposite, so that only moderate quantities of MA and high matrix molecular masses are needed for a good toughness/stiffness balance [95]. In general, little change in the tensile strength with respect to the neat PP matrix is observed. It has been reported by Houphouet-Boigny that tensile strength shows modest increases for clay contents up to 3 to 4 wt % and then slowly decreases when the clay content is further increased [51]. The preparation technique was again found to have an influence, injection moulded samples showing higher strengths than the extruded calendered samples. The mechanical behaviour of these PP-based materials will be further analyzed in Chapter 6. In general, the elongation at break is found to be significantly lowered for PP clay nanocomposites.

In the case of PE/clay nanocomposite films, only small stiffness increases were observed in blown films modified with MA and containing 1.5 wt % of MMT [96]. *In-situ* polymerization was more effective in reinforcing PE nanocomposites containing 4.5 wt % of hectorite. In one system, the tensile modulus increased by about 85 % [31] while the tensile strength and elongation at

break remained unchanged. For higher clay loadings the elongation at break decreased drastically.

In the PMMA/MMT nanocomposites prepared by emulsion polymerization by Lee and co-workers, tensile modulus increases of about 50 % were obtained, together with small increases in tensile strength [67]. The same range of stiffness increases were found for the PMMA/sodium-MMT nanocomposites produced by Choi at al. and tested by DMA [68]. In this case, higher reinforcement was observed in the rubbery state of the PMMA matrix. More contradictory results were obtained for both the tensile modulus and tensile strength of PMMA/MMT nanocomposites by Su et al. [97]. Although some beneficial effect of clay was observed, the influence of the total clay content remained unclear.

PS/clay nanocomposites always show an increase in tensile modulus with clay content [13, 14, 65, 99], while dramatic decreases in tensile strength and elongation at break are generally observed, even at low filler loadings [64, 98]. Only when a particularly good interaction is established between the clay and the PS matrix, is a small increase in tensile strength observed at around 1-2 wt % of clay, but it decreases rapidly at higher loadings [100, 101]. These results appear independent of the fabrication technique and the degree of clay dispersion.

Polyurethane (PU)/MMT nanocomposites obtained mixing the clay with HBPs also showed an increase in tensile modulus. The presence of the HBP resulted in a higher degree of exfoliation of the MMT and hence in a higher reinforcement. At 4.9 wt % of MMT, the tensile modulus was more than doubled with the HBP, while without HBP it remained almost unchanged [62, 102]. The tensile modulus depends not only on the processing technique [102] but also the type of MMT employed and hence its specific interactions with the HBP [62]. The best reinforcement was obtained when the PU matrix is in the rubbery state [102].

To summarize, it may be concluded that, in general, the addition of clay platelets to thermoplastic polymers results in significant increases in stiffness, depending on the total clay content and the particular interactions between the filler and the polymer matrix. In polar matrices such as nylons or PMMA, improvements in tensile strength may also be obtained by clay addition, while in the case of PP and PE the fracture resistance remains constant at low clay loadings and then slightly decreases. In PS however, the tensile strength is severely decreased by clay addition in the absence of favourable interactions between the PS and the clay. The elongation at break, on the other hand, always decreases in the presence of clay platelets. Results obtained by various authors for stiffness and tensile strength in different matrices are summarized in Fig. 2.7. From these data is seen that clay contents are generally limited in the literature to a maximum of around 10 wt %.

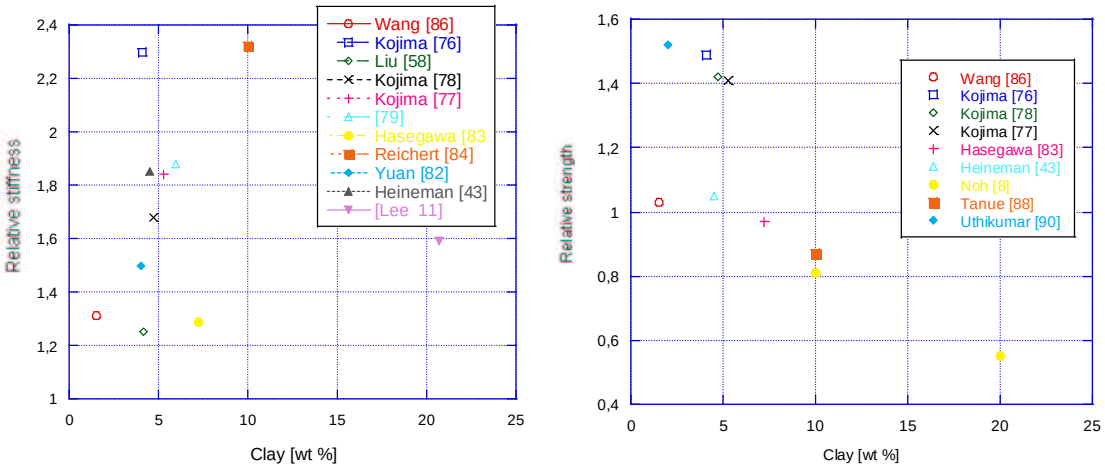

Fig. 2.7 Examples from the literature of the stiffness and strength variation with clay content in different matrices.

2.2.2 Thermal properties of polymer/clay nanocomposites

The thermal stability of polymer/clay nanocomposites is usually studied by thermogravimetric analysis (TGA). In this technique, the sample mass loss is recorded as a function of temperature. The incorporation of the clay into the polymer matrix enhances the thermal stability, the clay platelets acting as a mass transport barrier to degradation products and as thermal insulators [-105]. Burnside at al. found an increase of 140 K in the temperature corresponding to the point of 50 % mass loss for polydimethylsiloxane (PDMS) nanocomposites filled with 10 wt % MMT [39] as shown in Fig. 2.8.

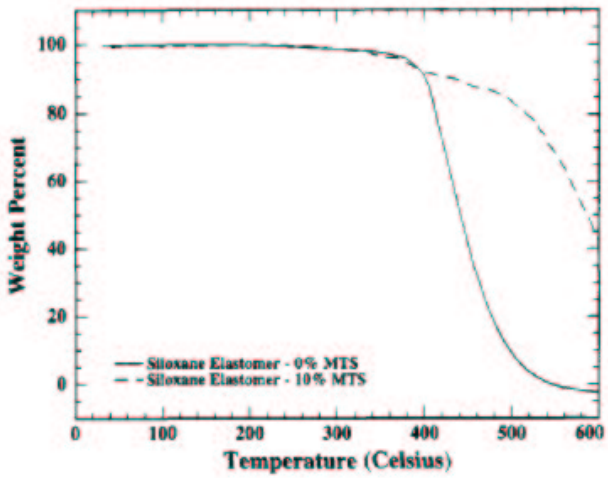

Fig. 2.8 TGA analysis of PDMS (solid line) and PDMS/clay nanocomposites (dashed line) [39]

Another measure of the thermal stability of polymer/clay nanocomposites is the heat deflection temperature (HDT). In this case the sample is positioned on bearings at both extremities and loaded. The temperature at which a specific deflection occurs is recorded. In the

case of nylon-6/MMT nanocomposites HDT increased from 65° C for the pure matrix to 152° C [88] for a clay content of 4.7 wt %. Similar results were also obtained for PP [106].

Flame retardance was also observed in polymer/clay nanocomposites and the subject has been extensively reviewed by Gilman [107]. The most common method to measure this property is cone calorimetry. This provides a measure of the heat release rate (HRR) and the mass loss rate (MLR) as a function of time. In PP/MMT with 8 wt % clay loading the peak HRR is reduced by about 57 % with respect to the neat matrix [108]. Significant decreases in peak HRR were observed on clay addition to PS, PA6, PA12, PP and ABS nanocomposites [107, 109]. The decrease in peak HRR is attributed to the reduced mass loss rate and the resulting lower fuel feed rate to the gas phase in the presence of clay platelets.

2.2.3 Barrier properties of polymer/clay nanocomposites

Barrier properties are of great importance in applications such as food packaging and coatings. High aspect ratio platelet-like fillers are very efficient in decreasing the gas permeability of polymer matrices. This may be due to an increase in the so-called “tortuosity factor”, the path that a molecule must follow to diffuse through a certain material thickness. PP/MMT is of particular interest for the packaging industry. This polymer offers a strong barrier against humidity but it is relatively permeable to oxygen. Osman et al. showed that the oxygen permeation coefficient in PP/MMT nanocomposites decreased strongly with increasing clay content [110]. In the case of hygroscopic barrier polymers, a reduction in water absorption rates by about 40 % was observed in PA6/clay nanocomposites with 5 wt % MMT [246] and a decrease of up to 80 % was found for 5 vol % polycaprolactone/MMT nanocomposites [111].

It has been pointed out by many authors that the best improvements in barrier properties of polymer/clay nanocomposites are obtained with a fully exfoliated morphology rather than with partial intercalation [58, 112] and that poorly oriented platelets should be less effective than aligned platelets in reducing permeability [112].

2.2.4 Rheological properties of polymer/clay nanocomposites

Clay dispersion in a polymeric matrix strongly influences the rheological properties. The response in nanocomposite systems is characterized by an increased viscosity and a non terminal behaviour of the storage and loss moduli in oscillating shear in the limit of low frequencies [113,114, 102]. These effects were also observed in MMT/HBP mixtures by Rodlert et al. [62, 115, 116]. In this case just 1 wt % of MMT gave rise to a drastic change of rheological behaviour [62]. Clay nanocomposites undergo strong shear thinning in comparison to the pure matrix as a function of frequency, and the Newtonian plateau is shifted toward lower frequencies [117-119,102]. This is an indication of a more solid-like behaviour, presumably due to the effect of percolated contacts between the clay platelets. The application of large strains during oscillating shear deformation leads to the alignment of the clay platelets and the break-up of the percolated structure [120-122].

2.3 Effect of filler size and dispersion in polymer/clay nanocomposites

The effect of filler quantity, size and dispersion has been analysed not only for clay fillers but also for many other types of particulate reinforcement agents such as silica, $CaCO_3$ and glass beads. The importance of these parameters has been emphasized by many authors, especially for fillers with nanometric dimensions, where the specific surface area of the single particle becomes very large with respect to more common micron sized reinforcements. The effect of filler size on stiffness with and without surface modification has been demonstrated for different fillers and polymeric systems in [123]. Tensile strength and impact properties can be improved by decreasing the filler size and increasing phase adhesion [124]. The reinforcement effect has been shown to be weakly dependent on filler size in the 1 to 50 micron range, but it is strong when the particle dimensions are in the 0.1 to 1 micron range [125]. Many other studies may be found in the literature of the effect of filler size on the properties of composite materials, and the greatest benefits are obtained when particle dimensions are kept to the nanometric scale. This is especially true at relatively high loadings, because of the large amount of interphase that is created [126-128].

Property improvements in clay nanocomposites are obtained at low loadings (few percent), but when the filler content is increased, a plateau is often reached [129, 130]. In general, the better the exfoliation of the clay, the greater is the reinforcement [131, 132]. Fig. 2.9

(a) shows the results for the elastic modulus of epoxy/Cloisite 30B and epoxy/NanomerI.28E nanocomposites. The better reinforcement in the first material was ascribed to the higher degree of clay dispersion, as shown in Fig.2.9 (b) and (c) [133].

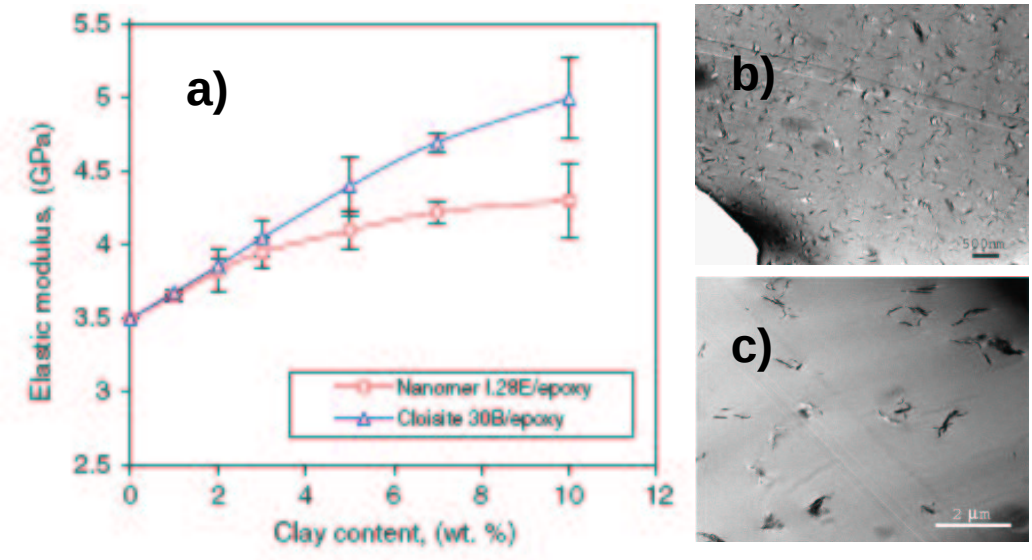

Fig. 2.9 Elastic modulus of (a) epoxy/clay nanocomposites and microstructure of (b) epoxy/Cloisite 30 B and (c) epoxy/Nanomer I.28E respectively [133]

2.4 The reinforcement in nanocomposites

The reinforcement in nanocomposite can be analyzed in terms of two different effects: the role of the interphase, which becomes very important owing to the high specific surface area of the filler, and the classical geometrical reinforcement as in conventional composite materials. In what follows these will be discussed in more detail. Basic results for foam mechanics are also summarised since these will be required in the following chapters.

2.4.1 The role of the interphase.

In composite materials it is generally accepted that three different phases must be considered: the matrix, the filler and the so-called interphase. This latter is formed by those molecular chains which strongly interact with the filler surface. The importance of the adhesion between matrix and filler at the interphase is recognised to be a crucial issue for the final materials properties [134]. Considerable effort has therefore been devoted to functionalization of the filler surface.

Some authors consider the reinforcement to be the result of the immobilization of polymeric chains at the filler surface, either by chemical reaction with surface modified fillers or entanglement with a surface modifier [10, 135]. Attempts have been made to estimate experimentally the interphase volume but the results are strongly dependent on the technique used (FTIR vs. TEM/TGA) and are based on various assumptions [136-139]. The filler particles are considered to be perfectly spherical, which is not necessarily realistic, and the use of TGA does not appear to provide realistic results. In some cases, experimental results have been fitted by assuming that the interphase has intermediate properties between the filler and the bulk matrix with a continuous gradient in modulus, but no physical evidence has been provided for this [140-142]. A more efficient technique for revealing the presence of a partially blocked layer on the filler particle surface is solid state nuclear magnetic resonance (NMR). It has been applied to filled rubbers by studying the magnetization decay after a pulse sequence of a magnetic field [143-146]. The relaxation process showed a rapidly decaying component corresponding to the unbound matrix and a slowly decaying component corresponding to the bound matrix. In the cited cases, the interphase thickness was estimated to be in the range of 1-2 nm [143]. More generally NMR has been employed to study the nature of the interactions in composite materials [147, 148]. It is a very local and sensitive technique, but not widely available.

Another technique that suggests the existence of an interphase is dynamic mechanical analysis (DMA). Eisenberg et al. found two loss factor peaks in polymer/silica nanocomposites, one corresponding to the conventional α transition of the matrix and the second at higher temperatures [149,150]. These findings were interpreted as the relaxation of an immobilized portion of the matrix constituting an interphase. The same results received a different interpretation by other authors, who proposed that the second peak in the loss factor diagram could arise from the formation of a macroscopic gel in highly filled systems [151]. It should be emphasized that the presence of a peak in dynamic loss curves does not necessarily indicate the occurrence of a glass transition. A simple method for the calculation of the interphase thickness using DMA was proposed by Iisaka and Shibayama [152]. From the ratio of the loss moduli at T_α of the composite to that of the neat matrix they derived a parameter that is related to the interphase thickness. The calculations for filled PMMA and PS nanocomposites gave interphase thicknesses ranging from 60 nm to 1 μm, which appear quite unrealistic. A calculation of the interphase thickness by normalizing the area under the loss tangent peak curves was applied by Arrighi et al. to SBR/silica nanocomposites and the results were consistent with those of NMR experiments [153]. The nanocomposites showed the conventional loss tangent peak of SBR and a peak at higher temperature that was ascribed to the relaxation of the bound interphase. The

relative peak areas corresponding to the two matrix portions were considered to represent their volume fraction. The interphase thickness was obtained by geometric considerations.

One important technique for the study the dynamics of polymer chains in the vicinity of filler particles is differential scanning calorimetry (DSC). In cases where two different glass transitions can be detected, the volume fraction of the bound layer can be calculated by analyzing the step heights in heat capacity-temperature plots (see Fig. 2.10):

$$\frac{\phi_B}{\phi_M} = \frac{\Delta C_B}{\Delta C_M} \qquad \text{eq. 2.1}$$

where ϕ_B and ϕ_M represent the volume fraction of the bound layer and of the matrix and ΔC_B and ΔC_M are the heat flow step in correspondence of the secondary and primary glass transition [154].

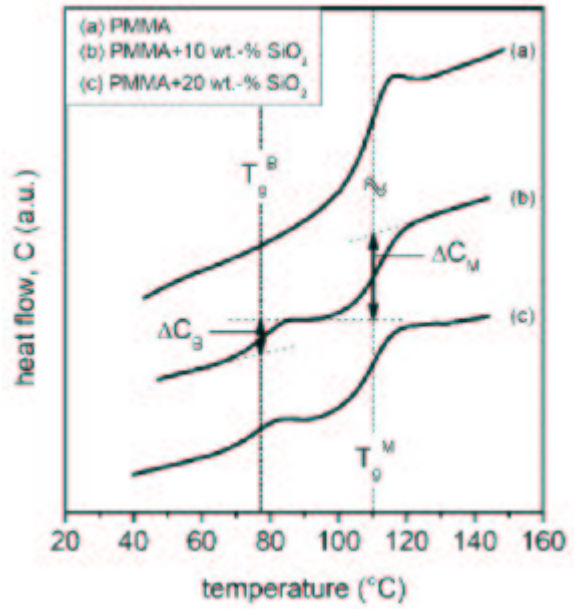

Fig. 2.10 Heat flow diagrams for PMMA/SiO_2 nanocomposites [154]

In the case of PA6/clay nanocomposites a restriction in chain mobility was observed in the presence of clay due to the formation of γ polymorph in the vicinity of the filler platelets [155]. The total amount of this phase is strongly dependent on the type of clay functionalization.

One very important indication of the existence of an interphase in polymer nanocomposites is a decrease in the height of the heat capacity step at the glass transition when the filler content is increased [156]. Some authors proposed that the polymer matrix trapped inside filler aggregates (for instance, intercalated polymer) does not take part to the glass transition [157]. It was found that when the spacing *d* between the clay platelets is less than the characteristic Donth's length for the glass transition (the size of the region of cooperative motion),

the intercalated material does not undergo a thermal transition [158, 159]. The decrease of the glass transition intensity with increasing filler content was explained by a partial suppression of the cooperative chain motion due to confinement effects and to surface interaction between the matrix and the filler particles [160]. Quantification of the amount of interphase was carried out by analogy with the analysis of semicrystalline polymers. It has been shown that in semicrystalline polymers a rigid amorphous fraction (RAF) is present, consisting of the amorphous portion that is in contact with the crystallites and which does not show a glass transition [161]. The weight fraction of the RAF can be obtained by the following equation:

$$\phi_{RAF} = 1 - \phi_C - \phi_{AM} = 1 - \phi_C - \frac{\Delta C_p}{\Delta C_{p,pure}} \qquad \text{eq. 2.2}$$

where ϕ_C is the crystalline fraction, ϕ_{AM} is the mobile amorphous fraction (MAF), ΔC_p and $\Delta C_{p,pure}$ are the heat capacity increments at the glass transition for the semicrystalline and the fully amorphous polymer respectively. Using the same criteria it was proposed by Sargsyan et al. that the amount of immobilized polymer in nanocomposites based on amorphous polymers could be described by [162]:

$$\phi_{RAF} = 1 - filler - \frac{\Delta C_p}{\Delta C_{p,pure}} \qquad \text{eq. 2.3}$$

In nanocomposites with amorphous matrix the amount of immobilized interphase can therefore be estimated by a measurement of the heat capacity at the glass transition for the pure matrix, $\Delta C_{p,pure}$, and the nanocomposites ΔC_p. Examples of the decrease of the heat flow step at T_g with increasing filler content are given in Fig. 2.11 together with estimates of RAF for PMMA/laponite nanocomposites [162].

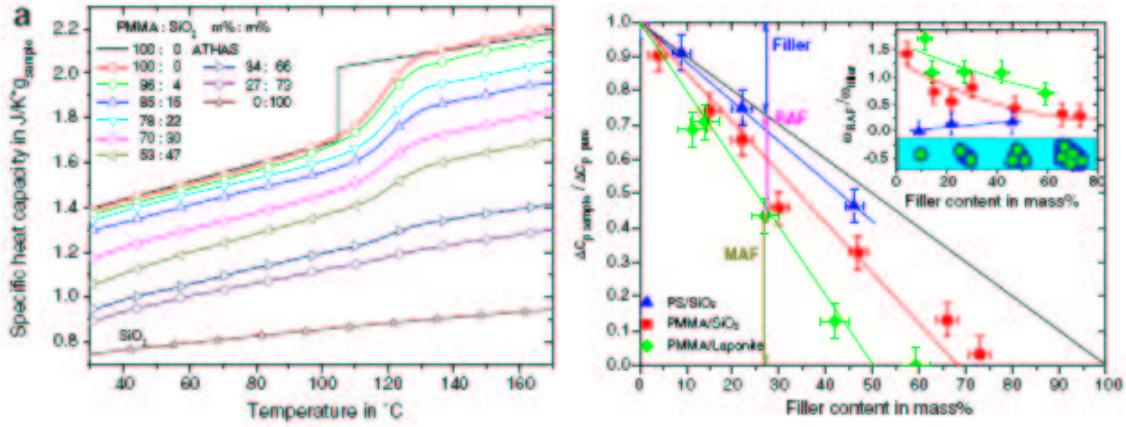

Fig. 2.11 Effect of the increase of filler content on the heat capacity signal (left) and RAF determination (right) for PMMA/SiO_2 nanocomposites [162].

Further confirmation of the presence of an immobilized portion of matrix in nanocomposites was provided by dielectric relaxation spectroscopy [163,164]. The decrease in cooperative chain motion was again attributed to the effect of intercalation [163] or to the formation of rigid regions between the filler particles [164].

2.4.2 Geometric reinforcement.

The matrix chain mobility is crucial for the development of new energy dissipating mechanisms that can improve the mechanical properties of a composite material [165]. It has been pointed out that below T_g the mobility of the nanoparticles under an applied stress is restricted and they therefore act as conventional fillers, often initiating crack formation and leading to brittle behaviour. On the other hand above T_g, cooperative motion is possible and anisotropic particles are able orient in the direction of the applied stress for example.

If clay platelets are considered to be geometric reinforcing agents, the stiffness increases can be described by models developed for conventional composites. Several models have been developed to account for reinforcement by rigid particles in a rigid matrix. The most intuitive equations come from the Voigt and Reuss models:

$$E_c = E_m\phi_m + E_f\phi_f \qquad \text{(Voigt)} \qquad \text{eq. 2.4}$$

$$\frac{1}{E_c} = \frac{\phi_m}{E_m} + \frac{\phi_f}{E_f} \qquad \text{(Reuss)} \qquad \text{eq. 2.5}$$

where E and ϕ are the Young's modulus and the volume fraction and the subscripts c,m and f refer to the composite, matrix and filler respectively. These equations describe a series and parallel model. The Hirsch model is a combination of the two:

$$E_c = x(E_m\phi_m + E_f\phi_f) + (1-x)\frac{E_f E_m}{E_m\phi_f + E_f\phi_m} \qquad \text{eq. 2.6}$$

where x is a parameter which represents the stress transfer from the matrix to the filler.

Many authors make use of the semi-empirical Halpin-Tsai model (H-T) or the Mori-Tanaka model (M-T). These take into account the aspect ratio of the filler and its orientation with respect to the applied stress. The H-T model was obtained by interpolating numerical solutions for aligned composites [166]. The M-T model is based on a non dilute composite containing identical spheroids. Analytical solutions for the elastic modulus in the case of an isotropic matrix filled with aligned spheroidal inclusions were derived by Tandon and Weng [167] and will be

presented in detail in chapter 4. For dilute systems, the Mori-Tanaka model may also be approximated by the Norris equations for the bulk modulus *K* and the shear modulus *G:*

$$K = K_0 + \frac{4}{9}\phi\left[\frac{\pi}{8\alpha}\frac{3-4\nu_0}{G_0(1-\nu_0)} + \frac{1-\nu_1}{G_1(1+\nu_1)}\right]^{-1} \qquad \text{eq. 2.7}$$

$$G = G_0 + \frac{1}{15}\phi\left[\frac{\pi}{8\alpha}\frac{3-4\nu_0}{G_0(1-\nu_0)} + \frac{1-\nu_1}{G_1(1+\nu_1)}\right]^{-1} + \frac{2}{5}\phi\left[\frac{\pi}{16\alpha}\frac{7-8\nu_0}{G_0(1-\nu_0)} + \frac{1}{G_1}\right]^{-1} \qquad \text{eq. 2.8}$$

where K_0 is the bulk modulus of the matrix, ν_0 and ν_1 are the Poisson's ratio of the matrix and of the clay, and G_0 and G_1, the shear moduli of the matrix and clay respectively [168]. The Young's modulus is obtained from:

$$K = \frac{E}{3(1-2\nu)} \qquad G = \frac{E}{2(1+\nu)} \qquad E = \frac{9KG}{3K+G} \qquad \text{eq. 2.9}$$

The above models have been extensively used to predict clay nanocomposite stiffness both in the glassy and rubbery state of the matrix. A recent paper by Hui and Shia presents a simplified version of the Mori-Tanaka model that does not require the construction of the Eshelby's tensor for unidirectional aligned composites [169].

Recent developments in modelling using conventional composite models have involved the introduction of the interphase as a third phase [142, 170-172] or the effects of clay stacking [173-175]. However, no direct measurements of the interphase properties are available and this remains a major limitation. On the other hand, attempts to take into account clay aggregation are more realistic.

Another effect that has been observed for clay/polymer composites and other filled systems is the creation of a 3D percolation structure when the filler content is sufficiently high. Normally clay platelets are considered to be disk shaped inclusions. The geometrical percolation threshold of overlapping ellipsoids, which approximate platelets, is strongly dependent on the aspect ratio [176]. When the aspect ratio increases the percolation threshold rapidly decreases. The dependence on clay concentration of the distance *d* between clay platelets has been shown to scale as $\varphi^{-1/3}$ where φ is the clay volume fraction [177]. The percolation of filler-filler contacts, especially when the matrix becomes soft, has often been invoked to account for the creation of a percolation network. Experimentally this may be seen from rheological measurements [178,179]. As more clay is added to clay-based nanocomposites, the onset of the Newtonian plateau of the shear viscosity shifts toward lower shear rates, i.e. increasingly solid-like behaviour [117,118]. The nanocomposites also show much longer relaxation times than the pure matrix and the stress

relaxation becomes independent of temperature, in sharp contrast with the behaviour of the matrix [119].

2.4.3 Basic foam mechanics.

In subsequent chapters the properties of nanocomposite films with a cellular-like morphology will be presented and discussed. This morphology derives directly from the latex particle morphology, in which the clay platelets are attached to the particle surfaces. When clay content is high enough, a partially percolated structure is formed. This will be treated from the mechanical point of view as a clay-based foam filled with polymer. For this reason it is useful to introduce at this point the principal mechanical models that have been developed for cellular materials. Attention is focused mainly on the results of Gibson and Ashby [180] who analyzed the mechanical behaviour of isotropic foams deformed under compression. According to their results, in a stress vs. strain diagram three different regimes may be observed for a cellular solid: a linear elastic regime, a non linear elastic regime and a hardening regime. Each corresponds to a structural change in the foam. The linear elastic response is associated with cell wall bending for open cell materials and the cell wall stretching for closed cell systems. The non linear regime is associated with cell wall buckling for plastic materials and cell wall crushing for brittle materials. Finally, hardening is associated with cell densification. It was shown that the results are the same when the foam is deformed under tension in the linear elastic regime, while for the non linear regime, cell wall alignment or brittle crack propagation are observed. In the following analysis, attention is focused on the linear elastic response. Gibson and Ashby proposed the following general equation for the foam modulus *E'*:

$$\frac{E'}{E_s} = C\left(\frac{\rho}{\rho_s}\right)^n \qquad \text{eq. 2.10}$$

where E_s is the matrix modulus and ρ and ρ_s are the foam density and the matrix density respectively. The reduced density depends on the foam cell geometry and can be calculated exactly (see [180] for a complete treatment). *C* is a constant of the order of the unity and *n* is a number ranging in most cases from 1 to 3. Ashby gives $n = 1$ for closed cell foams and $n = 2$ for open cell foams. Taking eq. 2.10 as a basis, many authors have attempted to verify the reduced density dependence and to analyze the effect of non periodicity and defects on the foam modulus, starting from a tetrakaidecahedral cell foam. Zhu et al. calculated the elastic constants

of such a foam with open cells as a function of the edge cross section. If bending is the only deformation process, the quadratic dependence of the modulus is confirmed. When twisting or edge torsion are introduced, however, the exponent decreases by about 5 % [181]. The same authors showed the importance of the tensile yielding properties of the cell faces for closed cell foams, confirming that for closed cell materials, cell wall stretching largely dominates bending [182]. Grenestedt reviewed scaling laws for open and closed cell foams for perfect foams with different cell morphologies. He used both an analytical and numerical approach and found similar results to Ashby [183]. Simone et al. studied the effect of the distribution of the material between the cell faces and edges on the stiffness of closed tetrakaidecahedral cell foam by numerical simulation and again found a linear dependence on reduced density [184]. The effect of cell irregularity in open cell foams has been studied by several authors. Random cell systems were generated numerically and a more complex dependence of the stiffness on *n* was found than indicated for the cell structures described by eq. 2.10 [185, 186]. The same was found for closed cell foams [187, 188] and for 2D honeycombs [189, 190]. In this latter case, more disordered structures lead to a sharp decrease in modulus. The presence of a few missing walls can result in a stiffness decrease of about 50 % [191] and the stiffness reaches zero when 35 % of the cell walls are removed [190]. The presence of cell wall waviness, thickness variations, fractured cell walls and misalignments was also shown to degrade significantly the mechanical properties of cellular materials [192, 193]. Hence, even small defects that do not alter the density can be important. In general, it may be concluded that a decrease in connectivity (more disorder) results in an increase of the power law exponent in eq. 2.10 but that the effect of defects can not be accounted for in a simple way.

The presence of a gas or a liquid within the cells changes the mechanical response of the foam. The presence of a gas in closed cell foams can be accounted for by adding an extra term to eq. 2.10 [180]. The problem is different when a liquid is present in open cell foams. In this case, bending of the cell walls becomes negligible with respect to stretching, until the liquid begins to flow from one cell to another. This increases the foam modulus of a open cell foam to the same level as that of closed cell foams, giving a linear dependence of the modulus on the reduced density [194].

2.5 Techniques for the study of the morphology of polymer-based nanocomposites

One of the most important issues in nanocomposites is the study of the relationship between the morphology and the macroscopic properties. In this section, the most common techniques for investigating of the morphology of nanocomposite materials are described. Perhaps the most widely used technique is transmission electron microscopy (TEM). Almost all papers on nanocomposites show TEM pictures that depict filler size and dispersion in the matrix. This technique is very powerful for the study of polymer/clay nanocomposites because the degree of clay exfoliation and dispersion can be accessed directly. The main limitation is the need to use of very thin samples and because of this the operator cannot determine directly the filler arrangement in 3D. Moreover the volume probed by the electron beam is generally very small and is not necessarily representative of the overall composite microstructure [195]. It follows that many regions of the sample must be observed in order to gain a global picture of the morphology. Many polymeric matrices also suffer from beam exposure and careful sample preparation is needed, with the use of staining agents. Finally thin sectioning of low T_g polymers is particularly difficult, often resulting in poor section quality. All these factors strongly limit the use of TEM, and extensive image analysis is required when calculating the mean dimensions and distances between the particles and/or aggregates [196-200]. TEM tomography also allows the 3D reconstruction of the dispersion of the filler in the matrix in a localized volume (some hundreds of cubic nanometer). By acquisition of several images of the region of interest at different tilt angles with respect to the incident electron beam, the dispersion of the clay filler may be reconstructed [201, 202]. The clay platelets may then be approximated by ellipsoids and their anisotropy characterized by the length of the three semi-axes. Typical results are shown in Fig.2.12.

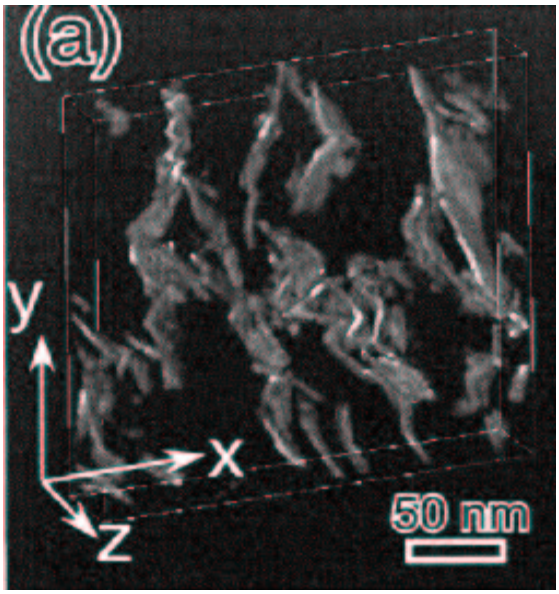

Fig. 2.12 3D Reconstruction of clay dispersion and orientation by TEM tomography [201]

To obtain a more complete idea of the nanocomposite microstructure, small angle X-ray scattering (SAXS) and wide angle X-ray scattering (WAXS) are generally used. From the symmetry of the SAXS and WAXS 2D spectra the isotropicity of the sample may be investigated, for example. In general, when the spherical symmetry of the diffraction pattern is lost, preferential orientation of the filler is present. Four characteristic types of morphology have been described in PE-clay composites [203,204] when increasing amounts of filler:

Stage I: corresponds to the totally exfoliated morphology.

Stage II: corresponds again to exfoliation, but the clay platelets are now aligned because of steric interactions.

Stage III: the clay starts to form aggregates and both intercalated and exfoliated morphologies are present.

Stage IV: only aggregates are present in the matrix.

The 2D-SAXS diffraction patterns are shown schematically in Fig. 2.13.

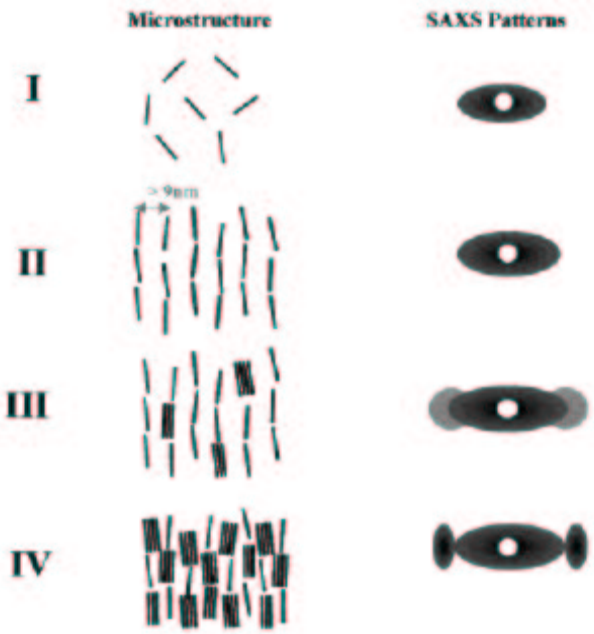

Fig. 2.13 Evolution of the 2D SAXS diffraction patterns with clay content in PE/clay nanocomposites [203].

The level of orientation and dispersion of the clay can be studied by combining SAXS and WAXS analysis [205-207]. In order to fully characterize these parameters, 2D diffraction spectra must be taken for all the possible orientations of the film, as shown in Fig. 2.14:

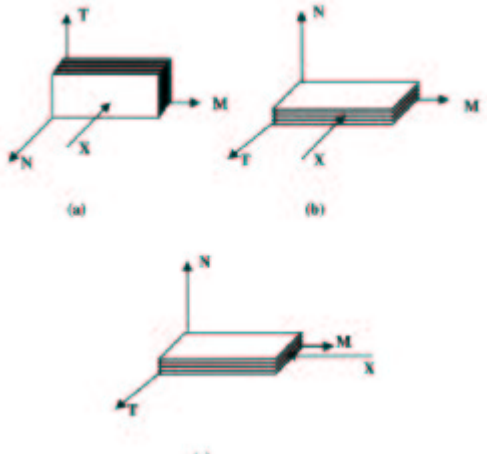

Fig. 2.14 Different orientations necessary for full characterization of clay orientation by SAXS and WAXS. The letter "x" indicates the direction of the X-rays [207].

Normally for compression molded specimens a preferential orientation of the clay layers parallel to the film surface is found [205, 208], while for extruded clay nanocomposites a preferential orientation parallel to the flow direction is observed [209]. Not only the dispersion, but also the type (modified vs. unmodified clay) and the size distribution of the aggregates can be

analyzed by SAXS and WAXS [206, 207]. The size of the diffracting clay units may in principle be determined from WAXS using the following equation [210]:

$$d = \frac{0.9\lambda}{\Delta(2\theta)\cos\theta} \qquad \text{eq. 2.11}$$

where λ is the wavelength of the beam, $\Delta(2\theta)$ is the width at half maximum of the diffraction peak of clay structure and θ is the peak position. Another possibility for obtaining a size distribution of the clay tactoids by SAXS was proposed by Vermogen et al. [211]. They suggested the intensity of the SAXS spectra to be a convolution of signals coming from families of tactoids of different sizes. Using a fitting procedure they obtained the relative frequency of tactoids in a given size range. Unfortunately the method of choosing the size range is arbitrary and may not be statistically representative

Another technique that may be useful for studying the orientation of clay tactoids in a polymeric matrix is etching. By the use of mild plasma treatments very thin layers of polymer may be removed from a specimen. In this way clay aggregates emerge at the surface and can be observed by conventional imaging systems e.g. scanning electron microscopy (SEM) for example [212]. In this case it is possible to work with bulk samples and sample preparation is generally less difficult than for TEM.

Atomic force microscopy (AFM) has also been used to investigate the morphology of polymer/clay nanocomposites. In this case the difference in hardness between the two components is exploited to create phase images with colour contrast [213]. It is necessary to use very flat surfaces, otherwise it becomes difficult to follow the surface profile with the AFM cantilever [214]. In the case of microtomed samples, single platelets, tactoids and stacks can be observed. Moreover phenomena such as the bending and breaking of clay flakes and the extent of clay aggregation can be imaged [215, 216]. The drawback of this technique is image interpretation, especially when the surface-tip contact is not optimal because of surface roughness. The use of AFM to study nanocomposites material morphology therefore remains limited.

2.6 Microdeformation mechanisms in polymers

One of the main objectives of this thesis is to establish a relationship between the morphological structure of polymer/clay nanocomposites and their mechanical properties. The goal is therefore to study and understand to what extent the clay modifies the deformation mechanisms of the neat

matrix at the microscopic scale and how this relates to macroscopic behaviour. While most of the literature is focused on the synthetic developments and on the study of engineering properties of polymer/clay nanocomposites, the study of the effect of the clay on the deformation mechanisms of both amorphous and semicrystalline polymers is limited and the relationship with the macroscopic material response is still not clear. A particular morphology given by the synthetic step could in principle affect the final deformation behaviour of the material, but no evidence of this has been provided up to now.

In this section, therefore, current knowledge on the deformation mechanisms of amorphous and semicrystalline polymers is summarized, along with results obtained previously for polymer nanocomposite materials.

2.6.1 Deformation mechanisms in amorphous polymers.

Amorphous glassy polymers deform preferentially by shear deformation and/or crazing. While the first mechanism is normally associated with ductile behaviour, crazing is associated with brittle failure at low strains. The competition between these mechanisms is related to temperature and the entanglement network parameters [217, 218]. In the glassy state amorphous polymers are modelled as a network of entangled chains with physical entanglement points. The key parameters are the entanglement density, v_e, the root mean square distance between two network points, d_e, the chain contour length between two network points, l_e and the mean molecular weight between two network points, M_e. The maximum extension ratio of a single strand is:

$$\lambda_{\max} = \frac{l_e}{d_e} \qquad \text{eq. 2.12}$$

In general, in the glassy state, highly entangled polymers deform by shear, whereas crazing becomes dominant in less entangled systems. Crazes may be described as microcracks whose faces are connected by stretched fibrils with a diameter ranging from 5 to 30 nm (Fig. 2.15). The fibrils are separated by voids representing between 30 to 60 % of the craze volume. The microstructure of crazes in PS and PMMA has been extensively studied by interferometric microscopy by Döll and Schirrer mainly [219, 220]. Typical values are as follows:

- length of the stretched fibrils: 2 to 30 μm
- interfibrillar distances: 20 to 60 nm
- fibril strain: 100 % to 600 %

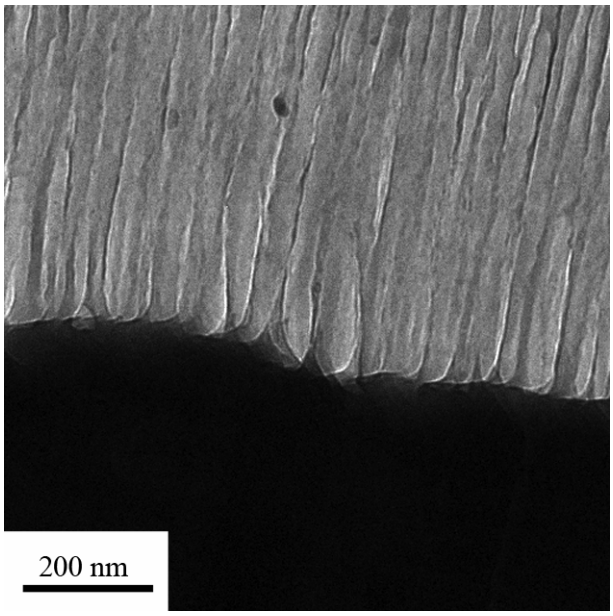

Fig. 2.15 Typical fribrillar structure of a craze in PS.

The initiation point of a craze is a region of localized deformation in which the development of a triaxial stress favours the formation of microcavities. It is now widely accepted that the point of craze initiation is generally associated with a defect or a density variation in which the stress is concentrated. Other theories have invoked e.g. local devitrification under stress, but are no longer current (see [221, 222] for a review).

After nucleation, crazes grow and may eventually evolve into cracks. Craze growth involves two phenomena: craze tip advance and craze thickening [217]. In early models, craze advance was believed to occur through repeated nucleation of voids at the craze tip, but current models are based on the meniscus instability [223]. The hypothesis in this case is that a wedge-shaped zone of strain softened polymer is formed ahead of the craze tip. The voids then propagate into this “fluid” with a characteristic spacing determined by the local stress and the polymer surface energy. Craze thickening implies a mechanism of surface drawing in which the polymer chains flow from the bulk into fibrils. The zone that feeds the fibrils is known as the “active zone” (Fig.2.16).

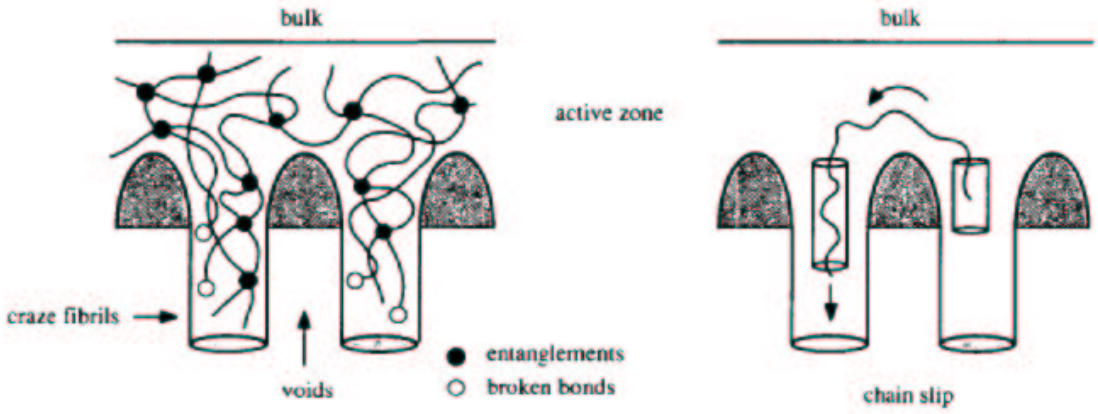

Fig. 2.16 Drawing mechanism during crazing: entanglement loss by chain scission (left) and disentanglement (right).

As shown in Fig. 2.16, craze fibril extension requires entanglement loss and this may occur by chain scission or chain slip. At temperatures far below T_g the chain mobility is low and scission is the only possible mechanism of entanglement loss. On increasing the temperature chain disentanglement becomes possible but only at relatively low molecular weights [224]. The stress required for crazing via chain scission is given by [217]:

$$S = A\left(\Gamma_0 + \frac{\nu_e d_e U}{4}\right)^{1/2} \qquad \text{eq. 2.13}$$

where A is a temperature and strain dependent factor, Γ_0 is the Van der Waals surface tension and U is the energy for chain scission. Highly entangled polymers deform preferentially by shear because the stress required for crazing is greater than the yield stress, although crazing may become possible at high temperatures through chain disentanglement.

In low entanglement density polymers such PS, the deformation mechanism is related to three parameters: molecular weight, deformation velocity and temperature. At fixed molecular weight, when the temperature is raised towards glass transition a change from a scission dominated crazing regime to a disentanglement crazing regime is observed if the deformation velocity is low, while a change from a scission dominated crazing regime to a shear deformation regime is seen if the deformation velocity is high. The effect of reducing the molecular weight is to favour disentanglement with respect to chain scission [225].

In the case of high entanglement density polymers such PC or PES, shear deformation is dominant at low temperature and on increasing the temperature a change to a disentanglement crazing regime is observed. The effect of increasing molecular weight in this case is to increase the temperature at which the transition takes place [226]. It follows that at fixed molecular weight, a slower deformation rate velocity favours the disentanglement process.

Well below T_g the fibril extension ratio is expected to be constant for a given polymer. An increase in temperature may result in an increase in extension ratio if disentanglement takes place, as shown in Fig. 2.17 for different molecular weights of PS [227]. It results that disentanglement is unlikely for high molecular weight PS.

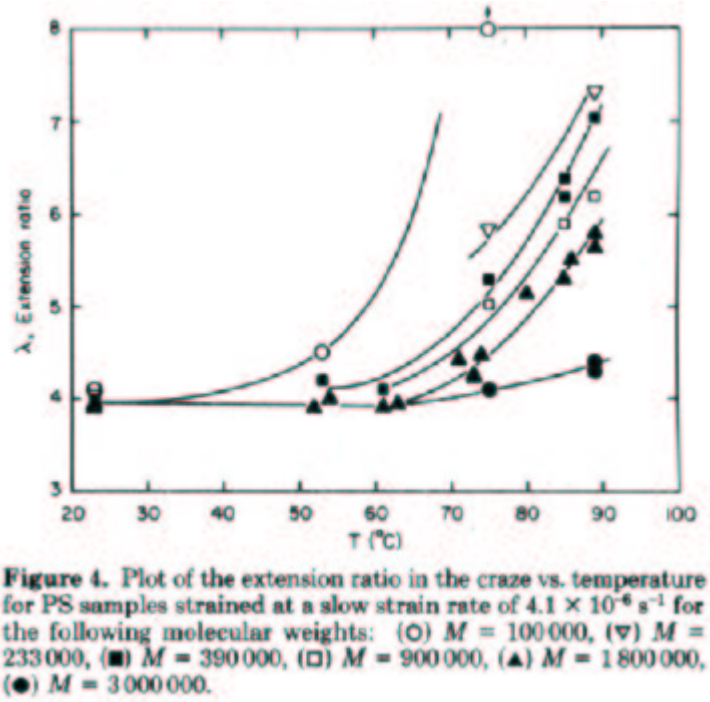

Figure 4. Plot of the extension ratio in the craze vs. temperature for PS samples strained at a slow strain rate of 4.1×10^{-6} s^{-1} for the following molecular weights: (○) M = 100 000, (▽) M = 233 000, (■) M = 390 000, (□) M = 900 000, (▲) M = 1 800 000, (●) M = 3 000 000.

Fig. 2.17 Increase in the extension ratio with temperature for different PS molecular weight [227].

Brown has also developed a model that relates the fracture toughness K_{IC} i.e. the critical stress intensity factor of the polymer and the entanglement density for amorphous polymers in which fracture is governed by propagation of a single craze ahead of the crack tip [228]. The crack is assumed to propagate by successive breakdown of the craze fibrils at the crack tip when a critical craze width is reached. The role of cross-tie fibrils, which link the primary load bearing fibrils is important. These prevent the complete relaxation of broken fibrils by transferring the stress laterally with respect to the crazing direction. This induces a stress concentration in the centre of the craze which is sufficient to lead to fibril breakdown. According to Brown the critical strain energy release rate can be expressed by

$$G_c = (\sigma_f^2 2\pi D / S\lambda^2)(E_2 / E_1)^{0.5}(1-1/\lambda) \qquad \text{eq. 2.14}$$

where σ_f is the maximum fibril stress, D is the fibril diameter, λ is the fibril extension ratio, S is the stress at the craze/bulk interface and E_1 and E_2 are the tensile moduli of the craze normal and parallel to the fibril.

The entanglement network model accounts for the craze to shear deformation transition as the entanglement density increases [229]. However the point at which such transition happens is also found to be dependent on the method of polymer preparation, on the film thickness and on the stress state [230]. As discussed above shear deformation is the dominant deformation mechanism in high entanglement density amorphous polymers. In this case the deformation consists of shear bands running at 45° with respect to the loading direction, or a plastic instability that results in necking accompanied by plastic flow, a process known as cold drawing. In contrast to crazing, shear deformation does not involve a change in volume but involves only the cooperative slip of chains without void formation. Since the polymer chains must be sufficiently mobile to initiate slip process, the yielding behaviour is strongly dependent on temperature and strain rate.

2.6.2 Deformation mechanisms in semicrystalline polymers

Semicrystalline polymers contain amorphous and crystalline regions. The crystalline portion is often organized into spherulites of several tens of microns in diameter, and within the spherulites, lamellae of about 10-20 nm are present. A more realistic model should also take into account the presence of amorphous interfaces between crystallites and amorphous domains, whose mobility is strongly reduced because of the constraints induced by the crystallites and the amorphous interlamellar material. This kind of structure has a strong influence on the microdeformation mechanisms, as shown for example by X-ray scattering and electron microscopy, and several reviews are available [231-234]. In general the deformation mechanism is analyzed in terms of the individual components of the material.

The deformation in the amorphous zones depends on the orientation with respect to loading direction as depicted in Fig. 2.18. The interlamellar slip involves shear deformation of the amorphous zones between lamellae, while tensile deformation can cause interlamellar separation and stretching of the amorphous zone between lamellae. In the bulk, this is frequently accompanied by cavitation processes that result in the formation of crazes [232].

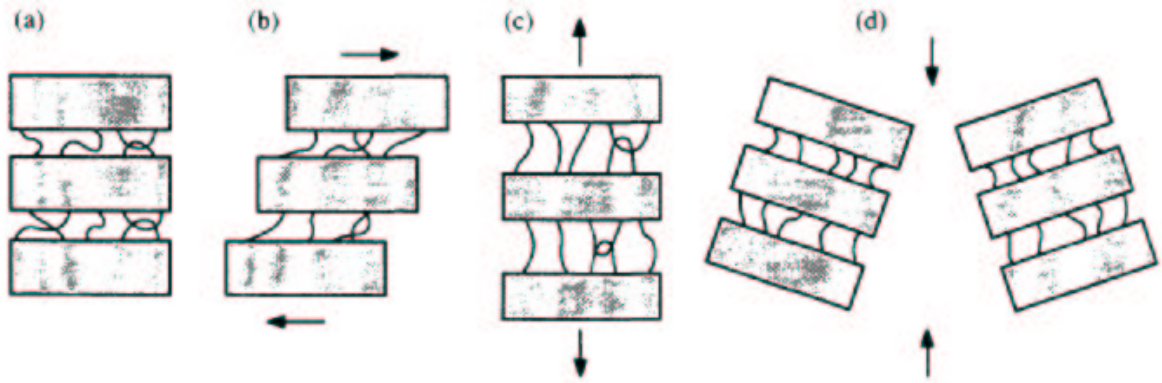

Fig.2.18 Deformation in amorphous regions of semicrystalline polymers: (a) undeformed state, (b) interlamellar slip, (c) interlamellar separation, (d) stack rotation (after [233]).

The basic deformation mechanisms in polymer crystals are crystallographic shear processes, mechanical twinning and martensitic phase transformations [233, 235]. Of these, slip processes are the most important. The slip process is mainly parallel to the chain axis [233, 226]. In this case, one observes “block slip” and “fine slip” (Fig. 2.19). Block slip involves just one slip plane, while fine slip presents several slip planes. Another deformation mechanism that is observed in semicrystalline polymers results from chain unfolding or lamellar break-up.

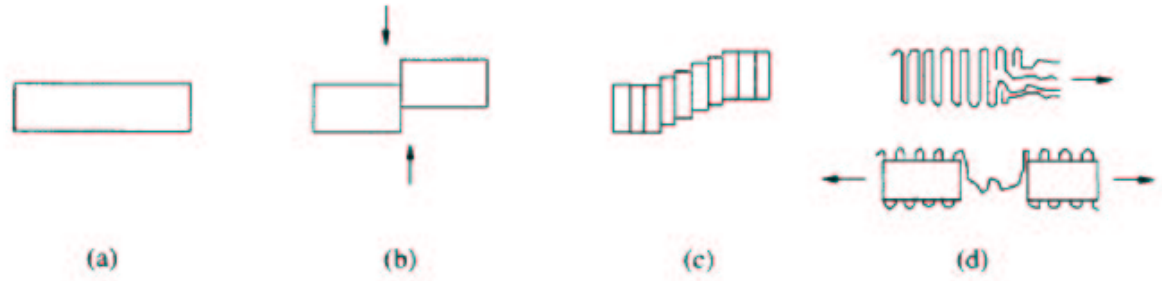

Fig.2.19 Deformation of polymer crystals: (a) undeformed state, (b) block slip, (c) fine slip, (d) chain unfolding and lamellar break-up.

In general the large deformation behaviour of semicrystalline polyolefines is divided into two stages: (1) the destruction of the spherulitic structure by chain slip or lamellar break-up and (2) the alignment of crystalline blocks with the chains parallel to the loading direction [235]. This leads to a highly oriented microfibrillar structure in the deformation direction.

Craze-like or fibrillar deformation is observed in semicrystalline polymers at temperatures below and above the T_g. Friederich proposed the following formation mechanism [232]: (1) shear in the interlamellar regions and lamellar orientation, (2) lamellar fracture and pull-out of crystal blocks to form fibrils, (3) fibril growth. An increase of the interlamellar connectivity by increasing

the molecular weight was found to favour shear deformation with respect to craze deformation. On the other hand, high strain rates and low temperatures promote crazing [237-239].

2.6.3 Microdeformation in nanocomposite materials

There are few reports in the literature on the microdeformation mechanisms of clay nanocomposites and materials containing other type of nanoparticles. Composites often undergo failure initiation in the form of debonding between the matrix and the filler and it has been reported that small particle sizes require higher stress levels to start debonding [125]. Indeed different failure mechanisms have been found for different filler sizes in the case of polyamide/silica composites. When the dimensions are greater than 50 nm the system undergoes a single debonding process, but when they are around 10 nm, aggregates form, and the matrix that is incorporated in the aggregates undergoes fibrillation [126]. These different mechanisms are illustrated in Fig. 2.20. Lee et al. showed that nanoparticles tend to align along the deformation direction in the pre-craze stage and then they enter the crazed material, forming aggregates [240]. This shows that nanofillers play a role in matrix deformation.

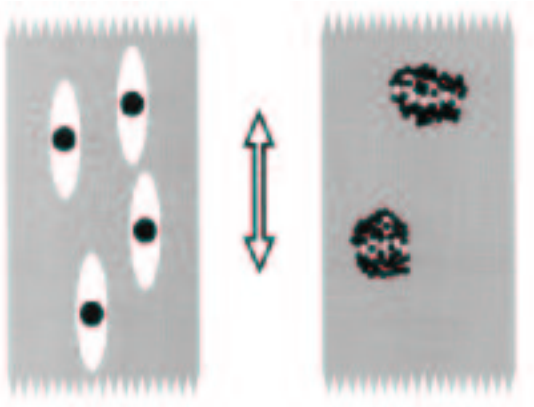

Fig. 2.20 Different failure mechanism for big and small fillers (after [126]).

In the case of clay nanocomposites, in situ deformation experiments in polyamide-12 (PA12) showed that microvoids are formed inside the layered silicate stacks and according to their orientation with respect to the applied stress they split or slide against each other [241]. The clay platelets act as load bearing elements during cavitation, dissipating energy and preventing rapid failure. As a result, the toughness of these nanocomposites was enhanced. However, Chen and al. found that clay in polyamide-66 (PA66) severely decreased the local matrix plasticity of

the material at the crack tip [242]. This turned out the have a negative effect on toughness. In PP/clay nanocomposites SAXS experiments showed that the clay favours matrix crazing owing to interface cavitation. At low clay loadings the crazes can develop fully but at high clay contents the crazes become so numerous that their growth is limited and the material undergoes failure. This is beneficial for toughness at low clay loadings but becomes detrimental at high loadings, where the matrix plasticity is strongly affected [243]. The same results were found for polyamide-6 (PA6)/clay nanocomposites [244]. The effect on clay dispersion was studied by Kim et al. on PA6/MMT nanocomposites. When good dispersion is present, microvoiding at the platelet/matrix interface is observed and when the clay is aggregated large voids were found in the aggregate centres [245].The debonding at the matrix filler interface is due to the stress concentrations at the particle boundaries, due in turn to the large difference in stiffness between the filler and the matrix [134].

2.7 Conclusions

A range of techniques have been developed to produce polymer/clay nanocomposites and these are well established in academia and industry. It is now widely accepted that the improvements observed in mechanical properties are linked to the high specific surface area of the clay platelets, which determines the extent of the interphase. On the other hand, the properties and extent of the interphase are still unclear and this remains an important point for investigation. Another crucial issue is the clay dispersion in the matrix. Emulsion techniques appear very promising, offering the possibility of introducing large amounts of clay, increasing the overall interphase volume without generating extensive aggregation. While the mechanisms of deformation and fracture in both amorphous and crystalline matrices have been extensively investigated, few reports exist on the effect of clay. Attempts to combine the results of mechanical tests with observation of the microscopic behaviour under deformation are required to acquire a deeper understanding of structure property relationships in polymer/clay nanocomposites at large deformations.

2.8 Bibliography

[1] S.S. Ray, M. Okamoto, *Polymer/layered silicate nanocomposites: a review from preparation to processing.* Progr. Polym. Sci. **28** (2003) 1539

[2] X. Kornmann, H. Lindberg, L.A. Bergund, *Synthesis of epoxy-clay nanocomposites: influence of the nature of the clay on structure.* Polymer **42** (2001) 1303

[3] X. Kornmann, H. Lindberg, L.A. Bergund, *Synthesis of epoxy-clay nanocomposites: influence of the nature of the curing agent on structure.* Polymer **42** (2001) 4493

[4] O. Becker, Y.B. Cheng, R.J. Varley, G.P. Simon, *Layered silicate nanocomposites based on various high-functionality epoxy resins: the influence of cure temperature on morphology, mechanical properties and free volume.* Macromolecules **36** (2003)1616

[5] H.R. Dennis, D. Hunter, D. Chang, S. Kim, D.R. Paul, *Effect of melt processing condition on the extent of exfoliation in organoclay-based nanocomposites.* Polymer **42** (2001) 9513

[6] A. Okada, A. Usuki, *The chemistry of polymer-clay hybrids.* Mat. Sci. Eng. C, **3** (1995) 109

[7] T. Lan, P.D. Kaviratna, T.J. Pinnavaia, *Mechanism of clay tactoid exfoliation in epoxy-clay nanocomposites.* Chem. Mat. **7** (1995) 2144

[8] T. Lan, T.J. Pinnavaia, *On the nature of polyimide-clay hybrid nanocomposites.* Chem. Mat. **6** (1994) 573

[9] N.N. Herrera, J.M. Letoffe, J.L. Putaux, L. David, E. Bourgeat-Lami, *Aqueous Dispersions of Silane-Functionalized Laponite Clay Platelets. A First Step toward the Elaboration of Water-Based Polymer/Clay Nanocomposites* Langmuir **20** (2004) 1564

[10] Y.T. Vu, J.E. Mark, L.H. Pham, M. Engelhardt, *Clay nanolayer reinforcement of cis-1,4-polyisoprene and epoxidized natural rubber.* Journ. of Appl. Polym. Sci. **82** (2001) 1391

[11] N.N. Herrera, J.L. Putaux, L. David, E. Bourgeat-Lami, *Polymer/Laponite composite colloids through emulsion polymerization: influence of the clay modification level on particle morphology*. Macromolecules **39** (2006) 9177

[12] C.R. Tseng, H.I. Lee, F.C. Chang, *Crystallization kinetics and crystallization behaviour of syndiotactic polystyrene/clay nanocomposites.* Journ. Polym. Sci. Part B, **39** (2001) 2097

[13] C.Ding, B. Guo, H. He, D. Jia, H. Hong, *Preparation and structure of highly confined intercalated polystyrene/montmorillonite nanocomposite via a two-step method.* Eur. Pol. Journ. **41** (2005) 1781

[14] W.Xie, J.M.Hwu, G.J. Jiang, T.M. Buthelezi, W.P. Pan, *A study of the effect of surfactants on the properties of polystyrene-montmorillonite nanocomposites.* Pol. Eng. Sci. **43** (2003) 214

[15] M. Ogawa, S. Okumoto, K. Kuroda*, Control of Interlayer Microstructures of a Layered Silicate by Surface Modification with Organochlorosilanes.* Journ. Am. Chem. Soc. **120** (1998) 7361

[16] N.N. Herrera, J-L. Putaux, E. Bourgeat-Lami, *Synthesis of polymer/laponite nanocomposite latex particles via emulsion polymerization using silylated and cation-exchanged laponite clay platelets.* Progr. In Solid State Chem. **34** (2006) 121

[17] J. Yang, H. Fan, Z. Bu, B. Li, *The preparation of MMT-supported initiator and its application in emulsion polymerization of styrene.* Acta Polimerica Sinica **6** (2006) 779.

[18] J. Rubio, J.A. Kitchener, *Mechanism of adsorption of poly(ethylene oxide) flocculant on silica.* Journ. Coll. Interf. Sci. **57** (1976) 132

[19] Y.H. Shen, *Sorption of non-ionic surfactants to soil: the role of soil mineral composition.* Mat. Sci. Eng. Part A Chemosphere **41** (2000) 711

[20] N. Ogata, S. Kawakage, T. Oghihara*, Poly(vinyl alcohol)-clay and poly(ethylene oxide)-clay blends prepared using water as solvent.* Journ. Appl. Polym. Sci. **66** (1997) 573

[21] A. Usuki, M. Kawasumi, Y. Kojima, A. Okada, T. Kurauchi, O.J. Kamigaito, *Swelling behaviour of montmorillonite cation exchanged for V-amino acids by E-caprolactam.* Journ. Mater. Res. **8** (1993) 1174

[22] A Rehab, N. Salahuddin, *Nanocomposite materials based on polyurethane intercalated into montmorillonite.* Mat. Sci. Eng. A **399** (2005) 368

[23] L. Beron, Z. Wang, T.J. Pinnivaia, *Polymer-layered silicate nanocomposites: an overview.* Appl. Clay Sci. **15** (1999) 11

[24] V. Halvatty, A. Oya, *Intercalation of methacrylamide into sodium, calcium and alkylammoium exchanged montmorillonites.* Appl. Clay. Sci. **9** (1994) 199

[25] M. Kawasumi, M. Hasegawan, A. Usuki, A. Okada, *Preparation and mechanical properties of polypropylene-clay hybrids.* Macromolecules **30** (1997) 6333

[26] A. Usuki, M. Kawasumi, Y. Kojima, A. Okada, T. Kurauchi, O.J. Kamigaito, *Synthesis of nylon 6 clay hybrids.* Journ. Mater. Res. **8** (1993) 1179

[27] J.G. Doh, I. Cho, *Synthesis and properties of polystyrene-organoammonium montmorillonite hybrids.* Pol. Bull. **41** (1998) 511

[28] C.R. Tseng, J.Y. Wu, H.Y. Lee, F.C. Chang, *Preparation and characterization of polystyrene clay nanocomposites by free-radical polymerization.* J. Appl. Pol. Sci. **85** (2002) 1370

[29] T. X. Xie, G.S. Yang, X. P. Fang, F.C. Ou, *Synthesis and characterization of poly(methylmethacylate)/montmorillonite nanocomposite by in-situ bulk polymerization.* J. Appl. Pol. Sci. **89** (2003) 2256

[30] Y. Li, B. Zhao, S.B. Xie, S.M. Zhang, *Synthesis and properties of poly(methylmethacrylate)/montmorillonite (PMMA/MMT) nanocomposites.* Pol. Int. **52** (2003) 892

[31] J. Heineman, P. Reichert, R. Thomann, R. Mulhaupt, *Polyolefin nanocomposites formed by melt compounding and transition metal catalyzed ethane homo-and co-polymerization in the presence of layered silicates.* Macrom. Rapid Comm. **20** (1999) 423

[32] M. Alexandre, P. Dubois, T. Sun, J.M. Garces, R. Jerome, *Polyethylene-layered silicate nanocomposites prepared by the polymerization-filling technique: synthesis and mechanical properties.* Polymer **43** (2002) 2123

[33] J.F. Rong, H.Q. Li, Z.H. Jing, X.Y. Hong, M. Sheng, *Novel organic/inorganic nanocomposites of polyethylene.* Journ. Appl. Polym. Sci. **82** (2001) 1829

[34] Y. Kurokawa, H. Yasuda, M. Kashiwagi. A. Oyo, *Structure and properties of a montmorillonite/polypropylene nanocomposite.* Journ. Mat. Sci. Lett. **16** (1997) 1670

[35] T. Sun, J.M. Garces, *High performance polypropylene clay nanocomposites by in situ polymerization with metallocene/clay catalyst.* Adv. Mat. **14** (2002) 128

[36] M.W. Weimer, H. Chen, E.P. Giannelis, D.Y. Sogah, *Direct synthesis of dispersed nanocomposites by in situ living free radical polymerization using a silicate-anchored initiator.* Journ. Am. Chem. Soc. **121** (1999) 1615

[37] C. Konn, F. Morel, E. Beyou, P. Chaumont, E. Bourgeat-Lami, *Nitroxide mediated polymerization of styrene initiated from the surface of laponite clay platelets.* Macromolecules **40** (2007) 7464

[38] R.A. Vaia, K.D. Jant, E.J. Kramer, E.P. Giannellis, *Microstructural evaluation of melt intercalated polymer-organically modified layered silicate nanocomposites.* Chem. Mat. **8** (1996) 2628

[39] S.D. Burniside, E.P. Giannellis, *Synthesis and properties of new poly(dimethylsiloxane) nanocomposites.* Chem. Mat. **7** (1995) 1597

[40] R.A Vaia, H. Ishii, E.P Giannelis, *Synthesis and properties of two-dimensional nanostructures by direct intercalation of polymer melts in layered silicates.* Chem. Mat. **5** (1993) 1694

[41] R.A. Vaia, E.P. Giannelis, *Lattice model of polymer melt intercalation in organically modified layered silicates.* Macromolecules **30** (1997) 7990

[42] O. Meincke, B. Hoffmann, C. Dietrich, C. Friederch, *Viscoelatsic properties of polystyrene nanocomposites based on layered silicates.* Macrom. Chem. Phys. **204** (2003) 823

[43] S.F. Wang, Y. Hu, Y. Tang, Z.Z. Wang, X.Y. Chen, W.C. Fan, *Preparation of polyethylene clay nanocomposites directly from Na^+ montmorillonite by a melt intercalation method.* Journ. Appl. Pol. Sci. **89** (2003) 2583

[44] K.H. Wang, M.H. Choi, C.M. Koo, M.Z. Xu, I.J. Chung, M.C. Jang, S.W. ChoiH.H. Song, *Morphology and physical properties of polyethylene/silicate nanocomposites prepared by melt intercalation.* Journ. Pol. Sci. Part B **40** (2002) 1454

[45] T.D. Fornes, P.J. Yoon, H. Keskkula, D.R. Paul, *Nylon 6 nanocomposites: the effect of matrix molecular weight.* Polymer **42** (2001) 9929

[46] L.M. Liu, Z.N. Qi, X.G. Zhu, *Study on nylon 6 nancomposites by melt intercalation process.* Journ. Appl. Pol. Sci. **71** (1999) 1133

[47] J.W. Cho, D.R. Paul, *Nylon 6 nanocomposites by melt compounding.* Polymer **42** (2001) 1083

[48] S. Boucard, J. Duchet, J.F. Gérard, P.Prele, S. Gonzalez, *Processing of polypropylene clay hybrids.* Macrom. Symp. **194** (2003) 241

[49] M.Kato, A. Usuki, A. Okada, *Synthesis of polypropylene oligomer-clay intercalation compounds.* Journ. Appl. Pol. Sci. **66** (1997) 1781

[50] C. Houphouet-Boigny, C.J.G. Plummer, M.D. Wakeman, J.-A.E. Månson, *Towards textiles-based fiber-reinforced thermoplastic nanocomposites : melt spun polypropylene-montmorillonite nanocomposite fibers.* Polym. Eng. Sci. **47** (2007) 1122

[51] C. Houphouet-Boigny, Ph.D. Thesis N° 3851 Ecole Polytechnique Fédérale de Lausanne (2007)

[52] C. Houphouet-Boigny, C.J.G. Plummer, M.D. Wakeman, J.-A.E. Månson, *Hybrid glass fiber-reinforced thermoplastic nanocomposites.* Journ Thermopl. Comp. Mat. **21** (2008) 103

[53] C.J.G. Plummer, S. Dalle Vacche, C. Houphouet-Boigny, V. Michaud, J.-A.E. Månson, *Hybrid glass mat reinforced polypropylene-montmorillonite nanocomposites*, Sol. State Phen. **151** (2009) 60

[54] A. Usuki, M. Kato, A. Okada, T. Kurauchi, *Synthesis of polypropylene-clay hybrid.* Journ. Appl. Polym. Sci **63** (1997) 137

[55] E. Manias, A. Touny, L. Wu, K. Strawhecker, B. Lu, T.C. Chung, *Polypropylene/montmorillonite nanocomposites. Review of the synthetic routes and material properties.* Chem. Mat. **13** (2001) 3516

[56] K.H. Wang, M.H. Choi, C.M. Koo, Y.S. Choi, I.J. Chung, *Synthesis and characterization of maleated polyethylene/clay nanocomposites.* Polymer **42** (2001) 9819

[57] D.C. Lee, L. W. Jang, *Characterization of epoxy-clay hybrid composite prepared by emulsion polymerization.* Journ. Appl. Polym. Sci. **68** (1998) 1997

[58] K.E. Strawhecker, E. Manias, *Structure and properties of poly(vinyl alcohol)/Na^+montmorillonite nanocomposites.* Chem. Mat. **12** (2000) 2943

[59] S.S. Hou, K. Schmidt-Rohr, *Polymer/clay nanocomposites from directly micellezed polymer/toluene in water and their characterization by WAXD and solid state NMR spectroscopy.* Chem. Mat. **15** (2003) 1938

[60] S.R. Lee, H.M. Park, H. Lim, T.Y. Kang, X.C. Li, W.J. Wo, C.S. Ha, *Microstructure, tensile properties and biodegradability of aliphatic polyester/clay nanocomposites.* Polymer **43** (2002) 2495

[61] C.J.G. Plummer, L. Garamszegi, Y. Leterrier, M. Rodlert, J.-A.E. Månson, *Hyperbranched polymer layered silicate nanocomposite.* Chem Mat. **14** (2002) 486

[62] M. Rodlert, C.J.G. Plummer, L. Garamszegi, Y. Leterrier, H.J.M. Grűnbauer, J.-A.E. Månson, *Hyperbranched polymer/montmorillonite clay nanocomposites*. Polymer **45** (2004) 949

[63] J.-C- Daniel, C. Pichot, *Les latex Synthétiques: élaboration, propriétés, application* (2006) 835 Lavoisier, Tec & Doc ed.

[64] M.W. Noh, D.C. Lee, *Synthesis and characterization of PS-clay nanocomposites by emulsion polymerization.* Polym. Bull. **42** (1999) 619.

[65] H. Li, Y. Yu, Y. Yang, *Synthesis of exfoliated polystyrene/montmorillonite nanocomposite by emulsion polymerization using a zwitterion as clay modifier.* Eur. Polym. Journ. **41** (2005) 2016.

[66]Y.K. Kim, Y.S. Choi, K.H. Wang, I.J. Chung, *Synthesis of exfoliated PS/Na–MMT nanocomposites via emulsion polymerization.* Chem. Mater. **14** (2002) 4990.

[67] D.C Lee, L.W. Jang, *Preparation and characterization of PMMA-clay hybrid composites by emulsion polymerization.* Journ. Appl. Polym. Sci. **61** (1996) 1117.

[68] Y.S. Choi, M.H. Choi, K.H. Wang, S.O. Kim, Y.K. Kim, I.J. Chung, *Synthesis of exfoliated PMMA/Na-MMT nanocompsites via soap free emulsion polymerization.* Macromolecules **34** (2001) 8976

[69] M.H. Noh, D.C. Lee, *Comparison of characteristics of SAN-MMT nanocomposites prepared by emulsion and solution polymerization.* Journ. Appl. Polym. Sci. 74 (1999) 2811

[70] N.N. Herrera, J-L. Putaux, L. David, F. De Hass, E. Bourgeat-Lami, *Polymer/Laponite Composite Latexes: Particle Morphology, Film Microstructure, and Properties.* Macrom. Rap. Comm. 28 (2007) 1567

[71] E.Bourgeat-Lami, N.Negrete-Herrera, J-L. Putaux, S.Reculusa, S.Ravaine, E.Duguet, *Designing organic/inorganic colloids by heterophase polymerization.* Macrom. Symp. **248** (2007) 213.

[72] C. Wang, F.Chu, C.Graillat, A.Guyot, *Hybrid acrylic-polyurethane latexes by miniemulsion polymerization.* Polym. React. Eng. **11** (2003) 541

[73] X.Wu, F.J. Schork, J.W.Gooch, *Hybrid miniemulsion polymerization of acrylic/alkyd systems and characterization of the resulting polyers.* Journ. Polym. Sci. Part A, **37** (1999) 4159

[74] H.Kawahara, T. Goto, K. Ohnishi, H.Ogura, H. Kage, Y.Matsuno, *Preparation of epoxy resin/acrylic composites latexes by miniemulsion polymerization method.* Journ. Of Appl .Polym. Sci. **81** (2001) 128

[75] P.Leons, V.L.Dimonie, E.S.Daniels, M.S.El-Aasser, ACS Symp. Ser. **801** (2002) 357

[76] J.G.Tsavalas, Y. Luo, L.Hudda, F.J.Schork, *Limiting conversion phenomenon in hybrid miniemulsion polymerization.* Polym. React. Eng **11** (2003) 277

[77] J.Tsavalas, J.W.Gooch, F.J.Schork, *Water-based crosslinkable coatings via miniemulsion polymerization of acrylic monomers in the presence of unsaturated polyester resin.* Journ. of Appl. Polym. Sci. **75** (2000) 916

[78] J.G.Tsavalas, Y.Luo, F.J.Schork, *Grafting mechanism in hybrid miniemulsion polymerization.* Journ. of Appl. Polym. Sci. **87** (2003) 1825

[79] J.W.Gooch, H.Dong, F.J. Schork, *Waterborne oil-modified polyurethane coatings via hybrid miniemulsion polymerization.* Journ. of Appl. Polym. Sci **76** (2000) 105

[80] S.T.Wang, F.J.Schork, G.W.Poehlein, J.W.Gooch, *Emulsion and miniemulsion copolymerization of acrylic monomers in the presence of alkyd resin.* Journ. of Appl. Polym. Sci. **60** (1996) 2069

[81] E.Bourgeat-Lami, V. Mellon, internal reports of the Napoleon project (2008)

[82] Q.H. Sun, F. J. Schork, Y.L. Deng, *Water-based polymer/clay nanocomposite suspension for improving water and moisture barrier in coating.* Comp. Sci. Tech. **67** (2007) 1823

[83] Z. Tong, Y. Deng, *Synthesis of water-based polystyrene-nanoclay composite suspension via miniemulsion polymerization.* Ind. Eng. Chem Res. **45** (2006) 2641

[84] Z. Tong, Y. Deng, *Synthesis of polystyrene encapsulated nanosaponite composite latex via miniemulsion polymerization.* Polymer **48** (2007) 4337

[85] Q.Sun, , J. Deng, Z.L. Wang, *Synthesis and characterization of polystyrene-encapsulated laponite composites via miniemulsion polymerization.* Macrom. Mat. Eng. **289** (2004) 288

[86] Y. Kojima, A. Usuki, M. Kawasumi, A. Okada, T. Kurauchi, O. Kamigaito, *One pot synthesis of nylon 6-clay hybrid.* Journ. Polym. Sci. Part A **31** (1993) 1755

[87] Y. Kojima, A. Usuki, M. Kawasumi, A. Okada, T. Kurauchi, O. Kamigaito, *Synthesis of nylon 6-clay hybrid by montmorillonite intercalated with epsilon-caprolactam.* Journ. Polym. Sci. Part A **31** (1993) 983

[88] Y. Kojima, A. Usuki, M. Kawasumi, A. Okada, Y. Fukushima, T. Kurauchi, O. Kamigaito, *Mechanical properties of nylon 6-clay hybrids.* Journ. Mat. Res. **8** (1993) 1185

[89] http://www.nanocor.com.products.asp.

[90] K. Wang, S. Liang, J. N. Deng, H. Yang, Q. Zhang, Q. Fu, X. Dong, D. J. Wang and C. C. Han, *The role of clay network on macromolecular chain mobility and relaxation in isotactic polypropylene/organoclay nanocomposites.* Polymer **47** (2006) 7131

[91] E. Moncada, R. Quijada and J. Retuert, *Comparative effect of metallocene and Ziegler-Natta polypropylene on the exfoliation of montmorillonite and hectorite clays to obtain nanocomposites.* Journ of Appl. Polym. Sci. **103** (2007) 698

[92] Q. Yuan, R. D. K. Misra, *Impact fracture behaviour of clay–reinforced polypropylene nanocomposites.* Polymer **47** (2006) 4421

[93] N. Hasegawa, M. Kawasumi, M. Kato, A. Usuki, A. Okada, *Preparation and mechanical properties of polypropylene-clay hybrids using a maleic anhydride-modified polypropylene oligomer.* Journ. Appl. Polym. Sci. **67** (1998) 87

[94] P. Reichert, H. Nitz, R. Brandsch, R. Thomann, R. Mulhaupt, *Poly(propylene)/organoclay nanocomposite formation: influence of compatibilizer functionality and organoclay modification.* Macrom. Mat. Eng. **275** (2000) 8

[95] C. H. Hong, Y. B. Lee, J. W. Bae, J. Y. Jho, B. U. Nam and T. W. Hwang, *Preparation and mechanical properties of polypropylene/clay nanocomposites for automotive parts application.* Journ. Appl. Polym. Sci. **98** (2005) 427

[96] K.H. Wang, C.M. Koo, I.J. Chung, *Physical properties of polyethylene/silicate nanocomposite blown films.* Journ. Appl. Polym. Sci. **89** (2003) 2131

[97] S. Su, C. Wilkie, *Exfoliated poly(methyl methacrylate) and polystyrene nanocomposites occur when the clay cation contains a vinyl monomer.* Journ. Polym. Sci. Part A **41** (2003) 1124

[98] S. Tanoue, L.A. Utracki, A. Garcia-Rejon, J. Tatibouët, M.R. Kamal, *Melt compounding of different grades polystyrene with organoclay. Part 3: Mechanical properties.* Polym. Eng. Sci. **45** (2005) 827

[99] N.N. Bhiwankar, R.A. Weiss, *Melt intercalation/exfoliation of polystyrene–sodium-montmorillonite nanocomposites using sulfonated polystyrene ionomer compatibilizers.* Polymer **47** (2006) 6684

[100] P. Uthirakumar, M.K. Song, C. Nah, Y.S. Lee, *Preparation and characterization of exfoliated polystyrene/clay nanocomposites using a cationic radical initiator-MMT hybrid.* Eur. Polym Journ. **41** (2005) 211

[101] M.V. Burmistr, K.M. Sukhyy, V.V. Shilov, P. Pissis, A. Spanoudaki, I.V. Sukha, V.I. Tomilo, Y.P. Gomza, *Synthesis, structure, thermal and mechanical properties of nanocomposites based*

on linear polymers and layered silicates modified by polymeric quaternary ammonium salts (ionenes).Polymer **46** (2005) 12226

[102] C.J.G. Plummer, M. Rodlert, J.-L. Bucaille, H.J.M. Grűnbauer, J.-A.E. Månson, *Correlating the rheological and mechanical response of polyurethane nanocomposites containing hyperbranched polymers.* Polymer **46** (2005) 6543

[103] Z.K. Zhu, Y. Yang, J. Yin, X.Y. Wang, Y.C. Ke, Z.N. Qi, *Preparation and properties of organosoluble montmorillonite/polyimide hybrid materials.* Journ. Appl. Polym. Sci **73** (1999) 2063

[104] A. Riva, M. Zanetti, M. Braglia, G. Camino, L. Falqui, *Thermal degradation and rheological behaviour of EVA/montmorillonite nanocomposites***.** Polym Degrad. Stab. **77** (2002) 299

[105] F. Dabrowski, S. Bourbigot, R. Delobel, M. Le Bras, *Kinetic modelling of the thermal degradation of polyamide-6 nanocomposites.* Eur. Polym. Journ. **36** (2000) 273

[106] H. L. Qin, S. M. Zhang, C. G. Zhao, M. Feng, M. S. Yang, Z. J. Shu and S. S. Yang, *Thermal stability and flammability of polypropylene/montmorillonite composites.* Polym Degrad. Stab. **85** (2004) 807

[107] J.W. Gilman, *Flammability and thermal stability studies of polymer layered silicate (clay) nanocomposites.* Applied Clay Sci. **15** (1999) 31

[108] Y. Tang, Y. Hu, B. G. Li, L. Liu, Z. Z. Wang, Z. Y. Chen, W. C. Fan, *Polypropylene/montmorillonite nanocomposites and intumescent, flame-retardant montmorillonite synergism in polypropylene nanocomposites.* Journ. Polym. Sci. Part A **42** (2004) 6163

[109] S.F. Wang, Y. Hu, Z.H. Lin, Z. Gui, Z.Z. Wang, Z.Y. Chen, W.C. Fan, *Flammability and thermal stability studies of ABS/Montmorillonite nanocomposite.* Polym. Intern. **52** (2003) 1045

[110] M. A. Osman, V. Mittal, U. W. Suter, *Poly(propylene)-Layered Silicate Nanocomposites: Gas Permeation Properties and Clay Exfoliation*. Macrom. Chem. Phys. **208** (2007) 68

[111] P.B. Messersmith, E.P. Giannelis*, Synthesis and barrier properties of poly(epsilon caprolactone)-layered silicate nanocomposites.* Journ. Poly. Sci. Part A **33** (1995) 1047

[112] M.A. Osman, V. Mittal., M. Morbidelli, U.W. Suter, *Polyurethane adhesive nanocomposite as a gas permeation barrier.* Macromolecules **34** (2003) 9851

[113] R. Krishnamoorti, R.A. Vaia, E.P. Giannelis, *Structure and dynamics of polymer-layered silicate nanocomposites.* Chem. Mat. **8** (1996) 1728

[114] R. Krishnamoorti, E. P. Giannelis, *Rheology of end tethered polymer layered silicate nanocomposite.* Macromolecules **30** (1997) 4097

[115] M. Rodlert, C.J.G. Plummer, H.J.M. Grűnbauer, J.-A.E. Månson, *Hyperbranched polymer/clay nanocomposites.* Adv. Eng. Mat. **6** (2004) 715

[116] M. Rodlert, C.J.G. Plummer, Y. Leterrier, J.-A.E. Månson, *Rheological behaviour of hyperbranched polymer/monmorillonite clay nanocomposites.* Journ. Rheol. **48** (2004) 1049

[117] B.J. Park, T.H. Kim, H.J. Choi, J.H. Lee, *Emulsion Polymerized Polystyrene/Montmorillonite Nanocomposite and its Viscoelastic Characteristics.* Journ.of Macrom, Sci. Part B **46** (2007) 341

[118] J.I. Sohn, C.H. Lee, S.T. Lim, T.H. Kim, H.J. Choi, M.S. Jhon, *Viscoelasticity and relaxation characteristics of polystyrene/clay nanocomposites.* Journ. Mat. Sci. **38** (2003) 1849

[119] Y. Zhong, Z. Zhu, S.-Q. Wang, *Synthesis and rheological properties of polystyrene/layered silicate nanocomposite.* Polymer **46** (2005) 3006

[120] M. J. Solomon, A. S. Almusallam, K. F. Seefeldt, A. Somwangthanaroj and P. Varadan, *Rheology of polypropylene/clay hybrid materials.* Macromolecules **34** (2001) 1864

[121] E. P. Giannelis, Krishnamoorti and E. Manias, *Polymer-Silicate Nanocomposites: Model Systems for Confined Polymers and Polymer Brushes*. Adv. Polym. Sci. **138** (1999) 107

[122] A. Abranyi, L. Szazdi, B. Pukanszky, G. J. Vancso and B. Pukanszky, *Formation and detection of clay network structure in polypropylene/ layered silicate nanocomposites.* Macrom. Rap. Comm. **27** (2006) 132

[123] P.H.T. Vollenberg, D. Heikens, *Particle size dependence of the Young's modulus of filled polymers:1. preliminary results.* Polymer **30** (1989) 1656

[124] S. Sun, C. Li, L. Zhang, H.L. Du, J.S. Burnell-Gray, *Interfacial structures and mechanical Properties of PVC composites reinforced by $CaCO_3$ with different particle sizes and surface treatments.* Polym. Int. **55** (2006) 158

[125] J. Cho, M.S. Joshi, C.T. Sun, *Effect of inclusion size on mechanical properties of polymeric composites with micro and nano particles.* Comp. Sci. Tech. **66** (2006) 1941

[126] E. Reynaud, T. Jouen, C. Gautheir, G. Vigier, J. Varlet, *Nanofillers in polymeric matrix: a study on silica reinforced PA6.* Polymer **42** (2001) 8759

[127] A. Lazzeri, Y.S. Thio, R.E. Cohen, *Volume strain measurements on $CaCO_3$/polypropylene particulate composites: the effect of particle size.* Journ. Appl. Polym. Sci. **91** (2004) 925

[128] Z.S. Petrovic, I. Javni, A. Waddon, G. Banhegyi, *Structure and properties of polyurethane-silica nanocomposites.* Journ. Appl. Polym. Sci. **76** (2000) 133

[129] M. Tortora, G. Gorrasi, V. Vittoria, G. Galli, S. Ritrovati, E. Chiellini, *Structural characterization and transport properties of organically modified montmorillonite/polyurethane nanocomposites.* Polymer **43** (2002) 6147

[130] Y.-Q. Zhang, J.-H. Lee, H.-J. Jang, C.-W. Nah, *Preparing PP/clay nanocomposites using a swelling agent.* Composites Part B **35** (2004) 133

[131] C.Il Park, O. Ok. Park, J.G. Lim, H.J. Kim, *The fabrication of syndiotactic polystyrene/organophilic clay nanocomposites and their properties.* Polymer **42** (2001) 7465

[132] J.J. Luo, I.M. Daniel, *Characterization and modeling of mechanical behaviour of polymer/clay nanocomposites.* Comp. Sci. Tech. **63** (2003) 1607

[133] A. Yasmin, J.J. Luo, J.L. Abot, I.M. Daniel, *Mechanical and thermal behaviour of clay/epoxy nanocomposites.* Comp. Sci. Tech. **66** (2006) 2415

[134] C.M Chan, J. Wu, J.X. Li, Y.K. Cheung, *Polypropylene/calcium carbonate nanocomposites.* Polymer **43** (2002) 2981

[135] B.B. Boonstra, *Role of particulate fillers in elastomer reinforcement: a review.* Polymer **20** (1979) 691

[136] D.Ciprari, K. Jacob, R. Tannenbaum, *Characterization of polymer nanocomposite interphase and its impact on mechanical properties.* Macromolecules **39** (2006) 6565

[137] E. Tadd, A. Zeno, M. Zubris, N. Dan, R. Tannenbaum, *Adsorption and polymer film formation on metal nanoclusters.* Macromolecules **36** (2003) 6497

[138] R. Tannenbaum, M. Zubris, K. David, D. Ciprari, K. Jacob, I. Jasiuk, N. Dan, *FTIR characterization of the reactive interface of cobalt oxide nanoparticles embedded in polymeric matrices.* J. Phys. Chem. B **110** (2006) 2227

[139] R. Tannenbaum, M. Zubris, E.P. Goldberg, S. Reich, N. Dan, *Polymer-directed nanocluster synthesis : control of particle size and morphology.* Macromolecules **38** (2005) 4254

[140] S. Saber- Samandari, A. Afaghi-Khatibi, *Evaluation of elastic modulus of polymer matrix nanocomposites.* Polym. Comp. **28** (2007) 405

[141] R.S. Fertig, M.R. Garnich, *Influence of constituent properties and microstructural parameters on the tensile modulus of a polymer/clay nanocomposite.* Comp. Sci. Tech. **64** (2004) 2577

[142] X.L. Ji, J.K. Jing, W. Jiang, B.Z. Jiang, *Tensile modulus of polymer nanocomposites.* Polym. Eng. Sci. **42** (2002) 983

[143] J. Berriot, F. Lequeux, L. Monnerie, H. Montes, D. Long, P. Sotta, *Filler elastomer interactions in model filled rubbers, a ^{1}H NMR study.* Journ. Non. Cryst. Sol. **307-310** (2002) 719

[144] P. Sotta, C. Fülber, D.E. Demco, B. Blümuch, H.W. Spiess, *Effect of residual dipolar interactions on the NMR relaxation in cross-linked elastomers.* Macromolecules **29** (1996) 6222

[145] G. Simon, K. Baumann, W. Gronski, *M_c determination and molecular dynamics in cross-linked 1,4-cis-polybutadiene : a comparison of transversal ^{1}H-and ^{2}H- NMR relaxation.* Macromolecules **25** (1992) 3624

[146] V.M. Ltivinov, P.A.M. Steeman, *EPDM-carbon black interactions and the reinforcement mechanisms, as studied by low-resolution ^{1}H-NMR.* Macromolecules *32* (1999) 8476

[147] K. Schmidt-Rhor, A. Rawal, X.W. Fang, *A new NMR method for determining the particle thickness in nanocomposites, using $T_{2,H}$-selective X{^{1}H} recoupling.* Journ. Chem. Phys. **126** (2007) 054701

[148] D.K. Yang, D.B. Zax, *Multidimensional ^{2}H NMR study of dynamical heterogeneity in polymer nanocomposites.* Solid State. Nucl. Magnet. Reson. **29** (2006) 153

[149] G. Tsagaropoulos, A. Eisenberg, *Direct observation of 2 glass transitions in silica-filled polymers. Implications for the morphology of random ionomers.* Macromolecules **28** (1995) 396

[150] G. Tsagaropoulos, A. Eisenberg, *Dynamic mechanical study of the factors affecting the two glass transition behavior of filled polymers. Similarities and differences with random ionomers.* Macrmolecules **28** (1995) 6067

[151] S. Salaniwal, S.K. Kumar, J.F. Douglas, *Amorphous solidification in polymer-platelet nanocomposites*. Phys. Rev. Lett. **89** (2002) 258301-1

[152] K. Iisaka, K. Shibayama, *Mechanical α-dispersion and interaction in filled polystyrene and polymethylmethacrylate.* Journ. Appl. Polym. Sci. **22** (1978)3135

[153] V. Arrighi, I.J. McEwen, H. Qian, M.B. Serrano Prieto, *The glass transition and intercalated layer in styrene-butadiene rubber containing silica nanofiller.* Polymer **44** (2003) 6259

[154] R. Lach, G.M. Kim, G.H. Michler, W. Grellmann, K. Albrecht, *Indentation fracture mechanics for toughness assessment of PMMA/SiO_2 nanocomposites.* Macrom. Mat. Eng. **291** (2006) 263

[155] H.E. Miltner, G. Van Assche, A. Posgay, B. Pukánszky, B. Van Mele, *Restricted chain segment mobility in poly(amide) 6/clay nanocomposites evidenced by quasi isothermal crystallization,* Polymer **47** (2006) 826

[156] D. Fragiadakis, P. Pissis, *Glass transition and segmental dynamics in poly(dimethylsiloxane)/silica nanocomposites studied by various techniques.* Journ. Non. Cryst. Sol. **353** (2007) 4344

[157] Y.Li, H. Ishida, *A study of morphology and intercalation kinetics of polystyrene-organoclay nanocomposites.* Macromolecules **38** (2005) 6513

[158] H. Xia, M. Song, *Characteristic length of dynamic glass transition based on polymer/clay intercalated nanocomposites.* Thermochim. Acta **429** (2005) 1

[159] J. Jin. M. Song, K.J. Yao, *A MTDSC analysis of phase transition in polyurethane-organoclay nanocomposites.* Thermochim. Acta **447** (2006) 202

[160] V.A. Bershtein, L.M. Egorova, P.N. Yakushev, P. Pissis, P. Sysel, L. Brozova, *Molecular dynamics in nanostructured polyimide-silica hybrid materials and their thermal stability.* Journ. Polym. Sci. Part B **40** (2002) 1056

[161] C. Schick, J. Dobbertin, M. Pötter, H. Dehne, A. Hensel, A. Wurm, A.M. Ghoneim, S. Weyer, *Separation of components of different molecular mobility by calorimetry, dynamic mechanical and dielectric spectroscopy.* Journ. Therm. Analysis **49** (1997) 499

[162] A. Sargsyan, A. Tonoyan, S. Davtyan, C. Schick, *The amount of immobilized polymer in PMMA SiO_2 determined from calorimetric data.* Eur. Polym. Journ. **43** (2007) 3113

[163] R.A. Vaia, B.B. Sauer, O.K. Tse, E.P. Giannelis, *Relaxations of confined chains in polymer nanocomposites: glass transition properties of poly(ethylene oxide) intercalated in montmorillonite,* Journ. Polym. Sci. Part B **35** (1997) 59

[164] J. G. Meier, M. Klüppel, *Carbon black networking in elastomers monitored by dynamic mechanical and dielectric spectroscopy.* Macrom. Mat. Eng. **293** (2008) 12

[165] D. Gersappe, *Molecular mechanisms of failure in polymer nanocomposites.* Phys. Rev. Lett. **89** (2002) 05831

[166] J.C. Halpin, J.L. Kardos, *The Halpin-Tsai equations: A review.* Pol.Eng Sci. **16** (1976) 344

[167] G.P. Tandon, G.J. Weng, *The effect of aspect ratio of inclusions on the elastic properties of unidirectionally aligned composites.* Polym. Comp. **5** (1984) 327

[168] A.N. Norris, *The mechanical properties of platelet reinforced composites.* Int. Journ. Sol. Struct. **26** (1990) 663

[169] C.Y. Hui, D. Shia, *Simple formulae for the effective moduli of unidirectional aligned composites.* Polym. Eng. Sci. **38** (1998) 774

[170] J. Wang, R. Pyrz, *Prediction of the overall moduli of layered silicate-reinforced nanocomposites—part II: analyses.* Comp. Sci. Tech. **64** (2004) 935

[171] S.S. Samander, A.A. Khatibi, *The Effect of interphase on the elastic modulus of polymer based nanocomposites.* Key Eng. Mat. **312** (2006) 199

[172] R.S. Fertig, M.R. Garnich, *Influence of constituent properties and microstructural parameters on the tensile modulus of a polymer/clay nanocomposite.* Comp. Sci. Tech. **64** (2004) 2577

[173] J.I. Weon, H.J. Sue, *Effects of clay orientation and aspect ratio on mechanical behaviour of nylon-6 nanocomposite.* Polymer **46** (2005) 6325

[174] H. Miyagawa, M.J. Rich, L.T. Drzal, *Amine-cured epoxy/clay nanocomposites. II. The effect of the nanoclay aspect ratio.* Journ. Polym. Phys. B **42** (2004) 4391

[175] Y.Q. Rao, J.M. Pochan, *Mechanics of polymer-clay nanocomposites.* Macromolecules **40** (2007) 290

[176] E.J. Garboczi, K.A. Snyder, J.F. Douglas, M.F. Thorpe, *Geometrical percolation threshold of overlapping ellipsoids.* Phys. Rev. E **52** (1995) 819

[177] S. Miyazaki, T. Karino, H. Endo, K. Haraguchi, M. Shibayama, *Clay concentration dependence of microstructure in deformed poly(N-isopropylacrylamide)-clay nanocomposite gels.* Macromolecules **39** (2006) 8112

[178] E.Chabert, M. Bonert, E. Bourgeat-Lami, J.-Y- Cavaillé, R. Dendievel, C. Gauthier, A. Zaoui, *Filler–filler interactions and viscoelastic behavior of polymer nanocomposites*. Mat. Sci. Eng. Part A **381** (2004) 320

[179] F.Dalmas, L. Chazeau, C.Gauthier, J.-Y. Cavaillé, R. Dendievel, *Large deformation mechanical behaviour of flexible nanofiber filled polymer nanocomposites.* Polymer **47** (2006) 2802

[180] L.J. Gibson, M.F. Ashby, Cellular solids: structure and properties (1988) Pergamon Press

[181] H.X.Zhu, J.F. Knott, N.J. Mills, *Analysis of the elastic properties of open cell foams with tetrakaidecahedral cells.* Journ. Mech. Phys. Solids **45** (1997) 319

[182] N.J. Mills, H.X.Zhu, *The high strain compression of closed-cell polymer foams.* Journ. . Mech. Phys. Solids **47** (1999) 669

[183] J.L. Grenestedt, *Effective elastic behaviour of some models for perfect cellular solids.* Int. Journ. Sol. Struct. **36** (1999) 1471.

[184] A.E. Simone, L.J. Gibson, *Effect of solid distribution on the stiffness and strength of metallic foams.* Acta Mater. **46** (1998) 2139

[185] H.X. Zhu, J.R. Hobdell, A.H. Windle, *Effect of cell irregularity on the elastic properties of open cell foams.* Acta Mater. **48** (2000) 4893

[186] A.P. Roberts, E.J. Garboczi, *Elastic properties of model random three-dimensional open-cell solids.* Journ. . Mech. Phys. Solids **50** (2002) 33

[187] A.P. Roberts, E.J. Garboczi, *Elastic moduli of model random three dimensional closed cell cellular solids.* Acta Mater. **49** (2001) 189

[188] J.L. Grenestedt, K. Tanaka, *Influence of the cell shape variations on the elastic stiffness of closed cell cellular solids*, Scipta Mater. **40** (1999) 71

[189] X.J. Ren, V.V. Silberschmidt, *Numerical modelling of low density cellular materials,* Comp. Mat. Sci. **43** (2008) 65

[190] M.J. Silva, L.J. Gibson, *The effect of non–periodic microstructure and defect on the compressive strength of two-dimensional cellular solids.* Int. Journ. Mech. Sci. **39** (1997) 549

[191] X.E. Guo, L.J. Gibson, *Behaviour of intact and damaged honeycombs: a finite element study.* Int. Journ. Mech. Sci. **41** (1999) 85

[192] J.L. Grenestedt, *Influence of wavy imperfections in cell walls on elastic stiffness of cellular solids.* Journ. . Mech. Phys. Solids **46** (1998) 29

[193] C. Chen, T.J. Lu, N.A. Fleck, *Effect of imperfections on the yielding of two-dimensional foams.* Journ. . Mech. Phys. Solids **47** (1999) 2235

[194] M.Warner, S.F. Edwards, *A scaling approach to elasticity and flow in solid foams.* Eurphys. Lett. **5** (1988) 623

[195] K. Masenelli-Varlot, G.Vigier, A. Vermogen, C. Gauthier, J.Y. Cavaillé, *Quantitative structural characterization of polymer/clay nanocomposites and discussion of an ideal microstructure, leading to the highest mechanical reinforcement.* Journ. Polym. Sci. Part B **45** (2007) 1243

[196] P.H. Nam, P.Maiti, M. Okamoto, T. Kotaka, N. Hasegawa, A. Usuki, *A hierarchical structure and properties of intercalated polypropylene/clay nanocomposites.* Polymer **42** (2001) 9633

[197] A. Ranade, N.A. D'Souza, B. Gnade, *Exfoliated and intercalated polyamide-imide nanocomposites with montmorillonite.* Polymer **43** (2002) 3759

[198] H.R. Dennis, D.L. Hunter, D. Chang, S. Kim, J.L White, J.W. Cho, D.R. Paul, *Effect of melt processing conditions on the extent of exfoliation in organoclay-based nanocomposites*. Polymer **42** (2001) 9513

[199] D. Marchant, K. Jayaraman, *Strategies for Optimizing Polypropylene–Clay Nanocomposite Structure.* Ind. Eng. Chem. Res. **41** (2002) 6402

[200] A. Vermogen, K. Masenelli-Varlot, G. Vigier, R. Séguéla, J. Duchet, S. Boucard, P.Prele, *Evaluation of the Structure and Dispersion in Polymer-Layered Silicate Nanocomposites.* Macromolecules **38** (2005) 9661

[201] H. Nishioka, K.-I. Nihara, T. Kaneko, J. Yamanaka, T. Inoue, T. Nishi, H. Jinnai, *Three dimensional structure of a polymer/clay nanocomposite characterized by transmission electron microtomography.* Comp. Interf. **13** (2006) 589

[202] N. Kawase, M. Kato, H. Nishioka, H. Jinnai, *Transmission electron microtomography without the missing wedge for quantitative structural analysis.* Ultramicroscopy **107** (2007) 8

[203] C.M. Koo, H.T. Ham, S.O. Kim, K.H. Wang, I.J. Chung, D.-C. Kim, W.-C- Zin, *Morphology evolution and anisotropic phase formation of the maleated polyethylene-layered silicate nanocomposites.* Macromolecules **35** (2002) 5116

[204] C.M. Koo, S.O. Kim, I.J. Chung, *Study of morphology evolution, orientational behaviour and anisotropic phase formation for highly filled polymer-layered silicate nanocomposites.* Macromolecules **36** (2003) 2748

[205] A.Famulari, P. Arosio, S. Filippi, C. Marazzato, P. Magagnini, L. Minkova, S.V. Meille, *Clay-induced preferred orientation in polyethylene/compatibilized clay nanocomposites.* Journ. Macrom. Sci. **46** (2007) 355

[206] A. Bafna, G. Beaucage, F. Mirabella, S. Metha, *3D hierarchical orientation in polymer-clay nanocomposites films.* Polymer **44** (2003) 1103

[207] A. Bafna, G. Beaucage, F. Mirabella, G. Skillas, S. Sukumaran, *Optical properties and orientation in polyethylene blown films.* Journ.. Appl. Polym. Sci. **39** (2001) 2923

[208] Y. Kojiima, A. Usuki, M. Kawasumi, A. Okada, T. Karauchi, O. Kamigaito, K. Kajii, *Fine structure of nylon-6-clay hybrid.* Journ. Polym. Sci. Part B **32** (1994) 625

[209] C. Houphouet-Boigny, Ph.D. Thesis N° 3851 Ecole Polytechnique Fédérale de Lausanne (2007)

[210] K. Varlot, E. Reynaud, M.H. Kloppfer, G. Vigier, J. Varlet, *Clay-reinforced polyamide: Preferential orientation of the montmorillonite sheets and the polyamide crystalline lamellae.* Journ. Polym. Sci. Part B **39** (2001) 1360

[211] A. Vermogen, K. Masenellli-Varlot, G. Vigier, B. Sixou, G. Thollet, J. Duchet-Rumeau, *Clay dispersion and aspect ratios in polymer-clay nanocomposites.* Journ. Nanosci. Nantech. **7** (2007) 3160

[212] S. Lingaiah, K.N. Shivakumar, R. Sadler, M. Sharpe, *A method of visualization of dispersion of nanoplatelets in nanocomposites.* Comp. Sci. Tech. **65** (2005) 2276

[213] D. Sikdar, D. Katti, K. Katti, B. Mohanty, *Effect of organic modifiers on dynamic and static nanomechanical properties and crystallinity of intercalated clay-polycaprolactam nanocomposites.* Journ. Appl. Polym. Sci. **105** (2007) 790

[214] L Kovarova, A. Kalendova, J.-F- Gerard, J. Malac, J. Simonik, Z. Weiss, *Structure analysis of PVC nanocomposites.* Macrom. Symp. **221** (2005) 105

[215] B. Yalcin, M. Cakmak, *The role of plasticizer on the exfoliation and dispersion and fracture behaviour of clay particles in PVC matrix: a comprehensive morphological study.* Polymer **45** (2004) 6623

[216] J. Xiong, Z. Zheng, H. Jiang, S. Ye, X. Wang, *Reinforcement of polyurethane composites with an organically modified montmorillonite.* Composites Part A **38** (2007) 132

[217] E.J. Kramer in: Advances in Polymer Science (ed. H.H. Kausch), 1983 Springer Berlin

[218] E.J. Kramer, L.L. Berger in: Advance in Polymer Science (ed. H.H. Kausch), 1990 Springer Berlin

[219] W. Döll, L. Könczöi, in: Crazing in Polymers 2, Advance in Polymer Science (ed. H.H. Kausch), 1990 Springer Berlin

[220] R. Schirrer, in: Crazing in Polymers 2, Advance in Polymer Science (ed. H.H. Kausch), 1990 Springer Berlin

[221] H.H. Kausch in: *Polymer fracture*, 1987 Springer-Verlag, 272-292

[222] G.H. Michler, *Electron microscopic investigations of initiation and growth of crazes in polystyrene.* Coll. Polym. Sci. **264** (1986) 522

[223] A.S. Argon, M.M. Salama, *Growth of crazes in glassy polymers.* Phil. Mag. **36** (1977) 1217

[224] H.H. Kausch, J.-L. Halary, C.J.G. Plummer, *Crazing and fracture in polymers: micro-mechanisms and effect of molecular variables.* Macrom. Symp. **214** (2004) 17

[225] A.M. Donald, *The effect of temperature on crazing mechanisms of polystyrene.* Journ. Mat. Sci. **20** (1985) 2630

[226] C.J.G. Plummer, A.M. Donald, *The deformation behaviour of polyethersulfone and polycarbonate.* Journ. Polym. Sci. Part B **27** (1989) 325

[227] L.L. Berger, E.J. Kramer, *Chain disentanglement during high temperature crazing of polystyrene.* Macromolecules **20** (1987) 1980

[228] H.R. Brown, *A molecular interpretation of the toughness of glassy polymers.* Macromolecules **24** (1991) 2752

[229] C.S. Henkee, E.J. Kramer, *Crazing and shear deformation in crosslinked polystyrene.* Journ. Polym. Sci. Part B **22** (1984) 721

[230] L.L. Berger, E.J. Kramer, *Effect of temperature on the transition from crazing to shear deformation in crosslinked polystyrene.* Journ. Mat. Sci. **23** (1988) 3536

[231] C.J.G. Plummer, N. Cudré-Mauroux. H.H. Kausch, *Deformation and entanglement in semicrystalline polymers.* Polym. Eng. Sci. **34** (1994) 318

[232] K. Friederich in: Advances on Polymer Science (ed. H.H. Kausch), 1983 Springer Berlin

[233] L.Lin, A.S. Argon, *Structure and plastic deformation of polyethylene.* Journ. Mat. Sci. **29** (1994) 294

[234] C.J.G. Plummer, H.H. Kausch, *Deformation and entanglement in semicrystalline polymers.* Journ. Macrom. Sci. part B **35** (1996) 637

[235] H. Zuo, G.L. Wilkes, *Orientation-dependent mechanical properties and deformation morphologies for uniaxially melt-extruded high-density polyethylene films having an initial stacked lamellar texture.* Journ. Mat. Sci. **33** (1998) 287

[236] W.W. Adams, D. Yang, E.L. Thomas, *Direct visualization of microstructural deformation process in polyethylene.* Journ. Mat. Sci. **21** (1986) 2239

[237] F. Ramsteier, G. Kanig, W. Heckmann, W. Gruber, *Improved low temperature impact strength of polypropylene by modification with polyethylene.* Polymer **24** (1983) 365

[238] B.Z. Jang, D.R. Uhlmann, J.B. Vander Sande, *Ductile brittle transition in polymers.* Journ. Appl. Polym. Sci. **29** (1984) 3409

[239] F. Ramsteiner, *Effect of the morphology of polypropylene containing propylene ethylene copolymers on the low temperature impact strength and stress whitening.* Acta Polym. **42** (1991) 584

[240] J.-Y. Lee, Q. Zhang, T. Emrick, A.J. Crosby, *Nanoparticles alignment and repulsion during failure of glassy polymer nanocomposites.* Macromolecules **39** (2006) 7392

[241] G.-M. Kim, D.-H. Lee, B. Hoffmann, J. Kressel, G. Stöppelmann*, Influence of nanofillers on the deformation process in layered silicate/polyamide-12 nanocomposites.* Polymer **42** (2001) 1095

[242] L. Chen, I.Y. Phang, S.-C. Wong, P.-P. Lv, T. Lu, *Embrittlement mechanisms of nylon 66/organoclay nanocomposites prepared by melt compounding process.* Mater. Manufact. Proc. **21** (2006) 153

[243] L. Cheng, S.-C. Wong, T. Liu, X. Lu, C. He, *Deformation mechanisms of nanoclay-reinforced maleic anhydride-modified polypropylene* Journ. Polym. Sci. Part B **42** (2004) 2759

[244] C. He, T. Liu, W. Chaubari Tjiu, H.-J. Sue and A.F. Yee, *Microdeformation and fracture mechanisms in polyamide 6/organoclay nanocomposites.* Macromolecules **41** (2008) 193

[245] G.-M. Kim, S. Goerlitz, G.H. Michler, *Deformation mechanism of nylon6/layered silicate nanocomposites. Role of the layered silicate.* Journ. Appl. Polym. Sci. **105** (2007) 38

[246] A. Okada, A. Usuki, *The chemistry of polymer-clay hybrids.* Mat. Sci. Eng. Part C **3** (1995) 109

Chapter 3

Materials and experimental techniques

In this section the preparation methods used for the different polymer clay nanocomposites investigated in this thesis are described. The characteristics of all the materials are also given in detail. The synthesis and characterization of polystyrene-based laponite nanocomposites obtained by conventional emulsion and miniemulsion polymerization are first presented, followed by acrylic systems and, finally, polypropylene-based nanocomposites. The experimental conditions for material testing are also specified.

3.1 Synthesis of Polystyrene-based laponite nanocomposites

3.1.1 Polystyrene/laponite latexes obtained by conventional emulsion polymerization

Polystyrene/laponite clay latexes were prepared by conventional emulsion polymerisation. Before discussing the reaction mechanism, a brief description of the laponite structure is given. Laponite is a fully synthetic smectic clay similar to natural hectorite. Each platelet consists of two outer tetrahedral silica sheets and a central octahedral magnesia sheet. Isomorphous substitution of magnesium with litium in the central sheet creates a negative charge that compensates the intraplatelet sodium ions. Reactive silanols are present at the edge of these stacks. A schematic of this structure is given in Fig. 3.1.

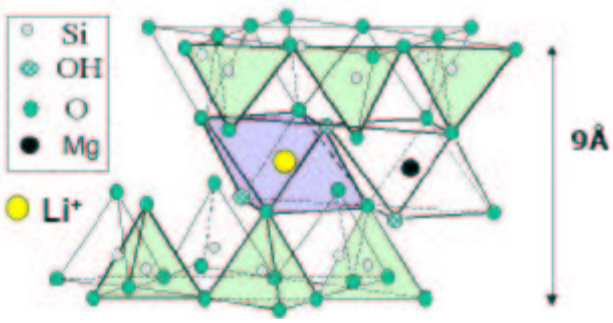

Fig. 3.1 Structure of a single laponite platelet.

The choice of laponite is derived from the fact that single platelets of this silicate have a very low aspect ratio (~50) (dimensions 50 nm in diameter and 1 nm in thickness). The specific surface area of laponite ranges from 370 to 900 m^2/g [1] and it has a cation exchange capacity (CEC) of 0.75 meq/100 g [2]. These characteristics make it an excellent candidate for the synthesis of nanocomposites (in particular the elevated surface area) and should promote homogeneous dispersion of the clay disks around the latex particles, since the clay platelet lateral dimensions are in the same colloidal size range as the latex particle diameter.

The first step of the process is the swelling of the clay. The laponite (Laponite RD, from Rockwood Additives Ltd. U.K.) was dispersed in water with the help of a peptizing agent (sodium pyrophosphate, Aldrich, 10 % by weight of laponite) and left under magnetic stirring for 2 hours. The pyrophosphate anions interact with the edge of the laponite platelet which has a partial positive charge.

A macromonomer (poly(ethylene oxyde) 1000 monomethyl ether methacrylate (PEO-MA), Polysciences, 5 % by weight of laponite) was then added in order to functionalize the hydrophilic laponite surface and make it compatible with the polymer matrix (see Fig.3.2) The interaction with the clay is electrostatic in this case and occurs between the hydroxyl groups of the clay and the ethylene oxide dipole (hydrogen bonding). A surfactant (sodium dodecyl sulphate (SDS), Acros Organics, 1 wt. % with respect to monomer) was also added to the mixture in order to create the emulsion, stabilizing the monomer droplets and the growing polymer particles.

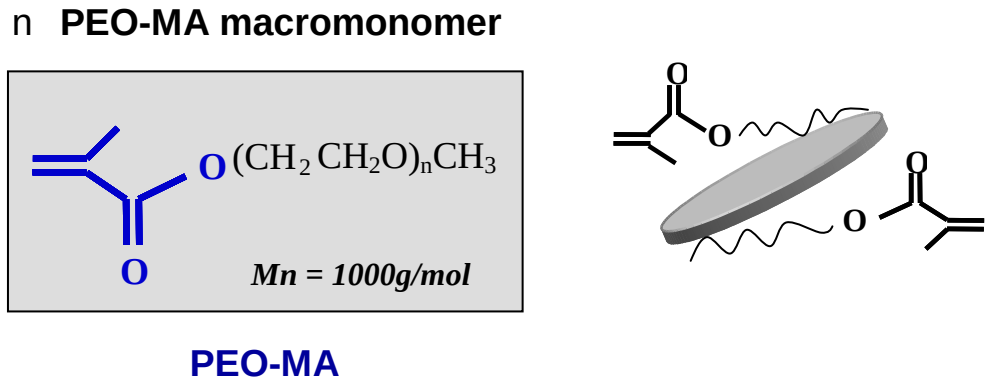

Fig. 3.2 Formula of the clay compatibilizer (PEO-MA) and schematic of its interaction with the clay platelets.

The monomer (styrene, Aldrich, 200 g/L) and the initiator (2, 2' azobis cyanopentanoic acid, Wako Chemicals, 0.5 wt % with respect to monomer) were degassed with nitrogen for ten minutes then the functionalized laponite suspension, the monomer and a catalyst were introduced into a reactor and emulsion polymerization allowed to proceed at 70 °C under nitrogen atmosphere for 4 hours under stirring [3]. A schematic of the reaction is given in Fig. 3.3. The reaction was monitored to check conversion and particle diameter evolution by taking small quantities of latex (4-5 ml). When the laponite content is increased, faster monomer conversion is obtained, the laponite having a stabilizing effect on the polymer spheres by accumulating at their surfaces.

Fig. 3.3 Schematic of the polymerization reaction.

Latex	Particle diameter (nm)	SDS content [g/L]	laponite/ monomer [wt %]	laponite/ monomer [vol %]	Solids content [%]	Conversion [%]
L0	82	2	0	0	16.6	97.8
L2.5	93	2	2.5	1	17.2	99.4
L5	86	2	5	2	17.5	99.2
L7.5	90.1	2	7.5	3	17.8	97.9
L10	78	2	10	3.9	17.5	94.1
L20	72	2	20	7.9	18.1	89.1
L30	167.7	2	30	11.9	20.4	97.4
L50	193	2	50	19.8	23.0	93.5

Table 1 The styrenic/laponite latex properties.

Several latexes were obtained with different clay contents. The principal material parameters are shown in Table 1, namely the laponite content with respect to the styrene monomer, the solids content of the latex dispersion and the final monomer conversion. Ash tests (2 hours at 500°C) made on dried latexes confirmed the approximate clay weight fraction with respect to the polymeric matrix (respectively 4, 6, 8.5, 17, 28 and 44 wt % for L5, L7.5, L10, L20, L30 and L50).

Dynamic light scattering (DLS) was used to measure the final polymer particle size. These measurements gave an average diameter of about 80-90 nm, apart from at the highest clay loadings, for which the size was roughly doubled. This could be an indication of a loss in colloidal stability when increasing the clay content, owing to some aggregation in solution as confirmed by TEM images (see section 4.1.2). The laponite platelets are assumed to be localized to the particle surfaces. Given the total amount of clay with respect to monomer and the density of PS (1.05 g/cc) and laponite (2.53 g/cc, the same value as montmorillonite) an estimate of the surface coverage of the latex particle may be made. Complete coverage would be obtained with a uniform distribution of about 9 platelets per latex particle, and there are roughly 4, 6, 9, 18, 32 and 57 platelets per particle for latexes L5, L7.5, L10, L20, L30 and L50 respectively in the event of full exfoliation. These results are obtained by geometrical considerations, taking the latex particle size to be 80 nm in diameter and the laponite platelets to be discs of 54 nm in diameter (as measured by TEM) and 1 nm in thickness. It follows that complete exfoliation is only possible in

the case of L10, or for lower clay contents, and that the particle surface area is insufficient to accommodate all the clay platelets in the other latexes, for which partial stacking is therefore expected (see Appendix 2 for calculation details).

3.1.2 Synthesis of functionalized laponite platelets for X-ray diffraction studies

Different functionalized laponite powder systems were prepared to investigate the role of the laponite concentration, the macromonomer (PEO) and the surfactant (SDS) on the exfoliation/intercalation of the laponite platelets. This was done in order to determine the real extent of polystyrene intercalation in the laponite galleries during the latex synthesis. Several aqueous solutions containing different laponite concentrations, the peptizing agent sodium pyrophosphate (10 % by weight of laponite) and the macromonomer PEO (5 % by weight of laponite) were prepared according to Table 2 and stirred for 2 hours to ensure maximum exfoliation of the laponite platelets and full reaction with the compatibilizing agents.

Laponite concentration (g/100ml)	Surfactant (g)	Peptizing agent (g)	Macromonomer PEO (g)	Platelet diameter (nm)
1	0	0.1	0.05	48 ± 3
2	0	0.2	0.1	50 ± 10
2	0.2	0.2	0.1	48 ± 5
4	0	0.4	0.2	42 ± 8

Table 2 Characteristics of the different laponite solutions.

The diameter of the laponite aggregates was analyzed by dynamic light scattering (DLS) in solution, showing complete exfoliation in each case. In a typical procedure one drop of the laponite solution was diluted about 100 times in distilled water to give an almost transparent solution before being analyzed. The aqueous solutions were then dried in an oven to give powders that could be studied by XRD. As will be shown in section 4.1.3, laponite platelet exfoliation will be lost in the nanocomposites due to aggregation on the latex particle surface.

3.1.3 Synthesis of PS/laponite nanocomposites by nitroxide mediated polymerization (NMP)

One of the disadvantages of the emulsion polymerization technique used here is the very high molecular masses obtained for the matrix. The products of emulsion polymerization are very often in the mass range 1 million g/mol. This makes it difficult to study the melt rheology of the latex based materials, because they show little tendency to flow. As discussed in section 2.1, incorporation of laponite platelets in a polymeric matrix with good control of the final molecular weight is possible via free radical controlled polymerization through NMP, although only limited amounts of clay can be incorporated in the matrix.

A detailed description of the synthetic protocol used here can be found in [4]. The basic idea of this technique is to exchange the cations of the laponite platelets in a controlled way with a quaternary ammonium alkoxyamine containing a nitroxide radical that can initiate the polymerization reaction with PS. The synthesis of the alkoxyamine is shown in Fig. 3.4.

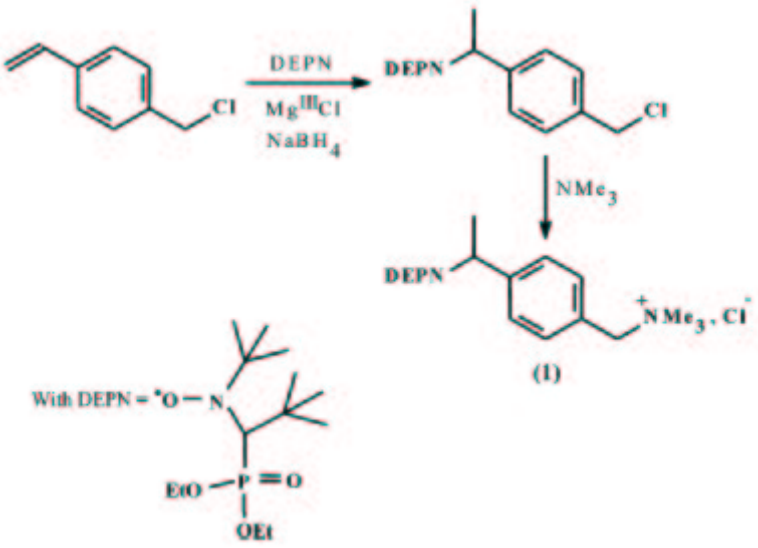

Fig. 3.4 Reaction mechanism for the synthesis of the alkoxyamine [4]

Typically, 16 g (0.11 mol) of chloromethylbenzene and 30.95 g (0.11 mol) of DEPN (see Fig. 3.4) were dissolved in 600 mL of a toluene/ethanol mixture (50/50 (v/v)). The solution was introduced into a 1 L reactor purged with argon and heated to 90 °C. Then, 10g (0.16 mol) of the Jacobsen catalyst, 8 g of the reducing agent NaBH4, and 15.3 g (0.11 mol) of di-*tert*-butyl peroxide were added to the reactor, and the mixture was stirred for 2 days. The mixture was then evaporated to dryness and partitioned between dichloromethane (300 mL) and water (600 mL), and the aqueous layer was further extracted with dichloromethane (3 times 200 mL). The combined organic layers were then evaporated to dryness. The crude product was purified with a column

chromatograph (carrier heptane and heptane/ethyl acetate: 80/20), and the desired chloromethylalkoxyamine was obtained as a white solid (yield 7.5g, 0.16 mol, 16%) and converted into a quaternary ammonium salt by reacting with trimethylamine in diethyl ether. In a typical procedure, 3.0 g (6.7 mmol) of the chlorine-terminated alkoxyamine initiator was dissolved in 10 mL of Et_2O and mixed with 1.58 mL (6.7mmol) of a 24% aqueous triethylamine solution. The mixture was allowed to react at 20 °C overnight. The resulting precipitate was filtered off, and the solid residue was dissolved in 20 mL of toluene. The solvent was evaporated in vacuum and dried to give the product in 68% yield (2.3 g, 4.5 mmol).

2.5 g of laponite RD were stirred for 2 hours in 125 g of water. Similar solutions containing 2.21 g of alkoxyamine were prepared, mixed drop by drop with the laponite solutions and stirred for 4 hours. The laponite solutions were centrifuged to recuperate the functionalized clay, which was washed with water three times and dried under vacuum. This procedure allowed preparation of laponite platelets with 95 % of exchanged cations [4]. The laponite functionalization reaction is shown in Fig. 3.5. The sodium ions that keep the laponite platelets together are exchanged with the quaternary ammonium alkoxyamine salt, which promotes clay exfoliation.

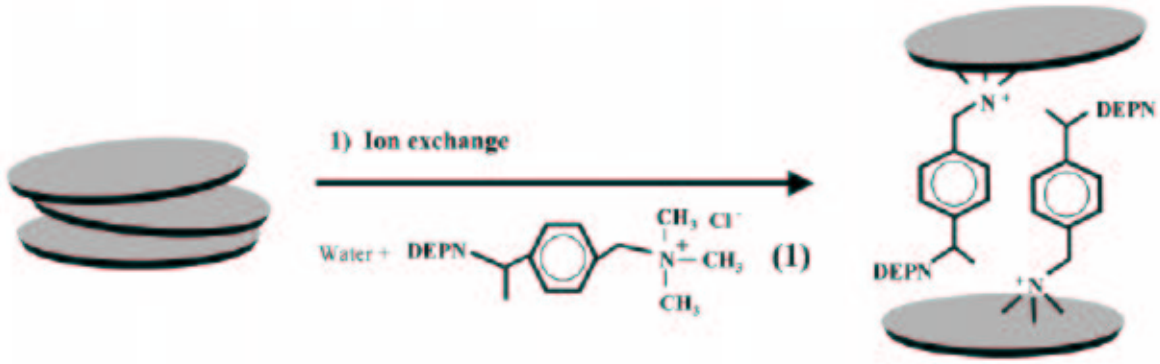

Fig. 3.5 Reaction scheme for the laponite functionalization reaction with the quaternary ammonium alkoxyamine [4].

A typical reaction procedure involved the required amount of laponite, taking into account the grafted alkoxyamine, 200 g of styrene and 200 g of toluene. The mixture was left under argon for 30 min and the temperature set to 120°C. A free radical (styril DEPN, see Fig. 3.6) was also added to keep the monomer/initiator molar ratio constant and equal to 1000. The reaction progressed via radical polymerization as in Fig. 3.3. Nanocomposites with 1 and 2.5 wt % of laponite were produced in this way with the molar masses given in Table 3 (evaluated by gel permeation chromatography (GPC)).

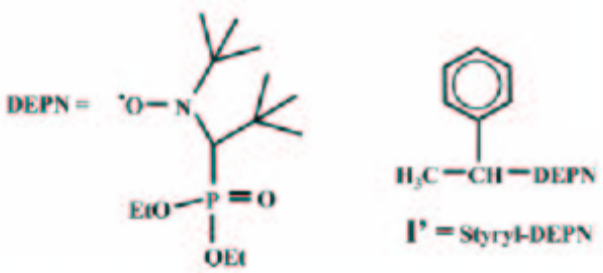

Fig. 3.6 Molecular structure of styril-DEPN used as free radical initiator [4].

Laponite content (wt%)	Laponite content (vol%)	M_n (g/mol.)
0	0	177000
1	0.4	164000
2.5	1	130000

Table 3 Molecular weight on PS/laponite nanocomposites from NMP.

The control of molecular weight was not fully optimized, but the values shown in Table 3 are adequate for melt rheology studies and enough to allow polymer film formation.

3.1.4 Polystyrene/laponite latexes obtained by miniemulsion polymerization

Two different partners in the Napoleon project (LCPP Lyon and ULM University) provided PS/laponite latexes obtained by miniemulsion polymerization. In this section the synthesis and most important materials parameters are summarized. The materials from LCPP showed different particle morphologies to the materials described in section 3.1.1, the laponite being incorporated into the latex particles. The laponite was at the particle surfaces in the samples from ULM.

In the materials from LCPP, the laponite (Laponite RD, from Rockwood Additives Ltd. U.K.) is modified in two steps. The first is grafting with a reactive silane γ-methacryloxy propyl trimethoxy silane (MPTMS) in order to functionalize the edges of the clay platelets. The second is a cationic exchange reaction with an ammonium salt didodecyldimethylammonium bromide (DDAB) in order to modify the basal faces of the clay platelets. In this case, partial substitution of the sodium cations between the clay platelets is obtained. The structures of MPTMS and DDAB are given in Fig. 3.7.

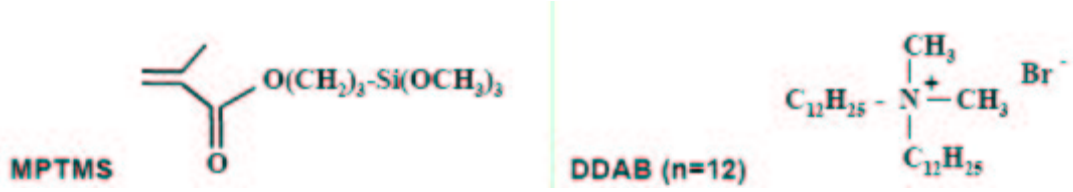

Fig. 3.7 Clay modifiers used by LCPP for miniemulsion polymerization of PS/laponite latexes.

The DDAB molecule is relatively large and is used to favor clay exfoliation by insertion between the clay stacks. The modified laponite is then dispersed with styrene monomer under stirring and strong sonication and a hydrophobe is added (Norsocryl, 6 % with respect to the monomer). The aqueous phase containing a surfactant (Dowfax 2A1, Dow chemicals, 2 wt %) is added to the monomer mixture and emulsified by sonication. The reaction takes place at 70 °C by introduction of the initiator (2, 2' azobis cyanopentanoic acid, Wako Chemicals, 1 wt %). The expected morphology for these latexes is given in Fig.3.8 and the materials parameters are given in Table 4.

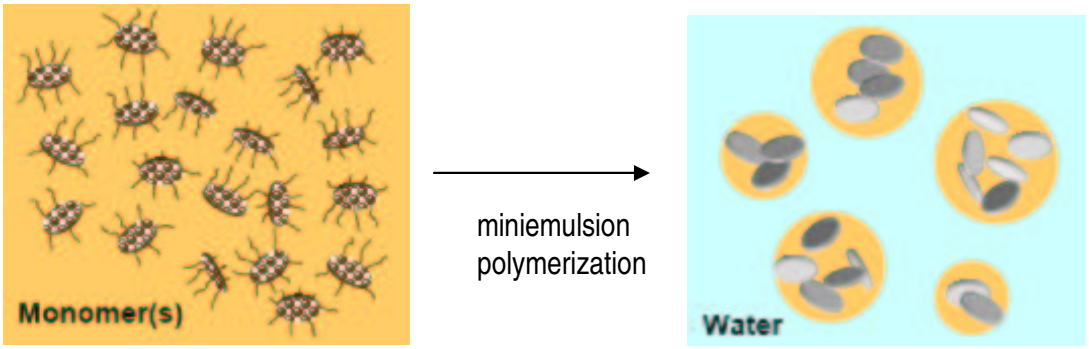

Fig. 3.8 Schematic of the synthetic strategy and expected final particle morphology LCPP samples.

Latex	Laponite /monomer [wt %]	Laponite /monomer [vol %]	Droplet diameter (nm)	Particle diameter (nm)	Conversion %	Solids content %	N_p/N_d
LCPP0	0	0	169	132	97	20	1.8
LCPP3	3	1.2	220	103	83	20	8.3
LCPP5	5	1.9	194	113	85	20	4.3
LCPP7	7	2.7	197	125	85	20	3.3

Table 4, LCPP latex properties.

From these data it is concluded that complete conversion of the monomer is not reached in the miniemulsions. The average particle size measured by DLS is still relatively large and from the ratio N_p/N_d between the number of latex particles N_p and the number of monomer droplets N_d it appears that renucleation phenomena have occurred (normally in miniemulsions there is a one to one conversion of droplets into particles). Ash tests have been performed on dried latexes and the results showed that nearly all the clay has been incorporated into the polymer particles (2.8, 4.7 and 6.8 wt % respectively). Cryo-TEM pictures showed the platelet distribution in the particles to be random, and many of the particles remained empty. Statistics are not available for the styrenics, but in the case of acrylics the proportion of filled particles was around 25 % [5].

Laponite RD (Rockwood Additives Ltd. U.K.) was again used for the materials from ULM. The clay was first swollen in water and then DDAB added as for the LCPP samples (see Fig. 3.7). The mixture was stirred for 4 days. Lutensol AT50, a long chain alcohol (BASF Chemicals) was added and the solution emulsified by sonication. Another aqueous dispersion containing the styrenic monomer, the commercial initiator V59 and Lutensol AT50 was prepared by sonication and mixed with the first solution. The reaction was carried out at 70 °C for 5 hours.

Latex	Laponite/monomer Wt %	Laponite/monomer Vol %	Solids content %	Droplet (nm)	Particle diameter(nm)
ULM5	5	2	22	126	131
ULM30	30	11.9	25	118	113

Table 5, ULM latex properties.

The materials obtained are summarized in Table 5. Very low solids contents were obtained (the objective of the Napoleon project is a minimum of 50 %), and particle sizes measured by DLS were relatively large. Ash tests performed on dried latex samples showed that the final amount of clay in the materials was less than given values (2 wt % and 13 wt % respectively). Applying the same calculations for as the L series (see section 3.1.1) it is suggested that complete exfoliation may be envisaged for both dispersions.

The latexes from LCPP and ULM obtained by miniemulsion polymerization were used in order to make comparisons with the latexes described in section 3.1.1. Attention has been focused on the difference between synthetic techniques and particle morphology for a given polymer matrix and clay filler.

3.2 Acrylic latexes

3.2.1 Acrylic/laponite latexes obtained by emulsion polymerization

A principal aim of studying acrylic/laponite latex based systems is to test whether they display the same reinforcement effects at high laponite loadings as observed in styrenic materials (see sections 4.1.4 and 4.1.6). The same reaction protocol as described for PS based latexes in section 3.1.1 was used to obtain 50/50 MMA/BA emulsions. The characteristics of the materials are given in Table 6.

Latex	Particle size (nm)	SDS content [g/L]	Laponite [wt %]	Laponite [vol %]	Solids [%]	Conversion [%]
A0	83	2	0	0	16.2	99
A10	1200	2	10	3.9	16.6	89
A20	1100	2	20	7.9	19.4	97
A30	1400	2	30	11.9	20.4	98
A50	1100	2	50	19.8	20.2	100

Table 6 Characteristics of acrylic latexes.

The size of the particles evaluated by DLS suggests that unstable colloidal dispersions are obtained in the case of highly filled latexes (particle aggregation, see section 5.1.1). This is also indicated by the presence of flocculated material in the water phase. The real laponite content was found to be 0.94, 0.21, 0.26, 0.41 wt% by ash tests for A10, A20, A30 and A50 respectively.

3.2.2 Acrylic/MMT latexes from emulsion and miniemulsion polymerization

Acrylic copolymers of MMA and BA (1:1) have also been obtained both by emulsion and miniemulsion polymerization in the presence of MMT platelets. The materials were in this case provided by the University of the Basque Country (UPV) and are referred to as the LNP series.

In the case of the miniemulsions, the monomers were purchased from Quimidroga. Sodium lauryl sulfate (SLS, Aldrich) was used as emulsifier and stearyl acrylate (SA, Aldrich) was

used as co-stabilizer. Ascorbic acid (AsAc, Aldrich) and tert-butyl hydroperoxide (TBHP, Panreac) were used as redox initiators. All the quantities are with respect to monomers. In a typical recipe, the oil phase was prepared dissolving SA (3 wt %) and the clay (Cloisite 30B, Southern clay, 3 wt %), in a 1:1 mixture of monomers (270 g) and left under stirring for 15 min. The aqueous phase was prepared dissolving SLS (4 wt %) in water (480 g). The solutions were mixed and stirred for 15 min and then sonicated to create the miniemulsion. The pH was kept around 9 with the help of boric acid to avoid coagulation. The reaction was carried out in a 1L glass reactor and the temperature was increased to 70 °C under nitrogen flow. The redox initiators (TBHP and AsAc, 2:1 molar ratio) were added in two separate streams (0.675 g and 1.35 g in 75 ml of water) and the reaction ran for 3 h. For comparison, conventional emulsions of the same materials were also obtained with Sodium montmorillonite (NaMMT). The clay was first modified with 2-methacryloyloxy ethyl hexadyldimethyl ammonium bromide. NaMMT (10 g) was dispersed in water (200 g) and the reactive specie (20 meq) was added and left for 3h under stirring at 5 °C. The reaction was carried out in a 1 L glass reactor in presence of modified NaMMT (3 wt %), SLS as above (4 wt %) and water (550 g). After stirring for 30 min, the monomers were added (135 g) and the temperature was raised to 75 °C. A 2.5 wt % (0.675 g) aqueous solution of KPS initiator (Aldrich) was added and the reaction ran for 1 h. At this point, a second batch of monomer and initiator (same quantities as before) were introduced and the reaction left to continue for 3 h. The characteristics of these latex dispersions are given in Table 7.

Latex	Clay content vol %	Solids content %	Droplets diameter (nm)	Particle diameter (nm)	Conversion %
LNP1	0	30	Emulsion	92	>99
LNP2	1.2 (NaMMT)	30	Emulsion	119	>99
LNP3	0	30	212	166	>99
LNP4	1.2 (30B)	30	86	127	>99

Table 7, LNP latex properties.

In this case, the monomer conversion reached optimum values and the solids content of the latex dispersion was increased in order to favor drying. Once again particle sizes in the miniemulsions were bigger than in the emulsions. SAXS measurements on films performed in UPV showed intercalation rather than exfoliation of the clay in the matrix for both LNP2 and LNP4. The location of the clay platelets with respect to acrylic latex particles was not determined.

3.3 Preparation of polypropylene (PP)/ MMT clay nanocomposites

Two different PP grades were studied for comparison with the styrenics obtained by emulsion polymerization. The technique used to disperse the clay in the matrix was melt blending in this case. The first grade of PP was the Moplen HP500V (Basell Industries) with a melt flow index of 120 g/10 min. Nanocomposites with a final clay content of about 2.4 vol % of clay were made using a premixed commercial PP masterbatch (Nanomer C.44PA, Nanocor) filled with 10 vol % of MMT clay and then diluted with Moplen PP. The materials were mixed 3 times with a 16 x 15 D twin screw extruder (Prism), with a screw speed of 40 rpm. The temperature was set to 200 °C, 200 °C and 180 °C from the feeder to the die. After the final extrusion step, the material underwent a calendering process at a speed of 1 rpm (Prism TSE calendar system). In this case, continuous films with a thickness of about 0.7 mm and width 80 mm were obtained for the nanocomposites and the neat matrix. 80 x 35 mm films were cut parallel to the calendering direction.

The second grade of PP was Borealis HH450FB with a melt flow index of 37 g/10 min. Nanocomposites with a final clay content of 2.4 vol % were again obtained using the same commercial premixed Nanomer PP masterbatch cited above diluted with Borealis PP with the help of the Prism extruder. The experimental temperature and screw speed were as given previously. In this case the final extrusion step was performed in a DSM micro-extruder and dumbbell-shaped samples were obtained with a DSM micro-injection machine. The temperature of the mold was set to 70 °C.

3.4 Experimental

3.4.1 Latex particle and clay morphology

A study of the latex particle morphology was performed by TEM. The diluted latex is spin coated onto a carbon coated copper grid as described in [6]. The rotation speed is 1460 r/min applied for 180 sec. The dilution depends on latex solids contents (20 times for 20 wt% and 50 times for 30 wt%). For styrenics no staining of the latex is required because this material offers enough contrast when using an electron beam. Acrylics can not be visualized without staining, being extremely sensitive to beam damage and hence almost electron transparent. Phosphotungstic acid (PTA) dissolved in the diluted latex (2 wt %) was generally used to improve contrast. The

preparation of staining solution was as follows: PTA was dissolved in water by sonication and the solution used for latex dilution [6, 7]. Observations were made with a Philips CM 20 transmission electron microscope operating at 200 KV.

Embedding latex particles in a suitable resin has also been tried [8, 9]. In this case water soluble melamine resins (Nanoplast FB 101 kit, Polysciences Inc.) have been used. The resin and the latex are mixed in the ratio 2:1 and the system dried and cured at 40 °C for 2 days to give a solid block that can be sectioned with an ultramicrotome (Reichert-Jung Ultracut E) equipped with a diamond knife (Diatome). This technique allows determination of the location of the clay with respect to the polymer latex particles. Unfortunately it can not be applied to all latex systems, because the presence of the resin hardener may cause the clay to precipitate depending on the latex formulation.

Single platelets of laponite can also be observed by TEM after staining. In this case a water solution is prepared (0.1 wt. %) and stained with a solution of ammonium molybdate and bacitracine. The preparation of the staining solution is as follows: ammonium molybdate (2 wt. %) is dissolved in distilled water and adjusted to pH 7 using HCL 1N. Bacitracine (2 wt. %) is previously dissolved in water and mixed with the ammonium molybdate solution (1:1 vol.). A drop of the laponite solution is deposited on a formvar coated copper grid and let to dry. Then a drop of the staining solution is deposited on the grid for 30 seconds and left to dry.

3.4.2 Film processing

Film formation is achieved in different ways depending on the polymer matrix of the composite system. For low T_g acrylic latexes a protocol for drying the latex suspensions at 30 °C at a relative humidity of 55 % is used. At clay loadings of 4 vol % or more, a consolidation step at 100 °C under a compressive force of 50 KN for 20 min is also required. In the case of styrenics compression moulding is needed for all loadings, since otherwise only dry powders are obtained. The healing process of latexes has already been investigated in literature and the healing time is dependent on the temperature [10, 11]. Based on these results, heating at 160 °C for 20 min. under a compression force of 10 KN was used for clay contents up to 7.9 vol % and the temperature was raised to 180 °C and the compressive force to 50 KN for higher loadings. For all materials a Fontijne-Holland press was used. Both for acrylic and styrenic materials transparent and crack free films were obtained with a thickness of about 0.3 mm.

3.4.3 Film morphology and degree of laponite intercalation

Film morphologies were investigated by TEM of thin sections obtained by ultramicrotomy (Reichert-Jung) at room temperature for styrenics, acrylics and PP based nanocomposites. Before sectioning, the films are embedded in epoxy resins (epoxy embedding medium kit, Fluka). Sections in the thickness range 40-100 nm were prepared with a diamond knife (Diatome AG). The instruments employed were a Philips CM20 operating at 200 KV for styrenics and a Philips CM10 operating at 80 KV for acrylics and polypropylene based materials. The degree of exfoliation has also been studied by X-Ray diffraction (XRD) (Siemens Kristalloflex 805, Cu K_α, λ=1.54 Å) in the range 2θ =1 to 10 °. The same machine was used to investigate the degree of laponite exfoliation/intercalation for the functionalized laponite batches described in section 3.1.2

3.4.4 Differential scanning calorimetry

Differential scanning calorimetry (DSC) (TA instruments Q100) was used to measure the glass transition temperature, T_g (5 mg of the specimen at a heating rate of 15 K/min). All experiments were carried out under nitrogen atmosphere and before any measure the samples were heated in order to eliminate their thermal history. For all materials, the T_g was defined as the inflection point of the heat flow/temperature diagram.

The quantification of the rigid amorphous fraction was carried out by modulated DSC (MDSC) after careful calibration of the machine with indium and sapphire standards. In general, for the present measurements, a modulated signal of ± 0.5° C was superimposed onto a heating ramp of 5K/min. The measured heat flow is separated in two parts, the deconvoluted heat flow (the same given by DSC) and the reversing heat flow, the difference between these signals being called the non-reversing heat flow. While the reversing component reflects all reversible processes such as vitrification-devitrification, the non-reversing component gives information on irreversible processes such as oxidation, curing, evaporation etc and non equilibrium phase transitions such as crystallization. The modulated technique gives a better precision in heat capacity measurements than conventional DSC, and the reversing component of the signal has been used all in the calculations.

3.4.5 Viscoelastic properties

Viscoelastic properties have been studied by dynamic mechanical analysis (DMA) as a function of temperature. Samples 10 mm wide and 30 mm long were tested with a heating rate of 5 K/min at a frequency of 1 Hz (TA Instrument, DMA Q800). In order to provide good statistics, 10 samples of each material have been tested. The storage modulus (*E'*), loss modulus (*E''*) and loss tangent (*tan δ*) values were recorded as a function of temperature.

3.4.6 Tensile tests.

For the L Latexes of section 3.1.1, tensile tests have been carried out on a miniature tensile test machine (Minimat, Polymer Labs) at a speed of 0.1 mm/min at room temperature on double edge notched specimens (DENT, Fig.3.9):

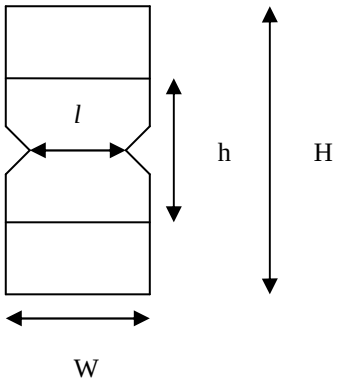

Fig. 3.9 DENT specimen geometry.

The use of this particular geometry is suggested by the essential work of fracture theory (EWF) [12]. This theory has been developed for the study of the fracture of thin films in which the geometrical requirements of linear elastic fracture mechanics (LEFM) or elastic-plastic fracture are not met. The basic idea is the division of the region around the crack tip into the so called "inner fracture process zone" (IFPZ) and an "outer plastic deformation zone" (OPDZ). The total energy associated with fracture can be separated into two parts. The first, called the essential work of fracture, W_e, (EWF), is specific to the material and represents the energy dissipated in the IPFZ. The second, called the non essential work of fracture, W_p, describes the energy dissipated

in the OPDZ and it is related to the geometry of the region surrounding the crack tip. Experimentally the protocol consists of measuring the fracture energy of DENT specimens for different values of the ligament length *l* (Fig. 3.9). The total energy W_f absorbed by the sample during fracture in tensile deformation is defined by:

$$\frac{W_f}{lt} = w_e + \beta w_p l \qquad \text{eq. 3.1}$$

where *t* is the thickness of the sample, β is a shape factor and *l* is the ligament length (see Fig. 3.9). w_e and w_p are called specific essential work of fracture and specific non-essential work of fracture. In this framework, load-displacement traces are measured together with the fracture energy and the specific essential work of fracture can be evaluated by extrapolating the work of fracture to zero ligament length. In order to assure the complete yielding of the materials short fracture ligament lengths are generally chosen. In the case of styrenics the notches were obtained on 10 x 20 x 0.3 mm^3 films by first cutting with scissors and then using a razor blade to increase notch sharpness. It must be underlined that because of the brittleness the notch quality is not optimal. For each material the ligament length was varied between 2 and 6 mm and for each ligament length 6 specimens were tested. Statistical treatment of the data is described elsewhere [12]. Further discussion of the EWF protocol will be given in chapter 6.

For the LNP samples, cyclic tensile tests were carried out with the DMA (TA Instrument, DMA Q800) on conventional rectangular specimens whose dimensions are 10 x 20 x 0.3 mm^3. Tensile tests of PP nanocomposites were performed using a UTS test machine (Test Systeme Gmbh) equipped with a 1 kN cell. A minimum of 6 specimens per material were tested and the deformation rate was fixed at 2 mm/min. The size of the dumbbell-shaped specimens was chosen according to the ISO 527 – 2 type 5A norm (Borealis PP). The size of the film specimens obtained by calendering was 80 x 35 x 0.7 mm^3 (Moplen PP). The notches were introduced into both types of specimen using a notched metal mask and a razor blade. This gave better results than for the styrenics. However, as already pointed out elsewhere, the notch quality still remains a critical issue for the PP studied here [14].

3.4.7 Study of the microdeformation mechanisms

The microdeformation mechanisms in styrenic thin films were studied by TEM using the copper grid technique developed by Kramer and co-workers [13]. Relatively thin sections of material (about 200 nm) of 3 x 3 mm^2 were cut from bulk specimens using the ultramicrotome (see 3.4.1).

They were picked up from water with a previously annealed 1 mm mesh copper grid (700°C for 1 hour under Argon). The films were then exposed to xylene vapor in order to minimize the wrinkles and deformed under tension with a miniature tensile machine (Minimat, Polymer Labs). The speed of the deformation was fixed at 0.1 mm/min. The deformation took place at room temperature and also at 95 °C and 120 °C (just below and above the T_g of PS matrix). Single squares were cut from the grid and observed by TEM. Fracture surfaces obtained from tensile tests were observed by scanning electron microscopy (SEM, FEI XLF 30) after coating with 15-20 nm of carbon to prevent surface charging.

PP and PP nanocomposite microdeformation mechanisms were also investigated by TEM and SEM, but the sample preparation was different. For both kinds of PP matrices, notched samples prepared as described in section 3.4.6 were deformed under tension with the UTS until stress whitening appeared at the notch tips. The notch tip region was cut out and embedded in an epoxy block and stained in a RuO_4 solution for 24 hours (see Fig. 3.10).

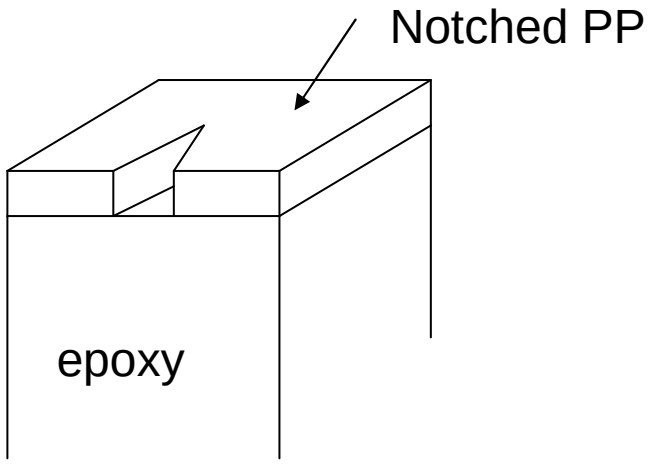

Fig. 3.10 Notched PP film mounted in an epoxy block for sectioning

The staining operation is useful not only to protect the sample from the electron beam of TEM but it also marks the deformation zones, which may hence be distinguished from damage due to cutting. The film was then sectioned at room temperature (thickness about 100-150 nm) and observed with TEM. In this case a TEM with an accelerating voltage of 200 kV (Philips CM20) and a low voltage 80kV TEM (Philips CM10) were used. Decreasing the accelerating voltage was done with the goal of increasing the contrast in the images. The embedded PP notched films were also observed by SEM after coating with a carbon layer. The fracture surfaces of the notched specimens were also analyzed by SEM.

3.4.8 Rheology

Rheology measurements were carried out on PS laponite nanocomposites obtained by NMP (see section 3.1.3). In this case parallel plate geometry with 25 mm discs has been used (ARES, Rheometric Scientific) at a temperature of 220 °C. Oscillatory shear measurements were performed as a function of frequency with a fixed strain of 2%. Rheology measurements have also been attempted on styrenics and acrylics obtained by conventional emulsion polymerization but because of the high molecular weight no terminal behavior was observed in either case. For this reason no further studies were carried out on emulsion based materials.

3.5 Bibliography

[1] L.A. Utraki, M. Sepher, E. Boccaleri, *Synthetic, layered nanoparticles for polymeric nanocomposites (PNCs).* Polym. Adv. Tech. **18** (2007) 1

[2] N. Negrete-herrera, S. Persoz, J.L. Putaux, L. David, E. Bourgeat-Lami, *Synthesis of polymer latex particles decorated with organically-modified laponite clay platelets via emulsion polymerization.* Journ. Nanosc. Nanotech. **6** (2006) 421

[3] E. Bourgeat-Lami, N.Negrete-Herrera, J-L. Putaux, S.Reculusa, S.Ravaine, E.Duguet, *Designing organic/inorganic colloids by heterophase polymerization*. Macrom. Symp. **248** (2007) 213

[4] C. Konn, F. Morel, E. Beyou, P. Chaumont, E. Bourgeat-Lami, *Nitroxide-mediated polymerization of styrene initiated from the surface of laponite clay platelets*. Macromolecules **40** (2007) 7464

[5] V. Mellon, E. Bourgeat-Lami, Napoleon 18th month internal report (2006)

[6] C. Gaillard, G. Fuchs, C.J.G. Plummer, P.A. Stadelmann, *The morphology of submicronsized core-shell latex particles: An electron microscopy study.* Micron **38** (2007) 522

[7] C. Gaillard, P.A. Stadelmann, C.J.G. Plummer, G. Fuchs, *Practical method for high-resolution imaging of polymers by low-voltage scanning electron microscopy*. Scanning **26** (2004) 12

[8] K. Bachuner, D. Frösch, *Melamine resins, a new class of water-soluble embedding media for electron microscopy.* Journ. Microscopy **130** (1983) 1

[9] D. Frösch, C. Westphal, *Melamine resins and their application in electron microscopy.* Electr. Microsc. Rev. **2** (1989) 231

[10] J.L. Keddie, P. Meredith, R.A.L. Jones, A.M. Donald, *Kinetics of film formation in acrylic lattices studied with multiple angle of incidence ellipsometry and environmental SEM*, Macroolecules **28** (1995) 2673

[11] R. Mezzenga J. Ruokolainen, G.H. Fredrickson, E.J. Kramer, *High internal phase emulsion by self-assembly of colloidal systems*, Macromolecules **36** (2003) 4466

[12] E.J. Clutton, *Fracture mechanics testing methods for polymers adhesives and composites*, ESIS publication 28, pg.177, Elsevier Science LTD 2001

[13] E.J. Kramer, L.L. Berger in: Advance in Polymer Science (ed. H.H. Kausch), 1990 Springer Berlin

[14] C. Houphouet-Boigny, Ph.D. Thesis N° 3851 Ecole Polytechnique Fédérale de Lausanne (2007)

Chapter 4

PS/laponite nanocomposites: morphology and low strain mechanical properties

This chapter describes the morphological, thermal and small strain mechanical properties of the polystyrene-based laponite nanocomposites prepared using the different synthetic techniques described in Chapter 3. Section 4.1 focuses on the behavior of PS/laponite nanocomposites obtained by conventional emulsion polymerization. After a discussion of the morphology of the latex particles and films, the thermal and mechanical properties of these latter are considered in detail. Models are proposed for the reinforcing effect of laponite and estimates are made of the extent of the immobilized interphase layer. Section 4.2 describes PS/laponite nanocomposites obtained by NMP and section 4.3 discusses the results of studies on styrenic latexes obtained by miniemulsion polymerization in the light of the results from section 4.1. Conclusions are given in section 4.4.

4.1 Experimental results from PS/laponite nanocomposites obtained by conventional emulsion polymerization

4.1.1 Laponite morphology

Spin cast specimens of laponite prepared as described in section 3.4.1 were observed by TEM. As seen in Fig. 4.1, the platelets were not disc-shaped but generally took the form of a rectangle with lateral dimensions in the range 30 to 80 nm. Analysis of 80 images suggested an average width of 54 nm, a value that will be assumed in the subsequent calculations.

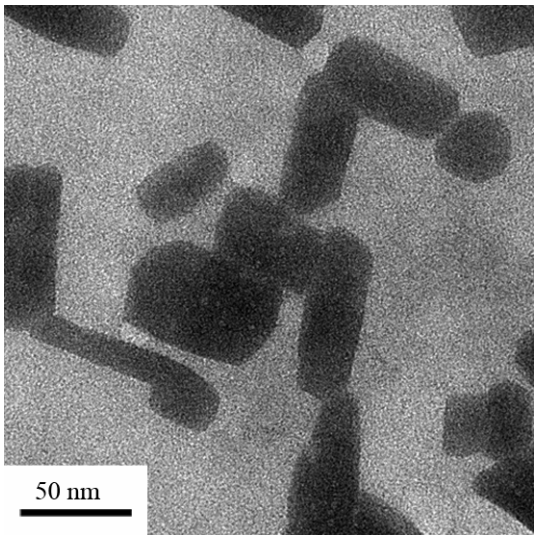

Fig. 4.1 TEM image of single laponite platelets.

4.1.1.1 Laponite intercalation in solution

This section concerns the effect of the laponite concentration and the surfactant and macromonomer on the exfoliation/intercalation of the laponite platelets during functionalization in water. It is known that the stacked structure of laponite undergoes swelling in aqueous media and this allows processes such as cation exchange and molecular grafting, already described in section 2.1, to take place. It was of particular interest to confirm that platelet functionalization is only partly responsible for the increase in the d_{001} spacing during preparation of the PS/laponite nanocomposites and hence that highly confined PS chains are present in the interlayer galleries in these latter, as invoked later in discussing the mechanical properties in the rubbery state (see section 4.1.6.4).

Specimens were prepared as described in section 3.1.2 and XRD measurements were carried out on the dry laponite platelets. The results are shown in Fig. 4.2.

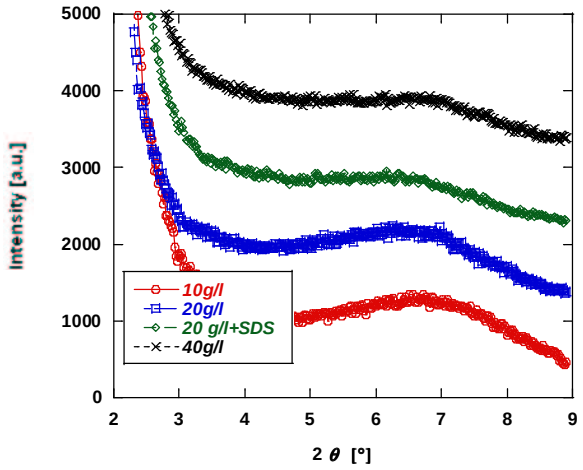

Fig. 4.2 Effect of laponite concentration and surfactant on laponite intercalation.

Neither the presence of SDS, nor the laponite concentration in water affected the intercalation process in the range considered. All the XRD curves showed a peak at around 2θ = 6.6° which corresponds to d_{001} of about 1.33 nm. This compares with 1.26 nm for the unmodified laponite and 1.48 for the nanocomposites (see section 4.1.3 and Fig. 4.7), so that although the macromonomer, which is present in all the samples, caused an increase in the basal spacing, the presence of a significant proportion of intercalated PS chains in the nanocomposites is verified. The use of the peptizing agent is not considered to be a possible cause of intercalation because it only interacts with the edges of the laponite platelets.

4.1.2 Latex particle morphology

Fig. 4.3 shows TEM images of spin-cast latex particles. The laponite platelets are generally observed to be attached to the particle surfaces. Moreover, as the laponite content is increased, it covers more of the particle surfaces (Fig. 4.3 (e) and (f)) and the thickness of the laponite shell also increases. This confirms partial stacking, which is necessary to accommodate all the laponite platelets at the particle surfaces as discussed previously in section 3.1.1. Further analysis of the stacking will be given in the next section in the context of the films.

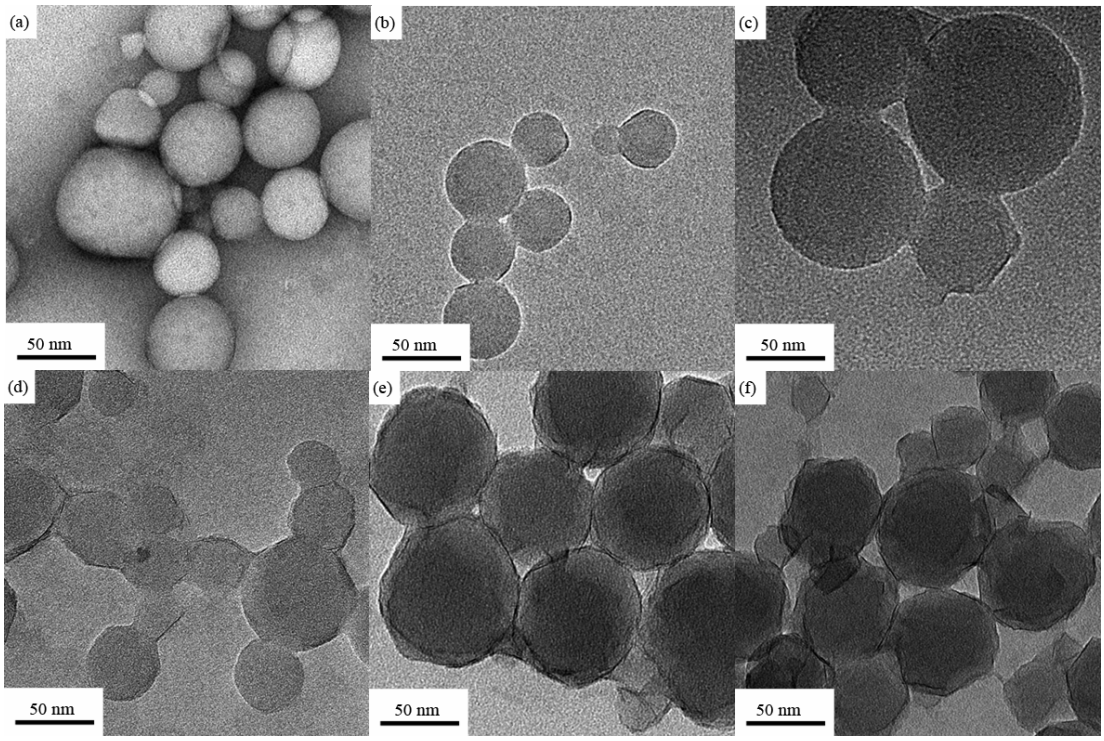

Fig. 4.3 TEM images of spin casted latex particles of (a) L0, (b) L7.5, (c) L10, (d) L20, (e) L30, (f) L50. The laponite corresponds to the black layer around the particles.

The TEM images in Fig. 4.4 show thin sections (60 nm) of particles embedded in melamine resin. In this case laponite platelets not attached to the PS particles were also visible. It is nevertheless concluded that although the laponite platelets were present in the aqueous phase of the latexes, they showed a clear tendency to adhere to the latex particles as a result of their chemical modification during synthesis.

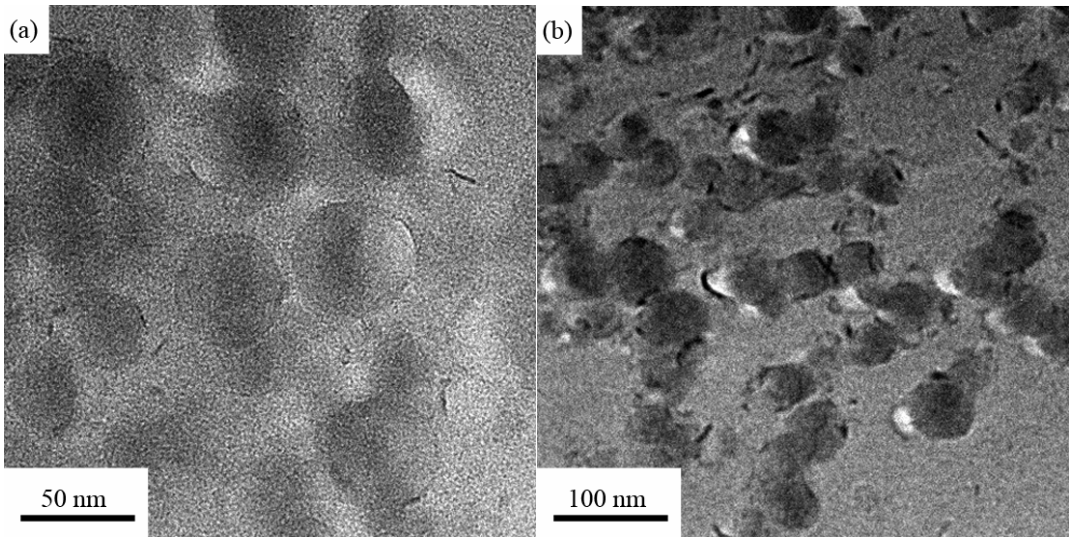

Fig. 4.4 TEM images of a thin section of (a) L10 and (b) L20 latexes embedded in melamine resin.

4.1.3 Film morphology

Thin films were obtained from the dry latex particles as described in section 3.4.2. Fig. 4.5 shows TEM images of thin sections of films obtained from latexes L5 to L50. A good dispersion of laponite was observed at low loadings (Fig. 4.5 (a)), while at high loadings, a 3D cellular arrangement of the laponite was visible (Fig. 4.5 (e) and (f)). This structure was only slightly deformed during the compression molding step, as may be seen from the micrographs.

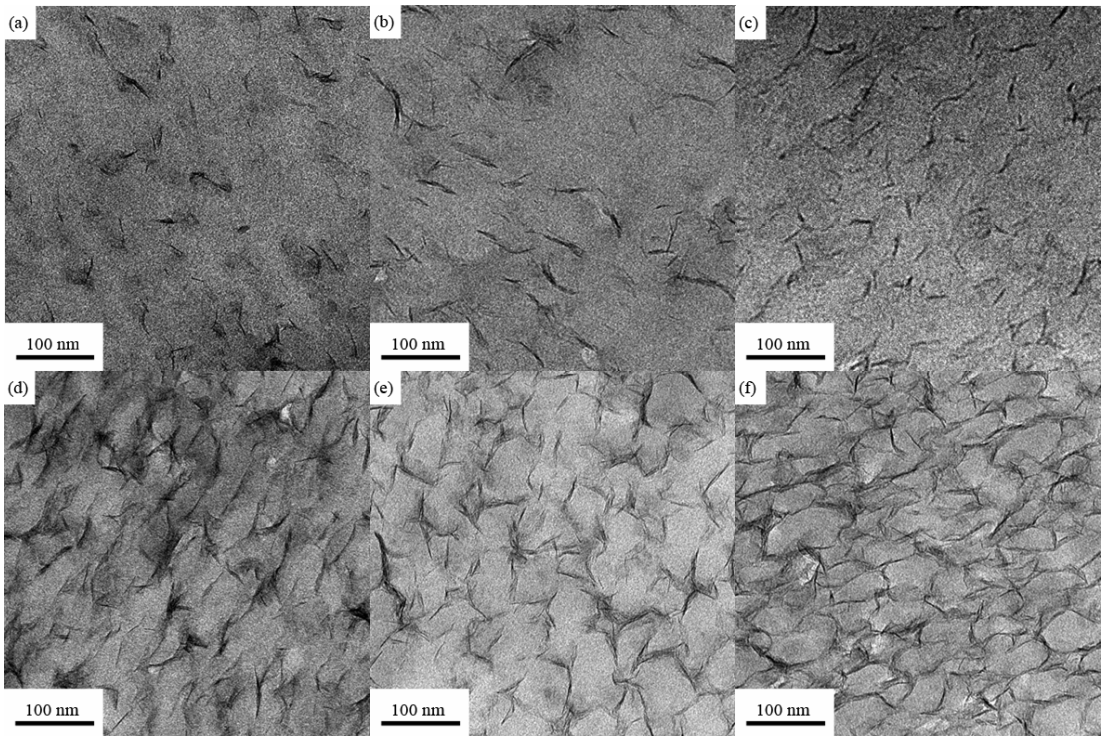

Fig. 4.5 TEM images of thin sections of film prepared from (a) L5, (b) L7.5, (c) L10, (d) L20, (e) L30 and (f) L50.

The presence of cellular arrangement of the laponite is a direct consequence of the single latex particle morphology. Higher magnification images of films prepared from L30 and L50 suggested that the degree of laponite platelet stacking was not significantly increased with respect to that of L20 (Fig. 4.6). The aggregate thickness was estimated by TEM image analysis to be of the order of 2 platelets for L5, 3 platelets for L7.5, 6 platelets for L10 and 7 platelets for L20, L30 and L50. The percolation threshold for contacts of overlapping discs placed on a 2D surface corresponds to a surface coverage of 0.676 and to a total disc area per unit surface of 1.12 [2, 3]. Taking the effective aspect ratio of the laponite aggregates to be 9 (54/6), the total volume fraction of laponite corresponding to percolation is hence estimated to be about 20 vol%

i.e. percolation is only expected for L50. This appears to be consistent with the TEM micrographs where the contacts between the laponite aggregates only appear continuous for L50 films.

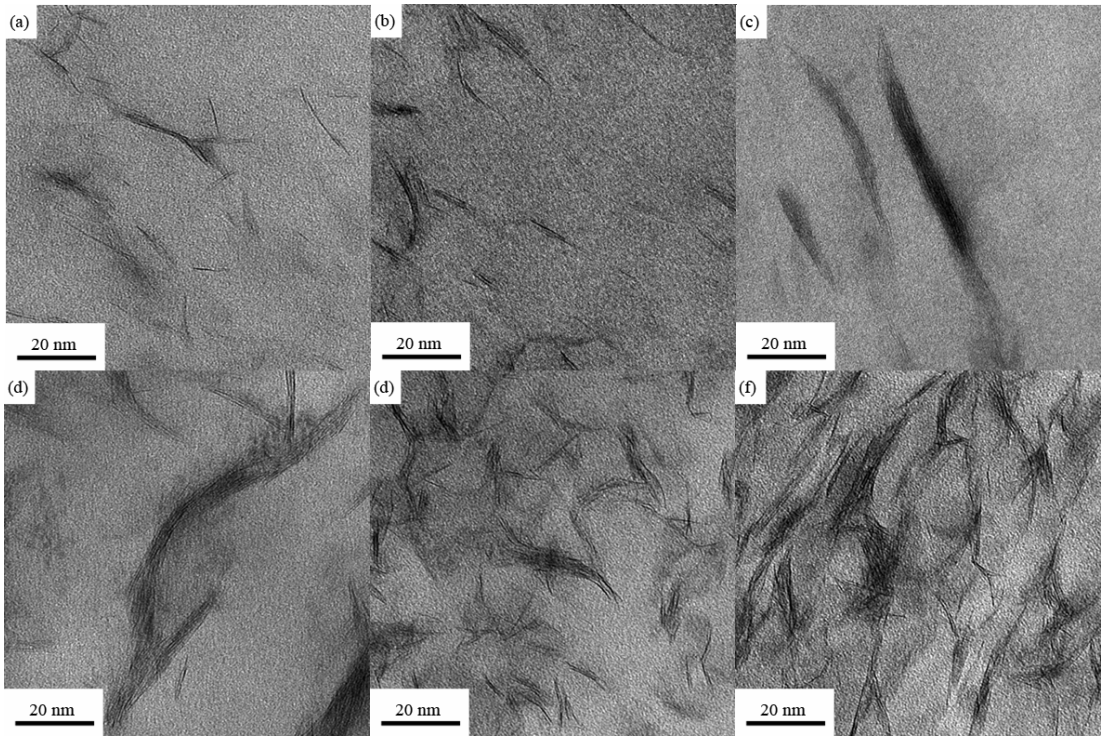

Fig. 4.6 High magnification TEM images of (a) L5, (b) L7.5, (c) L10, (d) L20, (e) L30 and (f) L50.

No changes in the extent of polymer intercalation in the laponite galleries were observed by XRD (Fig. 4.7). All the nanocomposites showed a diffraction peak at 2θ of around 6 ° which corresponds to d_{001} of about 1.48 nm for all the specimens, as compared with about 1.26 nm for the unmodified laponite, suggesting intercalation by the polymer (see section 4.1.1.1).

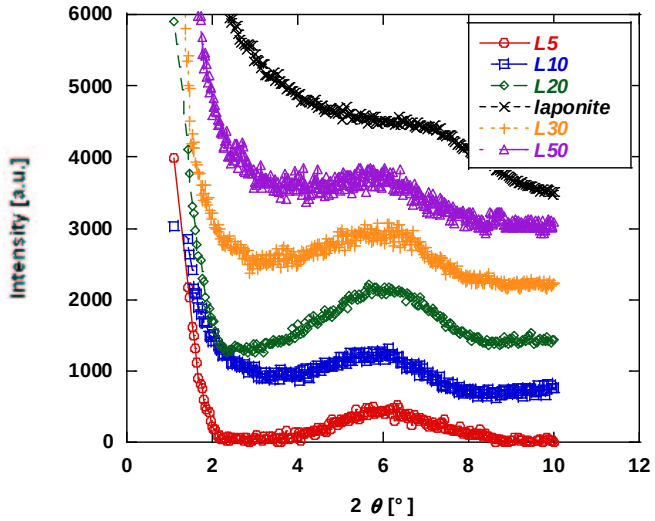

Fig. 4.7 XRD diffraction spectra of films prepared from L5, L10, L20, L30 and L50, showing no change in the degree of intercalation with laponite content.

4.1.4 Viscoelastic properties

Fig. 4.8 shows the effect of laponite content on the storage modulus, *E'*, and the loss factor, *tan* δ. Two different regimes of reinforcement were observed (Fig. 4.8 (a)). In the rubbery state, large storage modulus increases were found as a function of the overall laponite content, but in the glassy state L5 and L7.5 showed higher stiffness than L10 and L20 and similar stiffness to L30, as summarized in Table 8. The values of *E'* for the rubbery state were measured at 160 °C. The intensity of the peak in *tan* δ also decreased with increasing laponite content and a secondary transition was apparent in the high temperature regime for the highly filled systems L30 and L50 as shown in Fig. 4.8 (b). The decrease in *tan* δ is interpreted as an indication of a decrease in the total amount of matrix that contributes to the transition, owing to the presence of the laponite and to the immobilized interphase, which does not undergo the α relaxation. However, direct quantification of the degree of immobilization by normalization of the area under the loss tangent curves does not give reliable results [4]. The second relaxation peak has two possible explanations: it may be due to a higher relaxation temperature associated with the immobilized matrix, as proposed in [5, 6], in which case, it should be visible by DSC. Alternatively, the transition may correspond to the break-up of the percolation network formed by the laponite aggregates.

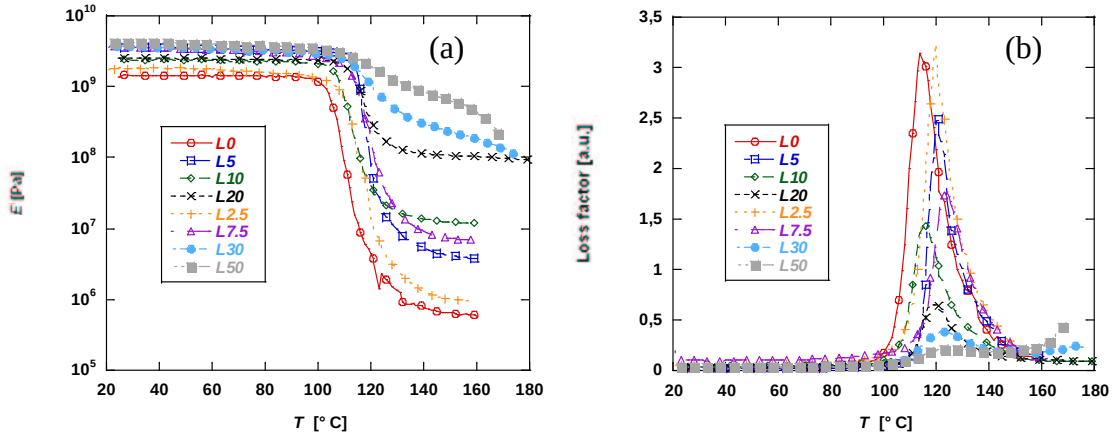

Fig. 4.8 (a) Storage moduli *E'* and (b) loss factor of L-series nanocomposites.

Sample	*E'* glassy state [GPa]	*E'* rubbery state [MPa]	*Tan δ* [°C]	T_g [°C]
L0	1.49	0.81	116	103
L2.5	1.80	0.95	120	112
L5	3.49	3.1	121	114
L75	3.46	6.93	124	113
L10	1.98	10.20	118	106
L20	2.01	102.3	119	111
L30	3.71	182	122	112
L50	4.10	432	126	112

Table 8 Results from DMA of L-series nanocomposites.

4.1.5 DSC measurements

T_g obtained from DSC scans showed similar trends to those in T_α, as shown in Table 8. No evidence of a second transition was found for L30 and L50 at high temperatures, however. This suggests that the origin of the second *tan δ* peak is mechanical rather than thermal. The increases in T_g in the nanocomposites may be ascribed to an immobilizing effect of the laponite. Evidence for an increase in the glass transition associated with filler particles has been reported previously in cases where there is a strong interaction with the matrix [7, 8].

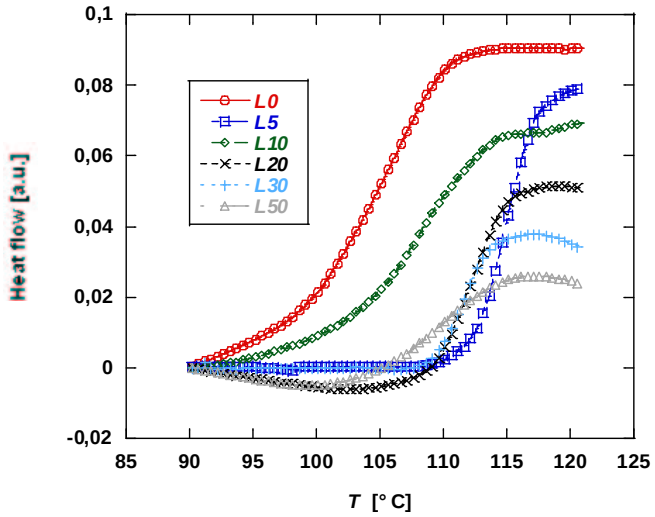

Fig.4.9 Normalized heat flow curves for L nanocomposites.

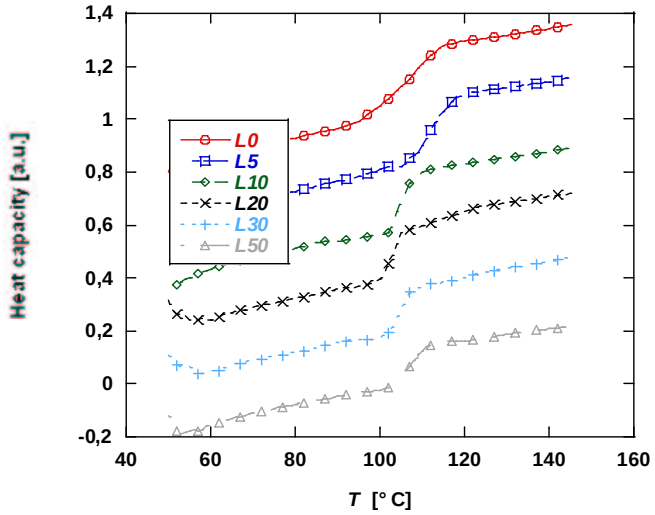

Fig. 4.10 MDSC heat capacity curves for L nanocomposites.

There was also a significant decrease in the intensity of the glass transition with increasing laponite content as shown in Fig. 4.9, where the signals have been normalized with respect to the weight of the PS matrix fraction in the nanocomposites. As discussed in section 2.4.1, the amount of the immobilized matrix at the filler surface may be estimated from precise measurements of the heat capacity by modulated DSC (MDSC) [9]. Results of measurements are given in Fig. 4.10 for the reversing heat capacities of the different nanocomposites. The change in heat capacity at T_g was obtained with the two tangents method proposed in [9]. Tangents to the MDSC traces are constructed far from the glass transition and the step in heat capacity estimated from the difference in the tangent at T_g. The rigid amorphous fraction (RAF) was then obtained from eq. 2.3 (section 2.4.1). The laponite contents obtained from ash tests given in section 3.1.1

were used for the calculations because they were assumed to be more accurate than the nominal laponite contents. The results are shown in Fig. 4.11, suggesting a linear dependence of the RAF on laponite content.

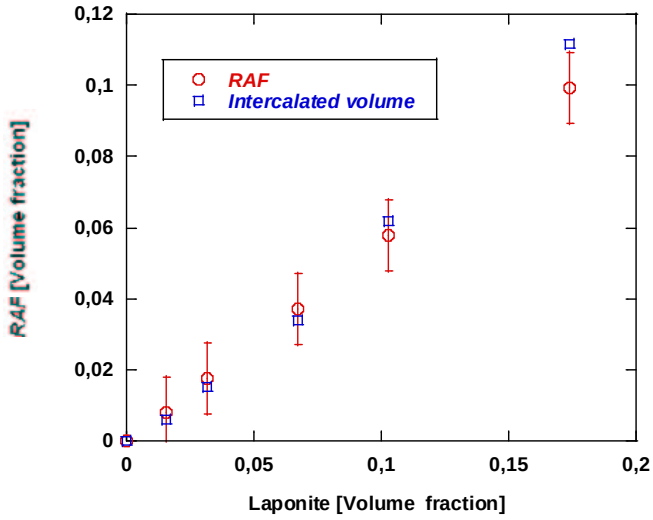

Fig. 4.11 RAF from MDSC as a function of laponite content and the intercalated matrix volume.

Assuming the latex particle to have a diameter of 80 nm and the aggregate thickness to be 9.88 nm (7 laponite layers, as discussed in section 4.1.3) it may be shown that the volume occupied by the laponite layer around each particle is 8.7 * 10^4 nm^3 in L50, for which complete coverage of the latex particle is assumed, taking into account the fact that the laponite aggregates are shared by two particles (see Appendix 3 for details of calculations). The volume fraction of the laponite is 0.24 in L50 (laponite density 2.53 g/cc), so that the volume of laponite per latex particle is 6.4 * 10^4 nm^3. The difference between these two values is comparable to the amount of polymer present in the laponite galleries which is approximately 9 % of the total volume. If the macromonomer volume is subtracted (roughly 5 % of the laponite volume, i.e. 3 * 10^3 nm^3), the total intercalated volume fraction of L50 is estimated to be about 8 % which compares with the measured RAF in Fig. 4.11. On the other hand, if an interphase thickness of about 2 nm is assumed to be present at the laponite aggregate surfaces, as proposed for silica in the literature [9], the total interphase volume fraction is more than doubled. This suggests that the RAF measurements provide an estimate of the extent of the strongly confined regions of the matrix, i.e. the intercalated matrix but not the total amount of matrix that interacts with filler surface. The amount of intercalated material was also estimated from the distance obtained from XRD for the other nanocomposites, giving volume fractions of 0.4, 1.4, 3.3, 6.2, 11.3 % for L5, L10, L20, L30 and L50 respectively (again see Appendix 3 for details). These results were again consistent with the RAF measurements, as shown in Fig. 4.11. It is important here to note that,

even after calibration of the instrument, the heat capacity measurements showed some experimental scatter. Consequently, the RAF values are estimated to contain en error of about ± 0.01, which makes it difficult to interpret the detailed trends in RAF, particularly at low laponite contents. However the correlations for the highly filled nanocomposites are thought to be reliable.

Decreases in the transition amplitude of the heat capacity at T_g have been discussed previously for strongly confined polymers, but without quantification [10-15]. It is ascribed to spatial confinement (for example a decrease in thin film thickness) or to physical confinement in nanopores or in gaps between nanoparticles. The conceptual equivalence between these two cases has been discussed in several papers [12, 16, 17]. The filler may be regarded as a substrate for the polymer and the matrix between two filler particles as a thin film whose thickness changes as a function of the filler-filler distance. Strong physical matrix confinement may not only account for correspondence between the RAF and the intercalated PS matrix, but also suggest an influence on the rest of the matrix in the vicinity of the laponite. The rms end-to-end distance associated with the entanglement molecular weight in PS chains is of the order of 6 nm, which is comparable with the laponite shell thickness, so that one might expect local modification of the rubbery modulus throughout the laponite-rich regions, although this is difficult to quantify directly. It has also been shown in the case of polyethylacrylate/silica nanocomposites, in which the silica is covalently bound to the matrix, that there is a long range gradient in the polymer glass transition temperature in the vicinity of the filler [7, 8]. It was proposed that the mechanisms of reinforcement in the rubbery state are the same as those that lead to the increase of T_g , i.e. partial chain immobilization, and that a glassy interphase of few nanometers in thickness is present at temperatures well above T_g. An abrupt increase in T_g and even a total absence of glass transition have been observed in supported thin polymer films when strong interactions between the polymer and the substrate are present [18-22]. It follows that the RAF may not show a distinct T_g, as suggested by the present measurements.

4.1.6 Modeling of mechanical properties

4.1.6.1 Theory

The experimental storage moduli obtained by DMA were initially compared with those obtained from classical micromechanical models, i.e. the Halpin-Tsai (H-T) and Mori-Tanaka (M-T) models. The assumptions underlying these theories are that both polymer and inclusions show homogeneous elastic properties. The composite is considered as a system in which the laponite

platelets are randomly distributed in the matrix. The reference system of Fig. 4.12 will be referred to when considering the platelets

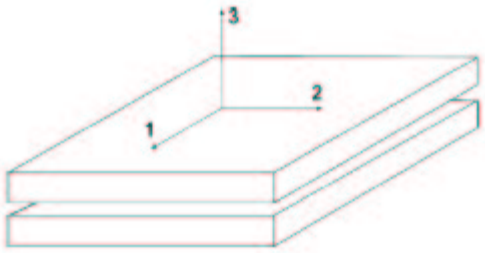

Fig. 4.12 Three axis reference system for stacked platelets used for calculations with the H-T and M-T models.

The H-T model gives the modulus of a uniaxial composite in the orientation direction as [23]:

$$E_{11} = E_m \frac{1+\xi\eta\phi}{1-\eta\phi} \qquad \text{eq. 4.1}$$

where

$$\eta = \frac{E_f / E_m - 1}{E_f / E_m + \xi} \qquad \text{eq. 4.2}$$

This corresponds to the in-plane modulus of a composite with the platelet orientation as in Fig. 4.12. In this case E_m and E_f are the matrix and laponite Young's moduli respectively, ϕ is the laponite volume fraction and $\xi = 2\alpha$ is a shape factor related to the laponite aspect ratio α. The value of E_f is taken to be the in-plane modulus of mica (178 GPa) [24]. The expression is the same for the transverse modulus E_{33} but with $\xi = 2$. It has been demonstrated, based on laminate theory, that the Young's modulus of an isotropic composite, i.e. with a random platelet orientation, may be written as [25]:

$$E_c = 0.49E_{11} + 0.51E_{33} \qquad \text{eq. 4.3}$$

The M-T model is an analytical micromechanical model often used to calculate the moduli of composite materials [39]. In the case of spheroidal aligned inclusions, Tandon and Weng derived the analytical solutions for the Young's modulus given in equations 4.4 and 4.5 [26]

$$E_{11} = \frac{E_m A}{A + \phi(A_1 + 2\nu_0 A_2)} \qquad \text{eq. 4.4}$$

$$E_{33} = \frac{2E_m A}{A + \phi(-2\nu_0 A_3 + (1-\nu_0)A_4 + (1+\nu_0)A_5 A)} \qquad \text{eq. 4.5}$$

where υ_0 is the Poisson's ratio of the matrix and A, A_1, A_2, A_3, A_4 and A_5 are the components of the Eshelby tensor [26].

Rather than considering single laponite platelets as the reinforcing elements, which would be unrealistic in view of the TEM and XRD observations, the so called "effective particle approach" was used for calculations with the H-T and M-T models [27]. The effective particle (i.e. the laponite aggregate) aspect ratio was identified with the average aspect ratios evaluated by TEM and given in Table 9. The effective particle volume fraction ϕ_{Part} has been calculated along with the laponite volume fraction in the particle χ. This allows calculation of the effective particle mechanical properties based on the model in Fig. 4.13 (equations 4.6 to 4.8):

$$E_{11} = \chi E_f + (1-\chi)E_m \qquad \text{eq. 4.6}$$

$$E_{33} = \frac{E_f E_m}{(1-2\beta\nu_0)[(1-\chi)E_f + \chi E_m]} \qquad \text{eq. 4.7}$$

$$\beta = \frac{E_f\nu_0 - E_m\nu_1}{(1-\nu_0)E_f + (1-\nu_1)E_m} \qquad \text{eq. 4.8}$$

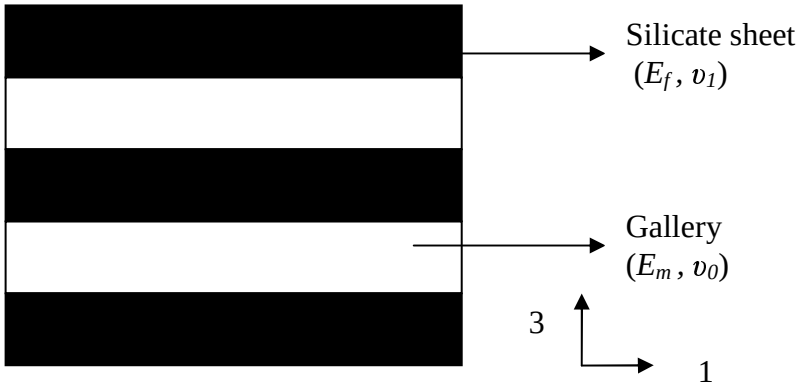

Fig. 4.13 The effective particle corresponding to the laponite aggregate.

It was assumed that the properties of the polymer in the interlayer galleries were isotropic and identical to those of the matrix. The Poisson's ratio of the silicate, ν_1, was taken to be 0.15 [28] and the Poisson's ratio ν_0 of the matrix to be 0.33 in the glassy state and 0.48 in the rubbery state [29, 30]

Sample	Aggregate thickness [nm]	Aspect ratio
L2.5	2.48	21.77
L5	2.48	21.77
L7.5	3.95	13.71
L10	8.4	6.45
L20	9.88	5.46
L30	9.88	5.46
L50	9.88	5.46

Table 9 Laponite aggregate size as a function of laponite content measured by TEM

4.1.6.2 The glassy state

The results of H-T and M-T calculations together with the experimental values for *E'* from DMA in the glassy state are shown in Fig. 4.14. At temperatures below T_g, the laponite platelets are assumed to act as simple geometrical reinforcing agents and can be considered as nodes in an already rigid structure. The effect of the laponite is very local because of the limited mobility of the polymer chains and this explains the weak enhancement of storage modulus in the glassy state. The non-monotonic behaviour in Fig. 4.14 can be explained as follows. The stiffness increase with laponite content up to 2 vol % is due to a higher degree of exfoliation of the laponite at low filler loadings leading to a higher aspect ratio of the laponite aggregates. When laponite content is increased further, aggregation starts to play an important role, the aspect ratio decreases and the stiffness also decreases. Only at very high laponite contents does the elastic modulus exceed the value at 2 vol %. The models appear consistent with the experimental behaviour and agreement to within an order of magnitude with the data is obtained.

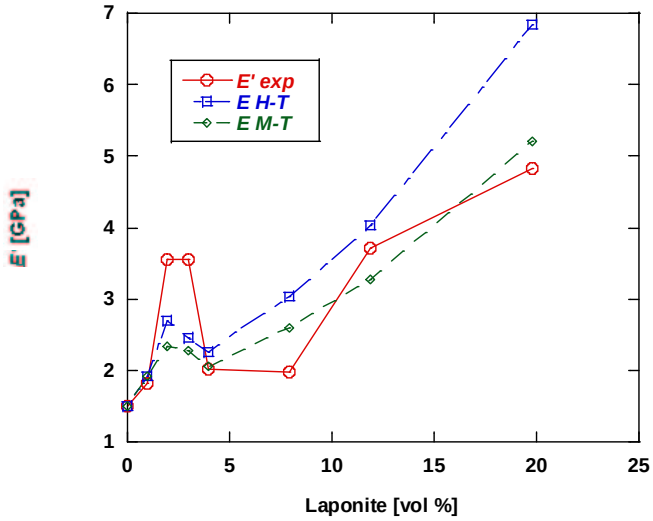

Fig 4.14 Comparison of the room temperature experimental storage modulus (E'_{exp}) with the values calculated from modified Halpin-Tsai ($E_{H\text{-}T}$) and Mori-Tanaka ($E_{M\text{-}T}$) models.

4.1.6.3 The rubbery state

The same calculations were repeated for the rubbery state at 160°C taking the modulus of the intercalated matrix to be equal to that of PS at the same temperature (0.8 MPa). The results are shown in Fig.4.15. The classical micromechanical models are totally inadequate for predict stiffness increases in the rubbery state in these nanocomposites, underestimating the experimental values by more than two orders of magnitude. This indicates that a different approach is required.

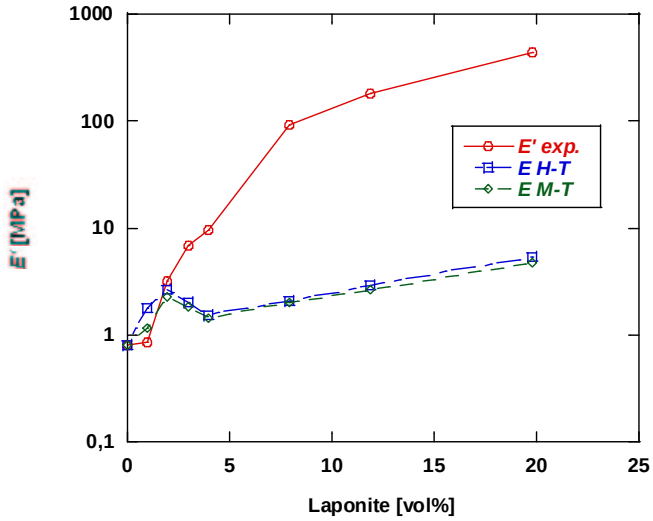

Fig. 4.15 Comparison of the experimental storage modulus (E'_{exp}) at 160 °C with the values calculated from modified Halpin-Tsai ($E_{H\text{-}T}$) and Mori-Tanaka ($E_{M\text{-}T}$) models.

It was previously shown by MDSC that part of the PS matrix remains immobilized in the presence of laponite. A first attempt to model the mechanical properties of the PS/laponite nanocomposites in the rubbery state again made use of the H-T and M-T models combined with the aggregate approach, but assuming the intercalated matrix to have the same properties as in the glassy state, i.e. the immobilized intercalated layer is taken into account. The rest of the matrix has the same properties as PS in the rubbery state. Such calculations still predict moduli of the same order of magnitude as those in Fig. 4.15, i.e. in the range of a few MPa for all laponite contents. This shows that is not possible, even by including the effect of the RAF, to model the mechanical properties of the nanocomposites on this basis.

4.1.6.4 The foam approach: modeling using a modified rule of mixture

As discussed in section 4.1.3, a cellular arrangement of the laponite is evident especially at high filler contents (see Fig.4.5). In the rubbery state, the nanocomposites structure might therefore be considered as a laponite-rich foam with open cells containing an uncompressible liquid (rubbery) matrix (Fig. 4.16).

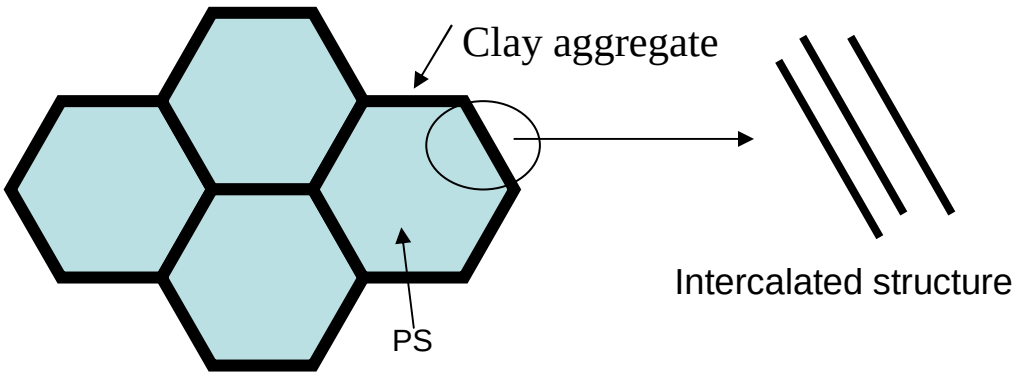

Fig. 4.16 Model of the cellular structure of the laponite nanocomposites.

Mechanical models have been developed both for open and closed cell foams [31] (see section 2.4.3 for a review). In dry open cell foams in compression, strain is achieved by bending of the cell walls. In foams filled with an incompressible liquid, on instantaneous application of a force, i.e. before the fluid starts to flow from one cell to another, the strain is accommodated by axial deformation of the cell walls [32]. It has also been shown that the equations governing the foam response in compression are also valid for tensile deformation in the linear elastic regime. The

situation at the moment of strain application, before the fluid starts flowing, is therefore assumed to describe the response of the PS/laponite nanocomposites.

A possible way of modeling the elastic response above T_g is to decouple the contribution of the cellular structure and the contribution of the rubbery PS matrix inside the cells. In this case the nanocomposite stiffness is estimated from:

$$E_c = \left(1 - \frac{\rho}{\rho_s}\right) E_m + C\left(\frac{\rho}{\rho_s}\right)^n E_1 \qquad \text{eq. 4.9}$$

where ρ is the foam density, ρ_s is the cell wall density, E_m is the rubbery PS matrix modulus (0.8 MPa) and E_1 is the cell wall modulus. $C \sim 1$ and n are constants that depend on the foam geometry (see section 2.4.3). According to Edwards, the dependence of the foam stiffness on the reduced density is linear in presence of an uncompressible filler as in the case of closed cell foams [32]. For this reason the value of the exponent n in eq. 4.9 will be taken to be equal to unity, although the real materials morphology does not resemble a closed cell foam at low laponite contents. On the other hand, at laponite contents higher than 7.9 vol %, a closed cell morphology is a more reasonable assumption in the rubbery state. Calculation of the cell wall modulus, E_1, was carried out as previously using the H-T equation:

$$E_1 = \frac{1 + 2\rho_s/\rho\,\alpha\phi}{1 - \rho_s/\rho\,\phi} E_{m,wall} \qquad \text{eq. 4.10}$$

where ϕ is the laponite aggregate volume fraction in the cell wall and $E_{m,wall}$ is the matrix stiffness in the cell walls, taken to be an adjustable parameter. ρ/ρ_s is the cell wall volume fraction and it can be estimated by simple geometrical calculations using the wall thicknesses in Table 9. In the cell walls two different kinds of matrix portion are present: the intercalated matrix forming RAF which is already included in the term ϕ and the matrix portion trapped between laponite aggregates or interacting with the aggregate surfaces that could form a partially immobilized interphase. This latter corresponds to $E_{m,wall}$ in eq. 4.10. Combination of eq. 4.9 and 4.10 gives good predictions of the experimental results in the nanocomposites at high laponite contents if $E_{m,wall}$ is taken to be 40 MPa, as shown in Fig. 4.17.

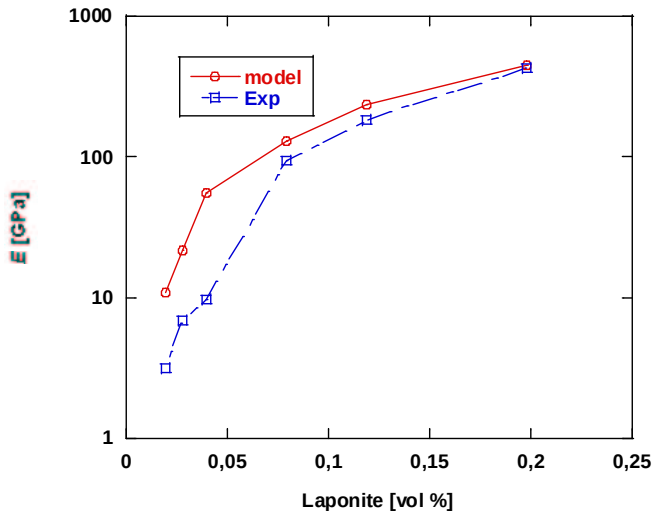

Fig. 4.17 Calculations (model) and experimental results (exp) for the L-series nanocomposite moduli in the rubbery state using the model of eq. 4.9, taking the matrix modulus in the cell walls equal to 40 MPa.

When the laponite content is low the predictions overestimate the experimental data. This may be accounted by the absence of a clear cellular structure under these conditions. For $E_f >> E_m$ and low laponite contents the H-T equation for the overall modulus (eq. 4.1 section 4.1.6.1) may be rewritten as

$$E \approx (1 + 2\alpha\phi)E_m \qquad \text{eq. 4.11}$$

If $E_{m,\,wall}$ is taken to be equal to E_m, then combining eq. 4.9 and 4.10 with $C = 1$ and $n = 1$ gives eq. 4.11 in the limit of small ϕ. This means that the predictions for a closed cell foam (or a open cell foam with a fluid inside) are similar to those of H-T in the low filler content limit as shown in Fig. 4.18 for $E_{m,\,wall} = E_m = 0.8$ MPa and assuming exfoliation, i.e. $\alpha = 54$ (cf. also Fig. 4.15). This also provides a rationale for the use of H-T in the glassy state. This analysis therefore suggests a cross over from a regime, at low laponite contents, where the cellular structure is not well defined and confinement effects play a minor role, to a regime where these effects become dominant.

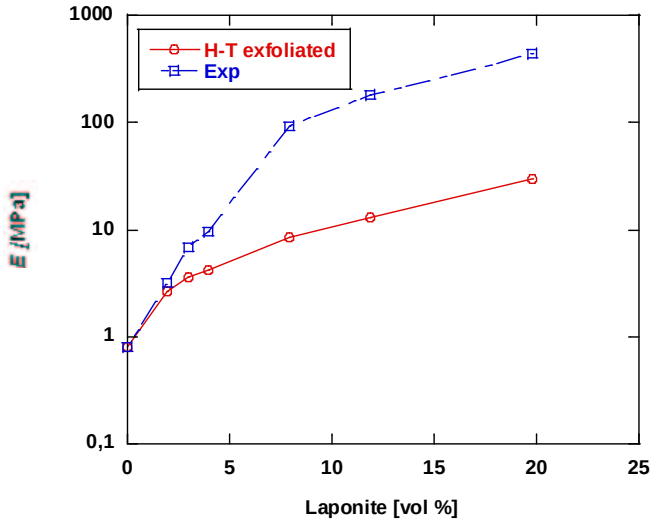

Fig. 4.18 Experimental storage moduli data for PS/laponite nanocomposites in the rubbery state (exp) compared with the predictions of eq. 4.11 (H-T exfoliated).

An alternative estimate of the cell wall modulus E_1 used in eq. 4.9 has been made using a model developed for mineralized collagen fibrils [33]. The geometry of the collagen structure is depicted in Fig. 4.19. This structure is very similar to that assumed for the laponite stacks in the cell walls of the L nanocomposites. Only the tensile stress along the longitudinal axis of the platelets was considered, i.e. transverse deformation was not taken into account, so that only upper bounds were obtained.

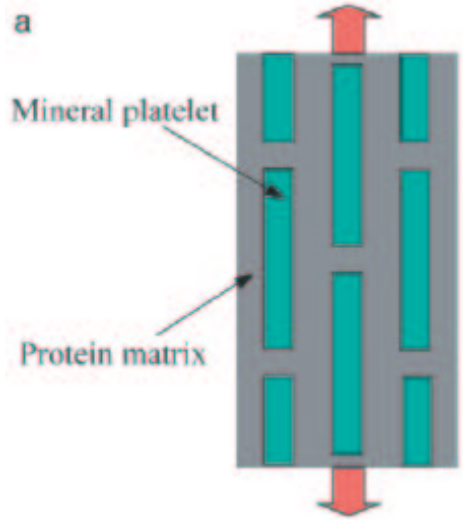

Fig. 4.19 A geometrical model for collagen [33].

The tensile modulus E_1 for the model of Fig. 4.19 is described by equation 4.12 [34]

$$E_1 = \frac{\phi^2}{\frac{\phi}{E_c} + \frac{4(1-\phi)}{G_p \alpha^2}} + (1-\phi)E_p \qquad \text{eq. 4.12}$$

where ϕ is the mineral volume fraction, α in the mineral aspect ratio, *E* and *G* are the tensile and shear moduli, and the subscripts "*c*" and "*p*" refer to laponite clay and polymer.

Although the "collagen model" may better reflect the structure of the laponite cell walls than H-T, it leads to similar predictions, from which one may conclude that the results are insensitive to the details of the micromechanical model chosen for the cell walls properties. Once again, an increase in cell wall matrix modulus appears essential in accounting for the experimental results, regardless of the micromechanical model used for the cell walls.

The main conclusion to be drawn from the modeling of the PS/laponite nanocomposite stiffness in the rubbery state is that an increase of the matrix modulus in the region around the laponite platelets must be invoked to fit the experimental data. This effect is the result of physical confinement of matrix chains and of strong interfacial interactions. Similar results will be obtained in FEM simulations described in section 7.2.

One of the critical points in the above analysis is the strong dependence of the results on the estimates of the thickness of laponite aggregates forming the cell walls, since the statistical analysis of the TEM images depends strongly on the length calibration of the scale bars given by the camera used for acquisition, which is a potential source of error. Another critical point is the mechanical anisotropy of the laponite aggregates. In principle these show a longitudinal stiffness that is much higher than the transverse stiffness (comparable to the matrix stiffness). For all the above calculations of the cell wall properties only the longitudinal component was considered. This choice will be justified in section 7.2 on the basis of finite element calculations, which show that the load tends to concentrate in the laponite aggregates parallel to the direction of the applied deformation, the transverse aggregates behaving almost like the matrix. This is consistent with the present foam models, in which the most important component of the deformation in tension and compression is the axial deformation of the cell walls.

4.1.6.5 Importance of the cellular structure

A further demonstration of the importance of the cellular structure for modeling the mechanical properties is given by the results of a simple experiment. Plane strain compression in a confined mold such as shown schematically in Fig. 4.20 could in principle break up the cellular structure and induce a partial orientation of the laponite platelets.

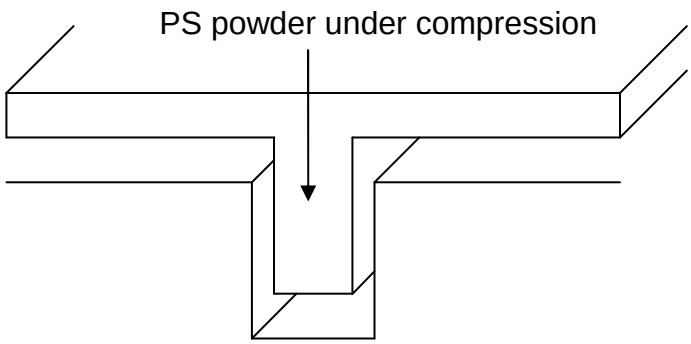

Fig. 4.20 Mold used to break up the nanocomposite cellular structure.

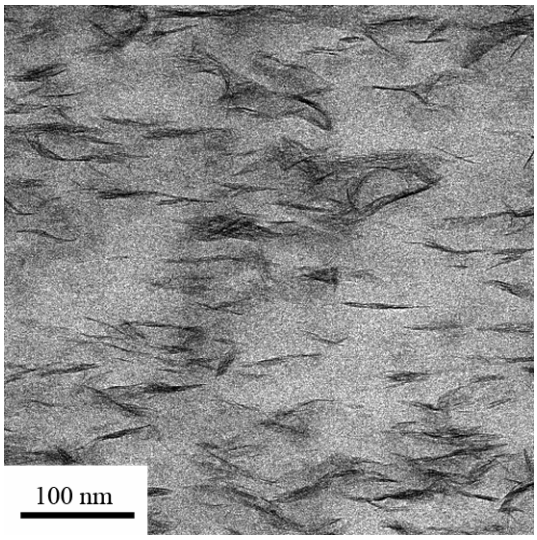

Fig. 4.21 TEM image of a film of L20 deformed in plane strain compression.

The observed effect on the film morphology of the deformation in plane strain compression is shown in Fig. 4.21 for L20 confirming both destruction of the cellular laponite structure and partial orientation.

In DMA scans the mechanical properties are unchanged in the glassy state after plane strain compression, while in the rubbery state a strong decrease in storage modulus is observed (Fig. 4.22). A slight increase observed in T_α could be accounted for in terms on increased orientation and dispersion of the laponite aggregates. The large decrease in stiffness in the rubbery state was attributed to the destruction of the cellular structure on the other hand. The Halpin-Tsai equations 4.1 and 4.2 can be used with the aggregate approach of Fig. 4.13 to model the properties of the deformed nanocomposite, taking the matrix modulus inside the aggregates to be equal to the glassy state (1.49 GPa) and the rest of the matrix to be in the rubbery state

(modulus about 0.8 MPa) and taking into account the orientation. A tensile modulus of about 5 MPa was found, which is comparable with the measured modulus of 10 MPa at 170 °C.

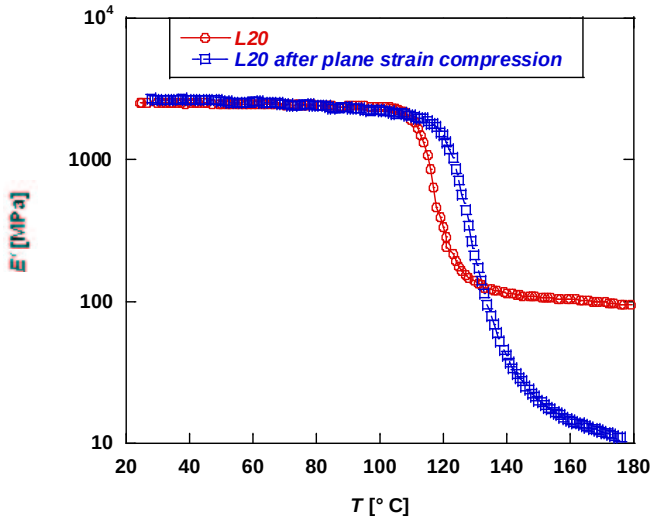

Fig. 4.22 Effect of breaking up the cellular structure of the laponite on the storage modulus of L20.

4.2 PS/laponite nanocomposites from nitroxide mediated polymerization (NMP)

As already discussed in section 3.1.3, the *in situ* NMP synthetic technique allows the production of polymer laponite nanocomposites with control of the molecular mass of the matrix, allowing rheological measurements that are not possible with the latex-based materials because of their high molecular weights. The characteristics of the materials are summarized in Table 3 (see section 3.1.3). Fig. 4.23 shows TEM images of samples with 0.4 and 1 vol % of laponite respectively. The TEM images show that NMP gives good laponite exfoliation and dispersion. This is a result of the *in situ* growth of chains on the laponite platelets.

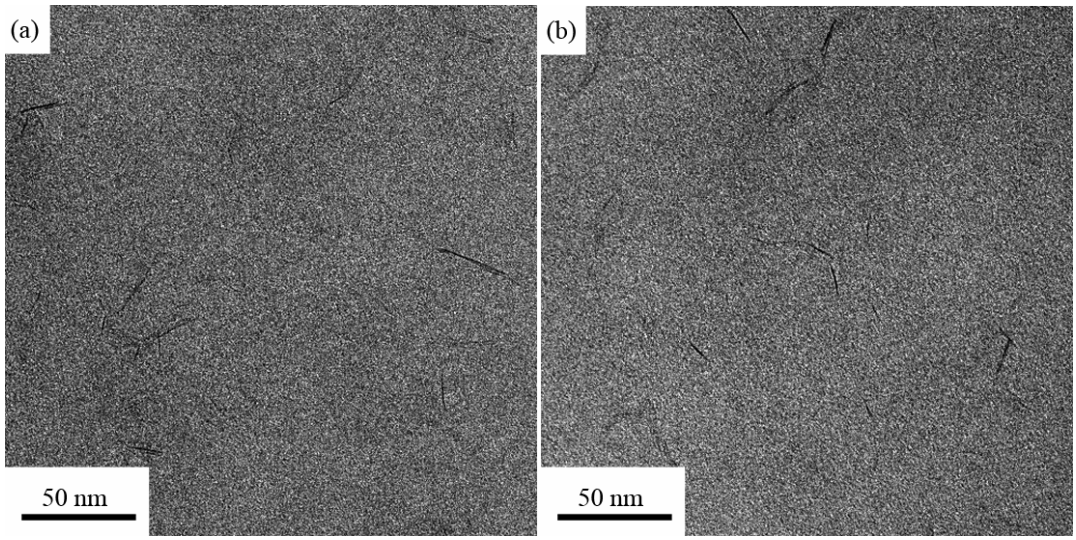

Fig. 4.23 TEM images showing (a) 0.4 vol % and (b) 1 vol % PS/laponite nanocomposite.

DMA scans were performed on thin films of the nanocomposites. As seen in Fig. 4.24, in the glassy state, small increases in storage modulus were observed with increasing laponite content, but in the rubbery state little reinforcement effect was observed. There were no significant shifts in T_α and T_g with respect to the matrix (see Table 10).

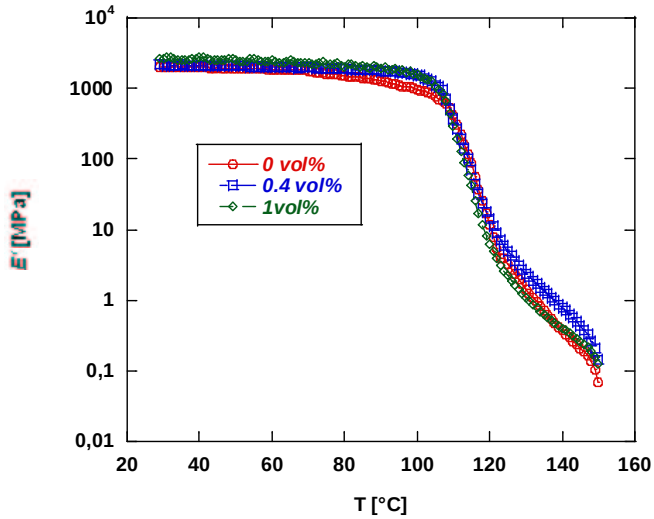

Fig. 4.24 DMA scans for NMP laponite nanocomposites. Percentage is by weight.

Laponite (vol %)	*E'* glassy state (GPa)	*E'*rubbery state (150°C) (Mpa	*Tg δ* (°C)	T_g (°C)
0	2.0	0.16	120	103
0.4	2.15	0.21	119	104
1	2.62	0.16	119	102

Table 10 DMA and DSC results for NMP laponite nanocomposites.

The results for storage modulus may be interpreted as follows: in the glassy state the laponite acts as a classical reinforcing element inducing a relative stiffness increase. At comparable laponite contents these are more important than in the case of the L nanocomposites (Table 8, section 4.1.4) owing to the better laponite dispersion leading to higher aspect ratios for the platelets. In the rubbery state, the stiffness remained almost unchanged and this could be ascribed to the lack of a cellular-like arrangement of the laponite. No T_g shifts were observed here Melt rheology measurements were performed as described in section 3.4.8. In this case the relatively low molecular mass allows good adhesion of the materials to the parallel plates of the rheometer. The results of oscillatory shear experiments are shown in Fig. 4.25,

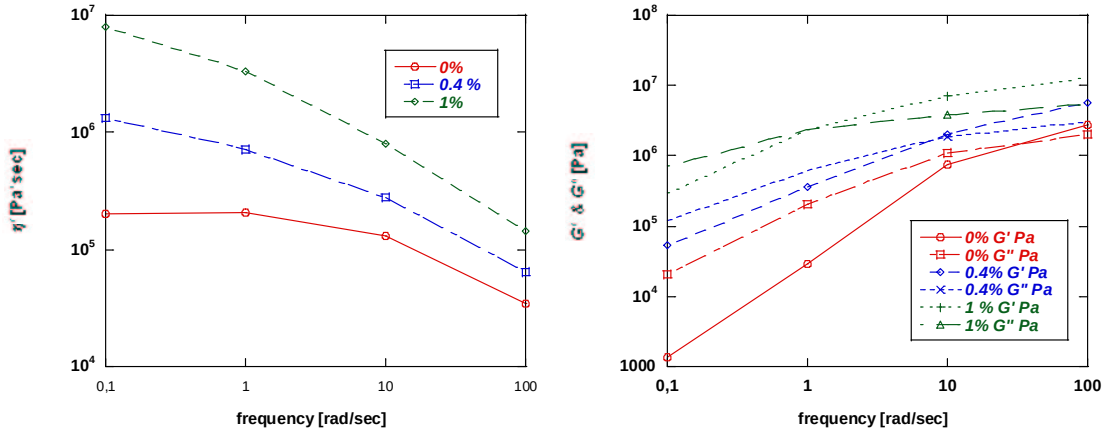

Fig. 4.25 Complex viscosity and storage and loss moduli of NMP nanocomposites.

Similar results to those in [34-36] were found. A Newtonian plateau in the complex viscosity η^* is observed in the low frequency region for the matrix, while increased η^* with laponite content in the nanocomposites, which also show more marked shear thinning. In presence of laponite the Newtonian plateau is not observed in the frequency range considered here. Both *G'* and *G"* show an increase with laponite content at all frequencies. The crossover point where the transition from liquid-like to solid-like behavior takes place is also shifted towards lower

frequencies. Terminal behavior was observed for *G'* and *G"* in the low frequency region for the matrix. All these results indicate increased solid-like behavior when the laponite content is increased. This has been attributed by several authors as the effect of filler-filler interactions and the creation of a filler percolation network [34-38]. Percolation of laponite-laponite contacts is not evident in these nanocomposites, as indicated by Fig. 4.23. However, it must be taken into account that only the edge-on platelets are visible and because of good exfoliation many other platelets are present which are not observed directly. This means that although a continuous 3D laponite structure has not been obtained as in the case of latex based styrenics, partially immobilized matrix bridges between platelets may exist accounting for rheological response.

4.3 PS/ laponite nanocomposites from miniemulsion polymerisation

4.3.1 Latex particle morphology

Miniemulsion polymerization is expected to provide very good control of the single latex particle morphology. PS/laponite latexes prepared by miniemulsion polymerization have been obtained in order to evaluate the effect of this technique on the final film properties. In the LCPP latexes (see section 3.1.4) the laponite is expected to be encapsulated in the PS particles, while it should again form a shell around them in the case of ULM latexes. TEM pictures of spin coated latex particles of the LCPP and ULM specimens are shown in Figs. 4.26 and 4.27, TEM pictures of latex particles embedded in melamine resin are shown in Fig. 4.28.

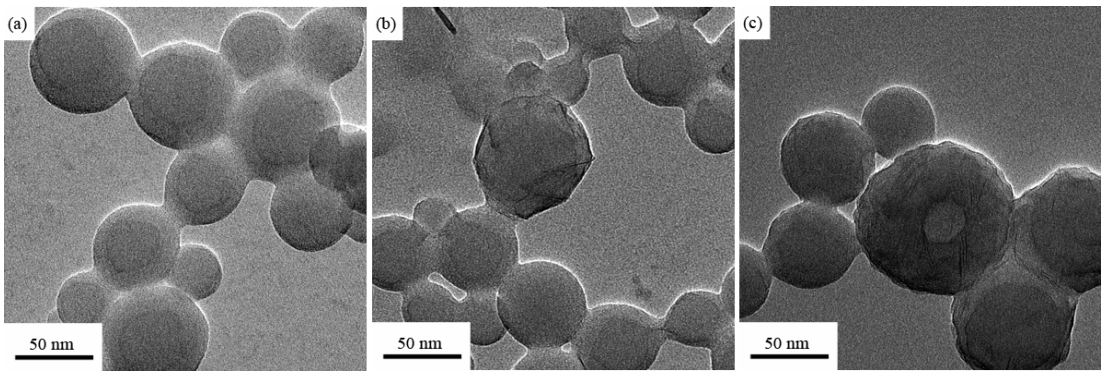

Fig. 4.26 TEM pictures of LCPP latexes: (a) LCPP0, (b) LCPP5, (c) LCPP7 (laponite platelets are visible inside the particles).

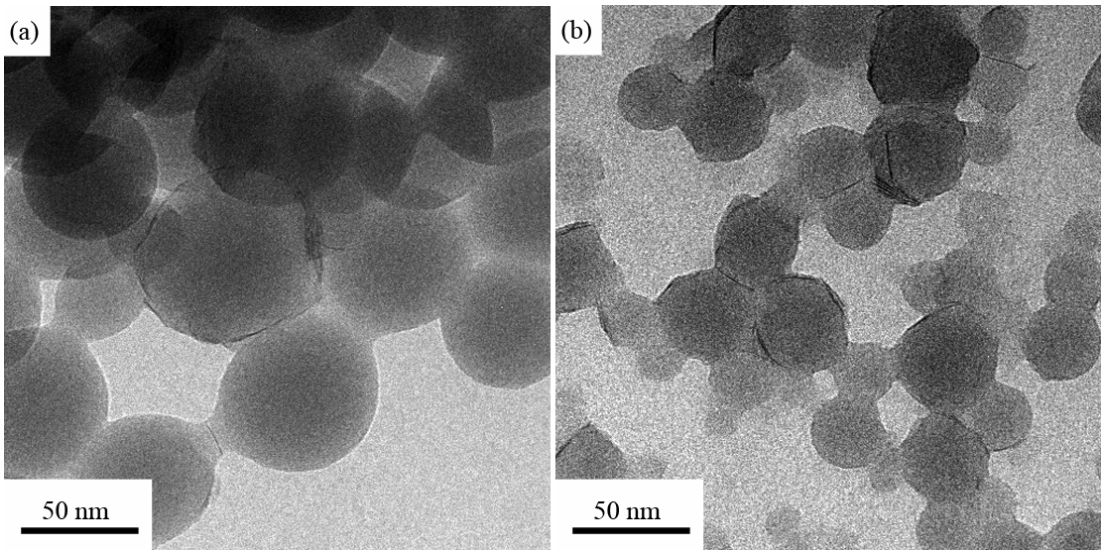

Fig. 4.27 TEM pictures of the ULM latexes: (a) ULM5 and (b) ULM30. The laponite platelets are visible at the particle surfaces.

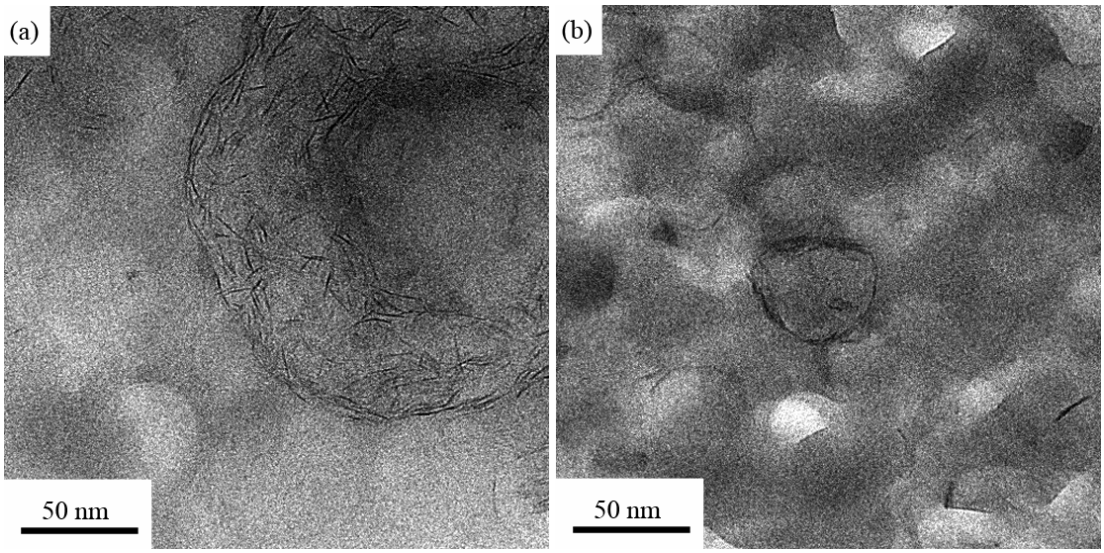

Fig. 4.28 Embedded (a) LCPP7 and (b) ULM30 latex particles in melamine resin.

Figs. 4.26, 4.27 and 4.28 show clearly the different morphology of the LCPP and ULM latexes. The former shows encapsulation of the laponite platelets inside the PS spheres, whereas for these latter the laponite is located on the particle surface. As seen in Figs. 4.26 and 4.28 a very high degree of exfoliation is obtained in the LCPP samples, but the laponite platelets are very poorly distributed among the PS particles. The particle size distribution is also relatively broad and the laponite tends to be encapsulated only in the largest particles. The miniemulsion process does not appear to lead to reduced particle size with respect to conventional emulsion polymerization in this case, the largest particles having diameters well over 100 nm.

In the ULM latexes, the degree of exfoliation decreases as the laponite content increase from 5 to 30 wt %. The laponite is more homogeneously distributed among the PS particles (Fig. 4.28), but the size distribution of PS particles is again broad although the average size of the particles imaged by TEM was lower than in Table 5 (see section 3.1.4).

4.3.2 Film morphology

Relatively thin films (0.3 mm) were obtained from both the LCPP and ULM latexes by compression moulding using the procedure reported in section 3.4.2. Unlike the L latex films of section 4.1, the LCPP and ULM based films were not transparent, which suggest laponite aggregation during processing. This is confirmed by TEM imaging of thin sections from the films. Fig.4.29 shows a TEM image of a thin section from a LCPP5 film: a good level of exfoliation is reached locally but the non uniform encapsulation strongly affects the overall laponite distribution in the film. A memory of the original particle structure can be clearly seen. Fig. 4.30 shows a TEM image from a ULM5 film. In this case laponite aggregation can be observed even at low filler concentrations and the aggregation increases as the laponite content increases.

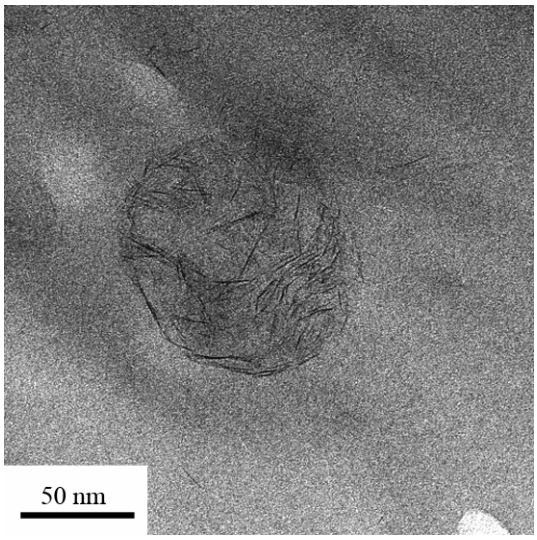

Fig. 4.29 TEM image of a thin section from a LCPP5 film.

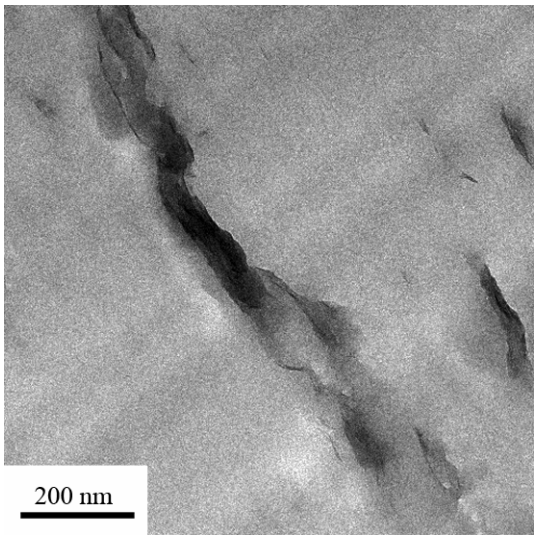

Fig. 4.30 TEM image of a thin section from a ULM5 film.

4.3.3 Viscoelastic properties

DMA results for LCPP0 and LCPP5 films are given in Fig. 4.31. No increases in storage modulus were found in either the glassy or rubbery state and no shift of the α transition temperature was observed as shown in Fig. 4.31. The laponite therefore does not significantly affect the viscoelastic properties of these films.

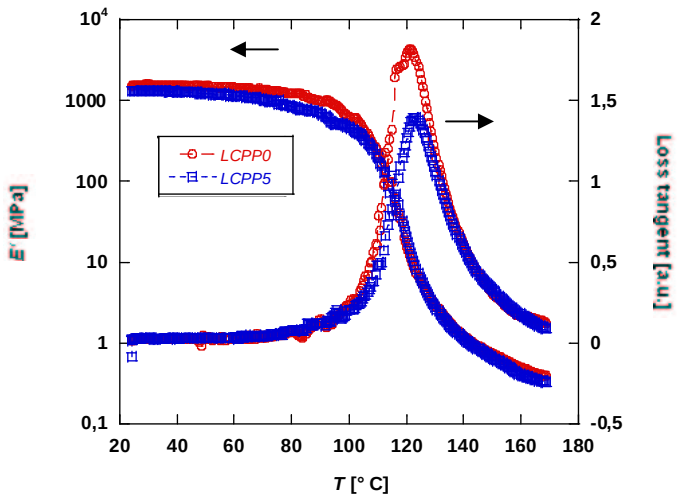

Fig. 4.31 Storage modulus (left axis) and loss tangent (right axis) for LCPP0 and LCPP5 films.

DMA results for the ULM specimens are given in Fig. 4.32. In this case no blank latex was supplied, so comparisons are made with LCPP0.

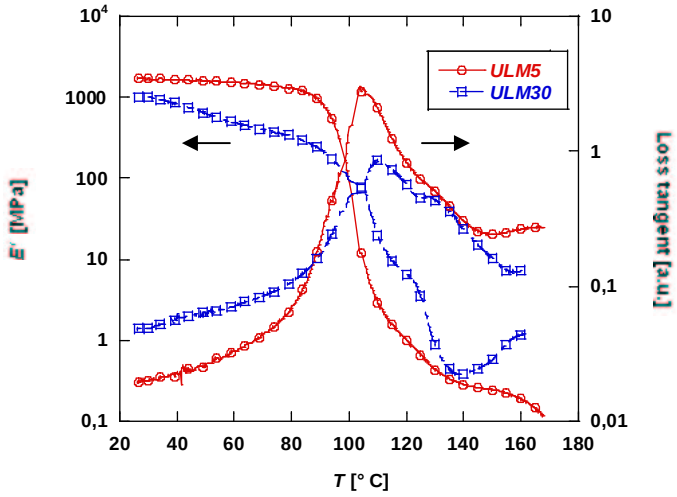

Fig. 4.32 Storage modulus (left axis) and loss tangent values (right axis) for ULM5 and ULM30 films.

Again, no significant reinforcement with respect to pure PS was observed for ULM5. Moreover the sample with the highest laponite content (ULM30) showed a decreased storage modulus *E'* in the glassy state with respect to pure PS and ULM5. In the rubbery state, a second transition in the loss tangent curve was visible, corresponding to a slight increase in storage modulus at high temperatures. This has already been observed in the highly filled styrenic L nanocomposites (see 4.1.4) and its origin was ascribed to the break-up of the percolating laponite network. The temperature corresponding to the loss tangent peak decreased as more laponite was added. The results for the LCPP and ULM films are summarized in Table 11.

Sample	*E'* glassy state [GPa]	*E'* rubbery state [MPa]	T_α [°C]
LCPP0	1.49	0.49	121
LCPP5	1.33	0.41	123
ULM5	1.80	0.23	110
ULM30	1.00	1.63	103

Table 11 Experimental results from DMA experiments on LCPP and ULM films.

4.3.4 DSC measurements

DSC curves for the LCPP and ULM films are shown in Fig.4.33. The same T_g value was found for all the LCPP samples (~93 °C) whereas slight differences were observed in the ULM samples (84°C for UML5 and 80°C for ULM30). These results are consistent with the trends in T_α. The low values found for the ULM samples are attributed to the relatively high amount of emulsifier used in the synthetic step which may have a plasticizing effect.

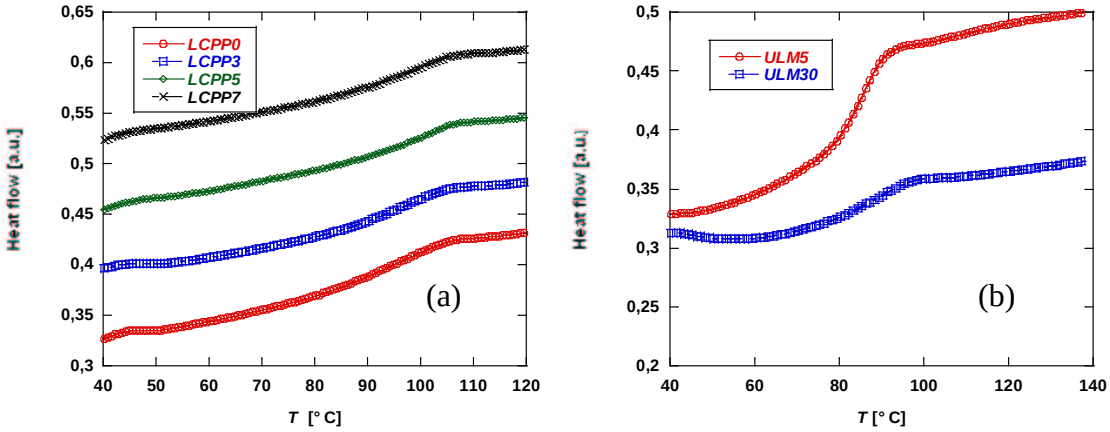

Fig. 4.33 DSC curves for (a) LCPP and (b) ULM latexes.

4.4 Conclusions

Conventional emulsion polymerization has been used successfully to control the nanocomposite morphology and allows the introduction of high amounts of filler without excessive aggregation. The functionalization of the laponite (surfactant and macromonomer) and the laponite concentration in water was not found to influence swelling in the absence of polymer. Good agreement was found between the size measurements on the laponite platelets in solution by DLS and by TEM after staining and drying.

Physical and mechanical properties were extensively studied by several experimental techniques. Two different regimes of reinforcement were identified in specimens derived from “armoured” latexes. In the glassy state stiffness increases were related mainly to laponite exfoliation, while in the rubbery state the overall laponite content was found to be the dominant factor and large stiffness increases were obtained. Two main factors may be important for this effect, the presence of a cellular arrangement of the laponite at high filler loadings and a strong confinement effect on chain mobility. Attempts were made to quantify the matrix immobilization

using DSC. The matrix fraction that did not contribute to T_g is identified with the intercalated matrix.

In the glassy state, modified classical micromechanical models that take into account partial laponite stacking are able to describe the observed modulus increases. However, in the rubbery state, the same models failed to predict the Young's modulus, even if the rigidification of the intercalated matrix was taken into account. The cellular arrangement of the laponite was therefore invoked in developing a geometrical model for the elastic response. In the rubbery state the assumption of an increased matrix modulus in the laponite rich cell walls was suggested to be necessary to explain the experimental data.

NMP provided a mean of obtaining low laponite content nanocomposites with a very high degree of exfoliation and a certain control of the molecular mass of the matrix. This permitted melt rheological measurements, which were impossible to carry out on the emulsion-based materials because of the high molecular masses obtained with this technique. It was shown that the increasingly solid-like behaviour in presence of laponite, generally ascribed to the effect of a percolated structure, was already apparent with laponite contents well below percolation threshold of platelets contacts. The reinforcing effect in the rubbery state for the NMP based nanocomposites was nevertheless found to be weaker than for the emulsion-based nanocomposites with similar laponite contents.

Miniemulsion polymerization was used to obtain two kinds of PS/laponite latexes with two different morphologies: encapsulated in the latexes provided by LCPP and armoured particles in latexes from ULM. In both cases the laponite was poorly dispersed in the matrix and no substantial reinforcement was found in DMA scans. Therefore the miniemulsions did not provide any significant improvement in microstructure control. However the materials tested in this thesis represent the very first attempts at using miniemulsion-based techniques and there has since been an intense effort to improve the synthetic strategy from various partners of the Napoleon project. The aims are to increase the solid contents and the reaction yield, providing better control of the 1 to 1 conversion between monomer droplets and particles, and significant progress has been made. Nevertheless extensive characterization of these materials is still lacking.

4.5 Bibliography.

[1] R. Ruggerone, C.J.G. Plummer, N. Negrete Herrera, E. Bourgeat-Lami, J.-A.E. Månson, *Highly filled polystyrene-laponite nanocomposites prepared by emulsion polymerization.* Eur. Pol. Journ. **45** (2009) 621

[2] J.A. Quintanilla, R.M. Ziff, *Asimmetry in the percolation thresholds of fully penetrable disks with two different radii.* Phys. Rev E **76** (2007) 051115

[3] W. Xia, M.F. Thorpe, *Percolation properties in random ellipses.* Phys. Rev A **38** (1988) 2650

[4] V. Arrighi, I.J. McEwen, H. Qian, M.B. Serrano Prieto, *The glass transition and interfacial layer in styrene-butadiene rubber containing silica nanofiller.* Polymer **44** (2003) 6259

[5] G. Tsagaropoulos, A. Eisenberg, *Direct observation of 2 glass transitions in silica-filled polymers-implications for the morphology of random ionomers.* Macromolecules **28** (1995) 369

[6] G. Tsagaropoulos, A. Eisenberg, *Dynamic mechanical study of the factors affecting the two glass transition behaviour of filled polymers-similarities and differences with random ionomers.* Macromolecules **28** (1995) 6067

[7] J. Berriot, H. Montes, F. Lequeux, D. Long, P. Sotta, *Evidence of the shift of the glass transition near particles in silica-filled elastomers.* Macromolecules **35** (2002) 9756

[8] J. Berriot, H. Montes, F. Lequeux, D. Long, P. Sotta, *Gradient of the glass transition temperature in filled elastomers.* Europhys. Lett. **64** (2003) 50

[9] A. Sargsyan, A. Tonoyan, S. Davtyan, C. Schick, *The amount of immobilized polymer in PMMA SiO_2 determined from calorimetric data.* Eur. Polym. Journ. **43** (2007) 3113

[10] Y.P. Koh, G.B. McKenna, S.L. Simon, *Calorimetric glass transition temperature and absolute heat capacity of polystyrene ultrathin films.* Journ. Polym. Sci. Part B **44** (2006) 3518

[11] C. Schonhals, H. Goering, C. Schick, *Segmental and chain dynamics of polymers: from the bulk to the confined state.* Journ. Non-Crystal Sol. **305** (2002) 140

[12] A. Bansal, H. Yang, C. Li, K. Cho, B. Benicewicz, S.K. Kumar, L.S. Schadler, *Quantitative equivalence between polymer nanocomposites and thin polymer films.* Nat. Mater. **4** (2005) 693

[13] V. Lupascu, H. Huth, C. Schik, M. Wubbenhorst, *Specific heat and dielectric relaxations in ultra-thin polystyrene layers*. Thermochim. Acta **432** (2005) 222

[14] E. Hempel, A. Huwe, K. Otto, F. Janowski, K. Schroter, E. Donth, *Characteristic length of glass transition from calorimetry for benzoin isobutylether in a series of nanometer pores.* Thermochim. Acta **337** (1999) 163

[15] O. Trofymluk, A. Levchenko, A. Navrotsky, *Interfacial effects on vitrification of confined glass-forming liquids.* Journ. Chem. Phys. **123** (2005) 194509

[16] R.D. Priestley, *Physical aging of confined glasses*, Soft matter **5** (2009) 919

[17] P. Rittigstein, R.D. Priestley, L.J. Broadbelt, J.M. Torkelson, *Model polymer nanocomposites provide an understanding of confinement effects in real nanocomposites,* Nature Mat. **6** (2007) 278

[18] I. Raptis, C.D. Diakoumakos, *Non destructive method for monitoring glass transitions in thin photoresist films.* Microel. Eng. **61-62** (2002) 829

[19] H.L. Huang, Y. Xu, H.Y. Low, *Effects of moisture sorption, glass transition temperature and morphology of poly(chloro-p-xylilene) film.* Polymer **46** (2005) 5949

[20] J.L. Keddie, R.A.L. Jones, R.A. Cory, *Interface and surface effects on the glass transition temperature in thin polymer films.* Faraday Disc. Chem. Soc. 98 (1994) 219

[21] J.H. Van Zanten, W.E. Wallace, W.L. Lu, *Influence of an impenetrable interface on a polymer glass-transition temperature.* Phys. Rev. E **52** (1995) R3329

[22] J.H. Van. Zanten, W.E. Wallace, W.L. Lu, *Effect of strongly favourable substrate interactions on the thermal properties of ultrathin polymer films.* Phys. Rev. E **53** (1996) R2053

[23] J.C. Halpin, J.L. Kardos, *The Halpin-Tsai equations: a review.* Pol. Eng. Sci. **16** (1976) 344

[24] C.J.G. Plummer, M. Rodlert, J.-L- Bucaille, H.J.M. Grűnbauer, J.-A.E. Månson, *Correlating the rheological and mechanical response of polyurethane nanocomposites containing hyperbranched polymers.* Polymer **46** (2005) 6543

[25] M. Van Es, F. Xirqiao, J. Van Turnhout, E. Van der Giessen, Specialty polymer additives principles and applications, 484 Blackwell science, Oxford (2001)

[26] G.P. Tandon, G.J. Weng, *The effect of the aspect ratio of the inclusions on the elastic properties of unidirectionally aligned composites.* Polym. Comp. **5** (1984) 327

[27] N. Sheng, M.C. Boyce, D.M. Parks, G.C. Rutledge, J.I Abes, R.E. Cohen, *Multiscale micromechanical modeling of polymer clay nanocomposites and the effective clay particle.* Polymer **45** (2004) 487

[28] V.A. Liopo, M.S. Metsik, A.V. Orekov, *Relationship between macro-modulus and micro-modulus of elasticity of mica crystals.* Russ. Phys. Journ. **16** (1973) 1478

[29] J.A. Rinde, *Poisson's ratio for rigid plastic foam.* Journ Appl. Polym. Sci. **14** (1970) 1913

[30] S.A. Hutcheson, G.B. McKenna, *Nanosphere embedding into polymer surfaces: A viscoelastic contact mechanics analysis*. Phys. Rev. Lett. **94** (2005) 076103

[31] L.J. Gibson, M.F. Ashby, *Cellular solids: structure and properties*, 1988 Pergamon Press

[32] M. Warner, S.F. Edwards, *A scaling approach to elasticity and flow in solid foams.* Europhys. Lett. **5** (1988) 623

[33] H.S. Gupta, S. Schratter, W. Tesch, P. Roschger, A. Berzanovich, T. Scoeberl, K. Klaushofer, P. Fratzl, *Two different correlations between nanoindentation modulus and mineral content in the bone-cartilage interface.* Journ. Struct. Biol. **149** (2005) 138

[34] B.J. Park, T.H. Kim, H.J. Choi, J.H. Lee, *Emulsion polymerized polystyrene/montmorillonite nanocomposite and its viscoelastic characteristics.* Journ.of Macrom. Sci. Part B **46** (2007) 341

[35] J.I. Sohn, C.H. Lee, S.T. Lim, T.H. Kim, H.J. Choi, M.S. Jhon, *Viscoelasticity and relaxation characteristics of polystyrene/clay nanocomposites.* Journ. of Mat. Sci. **38** (2003) 1849

[36] Y. Zhong, Z. Zhu, S.-Q. Wang, *Synthesis and rheological properties of polystyrene/layered silicate nanocomposites*. Polymer **46** (2005) 3006

[37] E.Chabert, M. Bonert, E. Bourgeat-Lami, J.-Y- Cavaillé, R. Dendievel, C. Gauthier, A. Zaoui, *Filler-filler interactions and viscoelastic behaviour of polymer nanocomposites*. Mat. Sci. Eng. Part A **381** (2004) 320

[38] F.Dalmas, L. Chazeau, C.Gauthier, J.-Y. Cavaillé, R. Dendievel, *Large deformation mechanical behaviour of flexible nanofiber filled polymer nanocomposites.* Polymer **47** (2006) 2802

[39] K. Tanaka, T. Mori, *Hardening of crystals by non-deforming particles and fibers.* Acta Met. **18** (1970) 931

Chapter 5

Acrylic/clay latexes

This chapter describes the results of an investigation of acrylic/clay nanocomposites, whose aim has been to demonstrate the generality of the conclusions drawn from the work on the styrenics. Section 5.1 gives results for acrylic/laponite latexes with the same morphology as those presented in section 4.1. Section 5.2 then gives results for acrylic/montmorillonite (MMT) latexes based on both conventional emulsion polymerization and miniemulsion polymerization. A particularity of these latter systems is the relatively high aspect ratio of the MMT platelets, which is expected to lead to percolation of inter-platelet contacts at significantly lower loadings than for laponite, for a given degree of dispersion.

5.1 Acrylic/laponite latexes from conventional emulsion polymerization

The preparation of the materials investigated in this section was described in section 3.2.1. The analysis of the latexes made use of the same methods as for the styrenics in section 4.1. First the particle morphology will be described, followed by the thermal and mechanical properties of films derived from the latexes.

5.1.1 Latex particle morphology

As already discussed in chapter 3, the acrylic latex particles required staining prior to TEM observation. Although the staining protocol was the same for all the latexes, the results were often difficult to reproduce. As shown in Fig. 5.1(a), the PTA stain gave good contrast with the neat latex particles, A0, but the quality of the images deteriorated with increasing laponite content.

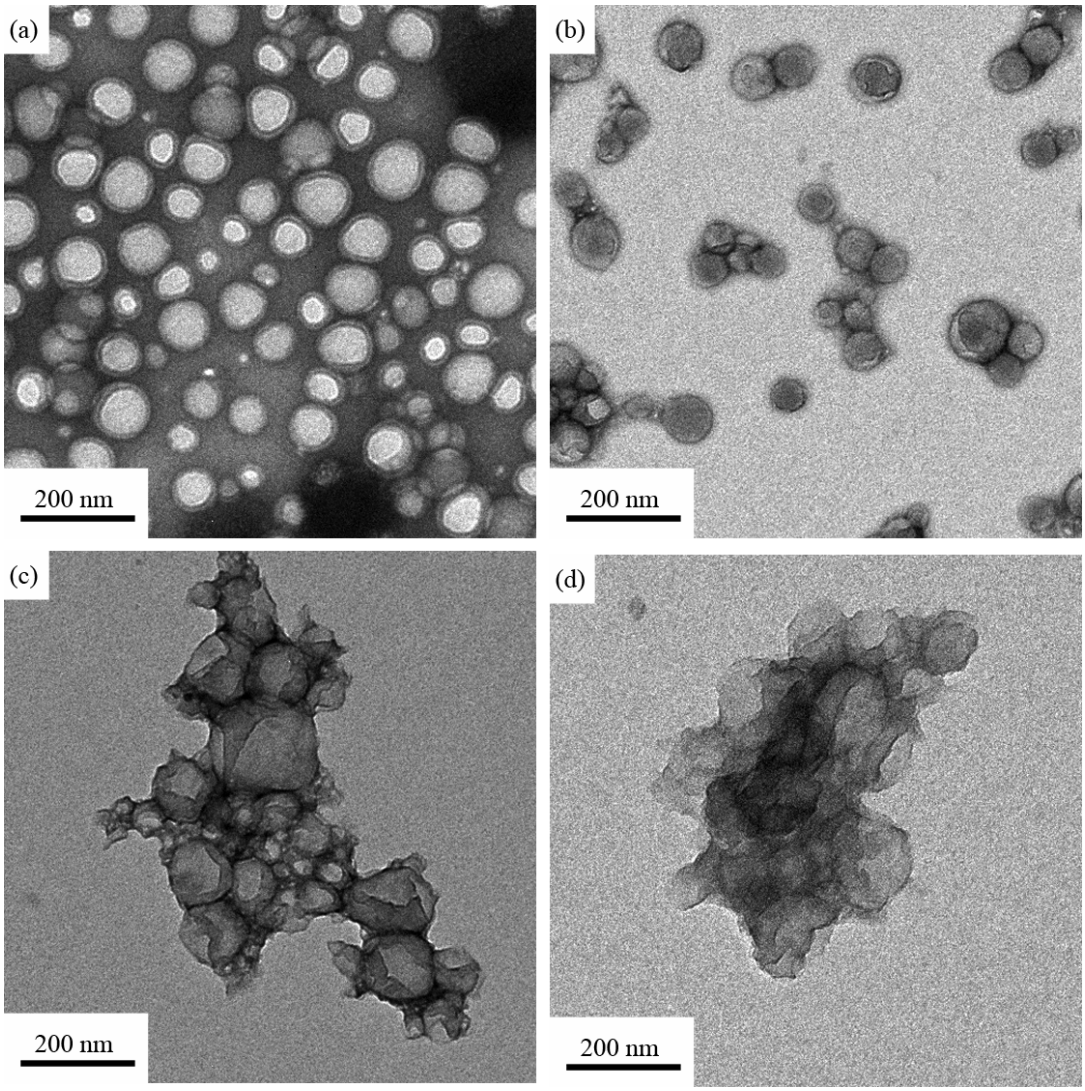

Fig. 5.1 TEM images of latex particles of (a) A0, (b) A10, (c) A20 and (d) A30 stained with PTA.

The strongly stained specimen of A0 in Fig. 5.1(a) showed no evidence of phase separation within the particles. This suggests that the morphology seen in Fig. 5.1 (b) for A10, where light and dark zones are visible at the particle surfaces, is an artefact of the staining procedure. As the laponite content was increased further, the particles became embedded locally

in a continuous phase that obscured any fine detail (Fig. 5.1 (c-d)). This may be related to the high filler content, the increase in the latex viscosity making it difficult to separate the particles, and to the very large particle sizes measured by DLS (section 3.2.1). It was consequently impossible to observe clearly the location of the laponite platelets. An alternative was to embed the latex particles in melamine resin as for the styrenics. The results are shown in Fig. 5.2. The laponite platelets are seen to be attached to the latex particle surfaces. However a non-negligible fraction of laponite was present in the original aqueous phase. The apparent size of the latex particles was also greater in Fig. 5.2 than in Fig. 5.1, but this is thought to be due to radiation damage. The unstained particles in Fig. 5.2 tended to undergo considerable mass loss when exposed to electron beam.

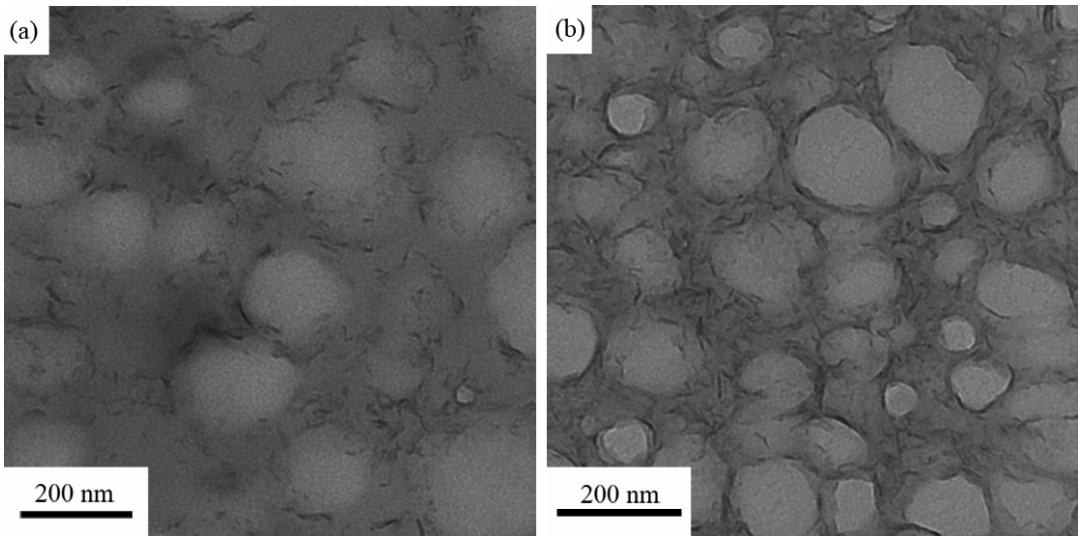

Fig. 5.2 TEM images of latex particles of (a) A20 and (b) A30 embedded in melamine resin.

5.1.2 Film morphology

Sections of about 80 nm in thickness were prepared from consolidated films with an ultramicrotome and observed by TEM. The structure appeared less well-defined than in the styrenic films, as shown in Fig. 5.3. On the other hand, the presence of the laponite network was more evident, presumably because of beam damage to the polymer. Thus, laponite aggregates could be observed that were not perfectly edge on to the beam, but thick enough to create contrast after degradation of the polymer. This is clearly seen in the case of the A50 film shown in

Fig. 5.3 (d). However, the matrix instability under the beam also made high resolution imaging difficult.

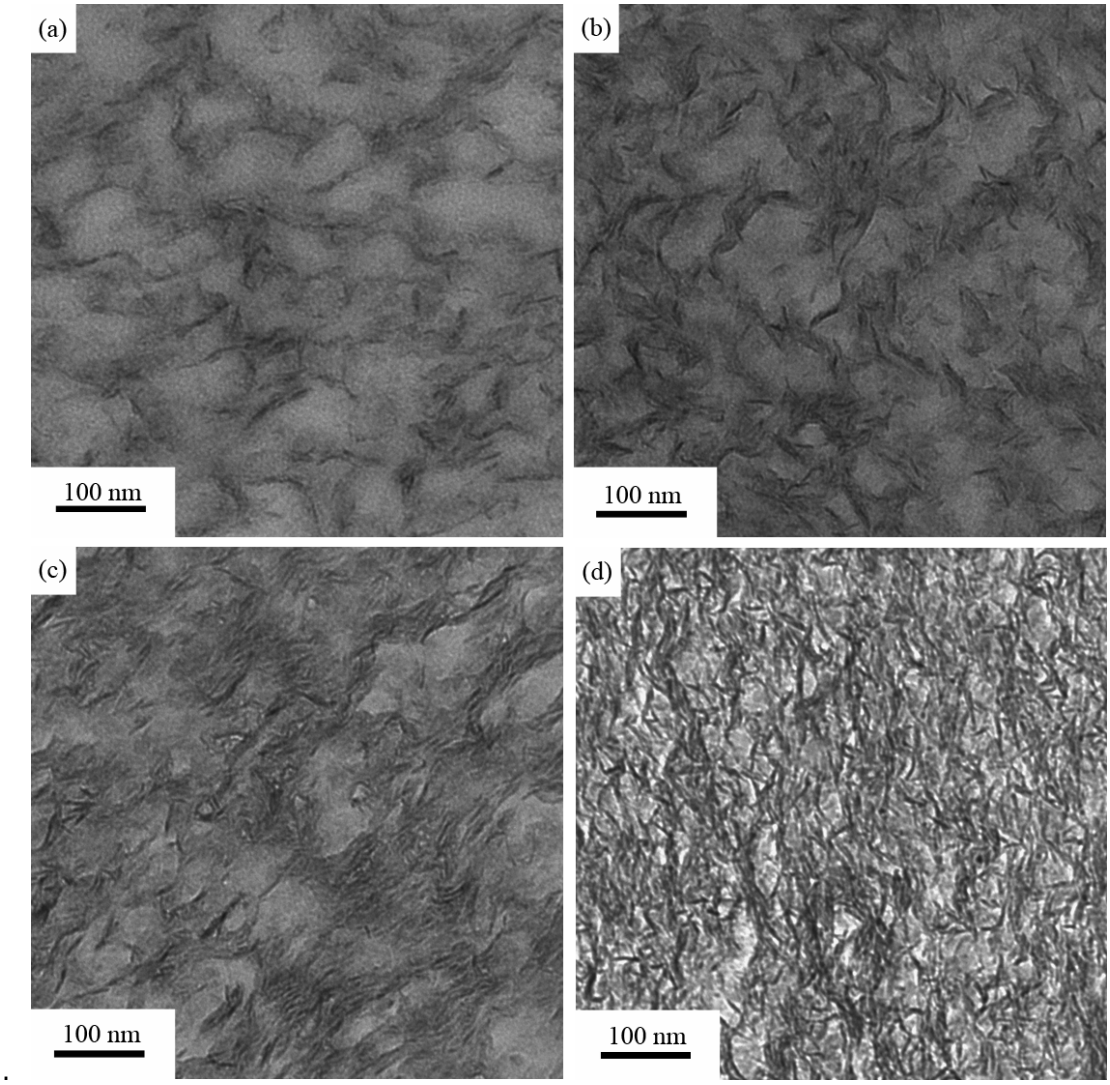

Fig. 5.3 TEM images of sections prepared from consolidated films of (a) A10, (b) A20, (c) A30 and (d) A50.

XRD spectra of films with laponite contents ranging from 0 to 11.9 vol % are shown in Fig. 5.4. While the neat matrix showed a flat spectrum with no sharp diffraction peaks, the nanocomposites showed a peak at 2θ values in the range 4 to 4.2°, corresponding to a basal spacing d_{001} of 2.05 to 2.20 nm. This means that laponite was not fully exfoliated, as also suggested by the TEM images. Hence, as in the case of the styrenics, a portion of matrix was intercalated in the laponite galleries and the same chain immobilization effect is therefore expected.

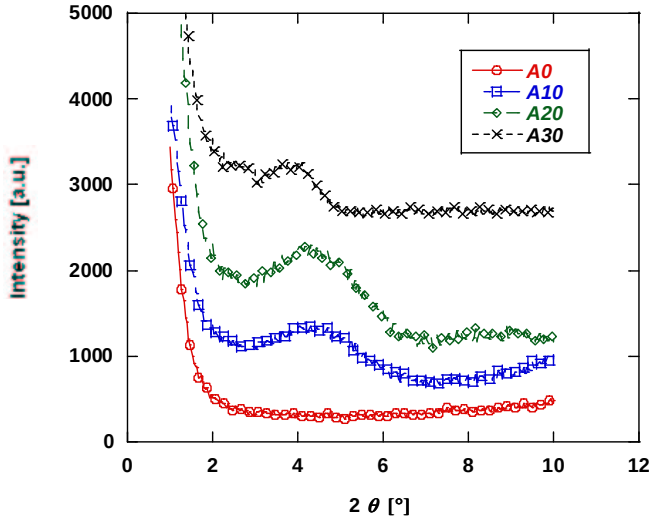

Fig. 5.4 XRD spectra from the acrylic nanocomposites.

5.1.3 Viscoelastic Properties

Fig. 5.5 shows the results of DMA scans for the acrylic/laponite films. As for the styrenics, two regimes of reinforcement were identified (see Fig. 5.5 (a)). In the glassy state the stiffness increases on laponite addition were relatively modest, but much larger increases were observed in the rubbery state. In contrast to the data for the styrenics in the glassy state, however, where the increases in the storage modulus were linked to changes in the extent of laponite dispersion, the reinforcement in the present case was dominated by the total laponite content. The values of T_α were also shifted towards higher temperatures and the intensity of the transition decreased with increasing laponite content (Fig. 5.5 (b)). In the case of A20 and A30 a small secondary peak in *tan* δ could be also observed at about 100 °C, while for A50 the transition was very broad.

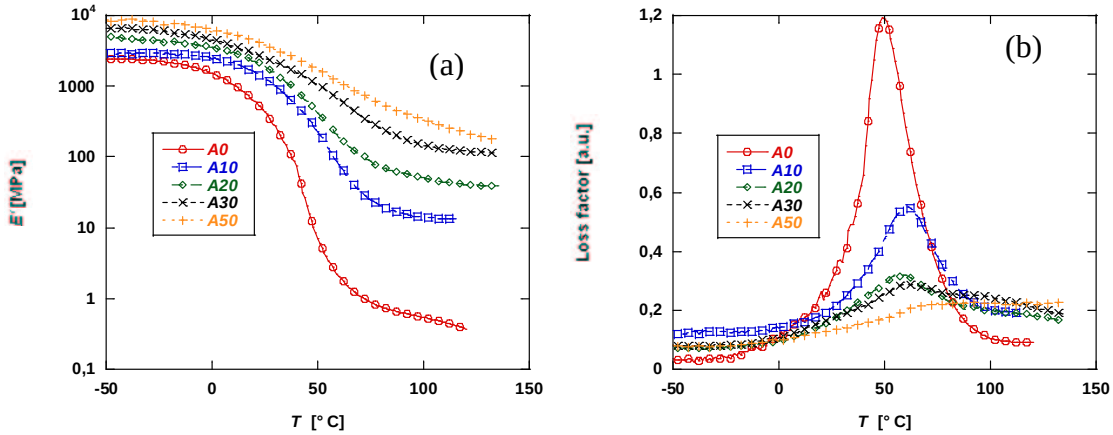

Fig. 5.5 (a) Storage modulus *E'* and (b) loss factor for the acrylic/laponite nanocomposites.

Table 12 summarizes these results.

Sample	*E'* glassy state [GPa]	*E'* rubbery state (120°C) [MPa]	T_α [°C]
A0	2.44	0.37	49
A10	3.01	13.5	60
A20	5.05	40.9	58
A30	6.66	121.5	61
A50	8.51	224.2	-

Table 12 Thermo-mechanical properties of the acrylic/laponite nanocomposites.

Similar acrylic nanocomposites, but with lower laponite contents (up to 7.5 wt.%), have been tested by other partners in the Napoleon consortium. These materials were obtained both by conventional emulsion and miniemulsion polymerization [1]. The same reinforcement effect was found for the storage modulus of emulsion and miniemulsion-based nanocomposites with the same morphology as the materials presented here, although the emulsion-based materials showed the greatest reinforcement. On the other hand, encapsulated systems showed almost no stiffness variations on laponite addition, presumably due to the poor laponite dispersion among the latex particles, as already discussed in chapter 4 for the styrenics. For the armoured particles, in which the laponite is attached to the particle surface, a shift of the loss modulus peak towards lower temperatures than for the neat matrix was observed. The origin of this shift, which is not reflected by the present observations, remains unclear, however. As will be discussed again in section 5.1.4, enrichment in MMA of the regions of the matrix close to the laponite platelets has been observed in materials prepared by conventional emulsion polymerization. The presence of this presumably more glassy interphase may explain the stiffness increases with respect to both armoured and encapsulated materials obtained by miniemulsion polymerization.

Attempts were made to break up the cellular structure considered to give rise to the storage modulus increases above T_g by subjecting the films to plane strain compression as previously for the styrenics (section 4.1.6.6). Latexes containing about 7.9 vol % of laponite were also prepared by mixing A50 or A30 with A0 by mechanical stirring and sonication. The aim here was to break up the cellular structure by introducing neat polymer particles. These latter latexes are referred to as A50+0 or A30+0. The overall laponite content was found to be 6.7 and 5.5 vol % for A50+0 and A30+0 respectively, which compares with 8.3 vol % for A20.

Fig. 5.6 shows DMA scans for these different samples along with a DMA scan for A20. In the glassy state, *E'* was similar in all the samples, although lower values were measured for A30+0, which had the lowest laponite content. In the rubbery state, A20 and A50+0 again showed similar *E'*, and A30+0 was even somewhat stiffer at high temperatures than the formers. On the other hand, A20 subjected to plane strain compression showed significantly reduced *E'* in this regime.

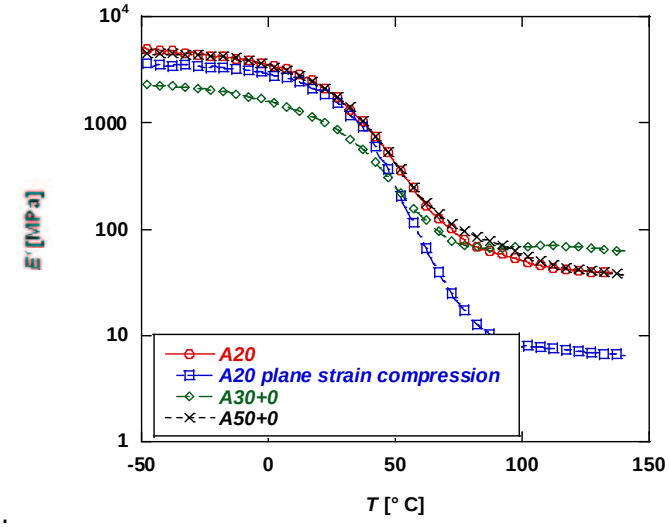

Fig. 5.6 DMA scans of modified latexes (see text for details) and A20.

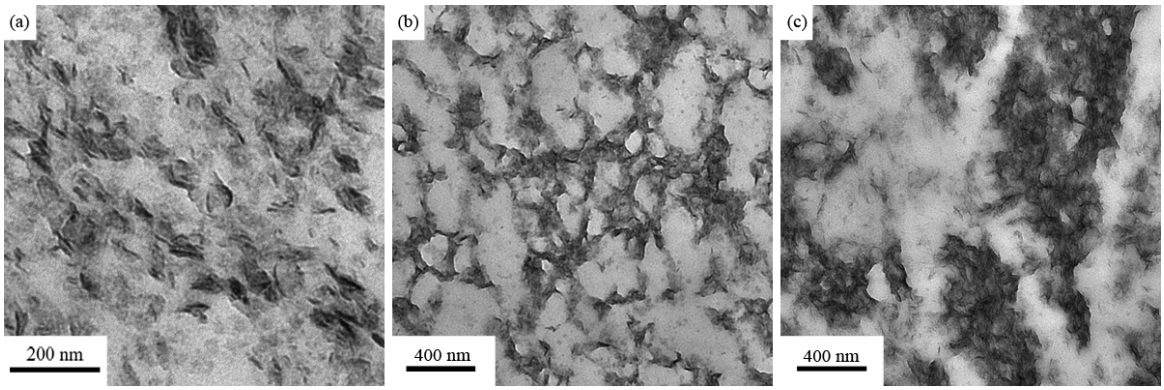

Fig. 5.7 TEM images of (a) A20 after plane strain compression, (b) A30+0 and (c) A50+0.

The microstructures of the different specimens are shown in Fig. 5.7. In the case of the sample subjected to plane strain compression (Fig. 5.7 (a)), the cellular structure of the nanocomposite was confirmed to be broken up, as observed previously for the styrenics (see section 4.1.6.6). This explains the sharp decrease in *E'* in the rubbery state with respect to that of the unmodified A20. On the other hand, in the case of A30+0, shown in Fig. 5.7 (b), mixing of the latexes did not break up the cellular structure locally, which remained clearly visible, although the effective cell size was somewhat increased. The persistence of the cellular structure resulted in

an increase in *E'* comparable to that in A20. Finally, in the case of sample A50+0, the mixing process was even less efficient (see Fig. 5.7 (c)), so that the films consisted of very large domains with comparable laponite contents to A50 interspersed with regions containing little or no laponite, so that the overall stiffness remained similar to that of A20.

These experiments demonstrate the flexibility of latex-based techniques for preparing materials with different microstructures by mixing different dispersions. However, incomplete mixing of latexes with different laponite contents resulted in a severe loss in transparency.

5.1.4 DSC measurements

Conventional DSC scans for the acrylic nanocomposites are shown in Fig. 5.8 (a). The curves did not show a single clear transition. A distinct step could be observed in some specimens at about 40 °C but globally the transition was very broad. This was confirmed by the MDSC heat capacity measurements shown in Fig. 5.8 (b), a very broad transition occurring between -80 and 80 °C. The curves were renormalized with respect to the polymer content, indicating a decrease in the transition amplitude with increasing laponite content, as already found for the styrenics (see section 4.1.5).

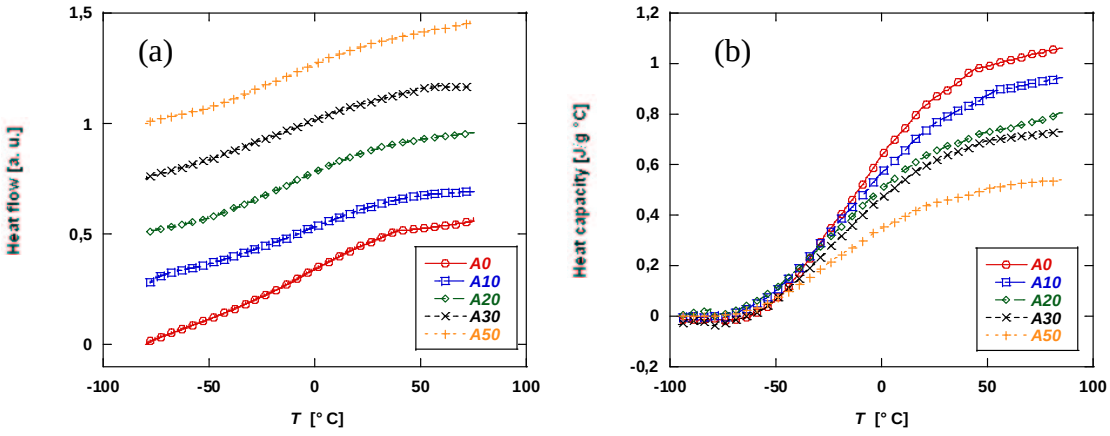

Fig. 5.8 (a) Conventional DSC thermograms for acrylic nanocomposites and (b) heat capacity measurements by MDSC on the same materials.

The thermal behaviour of these acrylic co-polymers was very similar to that of the gradient co-polymers studied by Torkelson et al [2-4]. These authors introduced the concept of a "glass transition breadth", ascribed to the presence in gradient copolymers of segments with different composition, which show different glass transition temperatures. In the case of MMA and

BA, the presence of MMA rich and BA rich segments may be attributed to the different reactivity ratios of the two monomers [1, 5]. It is possible that in the first stage of polymerization, the chains contain more units of the more reactive monomer (MMA). The same polymeric system was found by solvent extraction to show MMA enrichment in the chains attached to the laponite surface and BA enrichment in the unbound chains [1]. This was invoked to explain the broadening of the loss modulus peak in emulsion-based nanocomposites. However evidence of composition variations was also found for the neat matrix in the present case, so that they do not necessarily appear to be associated with the laponite.

The thermal transition of copolymers may be further characterized by the first derivative of the heat capacity signal [2-4]. A random structure generally shows a single peak and a block structure shows two distinct peaks, whereas a gradient copolymer shows a broad peak with local maxima. Fig. 5.9 shows the first derivatives of the heat flow for the neat matrix A0 and for the A50 nanocomposite. The curves show local maxima at the same temperatures, suggesting the same matrix structure to be present in both materials.

The heat capacity data were again used to estimate the RAF fraction as described in section 4.1.5. The overall transition and the step at about 40 °C were both considered in the calculations. In the first case, variations in the signal in the low temperature regime made quantification of the total amount of RAF difficult, whereas the step at 40 °C gave more reproducible results. As shown in Fig. 5.10, RAF similar to those of the styrenics were obtained (see Fig. 4.11). In principle, a higher RAF might be expected for the acrylics because of the increased interlayer spacing. However, this result may not be significant given the imprecision inherent in the analysis for the acrylics.

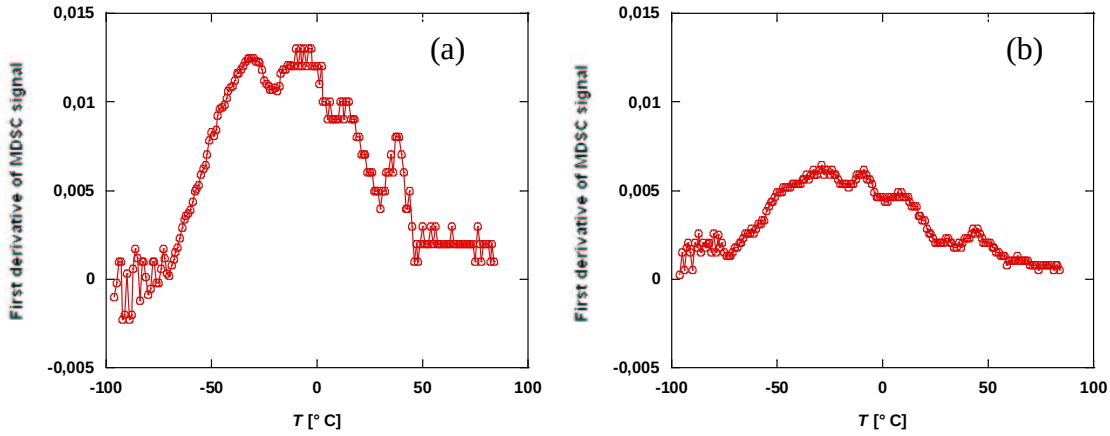

Fig. 5.9 First derivatives of the MDSC signals for (a) A0 and (b) A50.

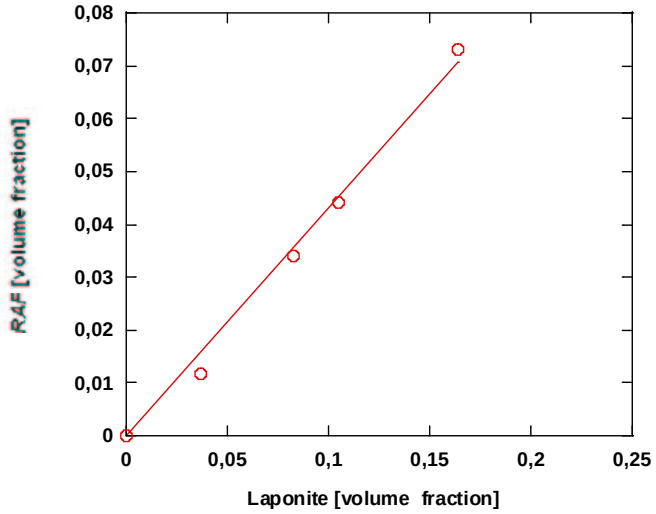

Fig. 5.10 RAF as a function of laponite content determined by ashing for acrylic nanocomposites.

5.2 Acrylic/MMT latexes

5.2.1 Latex particle morphology

Images of all the spin-coated LNP latexes stained with PTA are shown in Fig. 5.11. Unmodified latexes from emulsion and miniemulsion polymerization (respectively LNP1 and LNP3 in Fig. 5.11 (a) and (c)) showed a structured core-shell like morphology, while the composite particles appeared to be more homogeneous. Since in principle all the latex particles contained the same materials (MMA/BA 1:1), this was assumed to be a staining artefact rather than a reflection of the true particle morphology. Average particle sizes determined by image analysis were consistent with the data in Table 7 (see section 3.2.2), i.e. in the size range of 100 to 150 nm. No evidence for the MMT was found in the nanocomposite latexes LNP2 and LNP4 in Fig. 5.11 (b) and (d), so that the location of the filler could not be determined. The platelets were presumed to be at the particle surfaces or dispersed in the aqueous phase because none were observed inside the particles. Moreover, the mean platelet size of MMT (about 200 nm) is inconsistent with encapsulation. However, the total MMT content was very low (about 1.2 vol %) which may explain the difficulty in observing the MMT in the present case. MMT may also be masked by the presence of the stain around at particle boundaries. To solve this problem, embedding in melamine resin was attempted, but for these latexes, the resin hardener caused the latex

particles to flocculate, making it impossible to obtain adequate particle dispersions in the blocks used for sectioning.

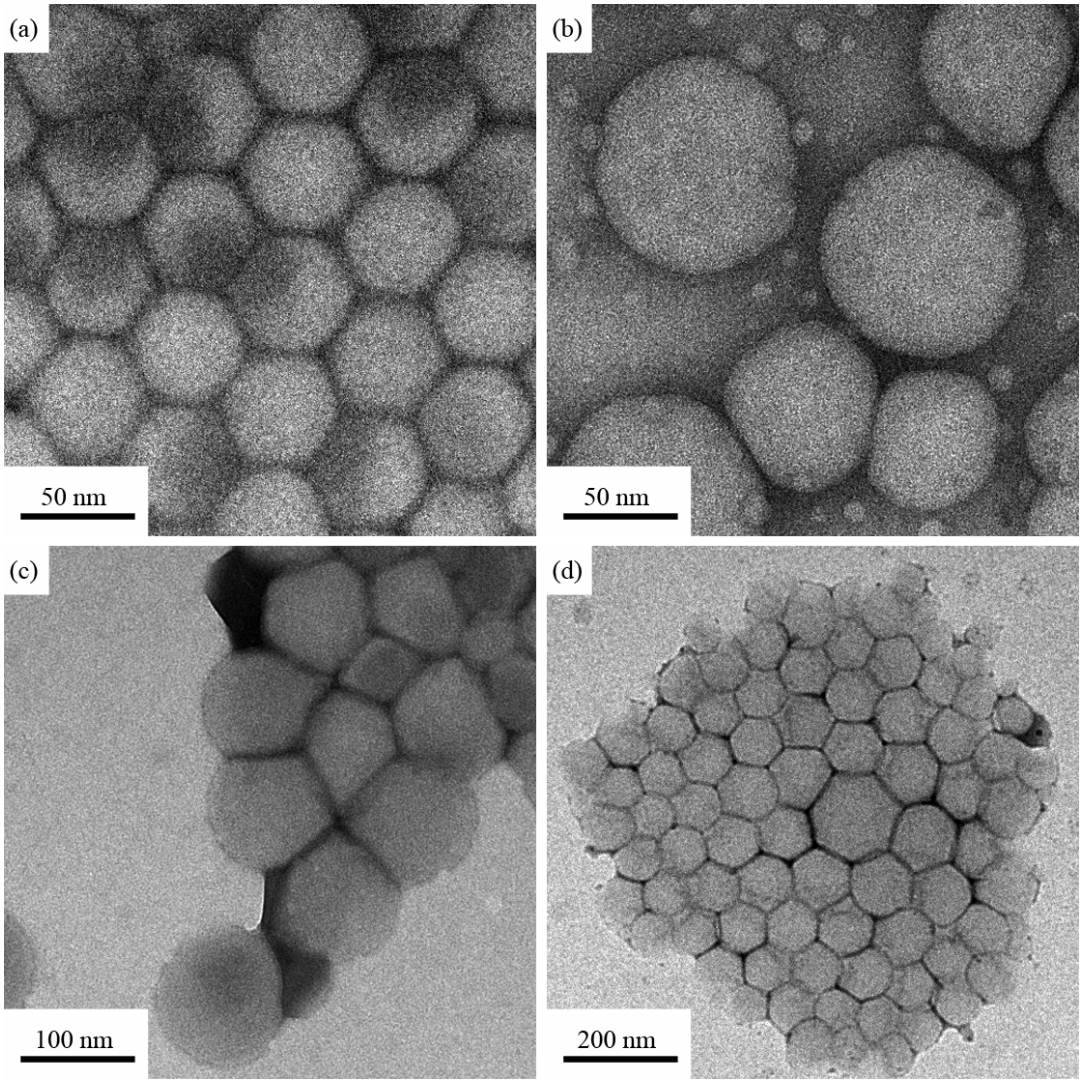

Fig. 5.11 TEM images of spin coated particles of (a) LNP1, (b) LNP2, (c) LNP3, and (d) LNP4 latexes (see Table 7 in section 3.2.2).

5.2.2 Film morphology

Thin films were obtained by drying the latexes according to the protocol described in section 3.4.2. The films were then sectioned with a ultramicrotome at -50 °C. Cryo sectioning was relatively difficult, so that the quality of TEM micrographs was not comparable with those obtained for styrenics. The results for the polymer/MMT composites are shown in Fig. 5.12. No significant differences in the extent of MMT exfoliation were apparent and intercalation appeared to be the

dominant morphology, with aggregation in the micron range occurring in both samples. The MMT intercalation was also confirmed by XRD (Fig. 5.13). The LNP2 and LNP4 nanocomposite films showed a diffraction peak around 2θ = 2.3 ° which implied a basal plane spacing, d_{001}, of 3.9 nm. The peaks at 4.6 ° and 6.8 ° are higher order peaks.

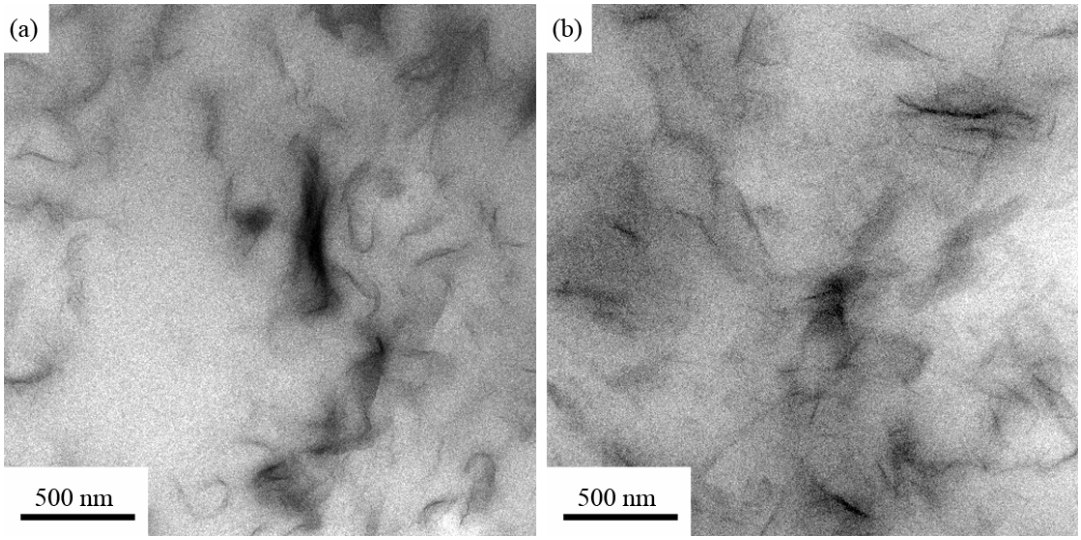

Fig. 5.12 TEM micrographs of (a) LNP2 and (b) LNP4 films.

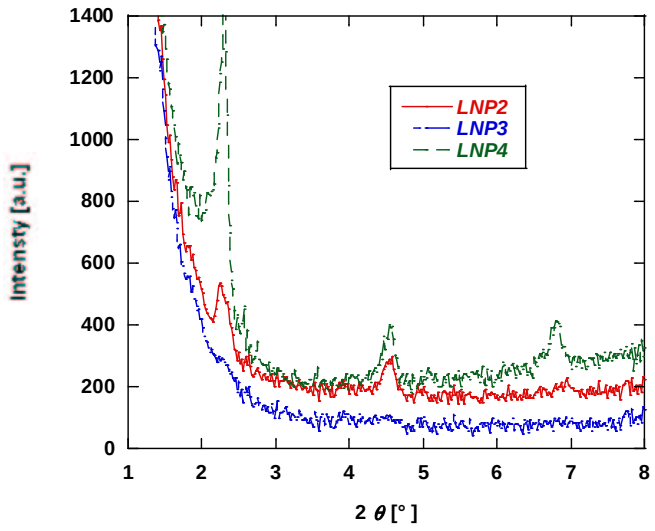

Fig. 5.13 XRD spectra of LNP films.

5.2.3 Viscoelastic properties

DMA results for consolidated films are given in Fig. 5.14. Slight increases in storage modulus were observed in the glassy state for the composite films (LNP2 and LNP4), while the reinforcement in the rubbery state was more enhanced, although the range of overall MMT contents did not allow systematic study of the trends. Similar results have been obtained independently by other authors [6]. Increases in the temperature of the loss tangent peaks with increasing MMT content were also observed, as summarized in Table 13.

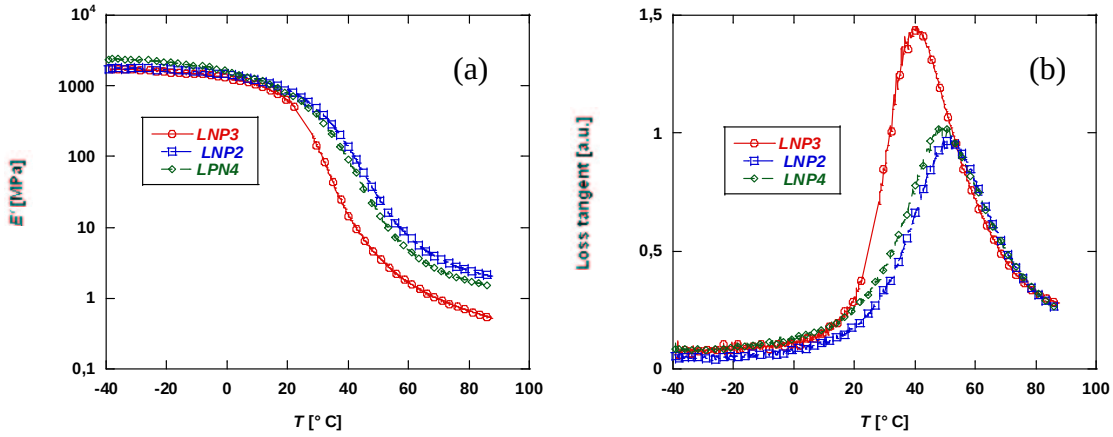

Fig. 5.14 (a) Storage modulus and (b) loss tangent values for LNP samples

Sample	*E'* glassy state GPa	*E'* rubbery state MPa	T_α °C
LNP3	1.71	0.52	39
LNP2	1.78	2.05	52
LNP4	2.37	1.45	50

Table 13 Results of DMA tests on LNP materials.

5.2.4 DSC measurements

The DSC scans showed similar shifts in T_g to those in the loss tangent peaks, as shown in Table 14 and Fig. 5.15. A broad transition was observed in the DSC scans, but the inflection point could be localized unambiguously, allowing the determination of the glass transition temperature for all the samples.

Sample	T_g °C
LNP2	18
LNP3	11
LNP4	16

Table 14 T_g of LNP samples.

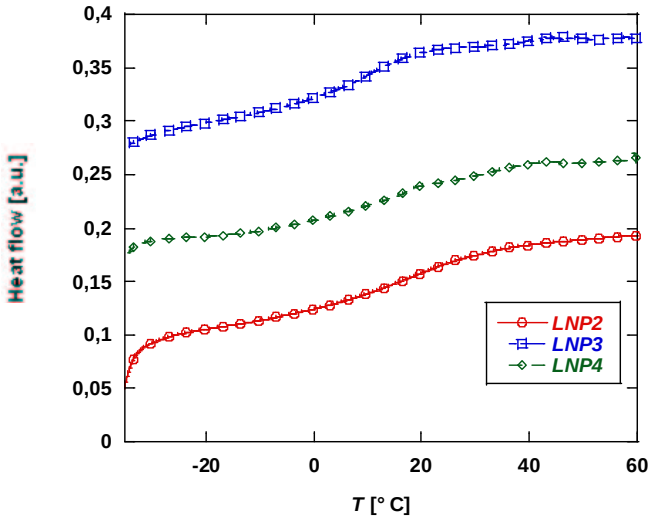

Fig. 5.15 DSC scans of the LNP materials.

5.2.5 Cyclic tensile tests

Since the LNP materials are in the rubbery state at room temperature, cyclic testing under tension is straightforward. In the present case the tensile strain is applied, partially recovered and re-applied several times as shown in Fig. 5.16. The goal of such experiments is to investigate the existence of a percolation network and its behaviour at large strains (cf. the plane strain experiment in section 5.1.3). Assuming the MMT clay to have an aspect ratio of at least 200 [7], the percolation threshold should be overcome at a loading of about 1.2 vol %, a condition that is difficult to reach with laponite at these concentrations, especially for non-exfoliated particles, as discussed elsewhere [8]. A drop in the tangent modulus at high strains would imply breakdown of the network. The measurements were performed at 90 °C and the results are shown in Fig. 5.16.

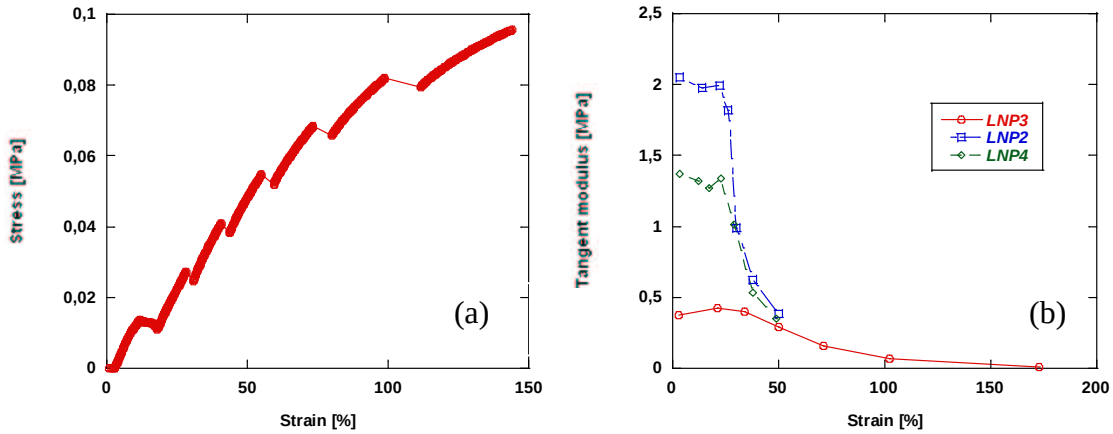

Fig. 5.16 Example of (a) the stress/strain profile applied to the material and (b) the evolution of the tangent modulus for the LNP materials.

The tangent modulus remained constant over a certain number of cycles (typically 3 or 4), and then decreased sharply. This decrease was very pronounced in the composites, but was smoother for the pure matrix. It may therefore be an indication of the destruction of a MMT percolation network. The elongation at break also decreased in the composites with respect to the pure matrix. Cyclic tensile tests have also been carried out elsewhere on acrylic/laponite nanocomposites [1]. Films derived from armoured latexes containing about 5 wt % of laponite presented a sharp decrease in tangent modulus after a first deformation to about 120 %. Then the tensile response remained relatively unchanged. On the other hand, the encapsulated nanocomposites did not show any change in tangent modulus during cyclic tensile deformation, which is a further confirmation of the importance the clay network effect. When the deformation reaches a certain value, and the network structure is destroyed, the material starts to behave more like the neat matrix, as in the case of samples deformed in plane strain compression (sections 4.1.6.6 and 5.1.3)

5.3 Conclusions

The acrylic/laponite nanocomposites showed similar mechanical properties to the styrenics described in chapter 4. The effect of chain confinement and the cellular arrangement of the laponite were again suggested to be responsible for the high degree of reinforcement observed in the rubbery state. This suggests PS/laponite nanocomposites to be a good model for other systems with the same morphology. The acrylics nevertheless showed relatively broad thermal transitions, which were explained in terms of the copolymerization reaction as in previous studies on analogous systems with lower laponite contents.

The use of miniemulsion polymerization did not as for styrenics appear to provide any substantial benefit to the mechanical properties with respect to conventional emulsion polymerization, again as found previously for the styrenics. Moreover, in the case of the acrylic/MMT nanocomposites, the morphology of the latexes was unclear, the MMT platelets not being visible in TEM micrographs of the latex particles. It was assumed however, that they were either attached to the latex particle surfaces or dispersed in the aqueous phase. Acrylic/MMT nanocomposites with low MMT contents were suggested to show percolation effects owing to the relatively high aspect ratios of the MMT platelets and on the basis of DMA experiments and cyclic tensile tests. These results were consistent with those obtained by other partners within the Napoleon project.

5.4 Bibliography

[1] J. Faucheux, *Relations microstructure propriétés dans les films nanostructurés elaborés par voie latex.* INSA Lyon thesis (2008).

[2] J.Kim, M.M. Mok, R.W. Sandoval, D.J. Woo, J.M. Torkelson, *Uniquely broad glass transition temperatures of gradient copolymers relative to random and block copolymers containing repulsive comonomers.* Macromolecules **39** (2006) 6152.

[3] M.K. Gray, H. Zhou, S.T. Nguyen, J.M. Torkelson, *Synthesis and glass transition behaviour of high molecular weight styrene/4-acetoxystyrene and styrene/4-hydroxystyrene gradient copolymers made via nitroxide mediated controlled radical polymerization.* Macromolecules **37** (2004) 5586

[4] C.L.H. Wong, J. Kim, J.M. Torkelson, *Breadth of glass transition temperature in styrene/acrylic acid block, random, and gradient copolymers: unusual sequence distribution effect.* Journ. Polym. Sci. Part B **45** (2007) 2842

[5] M. Fernandez Garcia, J.L. De la Fuente, M. Fernandez-Sanz, E.L. Madruga, *Glass transition temperatures of poly[(methylmethacrylate)-co-(butylacrylate)] synthesized by atom-transfer radical polymerization.* Macrom. Rapid Comm. **22** (2001) 1046

[6] G. Diaconu, M. Paulis, J.R. Leiza, *Towards the synthesis of high solids content waterborne poly(methylmethacrylate-co-butylacrylate)/montmorillonite nanocomposites.* Polymer **49**(2008) 2444

[7] K.H. Wang, M. Xu, Y.S. Choi, I.J. Chung, *Effect of the aspect ratio of clay on the melt extensional process of maleated polyethylene/clay nanocomposites.* Polym. Bull. **46** (2001) 499

[8] R. Ruggerone, C.J.G. Plummer, N. Negrete Herrera, E. Bourgeat-Lami, J.-A.E. Månson, *Highly filled polystyrene-laponite nanocomposites prepared by emulsion polymerization.* Eur. Polym. Journ. **45** (2009) 621

Chapter 6

Large deformations and microdeformation mechanisms in clay nanocomposites

This chapter describes the results of a study of the microdeformation mechanisms in the PS/laponite nanocomposites described in 4.1 and two different grades of PP/MMT nanocomposite. As well as providing an opportunity to compare two different materials, an important aim of this work was to investigate the influence of two different preparation techniques, namely emulsion polymerization and melt blending, on the deformation and fracture mechanisms. While latex based materials showed properties that depended on the single latex particle morphology, as discussed in chapter 4, in the extruded or injection molded PP nanocomposites the MMT platelets were randomly dispersed and oriented mainly in the original flow direction. In each case, the results of macroscopic mechanical tests will be interpreted in terms of *in-situ* observations of the deformation and fracture mechanisms.

6.1 Tensile tests of PS/laponite nanocomposites from conventional emulsion polymerization

Typical results from tensile tests using the DENT geometry are shown in Fig. 6.1 (a) for a ligament length of 3 mm. In this case L30 and L50 were not considered because they were too brittle for notching. The graph shows trends in the apparent stiffness similar to that of the storage modulus obtained by DMA in the glassy state. The fracture resistance was somewhat increased with respect to that of the matrix for laponite contents up to 2 vol% and then decreased strongly

with further increases in laponite content (Fig. 6.1 (b)). The elongation at break decreased at all laponite contents, but was particularly low for the highly filled materials. In many studies of styrenic laponite nanocomposites, both the elongation at break and the tensile strength have been found to decrease with laponite content [1-3]. This was accounted for in terms of poor adhesion between the laponite and the polymeric matrix [1]. On the other hand, when systematic improvements in adhesion are obtained by suitable surface functionalization of the platelets, the tensile strength has been found to increase [4,5].

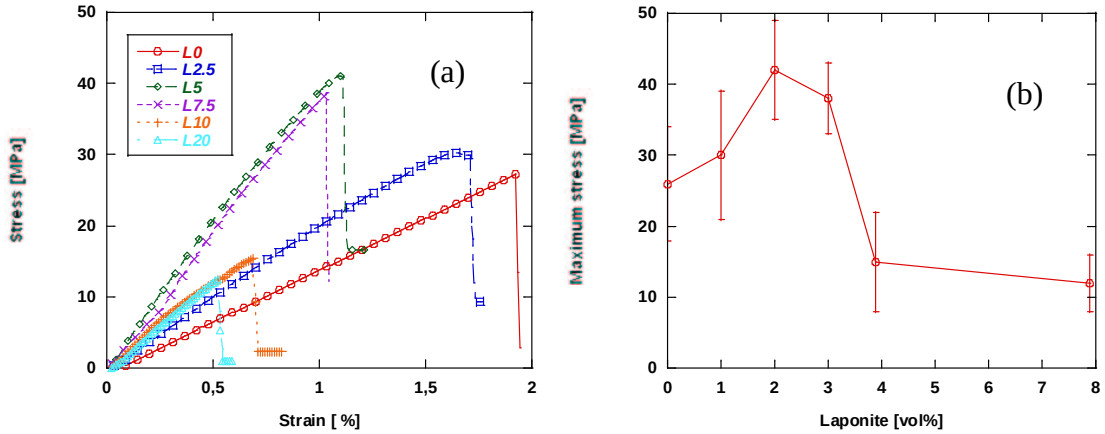

Fig. 6.1 (a) Stress-displacement curves of L nanocomposites for a ligament length of about 3 mm and (b) maximum stress as a function of laponite content.

Analysis according to the EWF protocol was considered invalid because of the very large dispersion in the results of tensile tests, mainly due to the brittleness of the materials. No dependence of W_f on the ligament length could therefore be established using eq. 3.1 (Fig. 6.2).

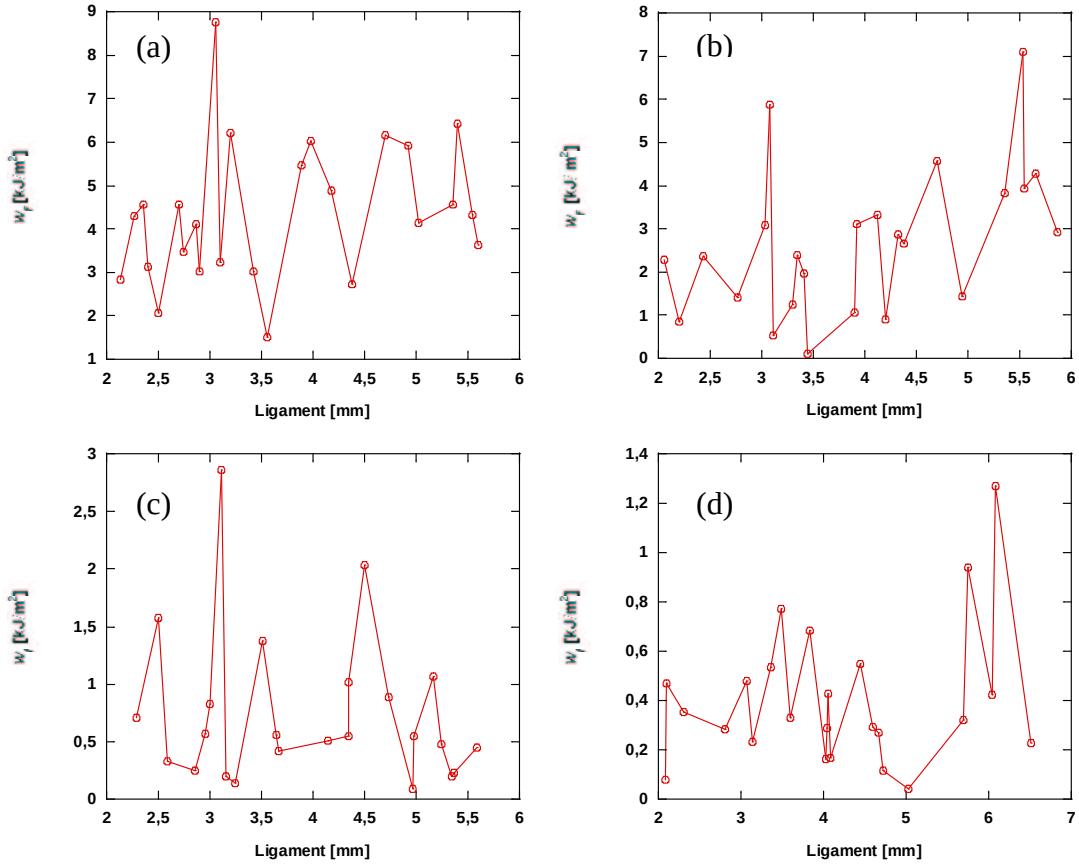

Fig. 6.2 Results of the EWF analysis for (a) L0, (b) L5, (c) L10, (d) L20 according to eq. 3.1 (see section 3.4.6).

6.2 Microdeformation and fracture mechanisms in PS/laponite nanocomposites

6.2.1 Microdeformation in the glassy and rubbery state and fractography

The microdeformation mechanisms in the PS/laponite nanocomposites were investigated using the copper grid technique described in section 3.4.7 [6, 7, 8]. First, results for the neat matrix and selected nanocomposites at room temperature are discussed. Fig. 6.3 shows TEM micrographs of microdeformation in (a) pure PS, (b) L5, (c) L10, and (d) L20. As stated in section 2.6.1, PS shows crazing at room temperature (Fig. 6.3 (a)). Crazing was also the main deformation mechanism in the laponite nanocomposites but some important differences could be observed. First, extensive coarse cavitation was seen within the crazes and this became more extenisve as

the laponite content increased (Fig. 6.3 (b-d)). The widths of the cavities were comparable with the original latex particle diameters of about 80 nm. Another important change with respect to crazing in pure PS is a decrease in local matrix drawability as inferred from an analysis of the craze fibril extension ratio

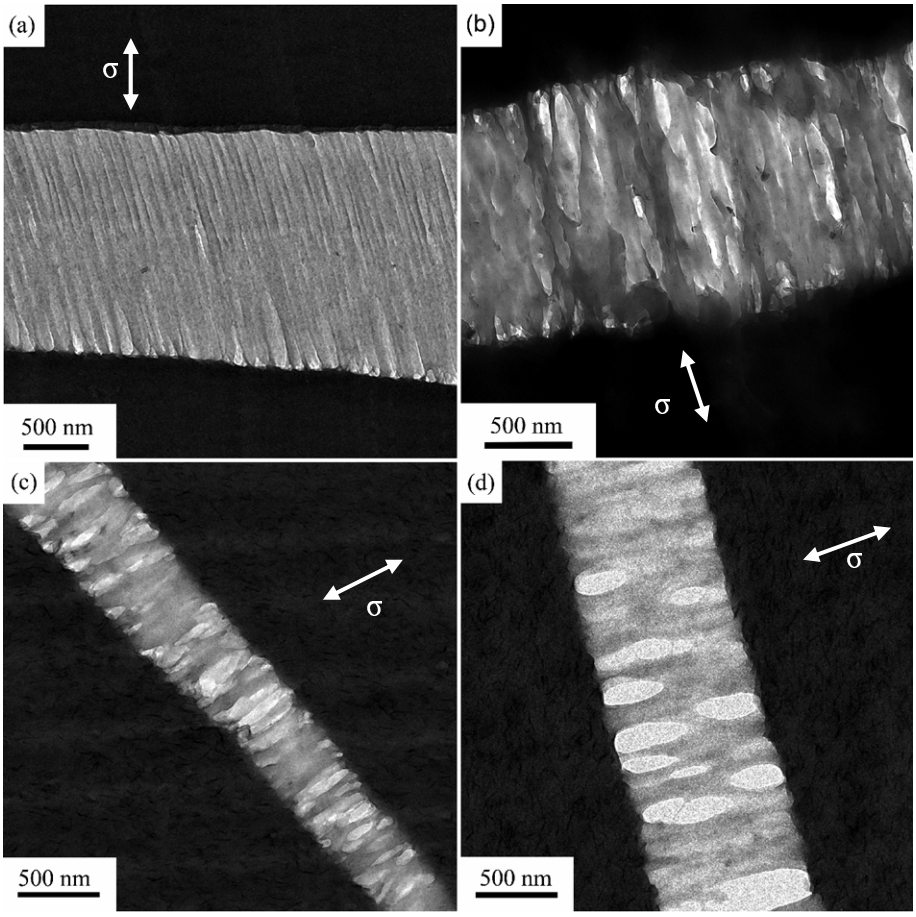

Fig. 6.3 Crazing mechanism at room temperature of (a) neat PS, (b) L5, (c) L10 and (d) L20. The direction of the deformation is indicated by the arrows.

These measurements were made directly from TEM images obtained with a Gatan 622 CCD camera, using the following eq. 6.1:

$$1/\lambda = 1 - \frac{\ln(\phi_c/\phi_f)}{\ln(\phi_h/\phi_f)} \qquad \text{eq. 6.1}$$

where ϕ_c, ϕ_h and ϕ_f are the average grey levels corresponding to a craze or deformation zone, the incident beam (e.g. a hole in the film) and the undeformed film respectively [7, 8].

The observed decrease in matrix draw ratio with laponite content is shown in Fig. 6.4, suggesting a nearly linear dependence. The corresponding loss in local matrix plasticity may be ascribed to the presence of the laponite platelets in the active zone. The active zone represents a

thin portion of matrix at the craze periphery which is transferred into craze fibrils by surface drawing (see section 2.6.1). Laponite platelets within a craze are seen in Fig. 6.5 for example. The decrease in matrix drawability may account for the decrease in fracture resistance at intermediate and high laponite contents observed in tensile tests. The reduced local plasticity presumably prevents the crazes from fully developing in the nanocomposites, decreasing the amount of dissipated energy during deformation and reducing the resistance to crack propagation, as outlined by Brown for a single craze preceding a crack (see section 2.6.1) [28].

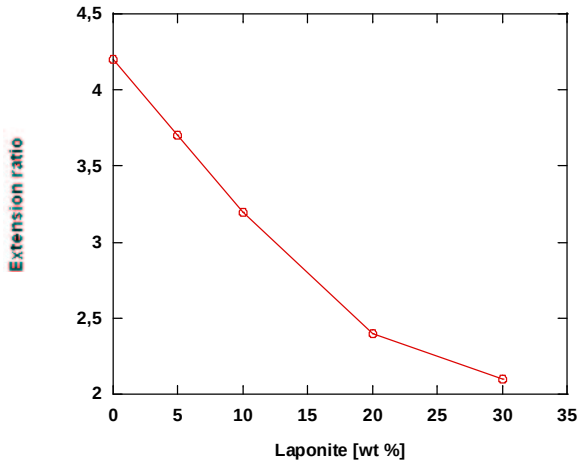

Fig. 6.4 Fibril draw ratio as a function of laponite content.

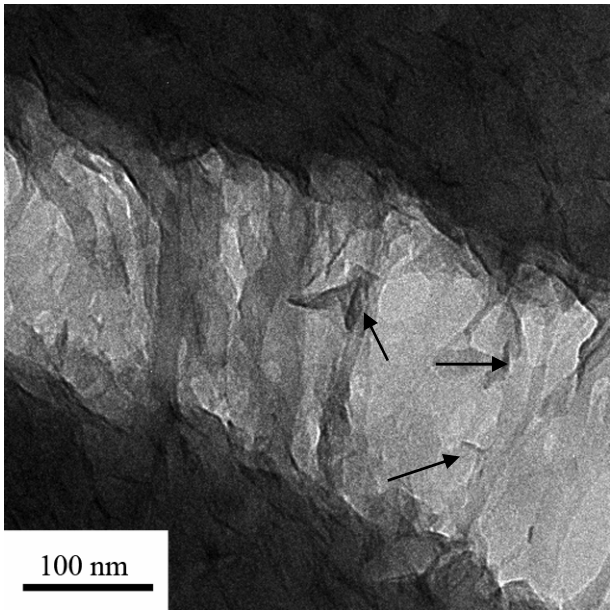

Fig. 6.5 Presence of laponite platelets in a craze in a L30 nanocomposite film.

Microdeformation was also investigated at 95 °C, i.e. just below the T_g of the matrix. The results are shown in Fig. 6.6. Whereas the matrix at this temperature shows more homogeneous deformation and less well defined crazing (Fig. 6.6 (a)), the nanocomposites continue to show the cavitation observed at room temperature (Fig. 6.6 (b-d)). In this case laponite aggregates are clearly visible in the deformed material.

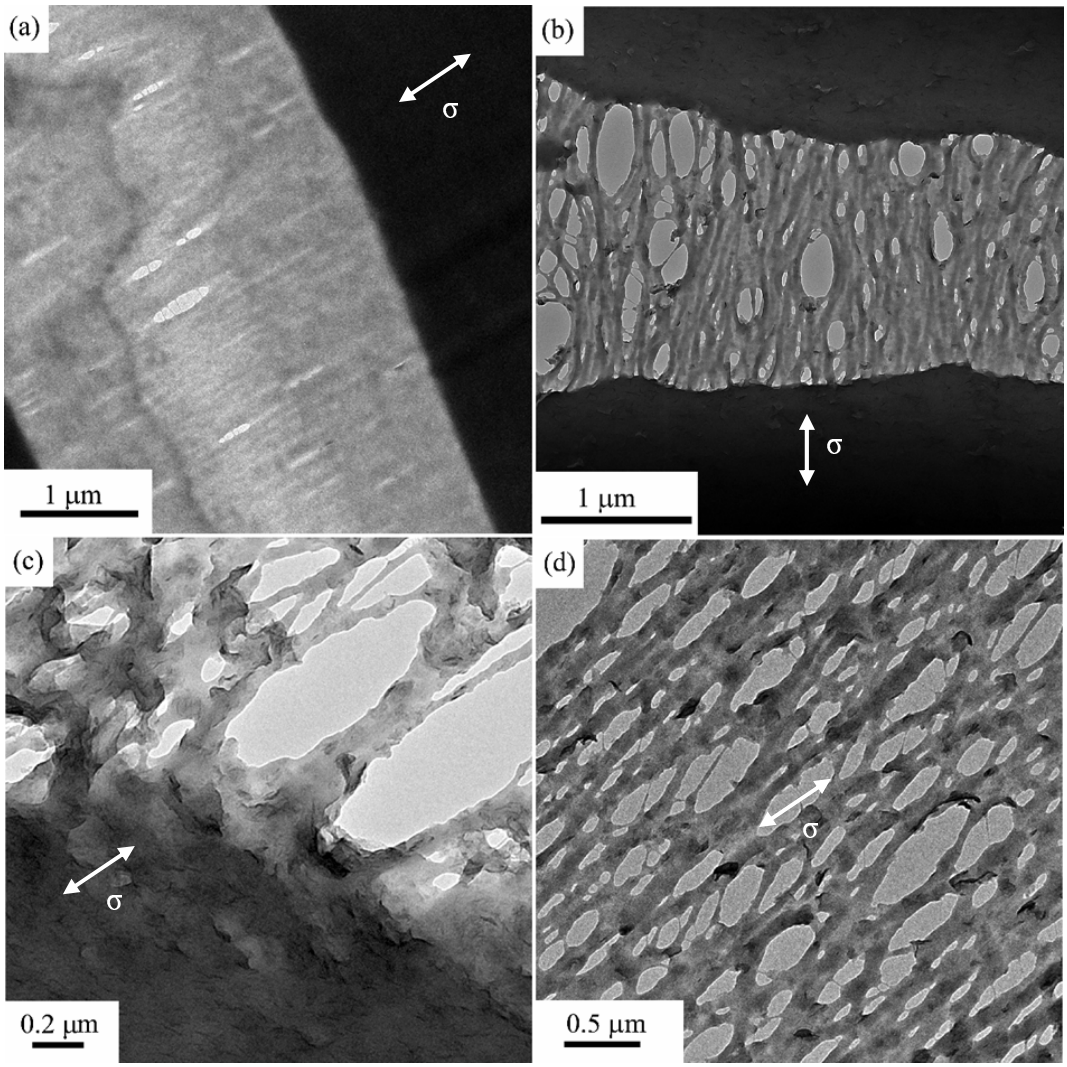

Fig. 6.6 Thin film deformation at 95°C for (a) L0, (b) L5, (c) L10 and (d) L20.

Failure initiation was difficult to identify unambiguously in the composite films. In general failure did not generally appear to be associated with matrix/laponite interface and the laponite aggregates did not show a clear tendency to break up. At low and intermediate laponite contents, cavitation was thought to occur within the original latex particles as shown in Fig. 6.7 (a), so that all the cavitated zones were surrounded by laponite stacks. At high laponite loadings where percolation of the aggregates was assumed, the crack path follows the particle boundaries (Fig. 6.7 (b)) leading to brittle failure. This is consistent with the results of tensile tests. Moreover, while

overall percolation is only reached at a laponite content of about 20 vol %, it may occur locally at lower laponite contents, again giving rise to brittle failure.

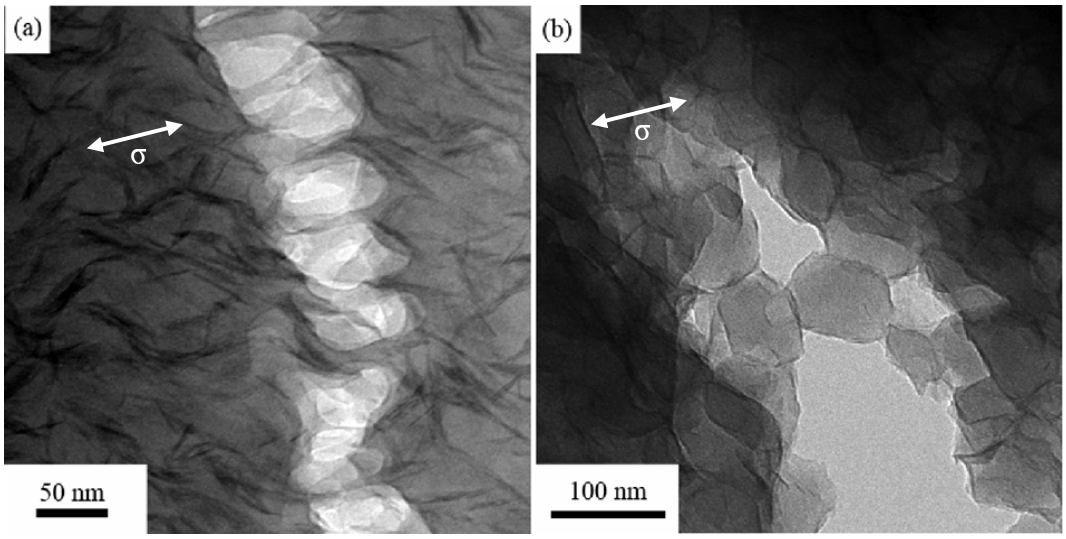

Fig. 6.7 Failure mechanisms in (a) L20 and (b) L50 nanocomposites in the glassy state.

At 120°C, i.e. above the matrix T_g, the matrix and the nanocomposites with low filler content showed only homogeneous deformation, and the highly filled nanocomposites showed localized deformation zones, as in Fig. 6.8. This indicates a yielding process, consistent with the presence of a continuous network of laponite and immobilized matrix evoked in sections 4.1.4. and 4.1.6 to account for the small strain response in the rubbery state.

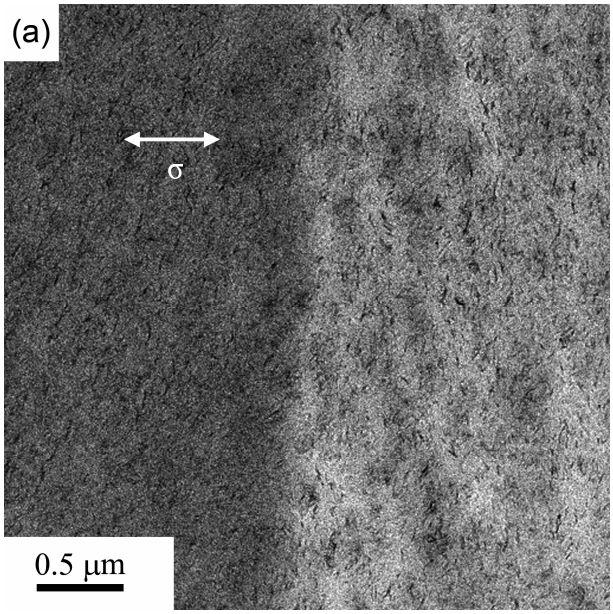

Fig. 6.8 Deformation zones for L20 film in the rubbery state (120 °C).

SEM images of fracture surfaces from the nanocomposite films were consistent with the results of thin film deformation. The fracture surfaces of samples of (a) L0, (b) L10 and (c) L20 are shown in Fig. 6.9. The neat matrix shows a highly fibrillated surface, presumably arising from fibril elongation and break-up in the final stages of craze rupture. When the laponite content is increased the surfaces become globally smoother, consistent with a decrease in matrix plastic flow in the presence of the laponite. L20 exhibits an almost featureless surface with small polymer "tufts". These "tufts" are about the same size as the cavities observed in the thin films (see Fig. 6.3).

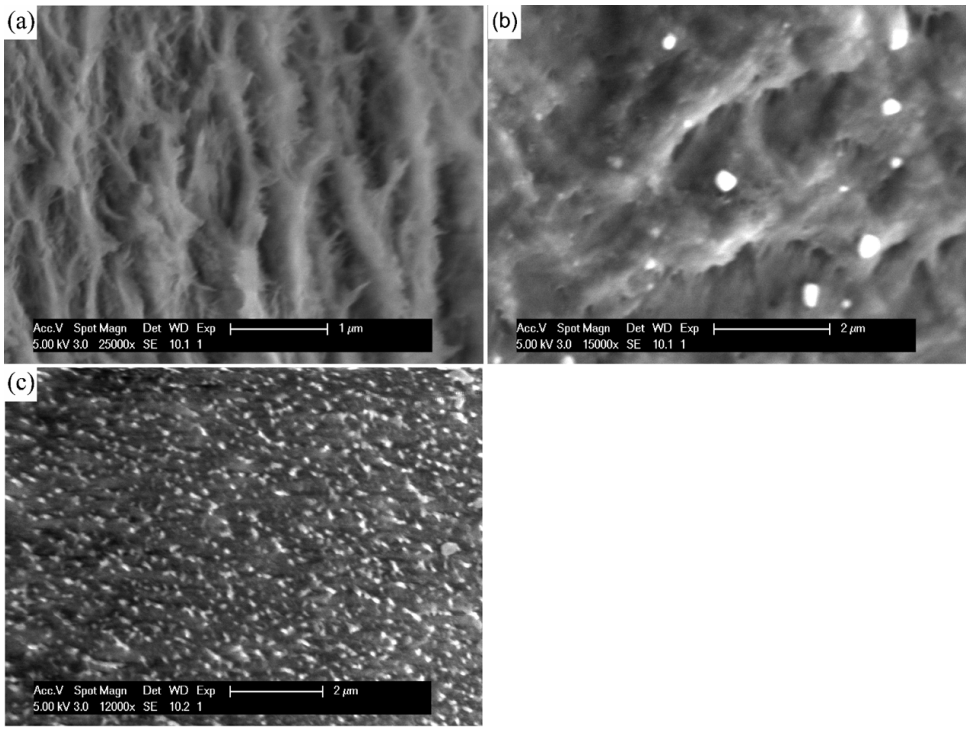

Fig. 6.9 SEM images of surface fracture of films of (a) L0, (b) L10 and (c) L20.

6.2.2 Discussion

While the physical and mechanical characterization of polymer-based nanocomposites has attracted the interest of many authors, there are few reports on the microdeformation mechanisms of these materials in the literature. Indeed to our knowledge, only one report on PS-based nanocomposite materials has been published [10]. It was found in this case that carbon nanotubes have little influence on the microdeformation mechanisms of the matrix and that the crazes were not substantially modified. This was possibly due to the low concentrations of

nanotubes investigated (about 1 wt %). Examples of microdeformation studies on nanocomposites with other types of matrix are also available. In the case of PLA/MMT nanocomposites, a decrease in matrix drawabilty was observed, similar to that found here for PS/laponite [11]. The MMT was shown to act as a preferential site of craze nucleation. The same effect was also observed in PA6/MMT. It was found that at a MMT content of around 7 wt % the number of crazes is so high that they can not fully develop, leading to reduced plasticity [12, 13]. Michler and coworkers showed that microvoids are generally generated at the interface between the clay and the matrix in the case of good dispersions and within the aggregates in the case of poor dispersions [14]. The presence of large voids in deformed clay nanocomposites has been attributed to the overlap of stress fields in the case of poor filler dispersions [15]. This effect was not marked in the present case. The presence of nanoparticles drawn into the craze material as shown in Fig. 6.5 was also reported elsewhere [16]. The deformation of nanomaterials with morphologies similar to that of the PS/laponite nanocomposites derived from armoured latexes has also been studied. PA66/rubber toughened nanocomposites with clay platelets around the rubber particle showed initial deformation by cavitation in the rubber particles and submicron voids with laponite at their boundaries were observed by TEM [17]. Another morphology that could be considered analogous to the present PS/laponite nanocomposites was described by Yee and coworkers. They studied the deformation of epoxy resins filled with thermoplastic particles. The rigid epoxy could be taken to correspond to the laponite network of the present system, with the thermoplastic particles playing an analogous role to the PS latex particles. It was shown that the thermoplastic particles are also able to cavitate during crack propagation [18].

6.3 Deformation mechanisms of extruded-calendered Moplen PP/MMT nanocomposites

The Moplen PP matrix is a high melt flow index PP grade. The high melt flow index is a consequence of a relatively low molecular weight, which accounts also for its relatively low ductility. The lamellar structure of the α-iPP phase of the neat matrix is shown in Fig. 6.10, illustrating the effectiveness of the staining process described in section 3.4. The staining operation has two main goals: the first is to prevent TEM beam damage to the thin section, the second being to stain the deformation zones in order to distinguish them from microtome-induced damage.

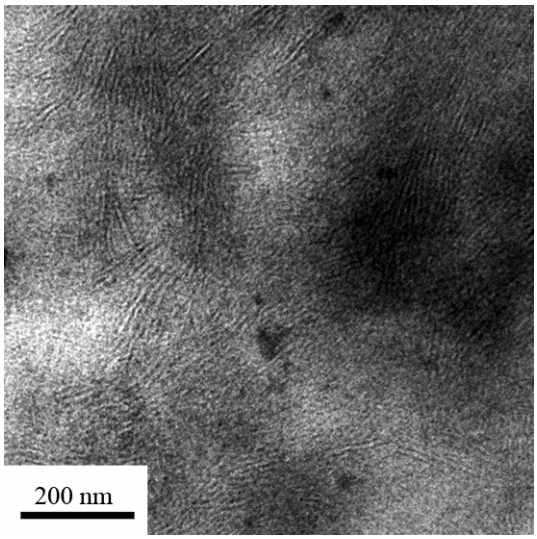

Fig. 6.10 TEM image of lamellar structure of the Moplen PP matrix after staining with RuO_4.

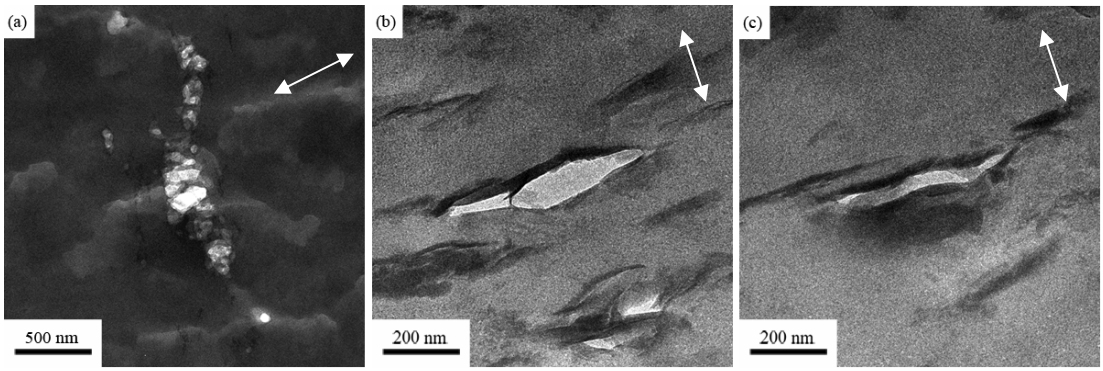

Fig. 6.11 Microdeformation mechanism of (a) neat Moplen PP and (b,c) 2.4 vol % MMT nanocomposites. The arrows indicate the deformation direction.

The use of the DENT configuration did not produce significant plastic deformation at the notch tips and the fracture behavior of the specimens was relatively brittle. The samples were therefore deformed in simple flexion to generate a stress whitened zone that could be sectioned and observed by TEM. Fig. 6.11 shows the result of such deformation in the neat matrix and in a 2.4 vol % MMT nanocomposite. In the neat matrix, deformation resulted in the formation of localized deformation zones containing submicron-sized voids (Fig. 6.11 (a)). In the nanocomposites, failure of the MMT/matrix interface (Fig. 6.11 (b)) and break up of MMT aggregates (Fig. 6.11 (c)) were the most apparent damage mechanisms. This may be ascribed to the stress concentrating effect of the MMT aggregates, leading to preferential interfacial break up owing to the intrinsic weakness of the MMT/PP interactions. The blackened area around the MMT

aggregate in the TEM images is the result of staining, indicating these features to result from the initial deformation and not from damage induced by the microtome.

6.4 Deformation mechanisms of extruded-injection molded Borealis PP/MMT nanocomposites

The PP from Borealis, which had a higher ductility than the Moplen PP, allowed the study of the microdeformation mechanisms with samples with the SEN geometry. After deformation, the notch tip was impregnated with epoxy resin and analyzed by both TEM and SEM imaging. The introduction of MMT resulted in significant changes in the micro-deformation mechanisms.

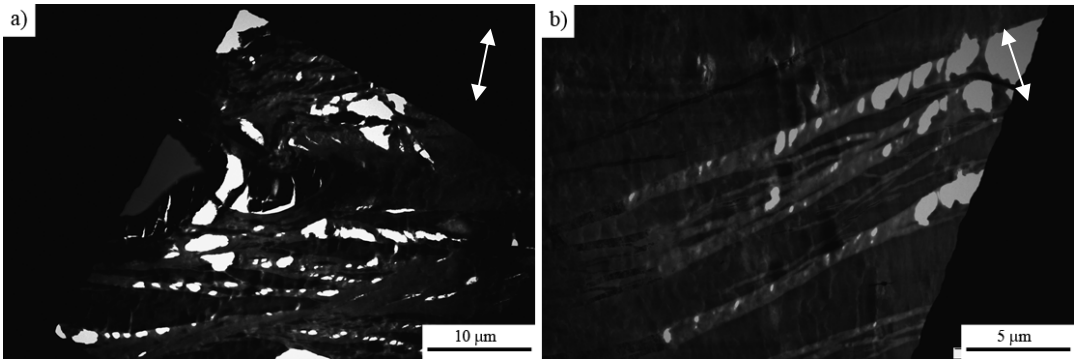

Fig. 6.12 TEM image of (a) the deformation at the crack tip and (b) detail of the fibrillar deformation mechanism in neat Borealis PP. The direction of the tensile stress is as indicated by the arrows

Fig. 6.12 (a) shows deformation in the neat PP. The notch filled with epoxy resin is visible at the left of the image. Around it, a very large deformation zone can be observed with evidence of matrix cavitation and fibrillar deformation, the size of these features being in the micron range. Higher magnification images show the apparent mechanism of fibrillation (Fig. 6.12 (b)): it is proposed that the polymer initially deforms homogeneously, but build-up of stresses results in the formation of voids, leading to craze-like features, as described in section 2.6.2. A better overview of the damage zone was provided by SEM imaging of the notched surface used for the sectioning. Fig. 6.13 shows a backscattered electron image, from which the deformation zone may be estimated to be about 200 μm long and 100 μm wide, implying substantial plasticity. The notch is indicated by an arrow. Some cracks are also visible, but are thought to be due to the

staining. Less aggressive staining with RuO_4 vapor exposure rather then immersion in RuO_4 eliminated the surfaces cracking as shown in Fig. 6.14.

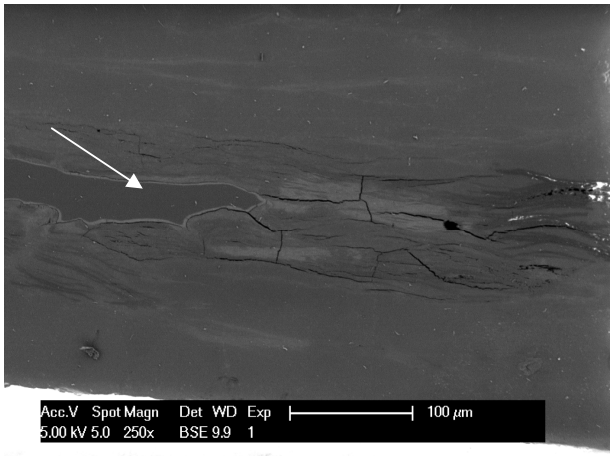

Fig. 6.13 Backscattered electron SEM image of the deformation zone behind the notch (indicated by the arrow) for Borealis PP.

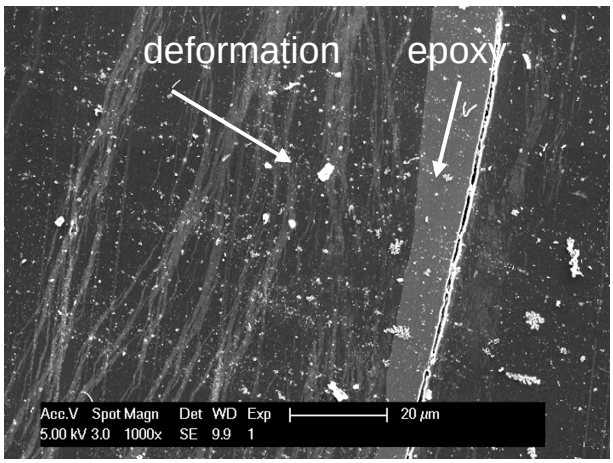

Fig. 6.14 Relatively artifact-free SEM image of the deformation zone in Borealis PP.

Fracture surfaces of the SEN specimens were also observed by SEM. Fig. 6.15 (a) shows the region of the fracture surface adjacent to the notch tip where extensive voiding can be observed. This is thought to be due to void coalescence at high strains. At higher magnifications shear lips were also visible (Fig. 6.15 (b)).

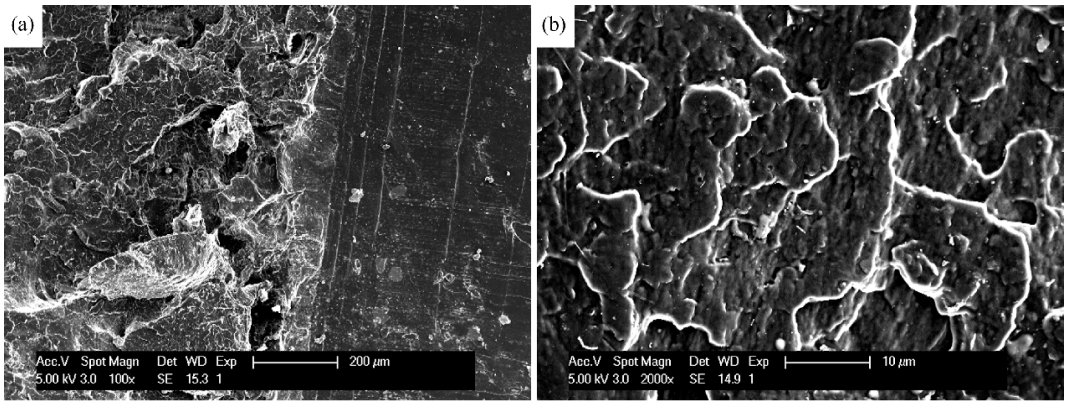

Fig. 6.15 SEM images of (a) a neat Borealis PP fracture surface and (b) a detail at higher magnification.

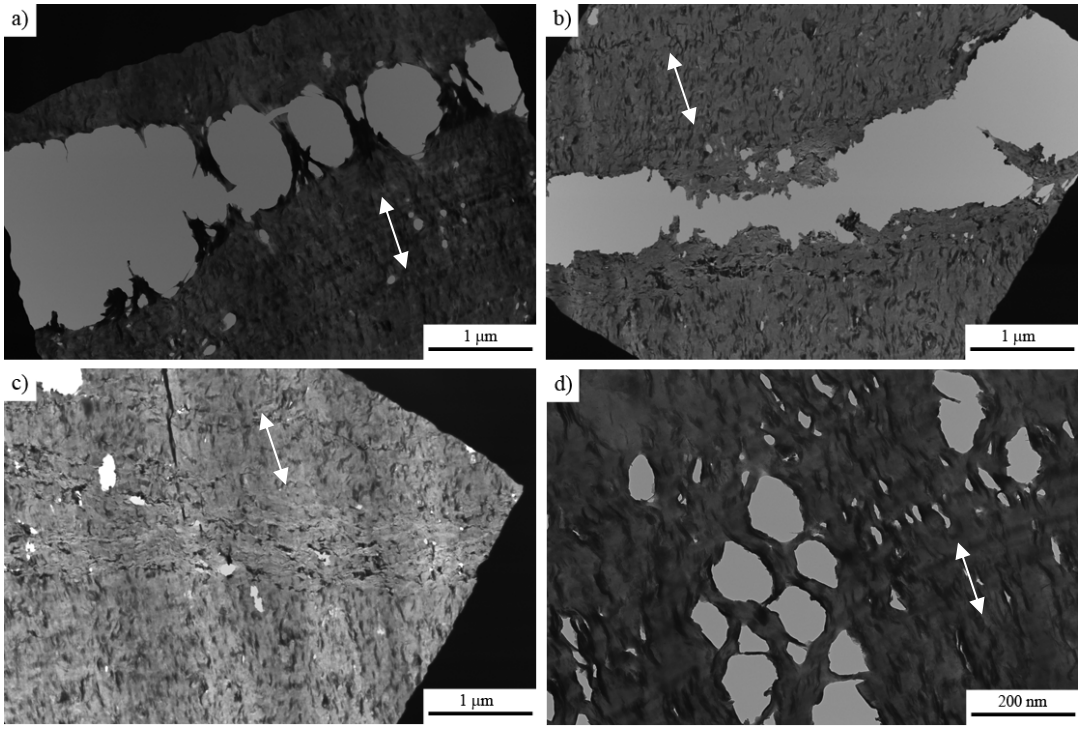

Fig. 6.16 TEM images of Borealis PP/2.4 vol% MMT: (a) craze-like deformation, (b,c) crack and crack tip and (d) mechanism of cavitation. The deformation direction is indicated by the arrows.

The behavior of the MMT nanocomposites contrasts with that of the neat matrix, the MMT causing a drastic change in deformation mechanism. In this case the craze-like deformation was dominant and no homogeneous shear bands were observed. Highly deformed fibrils could be observed, separated by micron-sized voids (Fig. 6.16 (a)). When the fibrils broke down, a change in the orientation of the MMT aggregates was observed, attributed to relaxation of the strained material (Fig. 6.16 (b)). The same morphology was found in the zone immediately behind the crack tip. Here the MMT platelets were rotated by 90° with respect to the undeformed material (Fig. 6.16 (c)). This was again attributed to relaxation of drawn material. All TEM images showed

relatively small scale cavitation. An increase in magnification revealed that, as for the Moplen PP, cavitation appeared to initiate at the MMT/matrix interface, as shown in Fig. 6.16 (d).

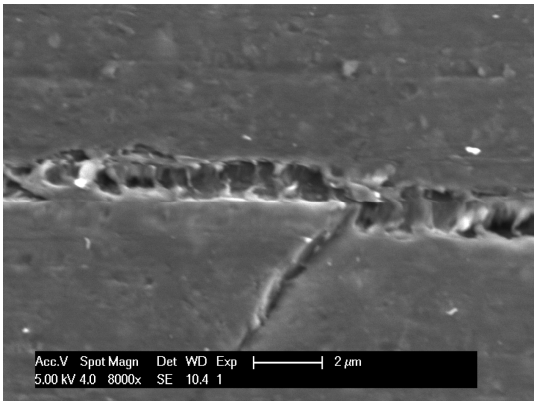

Fig. 6.17 SEM image of the crack zone in a Borealis PP/6 wt% MMT nanocomposite.

This fibrillar deformation mechanism was also observed by SEM imaging of the notched surfaces used for TEM sectioning (Fig. 6.17). The deformation was significantly more localized than in the neat matrix. This could be ascribed to a strong decrease in matrix ductility on MMT addition as will be discussed below. Extended zones of cavitation were also visible, as shown in Fig. 6.18. The origin of these is assumed to be as discussed previously in the case of Fig. 6.16 (d), with voids growing by coalescence of small cavities. In this case the deformation zones were around 10 µm in width and contained voids of 1-2 µm in diameter, as seen in Fig. 6.17.

The fracture surface of a SEN sample observed by SEM is shown in Fig. 6.19. The features visible in this case are different from those in Fig. 6.15. The fracture surface appears relatively smooth at low magnification (Fig. 6.19 (a)), but an increase in magnification showed small broken fibrils (Fig. 6.19 (b)). No shear lips were visible.

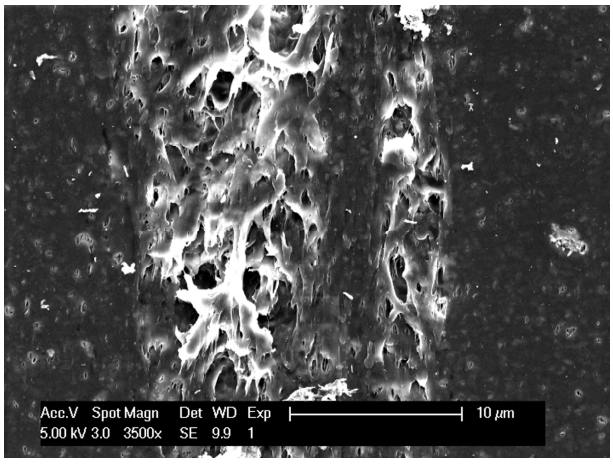

Fig. 6.18 SEM image of cavitation in a Borealis PP/2.4 vol% MMT nanocomposite.

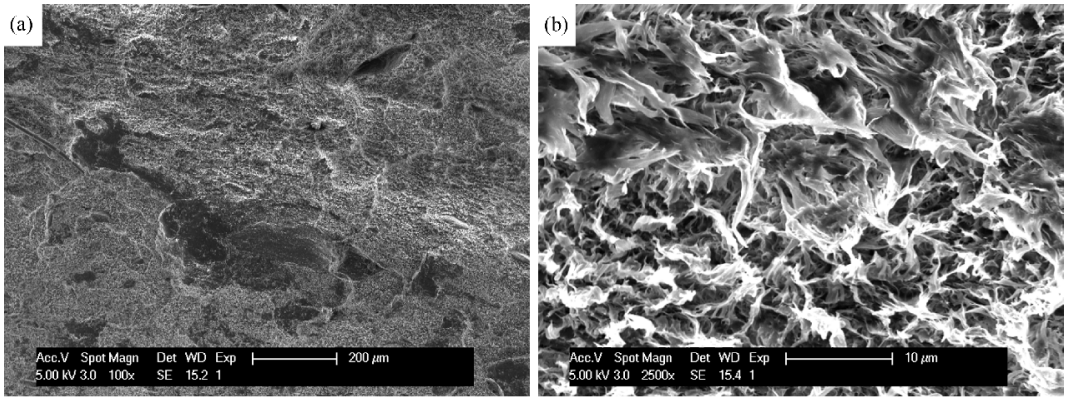

Fig. 6.19 SEM image of (a) a Borealis PP/2.4 vol% MMT nanocomposite fracture surface and (b) a detail at higher magnification.

6.5 Mechanical response of PP/MMT nanocomposites

The bulk mechanical properties of PP/MMT nanocomposites with both the Moplen and Borealis matrices have been extensively studied elsewhere [19, 20]. These results will be reviewed in what follows in the light of the microdeformation mechanisms described above.

6.5.1 Moplen PP/MMT nanocomposites

Nanocomposite films based on the Moplen matrix obtained by extrusion-calendering taken parallel to extrusion direction (MD) showed a gradual increase in tensile modulus with MMT contents, the tensile strength increasing up to 3.5 wt % MMT and then decreasing (Fig. 6.20). Samples deformed in the transverse direction (TD) and samples obtained by injection molding showed the same trends [19]. Similar results were found for the flexural modulus while the flexural strength decreased for all MMT contents [20] (see Fig. 6.21). In this case the samples were prepared by compression molding.

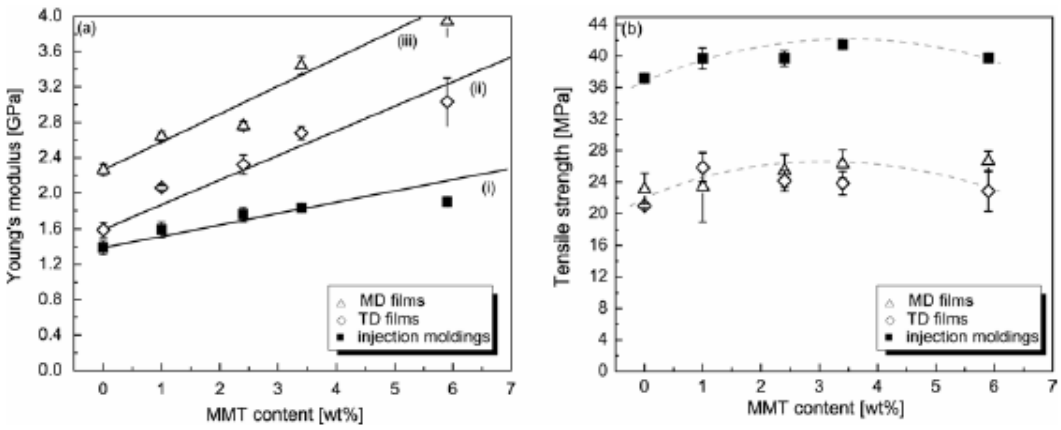

Fig. 6.20 Young's modulus (a) and tensile strength (b) of Moplen PP/MMT nanocomposites, [19].

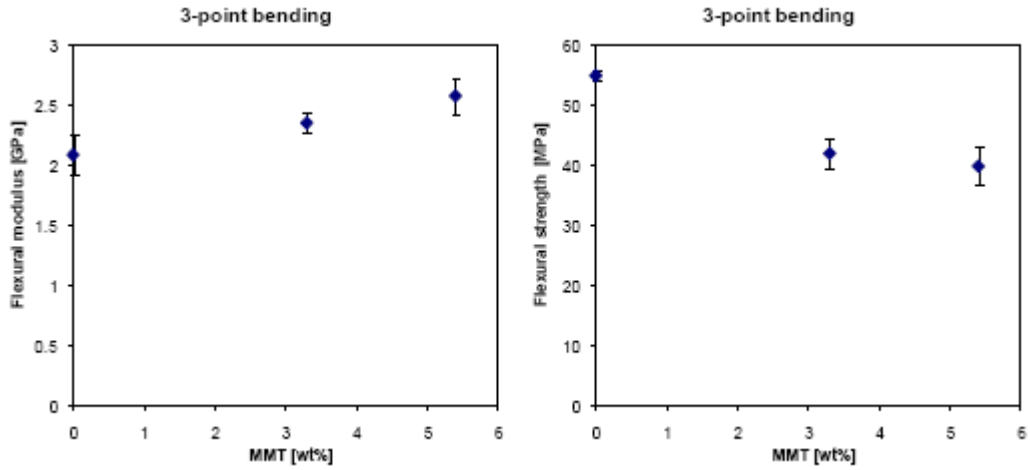

Fig. 6.21 Flexural modulus (left) and strength (right) of Moplen PP/MMT nanocomposites [20].

Both the neat matrix and the nanocomposites showed semi-brittle behavior in load-displacement experiments based on the EWF protocol (see section 3.4.6), deviating from linearity at a certain deformation and showing unstable crack propagation. The maximum load and displacement to failure decreased with increasing MMT content for a fixed ligament length, as shown in Fig. 6.22. The specific essential work of fracture w_e showed the same trends as the tensile strength in Fig. 6.20 in the extrusion direction (MD), increasing with MMT contents up to 3.5 wt % and then decreasing (see Fig. 6.23). A decrease with MMT content was observed in the transverse direction (TD).This means that MMT is only beneficial for fracture resistance at low concentrations and when the platelets are aligned in the tensile direction.

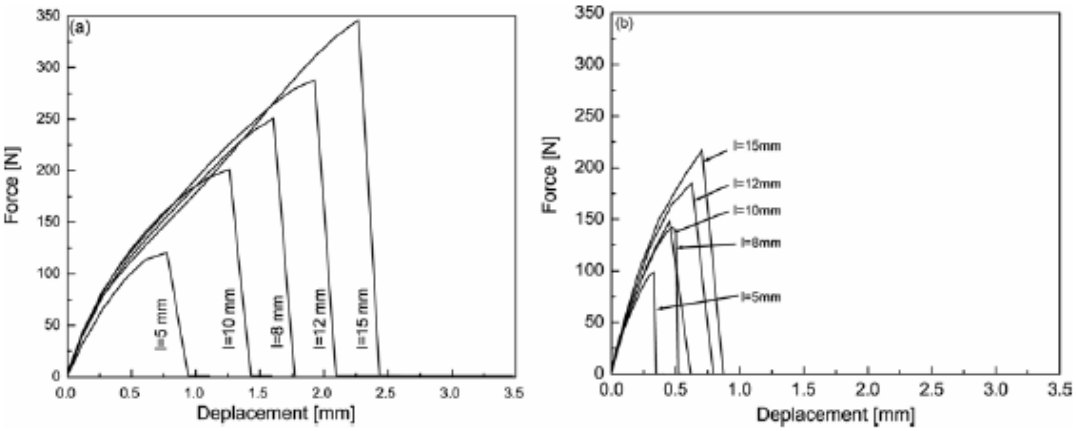

Fig. 6.22 Load-displacement curves for (a) Moplen PP and (b) PP/3.4 wt% MMT nanocomposites [19].

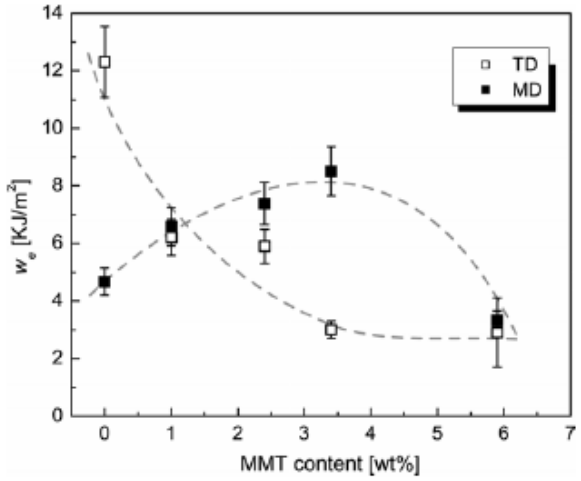

Fig. 6.23 Specific essential work of fracture for Moplen PP/MMT nanocomposites [19].

The deformation mechanisms of Moplen PP/MMT nanocomposites were also analyzed [19]. SEM images of fracture surfaces of the neat matrix showed shear lips similar to those of Fig. 6.15. This was considered as an indication of ductile instability, where initial ductile crack propagation is followed by unstable crack propagation when the stress attains a critical value. The fracture surfaces showed fewer features at about 6 wt % MMT loadings. Very small voids were observed, consistent with the observations in Fig. 6.19.

6.5.2 Borealis PP/MMT nanocomposites

MMT nanocomposites based on the Borealis matrix were obtained by injection molding or by melt spinning in form of fibers. The tensile modulus again increased with MMT content, while the tensile strength increased up to 4 wt % and then slowly decreased (Fig. 6.24). Both the neat

matrix and the nanocomposites showed more ductile behavior (yielding and necking) than for the Moplen based materials, reflecting the lower melt flow index and hence a higher plasticity than the former.

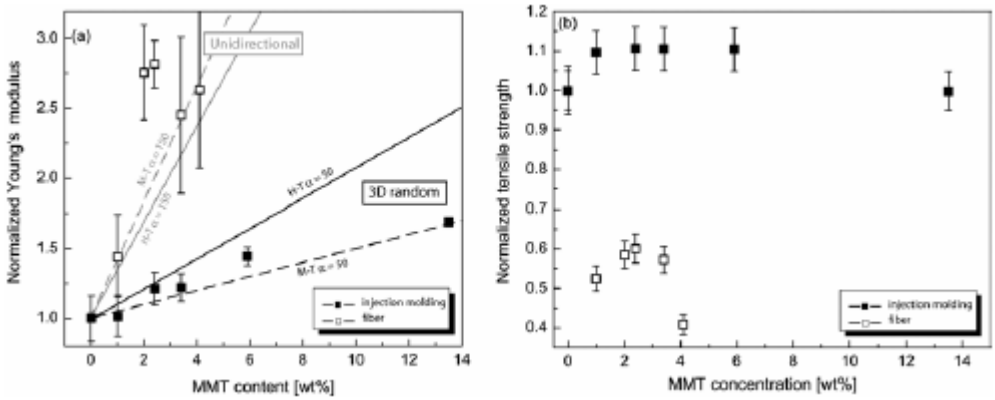

Fig. 6.24 (a) Normalized tensile modulus and (b) strength of Borealis PP/MMT nanocomposites [19].

6.5.3 Discussion

The results given in sections 6.3 and 6.4 showed that the MMT changes the microdeformation mechanisms of pure PP. When a sufficiently ductile PP matrix is deformed, large zones of shear deformation could be observed with some local fibrillation. Fibrillated deformation zones similar to those observed in Borealis PP (see Fig. 6.12) have been already reported in literature [21], where deformation was shown clearly to involve interlamellar separation and decrystallization. Large deformations also resulted in an orientation of both crystalline and amorphous regions [22]. The effect of deformation on the crystalline structure was not considered in the present study.

The MMT favors craze-like deformation, localized around the crack tip. Some cavitation is observed, attributed to failure of the MMT/matrix interface, suggesting poor adhesion between the two components. The voids can grow and eventually coalesce at large deformations. The presence of cavitation was also reported for PP/MMT nanocomposites by Deshmane and coworkers [24]. SAXS measurements have also indicated cavitation to occur during deformation of other types of PP nanocomposite [25].

The presence of clay in PP may lead to a change in the crystalline structure, e.g. by acting as nucleating centers [26, 27]. Both the α and β polymorphs were observed in the Borealis PP matrix nanocomposites suggesting a nucleating effect of the MMT but the crystallinity remained fixed at around 50 % [19]. Similar results were also obtained for the Moplen PP matrix

nanocomposites [19]. However, at this stage it is not clear whether these structural changes affect the deformation mechanisms.

The results of mechanical testing showed a decrease in tensile strength beyond MMT loadings of about 3 to 4 wt % and also a decrease in essential work of fracture, in the nanocomposites, suggesting a decrease in crack initiation resistance. This is consistent with the results of Deshmane et al. for PP/MMT nanocomposites, who showed that there is no change in fracture surface morphology for MMT contents up to 4 wt % [23]. The change in mechanical behavior may be explained by the decrease in ductility suggested by the thin film and fracture surface analysis. As in the case of the PS/laponite nanocomposites, relatively high MMT loadings cause embrittlement, unstable crack propagation being favored. In the case of PP-based nanocomposites the platelet orientation also plays an important role. As discussed in [19], testing the material parallel or perpendicular to the direction of extrusion can lead to very different mechanical behavior. In the present work, however, only results for samples taken parallel to extrusion direction, i.e. with the MMT approximately parallel to the deformation axis have been considered. It could clearly be of interest to investigate the effect of the orientation in future work.

6.6 Conclusions

The relationships between the macroscopic response of PS/laponite nanocomposites and their deformation mechanisms were analyzed in detail in this chapter and compared with the existing literature in this field. At laponite contents of up to 2 to 3 vol % the laponite did not significantly affect the microdeformation mechanisms. The high degree of laponite dispersion in the matrix not only resulted in a larger increase in tensile modulus than at higher laponite contents, but also an improvement in high strain properties. On the other hand, further increases in laponite content led to a rapid decrease in tensile strength and extension to break. An explanation of the embrittlement on laponite addition at room temperature was proposed, based on a decrease of local matrix drawability and cavitation at low and intermediate filler contents. For the highly filled materials the crack path follows the laponite rich regions of the particle interface resulting in extremely brittle behavior. The cellular arrangement of the laponite strongly influences the deformation mechanisms, and it is suggested that, at intermediate compositions, cavitation initiates in the PS-rich zones that correspond to the centers of the original latex particles. However, no unambiguous evidence for this was observed in the deformation of thin films. The laponite modifies the deformation mechanisms even at temperatures above T_g, promoting stress

delocalization and yielding via the presence of the laponite network, which behaves as a load bearing structure.

The results of mechanical studies performed previously on PP/MMT-based materials studied at LTC were interpreted in terms of studies of the microdeformation mechanisms. Two different extrusion grades of PP were considered. It was shown that when the molecular weight of the matrix was too low to permit extensive ductility, it is difficult to study the micro-deformation mechanisms of the nanocomposites. However, for both PP matrices, cavitation is thought to initiate at the MMT/polymer interface or within MMT aggregates, which are not reinforced to the same extent as for the PS/laponite interfaces, leading to localized craze-like or fibrillated deformation zones, rather than the homogeneous deformation that dominates in the matrix. This results in a ductile to brittle transition of the material when the MMT content is increased beyond 3 to 4 wt% MMT.

As a general conclusion, an increase in stiffness with clay content but a decrease in strength was observed above a certain loading for two different nanocomposite materials and preparation techniques. The latex route to PS/laponite nanocomposites nevertheless allows a better dispersion of the filler in the matrix and a better control of the final material morphology, and implies strong interactions between the clay and the matrix. This shifts the threshold for the decrease in ductility towards higher clay contents, i.e. from 3 to 4 wt % to 5 to 7 wt %. At very much higher loadings, the PS/laponite become highly brittle owing to crack propagation through the original latex particle boundaries, but it is not possible to achieve such loadings in PP.

6.7 Bibliography

[1] M.W. Noh, D.C. Lee, *Synthesis and characterization of PS-clay nanocomposites by emulsion polymerization.* Polym. Bull. **42** (1999) 619.

[2] S. Tanoue, L.A. Utracki, A. Garcia-Rejon, J. Tatibouët, M.R. Kamal, *Melt compounding organoclay of different grades polystyrene with organoclay. Part 3: Mechanical properties.* Polym. Eng. Sci. **45** (2005) 827

[3] M.Sepher, L.A.Utraki, X.Zheng, C. A Wilkie, *Polystyrenes with macro-intercalated organoclay. Part I. Compounding and characterization*. Polymer **46** (2005) 11569

[4] P. Uthirakumar, M.K. Song, C. Nah, Y.S. Lee, *Preparation and characterization of exfoliated polystyrene/clay nanocomposites using a cationic radical initiator-MMT hybrid.* Eur. Polym Journ. **41** (2005) 211

[5] M.V. Burmistr, K.M. Sukhyy, V.V. Shilov, P. Pissis, A. Spanoudaki, I.V. Sukha, V.I. Tomilo, Y.P. Gonza, *Synthesis, structure, thermal and mechanical properties of nanocomposites based on linear polymers and layered silicates modified by polymeric quaternary ammonium salts (ionenes).* Polymer **46** (2005) 12226

[6] E.J. Kramer, L.L. Berger in : Advance in Polymer Science (ed. H.H. Kausch), 1990 Springer Berlin

[7] C. Maestrini, E.J. Kramer, *Craze structure and stability in oriented polystyrene.* Polymer **32** (1991) 609

[8] C. Creton, E.J. Kramer, G. Hadziioannou, *Craze fibril extension ratio measurements in glassy block copolymers.* Colloid Polym. Sci. **270** (1992) 399

[9] G.P. Tandon, G.J. Weng, *The effect of aspect ratio of inclusions on the elastic properties of unidirectionally aligned composites.* Polym. Comp. **5** (1984) 327

[10] C.-C. Hsiao, T.S. Lin, L.Y. Cheng, C.-C. Ma, A.C.-M. Yang, *Nanomechanical properties of polystyrene thin films embedded with surface-grafted multiwalled carbon nanotubes.* Macromolecules **38** (2005) 4811

[11] L. Jiang, J. Zhang, M.P. Wolcott, *Comparison of polylactide/nano-sized calcium carbonate and polylactide/montmorillonite composites: Reinforcing effects and toughening mechanisms*. Polymer **48** (2007) 7623

[12] C. He, T. Liu, W. C Tjiu, H.-J. Sue, A.F. Yee, *Microdeformation and fracture mechanisms in polyamide-6/organoclay nanocomposites.* Macromolecules **41** (2008) 193

[13] L. Chen, I.Y. Phang, S.-C. Wong, P.-P. Lv, T. Lu, *Embrittlement mechanisms of nylon 66/organoclay nanocomposites prepared by melt-compounding process.* Mater. Manufact. Proc. **22** (2006) 153

[14] G.-M. Kim, S. Goerlitz, G.H. Michler, *Deformation mechanism of nylon 6/layered silicate nanocomposites: Role of the layered silicate.* Journ. Appl. Polym. Sci. **105** (2007) 38

[15] G.-M. Kim, D.-H. Lee, B. Hoffmann, J. Kressel, G. Stöppelmann, *Influence of nanofillers on the deformation process in layered silicate/polyamide-12 nanocomposites*. Polymer **42** (2001) 1095

[16] J.-Y. Lee, Q. Zhang, T. Emrick, A.J. Crosby, *Nanoparticle alignment and repulsion during failure of glassy polymer nanocomposites.* Macromolecules **39** (2006) 7392

[17] A. Dasari, Z.-Z. Yu, M. Yang, Q.-X. Zhang, X.-L. Xie, Y.-W. Mai, *Micro- and nano-scale deformation behaviour of nylon 66-based binary and ternary nanocomposites.* Comp. Sci. Tech. **66** (2006) 3097

[18] B.J. Cardwell, A.F. Yee, *Toughening of epoxies through thermoplastic crack bridging*. Journ. Mat. Sci. **33** (1998) 5473

[19] C. Houphouet-Boigny, Ph.D. Thesis N° 3851 Ecole Polytechnique Fédérale de Lausanne (2007)

[20] S. Dalle Vacche, Micro and Nanotechnology Master Thesis, Geneva University (2008)

[21] R. Gensler, Ph.D. Thesis N° 1863 Ecole Polytechnique Fédérale de Lausanne (1998)

[22] T.A. Hui, R. Adhikari, T. Lüpke, S. Henning, G.H. Michler*, Molecular deformation mechanisms of isotactic polypropylene in alpha- and beta-crystal forms by FTIR spectroscopy.* Journ. Polym. Sci Part B **42** (2004) 4478

[23] C. Deshmane, Q. Yuan, R.D.K. Misra, *High strength-toughness combination of melt intercalated nanoclay-reinforced thermoplastic olefins.* Mat. Sci. Eng. Part A **460-461** (2007) 277

[24] Q. Yuan, C. Deshmane, T.C. Pesacreta, R.D.K. Misra, *Nanoparticle effects on spherulitic structure and phase formation in polypropylene crystallized at moderately elevated pressures: The influence on fracture resistance*. Mat. Sci. Eng. Part A **480** (2008) 181

[25] X. Li, K. Schneider, B. Kretzschmar, M. Stamm, *Deformation behaviour of PP and PP/ZnO nanocomposites as studied by SAXS and WAXS.* Macromolecules **41** (2008) 4371

[26] J.S. Ma, S.M. Zhang, Z.N. Qi, G. Li, Y.L. Hu, *Crystallization behaviours of polypropylene/montmorillonite nanocomposites.* Journ. Appl. Polym. Sci. **83** (2002) 1978

[27] K. Wang, S. Liang, J.N. Deng, H. Yang, Q. Zhang, Q. Fu, X. Dong, D.J. Wang, CC. Han, *The role of clay network on macromolecular chain mobility and relaxation in isotactic polypropylene/organoclay nanocomposites.* Polymer **47** (2006) 7131

[28] H.R. Brown, *A molecular interpretation of the toughness of glassy polymers.* Macromolecules **24** (1991) 2752

Chapter 7

Finite element modeling (FEM) of PS/laponite nanocomposite deformation and stiffness

In this chapter the results of finite element modeling (FEM) of PS/laponite nanocomposite deformation mechanisms and stiffness are presented. As discussed in Chapter 6, the mechanisms of fracture initiation in PS/laponite nanocomposites were not fully clear from the TEM and SEM micrographs. Moreover, the role of the laponite aggregate anisotropy in the micromechanical model of section 4.1.6.4 requires further clarification. The aims of this chapter are twofold. The first is to investigate whether there are preferential zones for cavitation initiation under tensile deformation, i.e. zones where the hydrostatic stress is relatively high. The second is to estimate the tensile modulus of the PS nanocomposites, taking into account the effects of the matrix immobilization in the interphase and the material connectivity in the cellular structure. In section 7.1, FEM is used to reproduce the effect of deformation on the distribution of the hydrostatic stress, first in a single 2D latex particle with a laponite shell and then in an array of particles, which better represents the nanocomposite structure of the thin films. The results are discussed in the light of the TEM observations presented in the previous chapter. Section 7.2 describes refinements of the particle array in order to generate a more realistic arrangement of laponite platelets and implementation of a homogenization procedure to calculate the stiffness tensor components at different temperatures. These results are then compared with the experimental data obtained by DMA and tensile tests. The implied interphase properties are compared with those obtained from the analytical models of Chapter 4.

7.1 FE simulations of the stress field in PS/laponite nanocomposites

Before describing the simulations in detail, the principles of the FE calculations used here are briefly introduced. In solid mechanics, equilibrium is defined as

$$\sum_i F_i = 0 \qquad \text{eq. 7.1}$$

where F_i are the forces acting on a body. For an element of volume ΔV under deformation two forces must be taken into account, the gravity force F_g and the deformation force F_d , which may be written as

$$F_g = \rho g \qquad F_d = \frac{1}{\Delta V}\int \nabla \cdot \sigma dV \underset{\Delta V \to 0}{=} div\, \sigma \qquad \text{eq. 7.2}$$

where ρ is the mass density per unit volume, g is the gravitational force and σ is the stress. Eq. 7.1 may then be rewritten as [1]

$$\frac{\partial \sigma_{ij}}{\partial x_j} + \rho g_i = 0 \qquad \text{eq. 7.3}$$

In the case of linear elasticity, stress and strain components are related by the Hooke's law

$$\sigma_{ij} = C_{ijkl}\varepsilon_{kl} \qquad \text{eq. 7.4}$$

where σ_{ij} and ε_{kl} are the stress and strain vectors and C_{ijkl} is the stiffness tensor.

In FE calculations the properties of a solid are modelled with the help of a mesh that is superposed onto the solid structure, and the strain components may be rewritten as a function of the mesh node displacements, u_{lk} [1]

$$\varepsilon_{kl} = \frac{1}{2}\left(\frac{\partial u_l}{\partial x_k} + \frac{\partial u_k}{\partial x_l}\right) \qquad \text{eq. 7.5}$$

Inserting eq. 7.4 and 7.5 into 7.3 leads to

$$\frac{\partial}{\partial x_j}\left(C_{ijkl}\frac{1}{2}\left(\frac{\partial u_l}{\partial x_k} + \frac{\partial u_k}{\partial x_l}\right)\right) + \rho g_i = 0 \qquad \text{eq. 7.6}$$

This is the equation that will be solved in the simulations to be presented in what follows.

7.1.1. Single particle embedded in the composite medium

In a first approach, one isolated particle with a laponite shell thickness equal to that of the L20 nanocomposites (about 5 nm) was considered. The particle was embedded in a medium with properties equivalent to the average properties of the composite. In order to compare the results with those of analytical calculations, the particle was loaded in biaxial tension (case P/P) and in tension/compression (case P/-P), as shown in Fig. 7.1. The sum of the deformations is equivalent to a tensile deformation in the horizontal direction. The symmetry of the problem allowed consideration of just one quarter of the latex particle, with free surfaces where the loads are applied and constrained surfaces corresponding to the symmetry surfaces. The simulations have been carried out in two dimensions since this provides a reasonable approximation to the conditions of the thin film deformation experiments, in which very thin sections were deformed. Linear elastic behavior was assumed based on the results of tensile tests (Fig. 6.1) with a deformation of 1%.

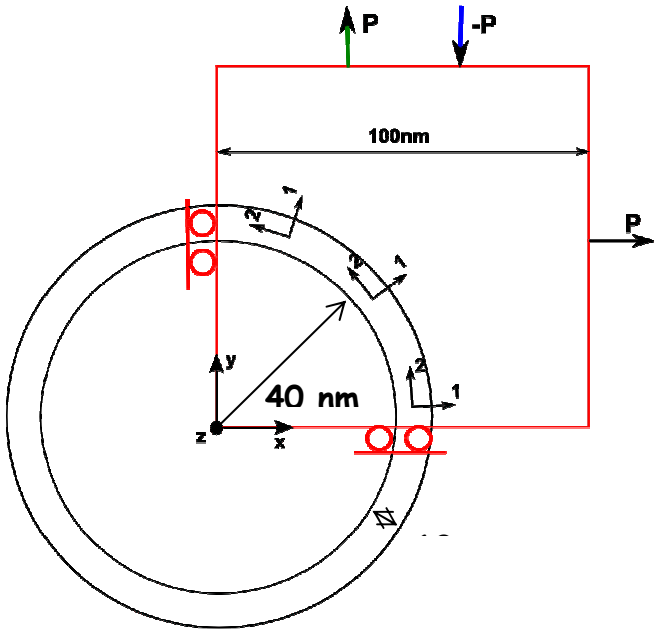

Fig. 7.1 Geometry used for FEM calculations in the single particle approach.

The data used for calculations were as follows:

- tensile modulus of the matrix E_m = 1.55 GPa
- Poisson's ratio of the matrix v_0 = 0.33
- tensile modulus of laponite E_f = 178 GPa
- Poisson's ratio of laponite v_1 = 0.15
- composite modulus E_c = 2 GPa

The tensile and shear properties for the laponite shell were estimated by H-T (see chapter 4 eqs. 4.1-4.2) and M-T [9] respectively according to the reference system in Fig. 7.2, and calculating the laponite volume fraction in the shell as previously done in chapter 4:

- $E_{11} = E_{22} = 34$ GPa
- $E_{33} = 3.5$ GPa
- $G_{12} = 0.8$ GPa
- $G_{23} = G_{13} = 8.4$ GPa
- $\nu_{12} = 0.28$

The above data were used for the calculations in the case where the laponite aggregates were taken to show orthotropic properties. In the isotropic case, the moduli E_{11} and E_{33} were combined as in eq. 4.3 (chapter 4) and the shear modulus was obtained from eq. 2.9 (chapter 2). The shell anisotropy was treated using a reference system in cylindrical coordinates for the laponite shell as shown in Fig. 7.1.

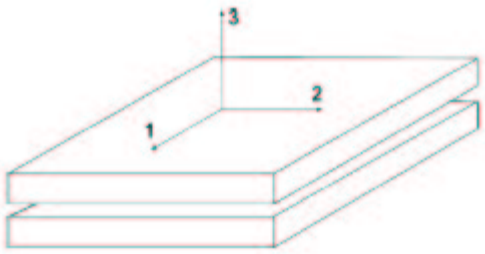

Fig. 7.2 Reference system for anisotropic properties of the laponite shell.

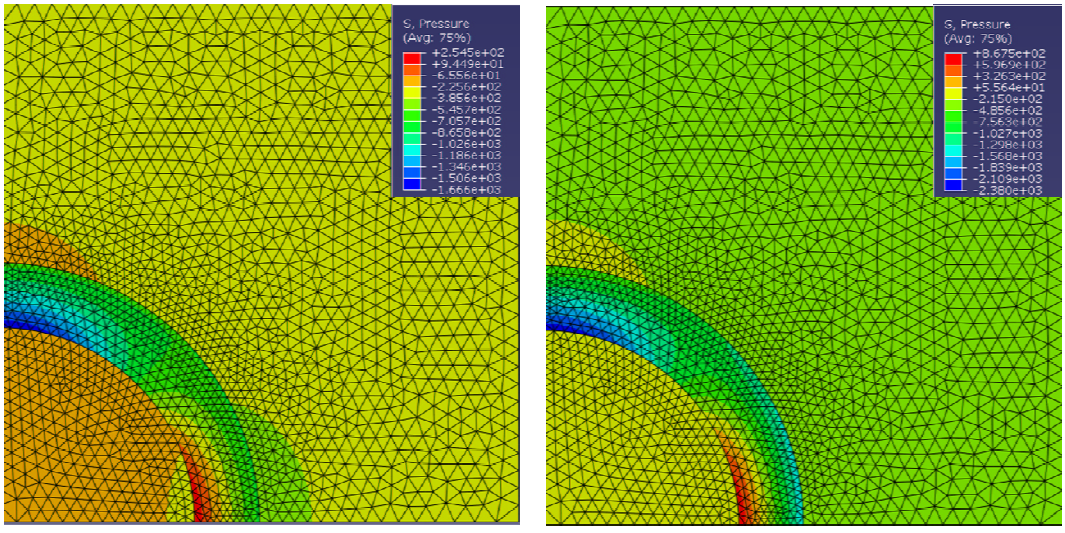

Fig. 7.3 Results of FEM calculations for the hydrostatic pressure for the isotropic (left) and anisotropic (right) case after 1% deformation.

In the following figures, the hydrostatic stress is defined according to Fig. 7.1 as:

$$P = -(\sigma_{xx} + \sigma_{yy} + \sigma_{zz})/3 = -(\sigma_{xx} + \sigma_{yy})/3 \qquad \text{eq. 7.7}$$

The results of the FEM calculations of *P* are compared in Fig. 7.3 for the isotropic (left) and anisotropic case (right) for a tensile deformation in the horizontal direction of 1%. It is clear that the inclusion of laponite aggregate anisotropy into the model does not change substantially the deformation behavior of a single latex particle. The highest negative stresses (the blue zones in the figures) were found in both cases to be situated in the laponite platelets aligned with the deformation direction. The effect of anisotropy was mainly observed in the absolute values of *P*, which increased somewhat.

Fig. 7.4 compares *P* for FEM calculations in the isotropic case and analytical results obtained as described in the Appendix I, indicating good agreement. The color scale in FE image has been altered in this case order to be consistent with that used for the analytical calculations.

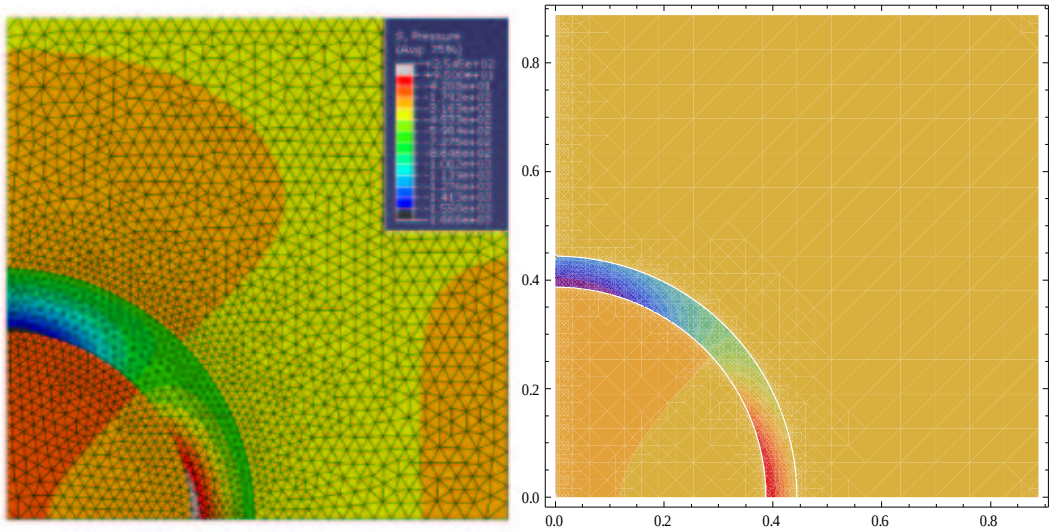

Fig. 7.4 Comparison between FE results (left) and analytical results (right) in the isotropic case.

7.1.2 Particle arrays

A particle array based on several L20 latex particles was also considered. The representative volume element (RVE) shown in Fig. 7.5 was used to generate the structure by translation in the *x* and *y* directions, with the aim of reducing possible edge effects inherent in the single particle approach.

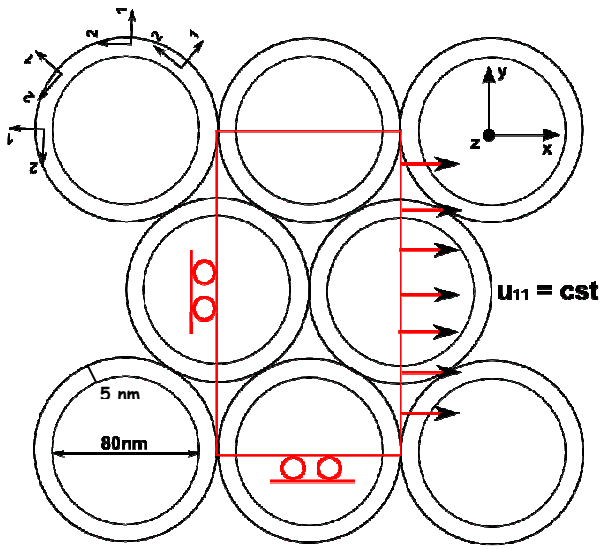

Fig. 7.5 Representative volume element (RVE) used to create a particle array.

The same data as in section 7.1.1 were used for calculations and neat matrix was placed in the particle interstices. The laponite anisotropy was not taken into account. Results for deformation (1 %) in the *x* and *y* direction are shown in Fig. 7.6. In this case the stress again concentrates in the laponite platelets oriented in the direction of the applied deformation while the stress in the matrix remains low.

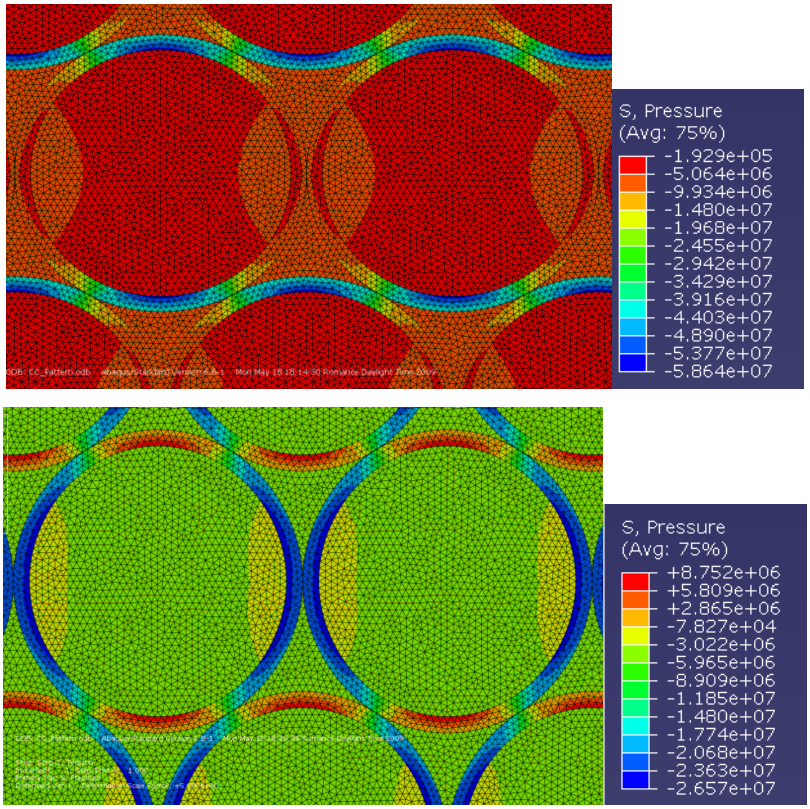

Fig. 7.6 Effects of 1% deformation on a latex particle array. The deformation is applied in horizontal direction in the upper image and in the vertical direction in the lower image.

The observed morphology of the PS/laponite nanocomposites provided the basis for further refinement of the model geometry. The RVE was modified by introducing a hexagonal particle array with both a continuous and discontinuous laponite shell as shown in Fig 7.7. In the case of the continuous array, the same materials properties were used as previously for the isotropic and anisotropic cases. For the discontinuous case, the laponite volume fraction in the aggregates (0.71 considering a 9.88 nm thick aggregate with 7 laponite layers) rather than in the laponite shell was considered. This led to the following input parameters (see section 7.1.1):

- $E_{11}=E_{22}$ = 93 GPa
- E_{33} = *11* GPa
- G_{12} = 1.9 GPa
- $G_{23}=G_{13}$ = 28 GPa
- v_{12} = 0.20

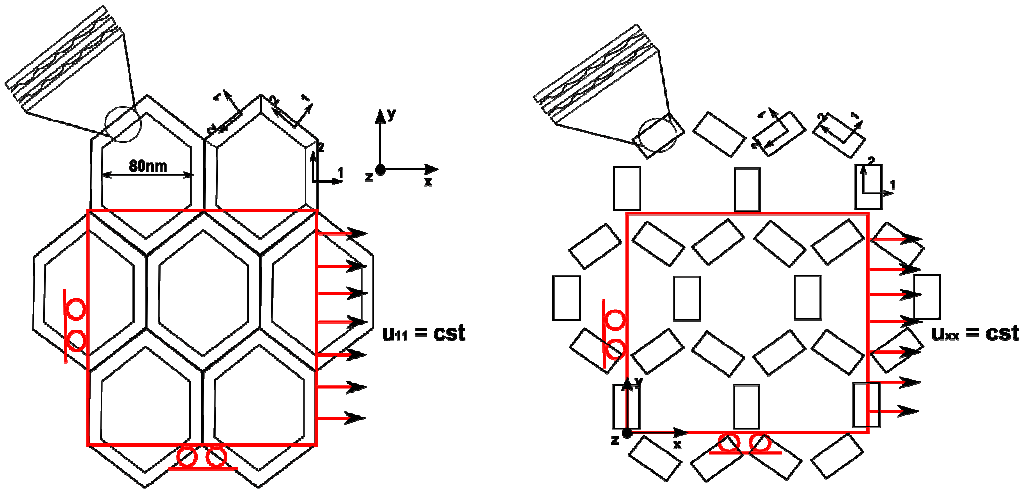

Fig. 7.7 Continuous and discontinuous hexagonal array used for FEM calculations.

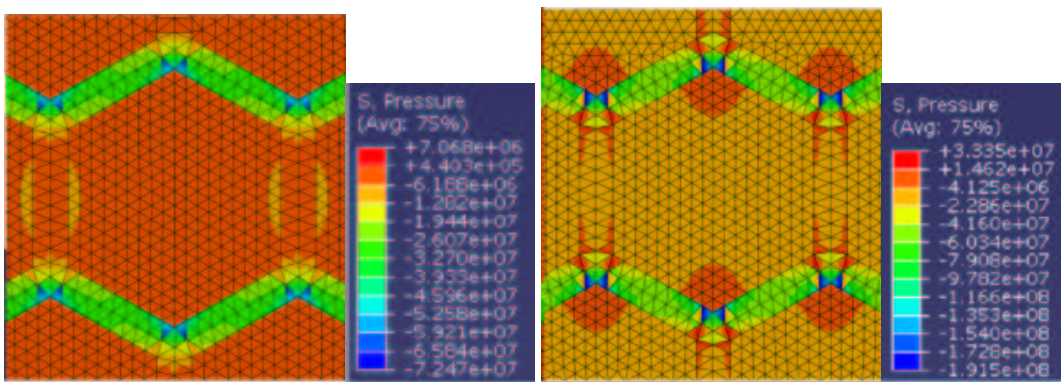

Fig. 7.8 Results of FE calculations for hydrostatic pressure for the isotropic (left) and anisotropic (right) cases after 1% deformation in the horizontal direction for the continuous laponite structure.

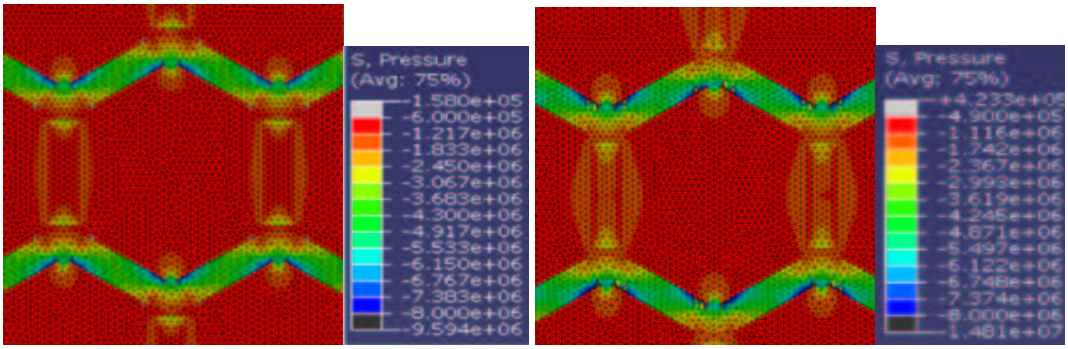

Fig. 7.9 Results of FEM calculations for hydrostatic pressure for the isotropic (left) and anisotropic (right) cases after 1% deformation in the horizontal direction for the discontinuous laponite structure.

In the isotropic case the input properties were calculated as described for the single particle model. The results for 1 % deformation in the horizontal direction for the two different structures are given in Figs. 7.8 - 7.9. Again, the stress concentrates mainly in the laponite aggregates oriented in the direction of the applied deformation, while the vertical aggregates show similar stresses to the matrix. Qualitatively very similar results were obtained when the deformation was applied in the vertical direction for the same arrays as shown in Fig. 7.10 and 7.11.

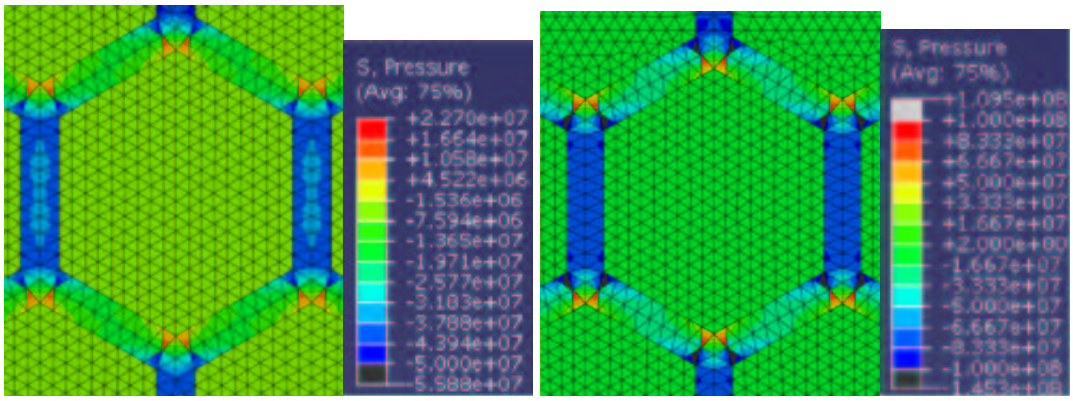

Fig. 7.10 Results of FEM calculations for hydrostatic pressure for the isotropic (left) and anisotropic (right) cases after 1 % deformation in the vertical direction for the continuous laponite structure.

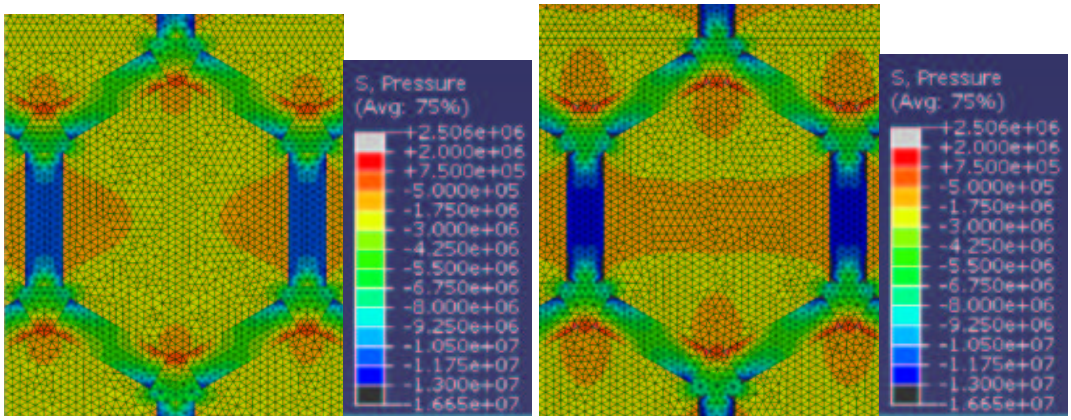

7.11 Results of FEM calculations for hydrostatic pressure for the isotropic (left) and anisotropic (right) cases after 1 % deformation in the vertical direction for the discontinuous laponite structure.

7.1.3 Discussion

Comparison of the above results suggests that the local stress levels in individual elements depends strongly on the particular geometry chosen for the calculations, but that the overall stress fields remain similar for a given applied deformation. The anisotropy of the laponite aggregates does not appear to play an important role, so that in a first approximation it is sufficient to consider the longitudinal tensile properties. This confirms the low strain mechanical response of closed cell foams (or open cell foams filled with a liquid) to be largely dominated by tensile deformation of the cell walls as assumed in chapter 2.

All the above simulations were carried out taking the nanocomposite to be at room temperature. FE simulations at 95 °C, i.e. just below the PS matrix glass transition temperature, were also performed. Similar stress fields were observed as at room temperature with a slight decrease in hydrostatic pressure, presumably due to the decrease in matrix tensile modulus from 1.5 to 0.5 GPa on raising T to 95 °C. This implied the deformation mechanisms to remain essentially unchanged, confirming the results of the thin film deformation experiments (section 6.2.1).

The FEM results suggest the stress to be concentrated mainly in the laponite platelets rather than in the matrix, where the hydrostatic pressure is relatively uniform. This means that, assuming the interfaces and the laponite aggregates to remain intact, cavitation could initiate anywhere in the matrix. However when considering a 3D sample, shear deformation effects may be important so that not only the hydrostatic pressure but also the stress field gradient must be

taken into account. In this case cavitation could initiate at the laponite/matrix interface where the stress gradient is high.

7.2 FEM calculation of the stiffness of PS/laponite nanocomposites

The aim of these calculations was to estimate the tensile modulus of the PS/laponite nanocomposites in the glassy and rubbery state for comparison with the experimental data. As already pointed out in Chapter 4, models that do not include the presence of an immobilized matrix fraction are unable to explain the extent of reinforcement in the rubbery state of the PS nanocomposites. The interphase thickness and properties are therefore incorporated as empirical parameters in the models and the possibility of a partially immobilized matrix layer between laponite aggregates is also considered, with the aim of establishing the importance of connectivity in the cellular structures formed by the latex-based nanocomposites.

7.2.1 Composite homogenization

As reviewed by Galli, materials property modeling approaches can be divided into two main groups [2]. The first includes methods that describe the material microstructure statistically (mean field or variational methods). The second includes methods that are based on modeling of a discrete portion of the material. Increases in computer computational power in recent years allowed the development of models of this latter type for both the linear and non-linear behavior of heterogeneous materials. Two different strategies for design of the representative volume element (RVE) have been considered. The materials morphology may be obtained directly from an experimental image onto which a mesh is superposed [3, 4] or it may take a more idealized form if some degree of periodicity or symmetry may be assumed [5]. In the present section, the latter approach was chosen, in order to simplify the calculations. As in the case of the stress field studies presented in the previous section, the simulations are two-dimensional. This is a limitation, because as reported by Galli, plane stress models generally tend to underestimate material properties [2]. However three dimensional modeling still remains relatively challenging and was beyond the scope of this work.

The methodology used to estimate the tensile modulus of the PS/laponite nanocomposites is based on the homogenization technique [6]. First some simplifications to the

problem are introduced. Under plane stress conditions the Hooke's law (eq. 7.4) can be rewritten as

$$\begin{bmatrix}\sigma_{11}\\ \sigma_{22}\\ \sigma_{12}\end{bmatrix}=\begin{bmatrix}C_{11} & C_{12} & C_{13}\\ C_{21} & C_{22} & C_{23}\\ C_{31} & C_{32} & C_{33}\end{bmatrix}\begin{bmatrix}\varepsilon_{11}\\ \varepsilon_{22}\\ \varepsilon_{12}\end{bmatrix} \qquad \text{eq. 7.8}$$

considering that $\sigma_{33} = \sigma_{23} = \sigma_{13} = 0$ and using the matrix notation [7]. From the macroscopic point of view the PS/laponite nanocomposites are isotropic materials. This simplifies the form of the stiffness tensor as follows

$$\begin{bmatrix}\sigma_{11}\\ \sigma_{22}\\ \sigma_{12}\end{bmatrix}=\begin{bmatrix}C_{11} & C_{12} & 0\\ C_{12} & C_{11} & 0\\ 0 & 0 & C_{33}\end{bmatrix}\begin{bmatrix}\varepsilon_{11}\\ \varepsilon_{22}\\ \varepsilon_{12}\end{bmatrix}=\frac{E}{1-\nu^2}\begin{bmatrix}1 & \nu & 0\\ \nu & 1 & 0\\ 0 & 0 & 1-\nu\end{bmatrix}\begin{bmatrix}\varepsilon_{11}\\ \varepsilon_{22}\\ \varepsilon_{12}\end{bmatrix} \qquad \text{eq. 7.9}$$

The stiffness tensor is now symmetric with only three components C_{ij}, which are directly related to the Young's modulus E and the Poisson's ratio ν. In the homogenization method an average stress tensor $\langle\sigma_{ij}\rangle$ and strain tensor $\langle\varepsilon_{ij}\rangle$ are calculated from the following equations

$$\left\langle\sigma_{ij}\right\rangle=\frac{1}{\Omega}\int_{\Omega}\sigma_{ij}(x)d\Omega \qquad \left\langle\varepsilon_{ij}\right\rangle=\frac{1}{\Omega}\int_{\Omega}\varepsilon_{ij}(x)d\Omega \qquad \text{eq. 7.10}$$

where Ω is the volume of the considered region and $\sigma_{ij}(x)$ and $\varepsilon_{ij}(x)$ are the local stress and strain fields. In practice, the material is divided into distinct volume elements and the stress components in each volume element are summed.

Under plane stress conditions and for a finite element mesh of k elements, the stress may be written as

$$\left\langle\sigma_{ij}\right\rangle=\frac{1}{A}\sum_{k}\sigma_{ij,k}A_k=\frac{1}{L}\sum_{k}F_{ij,k} \qquad \text{eq. 7.11}$$

where A is the total area considered, A_k is the area of the k-th element, and $F_{ij,k}$ is the reation force in the nodes over a contour length L. An analogous equation maybe written for the strain $\langle\varepsilon_{ij}\rangle$. With eq. 7.9 and 7.11, this leads to

$$\begin{bmatrix}\left\langle\sigma_{11}\right\rangle\\ \left\langle\sigma_{22}\right\rangle\\ \left\langle\sigma_{12}\right\rangle\end{bmatrix}=\begin{bmatrix}C_{11} & C_{12} & 0\\ C_{12} & C_{11} & 0\\ 0 & 0 & C_{33}\end{bmatrix}\begin{bmatrix}\left\langle\varepsilon_{11}\right\rangle\\ \left\langle\varepsilon_{22}\right\rangle\\ \left\langle\varepsilon_{12}\right\rangle\end{bmatrix} \qquad \text{eq. 7.12}$$

Eq. 7.12 allows the calculation of the stiffness tensor components C_{ij} from a finite element model by applying a certain strain and calculating the stress components from eq. 7.11.

7.2.2 Particle geometry refinement and choice of the RVE

In the simulations described previously only the diameter of the latex particles (80 nm) and the thickness of the laponite shell corresponding to 20 wt% of laponite loading (about 10 nm, considering neighboring particles) have been considered, since the aim was to provide a qualitative indication of the behavior of the PS/laponite nanocomposites. When effective properties of such materials are required, it is convenient to respect the overall laponite content and to adapt the geometrical parameters of the system to give the correct laponite loading. A RVE that has the correct laponite weight fraction (20 wt %) has been constructed. The hexagonal geometry used above was maintained. The size of the hexagonal particles and the thickness of the laponite aggregates are adjusted in order to maintain the overall laponite content. Only the length of the laponite platelets (54 nm) was kept constant. The laponite shell was considered to be discontinuous and triangular matrix elements were inserted at the hexagon corners (see Fig. 7.12).

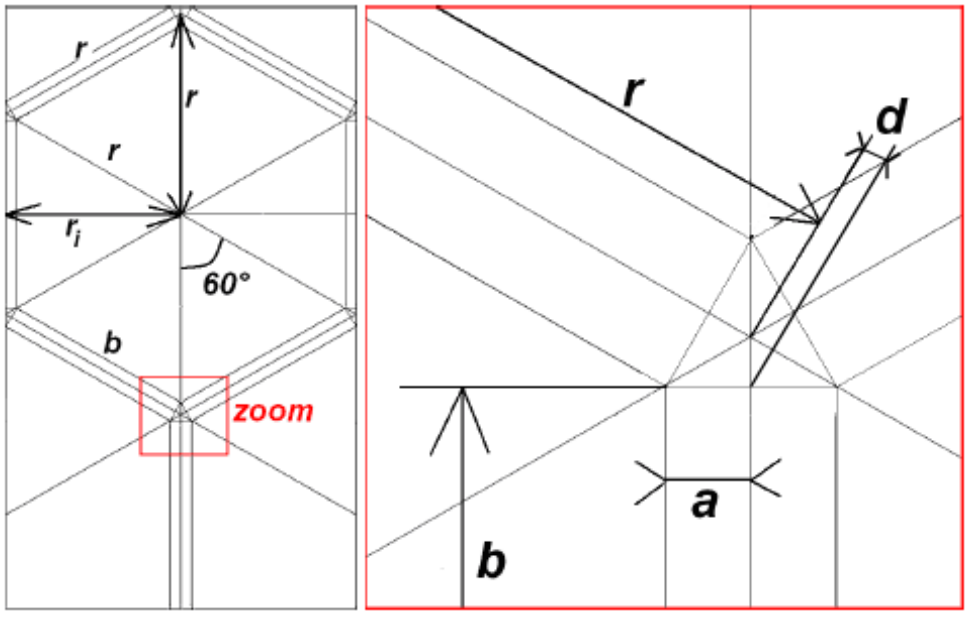

Fig. 7.12 RVE used for calculations. On the right side a zoom of the hexagon corner zone containing a triangle of matrix is shown.

The hypotheses on which the design of the RVE was based are as follows:

- the RVE geometry is hexagonal and represents the smallest unit cell for the material
- the laponite aggregates are only present in the contour of the hexagons
- the RVE must contain 20 wt% of laponite and 80 wt% of matrix and the intercalated matrix must be taken into account

- the length of the platelets is fixed (54 nm) but the thickness may vary with respect to the values obtained by TEM reported in section 4.1.6.1
- the laponite aggregates have all the same dimensions and are separated by matrix zones whose properties must be calculated
- an interphase can be considered at the aggregate surfaces; its thickness may be adjusted.

The design of the RVE was based on the following calculations. If the length of the sides of the hexagonal cell is *r*, the RVE area is (Fig. 7.12)

$$A_{RVE} = 3r2r_i \quad \text{with} \quad r_i = \frac{\sqrt{3}}{2}r \qquad \text{eq. 7.13}$$

Taking the length of the laponite aggregate *b* = 54 nm and the width of the laponite aggregate *2a*, the total area occupied by the aggregates in the RVE is

$$A_{aggr} = 5x2ab + 2ab = 12ab \qquad \text{eq. 7.14}$$

The distance *d* between the ends of the laponite aggregate and the centres of the matrix element at the hexagon corners is (Fig. 7.12)

$$d = a\frac{\sqrt{3}}{3} \qquad \text{eq. 7.15}$$

so that *r = 2d + b*

In the real nanocomposites, a laponite weight fraction of 0.2 corresponds to a volume fraction of 0.09, taking the density of PS to be 1 g/cm^3 and the density of laponite to be 2.53 g/cm^3. Here a 2D structure is considered, so 0.09 will be the area fraction of the laponite. The area fraction of the laponite in the aggregates is

$$\Phi_{lap,aggr} = \frac{0.09A_{RVE}}{A_{aggr}} \qquad \text{eq. 7.16}$$

If 2n is the number of laponite platelets in one aggregate, the area fraction of laponite in the aggregates may also be written as

$$\Phi_{lap,aggr} = \frac{2nt}{2nt + (2n-1)t_m} \qquad \text{eq. 7.17}$$

where *t* is the thickness of a single laponite platelet (1 nm) and t_m is the thickness of the intercalated matrix (0.48 nm). The following equation may also be used to relate the half width of the laponite aggregate *a* to the number of laponite platelets in one aggregate *2n*

$$a = nt_l + (n-0.5)t_m \qquad \text{eq. 7.18}$$

Substituting eq. 7.17 into eq. 7.16 and considering eq. 7.18, a linear system of equations with two unknown parameters (*a, n*) is obtained, which may be solved numerically. The results of the calculations are

n = 2.41

a = 3.33 nm

d = 1.92 nm

r = 57.84 nm

r_i = 50 nm

7.2.3 Implementation of boundary conditions

The RVE is designed such that an infinite material may be generated by its replication. For this purpose, boundary conditions must be imposed onto the RVE. Replication by translation in the x and y directions means that in principle a number of boundary conditions equal to the number of mesh nodes at the RVE boundaries is required. This somewhat tedious process can be avoided by imposing symmetry conditions onto the RVE boundaries [6]. The following displacement field for the periodic structure has been used

$$u_i(x,y) = \varepsilon_{ij}^0 x_j + u_i^*(x,y) \qquad \text{eq. 7.19}$$

where ε_{ij}^o is the global strain tensor and the first term on the right-hand side is a linear displacement field. The second term on the right-hand side, u_i^*, represents a modification of the displacement field due to the heterogeneous materials structure and has the same periodicity as the RVE. The displacement field of eq. 7.19 meets the requirement of continuity at the boundaries. The other condition to be met is that the tractions at opposite parallel boundaries of the RVE must be equal. If A^+ and A^- represent a pair of opposite boundary surfaces of the RVE, the displacements at these surfaces are

$$u_i^{A+} = \varepsilon_{ij}^0 x_j^{A+} + u_i^* \quad \text{and} \quad u_i^{A-} = \varepsilon_{ij}^0 x_j^{A-} + u_i^* \qquad \text{eq. 7.20}$$

for a given u_i^*. The difference between the above equations gives

$$u_i^{A+} - u_i^{A-} = \varepsilon_{ij}^0 (x_j^{A+} - x_j^{A-}) = \varepsilon_{ij}^0 \Delta x \qquad \text{eq. 7.21}$$

Since Δx is a constant for each pair of parallel boundary surfaces, the right side of this equation is also constant. Therefore instead of giving values of displacements for each node, the displacement between two opposite boundary surfaces is given. To implement these boundary conditions, the same mesh must be created for two coupled boundary surfaces.

In the simulations only tensile deformations were considered. This means that only two components of the stiffness tensor in eq. 7.9 need to be found: C_{11} and C_{12}. For their calculation all strain components except $\langle\varepsilon_{11}\rangle$ were set to zero so that $C_{11} = \langle\sigma_{11}\rangle/\langle\varepsilon_{11}\rangle$ and $C_{12} = \langle\sigma_{22}\rangle/\langle\varepsilon_{11}\rangle$. The symmetry of the stiffness tensor was checked by repeating the same operation with $\langle\varepsilon_{22}\rangle \neq 0$. The imposed strain was $\varepsilon = 0.5$ % for all calculations.

7.2.4 Results of FEM calculations

Several cases were considered:

1) simulation at room temperature with isotropic laponite aggregates and no interphase. The matrix elements in the hexagon corners are given the same properties as the rest of the matrix
2) simulation at room temperature with orthotropic laponite aggregates and no interphase. The matrix elements in the hexagon corners are given the same properties as the rest of the matrix
3) simulation at 160° with orthotropic laponite aggregates and no interphase. The matrix elements in the hexagon corners is been considered as partially immobilized with a tensile modulus of 10, 50 and 100 MPa
4) simulation at 160° with isotropic laponite aggregates with an interphase thickness 6 nm. The matrix elements in the hexagon corners is considered as partially immobilized with a tensile modulus of 100 MPa
5) simulation at 160° with orthotropic laponite aggregates with an interphase thickness of 2, 6 and 10 nm. The matrix elements in the hexagon corners are considered as partially immobilized with a tensile modulus of 100 MPa.

A further series of simulation was carried out in order to study the best choice of properties of the interphase and of the matrix elements in the hexagon corners to fit the experimental tensile modulus of 100 MPa, depending on the interphase thickness.

The input properties used for the calculations in case (2) were, for the laponite aggregates,

- $E_{11} = E_{22} = 93$ GPa
- $E_{33} = 11$ GPa
- $G_{12} = 1.9$ GPa
- $G_{23} = G_{13} = 28$ GPa
- $v_{12} = 0.20$

and for the matrix,

- tensile modulus E_m = 1.55 GPa
- Poisson's ratio v_0 = 0.33

The input properties for case (1) and (2) were obtained as discussed in section 7.1.1. For cases (3), (4) and (5), the properties of the laponite aggregates were taken to be the same as those at room temperature as suggested by the RAF analysis in Chapter 4 (section 4.1.5). The matrix was assumed in all cases to have a tensile modulus of 1 MPa and Poisson's ratio of 0.48 at 160 °C. The properties of the interphase and of the matrix elements in the hexagon corners were as described above.

Case	Results in [GPa] for $\begin{bmatrix} C_{11} & C_{12} \\ C_{21} & C_{22} \end{bmatrix}$
1	$\begin{bmatrix} 3.0 & 1.5 \\ 1.5 & 3.0 \end{bmatrix}$
2	$\begin{bmatrix} 2.7 & 1.3 \\ 1.3 & 2.7 \end{bmatrix}$
3	blocked matrix:10 MPa 50 MPa 100 MPa $\begin{bmatrix} 7.5 & 6.2 \\ 6.2 & 7.6 \end{bmatrix}*10^{-3}$ $\begin{bmatrix} 30.8 & 29.0 \\ 29.0 & 30.7 \end{bmatrix}*10^{-3}$ $\begin{bmatrix} 59.3 & 56.9 \\ 56.9 & 58.9 \end{bmatrix}*10^{-3}$
4	$\begin{bmatrix} 102.0 & 92.2 \\ 92.2 & 102.2 \end{bmatrix}*10^{-3}$
5	Interphase: 2 nm 6 nm 10 nm $\begin{bmatrix} 84.3 & 79.9 \\ 79.9 & 83.5 \end{bmatrix}*10^{-3}$ $\begin{bmatrix} 100.2 & 90.7 \\ 90.7 & 100.3 \end{bmatrix}*10^{-3}$ $\begin{bmatrix} 113.6 & 93.3 \\ 93.3 & 116.6 \end{bmatrix}*10^{-3}$

Table 14 Results of the FE calculations for the stiffness tensor components. All the results are in [GPa].

The results of the simulations are summarized in Table 14. A first remark is that the symmetry of the tensor is respected for all the calculations. In order to check whether the boundary conditions were correctly implemented, simulations were carried out on an extended pattern. In the simulations at room temperature (1) and (2), the results slightly overestimated the tensile modulus of the nanocomposites obtained experimentally (about 2 GPa). However the correct order of magnitude was obtained. The laponite aggregate anisotropy did not play an

important role at room temperature, the results for all the components of the stiffness tensor being similar. The results of simulations (3) showed that the presence of partially immobilized matrix elements between the laponite aggregates (hexagon corners) was not sufficient to account for the experimental data at 160 °C (experimental tensile modulus of 100 MPa). To obtain a reasonable fit, a modulus of 180 MPa was required for these elements. An interphase having the same properties of these elements has been considered on the laponite aggregate surface (case 5). The thickness was changed between 2 and 10 nm. These values were chosen because they are close to the route mean square end-to-end distance corresponding to the entanglement molar mass in PS (about 6 nm). In this case the experimental data were even exceeded.

A comparison between cases (4) and (5) with a 6 nm interphase thickness, shows that at high temperature the anisotropy of the laponite aggregates again did not play a significant role in the tensile properties. Fig. 7.13 shows the values of tensile modulus in the partially blocked matrix elements (hexagon corners and interphase) necessary to fit the experimental data as a function of interphase thickness. These values are higher than the 40 MPa found in section 4.1.6.4 but lower than the PS modulus in the glassy state.

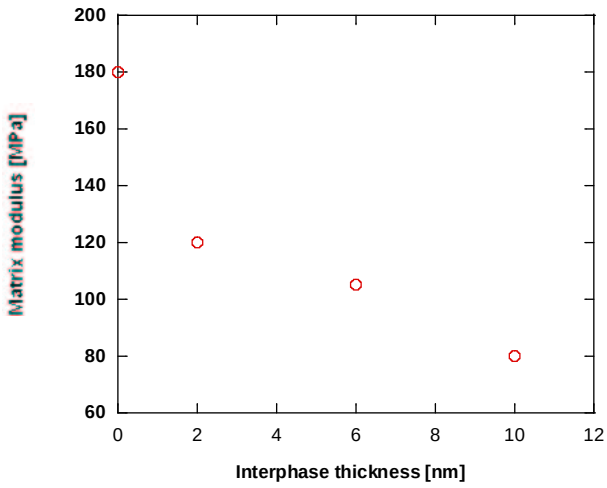

Fig. 7.13 Tensile modulus of the blocked matrix portion necessary to fit the experimental results as a function of interphase thickness.

7.3 Conclusions

In section 7.1 the results of a stress field analysis were presented for several material morphologies, going from a single latex particle embedded in the composite to particle arrays with different geometries. All the simulations provided the same qualitative results. The stress

concentrated mainly in the laponite platelets aligned in the direction of the applied tension and the laponite aggregate anisotropy was found to play a minor role in the global response, the transverse tensile response being similar to that of the PS matrix. The stress was relatively constant in the matrix so that, if the cavitation observed in Chapter 6 is associated with the matrix as opposed to interface failure or failure of the aggregates, it may occur anywhere. The results of FEM calculations were confirmed also by analytical results for the single particle case.

The simulations of PS nanocomposite stiffness confirmed the need to include partially immobilized matrix elements. From these results it may be concluded that not only the interphase at the laponite surface, but also the matrix elements that are constrained between the laponite aggregates must be taken into account. For the RVE geometry considered here, the partially immobilized matrix elements must have a tensile modulus in the range 100-200 MPa for interphase thicknesses not exceeding few nanometers. These values compare well with the results obtained from the *ad hoc* modified classical micromechanical models presented in Chapter 4.

7.4 Bibliography

[1] J.-M. Bethelot in: *Matériaux Composites,* Tec & Doc editors 1999 Paris, p.131

[2] M. Galli, EPFL Ph.D. Thesis n° 3869 (2007)

[3] A. Borbely, H. Biermann, and O. Hartmann. *FE investigation of the effect of particle distribution on the uniaxial stress-strain behaviour of particulate reinforced metal matrix composites.* Mat. Sci. Eng. Part A, **313** (2001) 34

[4] N. Chawla, X. Deng, and D.R.M. Schnell. *Thermal expansion anisotropy in extruded SiC particle reinforced 2080 aluminum alloy matrix composites. .* Mat. Sci. Eng. Part A, **426** (2006) 314

[5] H. D. Espinosa and P. D. Zavattieri. *A grain level model for the study of failure initiation and evolution in polycrystalline brittle materials. Part I: Theory and numerical implementation.* Mech. Mat., **35** (2003) 333

[6] H. Berger, S. Kurukuri, S. Kari, U. Gabbert, R. Rodriguez-Ramos, J. Bravo-Castillero, R. Guinovart-Diaz, *Numerical and analytical approaches for calculating the effective thermo-mechanical properties of a three-phase composite.* Journ. Therm. Stress **30** (2007) 801

[7] J.-M. Bethelot in: *Matériaux Composites,* Tec & Doc editors 1999 Paris, p. 121

Chapter 8

Conclusions and future work

This chapter summarises the main conclusions of this thesis. In section 8.1, the advantages and the limitations of water-based synthetic techniques for preparing styrenic and acrylic polymer/laponite (or MMT) nanocomposites are discussed. Particular attention is given to a comparison of results from conventional emulsion and miniemulsion polymerization, and a critical assessment is made of the current state of the art with regard to this latter technique and its applicability to the preparation of polymer/clay nanocomposites. In section 8.2, the results of the investigation of stiffness reinforcement by a percolating network of laponite-rich domains are reviewed, with emphasis on the effects of polymer chain confinement. In section 8.3, the influence of laponite on microdeformation mechanisms in the styrenic nanocomposites is considered in the light of their large strain macroscopic mechanical response. Section 8.4 describes the results of FE simulations of the distribution of hydrostatic stresses in the nanocomposites, and the role of the interphase on the tensile modulus in the rubbery state. Finally, section 8.5 is devoted to the wider implications of the present work and the perspectives for the development of latex-based nanocomposites in a range of applications.

8.1 Emulsion and miniemulsion polymerization for the preparation of polymer/laponite nanocomposites

The first goal of this thesis was to study the potential of latex-based techniques for the preparation of well-dispersed polymer/laponite nanocomposites with a wide range of laponite loadings. Emulsion polymerization was shown to provide improved control of the final morphology

and to overcome the processing problems associated with conventional preparation techniques, such as melt blending or in-situ polymerization, at high clay loadings. Functionalization of the laponite platelets allowed the preparation of “armoured” styrenic or acrylic latex particles in which the platelets formed a more or less continuous shell around a polymer-rich core. This resulted in a well-defined cellular arrangement of laponite rich domains in consolidated films obtained on drying. Extensive aggregation was avoided by swelling the laponite in water prior to the polymerization reaction. Whilst excellent laponite dispersions could be obtained for loadings of up to 5 to 7 wt %, some aggregation was observed at higher laponite contents. However, even at 50 wt % laponite, the average aggregate thickness was limited to about 10 nm, which is a remarkable result. Prior to the present work, effective morphological control at comparable maximum clay contents has only been achieved by layer-by-layer deposition, which remains difficult to extend to large scale applications [1,2]. Moreover, full monomer conversion was achieved after 3 to 4 hours in all syntheses at the laboratory scale, so that the requirements of the Napoleon project for VOC compound emissions were fully respected. This is an important result, in so far as the elimination of VOCs will be a compulsory requirement for the commercial development of dispersion-based products from 2010, as discussed in Chapter 1.

Miniemulsion polymerization is currently at a much earlier stage of development for polymer/clay nanocomposites than conventional emulsion polymerization, which has already been extensively optimized. Miniemulsion-based styrenic/laponite latexes with the armoured morphology, and latexes in which the laponite was encapsulated were provided for study, but in either case, poor laponite dispersion was observed in the matrix and there were consequently only limited improvements in mechanical properties. In the case of the latexes containing encapsulated laponite this was attributed to poor partitioning of the laponite platelets among the particles, about 75 % of the particles being free of laponite. However, the results of this preliminary investigation resulted in increased focus by the Napoleon consortium partners on improving the latex synthesis and significant advances have recently been achieved, as discussed in detail elsewhere [3, 4]. Although only a limited range of laponite contents were considered (up to 10 wt %), acrylic materials with the armoured morphology obtained by miniemulsion polymerization showed similar properties to the analogous materials obtained by conventional emulsion polymerization [4]. However the monomer conversion remains too low (about 80 %) to satisfy the VOC requirements referred to above [3], and the complex relationship between the laponite, monomer conversion, particle nucleation and stability of the final dispersion is still poorly understood, placing considerable limitations on the further development of miniemulsion polymerization for the preparation of polymer/laponite nanocomposites in the

immediate future. For this reason, the present thesis has focused on results obtained using conventional emulsion polymerization.

8.2 Small strain mechanical response

A major part of the thesis has been devoted to the investigation of the influence of the clay content on the small strain tensile response and the role of chain immobilization in the matrix interphase present at the clay surface. As discussed in Chapters 4 and 5 for both styrenics and acrylics, the emulsion-based nanocomposites showed two distinct regimes of reinforcement. Relatively small increases in Young's modulus were observed in the glassy state, and in the case of the styrenics, the degree of laponite dispersion was found to be an important parameter, specimens containing 5 to 7 wt % laponite showing higher moduli than at somewhat higher laponite contents, where the degree of aggregation was also greater, consistent with the predictions of simple micromechanical models.

In the rubbery state, on the other hand, depending on the loading, increases in Young's modulus by more than 2 orders of magnitude were obtained in the nanocomposites containing a cellular arrangement of the laponite, and it was impossible to account for these in terms of classical micromechanical models. It was also demonstrated that a proportion of the matrix, which corresponded well to that intercalated in the laponite stacks, did not undergo a glass to rubber transition at the glass transition temperature of the unmodified matrix, presumably because of strong physical confinement between the laponite platelets. This suggested that the matrix present in the cell walls could undergo total or partial immobilization, as is often invoked, albeit qualitatively, in order to explain property changes in a variety of nanocomposite materials, as discussed in section 2.4.1. The experimental data for the Young's modulus in the rubbery state at high laponite contents were therefore modelled assuming a filled foam structure, in which the matrix modulus in the (laponite-rich) cell walls was treated as an adjustable parameter. The results indicated an average tensile modulus some two to three orders of magnitude higher than for the unconstrained matrix in the rubbery state, depending on the details of the model, although significantly lower than the glassy modulus. At low laponite contents, the overall Young's moduli were closer to the predictions of the classical micromechanical models used to model the glassy response, which follows from the absence of a well-defined cellular structure under these conditions. The importance of the cellular arrangement of the laponite was confirmed by experiments in which this structure was broken up by pre-deformation in plane strain

compression, leading to significant decreases in the Young's modulus, or in which the laponite was initially randomly dispersed within the matrix.

8.3 Large deformations and microdeformation mechanisms

Another important goal of this thesis was to investigate how the laponite influences the microdeformation mechanisms of the matrix and how this is related to the morphology. It was also of interest to compare the results with results obtained for isotactic polypropylene-based montmorillonite clay nanocomposites prepared by conventional melt blending, which have already been the subject of extensive investigations within the institute. In the styrenics, the tensile strength at room temperature increased slightly at laponite contents up to about 5 wt %, but then decreased strongly with further increases in laponite concentration as the laponite started to aggregate and/or the cellular arrangement became better defined. This was linked to a decrease in the microscopic matrix drawability at high laponite contents, as observed by TEM, accompanied by coarse cavitation on a scale comparable with that of the original latex particles, which replaced crazing as the dominant deformation mechanism. At the highest laponite loadings (50 wt %), there was little ductility at the microscopic scale, the crack paths clearly following the particle boundaries, suggesting failure of laponite particle interfaces to be responsible for the very fragile macroscopic behaviour under these conditions. These trends were confirmed by inspection of bulk tensile sample fracture surfaces, with clear evidence of coarse voiding and fibrillation at 20 wt% laponite, for example. Localized deformation zones were also observed by TEM in the presence of the laponite even at temperatures above the glass transition temperature, where the unmodified matrix deformed homogeneously, suggesting the network of laponite aggregates/immobilized matrix, assumed to be responsible for the large stiffness increases in the rubbery state, to continue to show yielding behaviour.

Somewhat contrasting behaviour was observed in the polypropylene/montmorillonite nanocomposites, in that the MMT/matrix interface was found to be critical even at low loadings, indicating the importance of MMT platelet functionalization for reducing interfacial failure. Thus, whereas ductile deformation was observed in the neat polypropylene matrix, in the nanocomposites the dominant microdeformation was cavitation within, or at the interfaces of the MMT aggregates with the matrix, and, as with the styrenics, above a threshold of about 3 to 4 wt %, the MMT became detrimental to the tensile strength. The tensile properties were in this case also dependent on the orientation of the MMT introduced by the extruder used to prepare the test

specimens, with improved properties generally being observed when the deformation axis coincided with the orientation direction of the MMT.

These results, which are among the first detailed observations of microdeformation in this class of materials, clearly demonstrate the importance of parameters such the clay functionalization and preparation technique for the local, and hence the macroscopic materials response, and suggest fundamental limitations on the mechanical performance at high clay loadings for the present technology.

8.4 FEM results for microdeformation experiments and tensile modulus calculations

FE calculations were carried out in order to analyze in more detail the results of the microdeformation experiments on (i) the cellular styrenic/laponite nanocomposites in the glassy state and (ii) their tensile properties in the rubbery state. In the first instance, the hydrostatic stress field in thin films deformed under tension was investigated. Several two-dimensional geometries were considered, i.e. single latex particles and latex particle arrays with different geometries. It was found that only the laponite aggregates aligned with the direction of the deformation axis were highly load bearing, while the remaining aggregates showed similar stress levels to the matrix up to temperatures just below the glass transition temperature. The anisotropy of the laponite aggregates was also found to have little influence. Thus, although the stress concentrated in the aggregates, assuming these to remain stable during the microdeformation experiments, cavitation could be assumed to initiate anywhere within the matrix, in which the hydrostatic pressure was relatively uniform, consistent with the previous interpretation of the microdeformation behaviour at intermediate laponite contents.

Further simulations were carried out in order to model the Young's modulus of the nanocomposite in the rubbery state. It was again shown that to obtain results consistent with the experimental data, it was necessary to assume complete matrix immobilization in the intercalated structure of the laponite and partial immobilization in an interphase at a length scale similar to the entanglement distance. The fitted tensile modulus for this partially immobilized interphase was found to be consistent with the results of the micromechanical models referred to in section 8.2.

FEM could hence be used to confirm the hypotheses implicit in the models for the Young's moduli of the cellular nanocomposites in the rubbery state and provided further insight

into the stress distributions associated with microdeformation and failure in tensile tests at room temperature.

8.5 Overall conclusions and suggestions for future work

This work has shown that conventional emulsion polymerization can provide significantly enhanced control of the morphology of polymer/clay nanocomposites. Moreover the overall clay content can be increased to values that are usually impossible to achieve with conventional techniques. Most importantly, from a fundamental point of view, it has been possible to demonstrate and quantify a true "nano" effect, related to chain confinement, consistent with the general idea that a good degree of dispersion is necessary for obtaining the greatest property improvements. Regarding possible direct developments of the present work, it would clearly be of interest to improve the encapsulation techniques referred to in the context of miniemulsion polymerization, since this should eventually allow fabrication of nanocomposites with almost fully exfoliated clay platelets and a very high degree of dispersion. The mechanical response of such materials would be expected to contrast with that of the armoured latexes, in which the clay is concentrated at the original particle interfaces.

Concerning possible applications, as suggested by the Napoleon consortium, commercial development of clay/polymer nanocomposites in the form of latex dispersions will only be possible if the solids content can be increased from the actual values of about 20 % to at least 40 % by weight. The film formability will also need to be improved in the presence of relatively large amounts of clay. At present, even with a low T_g polymer, when the clay content is above 10 wt %, film formation requires an external pressure, which is clearly impractical for applications.

The potential applications of the armoured latex morphology are not restricted to the field of coatings (e.g. for improved mechanical properties at high temperature and improved barrier properties). It has been reported that carbon nanotubes/polymer nanocomposites with the nanotubes dispersed in water in a latex dispersion show very high electrical conductivity at very low weight contents (0.04-0.07 %) because of the excluded volume effect of the latex particles [5-8]. This could provide electrical properties comparable with those of carbon black composites, but without compromising polymer processability, since the filler content remains very low. Another field of possible application is the preparation of polymer foams reinforced with nanoparticles in the cell walls. The emulsion-based techniques are flexible enough to provide foams with different cell sizes and morphology [9]. Indeed, examples of foam preparation by high internal phase

emulsion (HIPE) have already been described in literature (see [10] for a review). Here water in oil systems are considered and the porosity of the material is provided by evaporating the water phase. In foams prepared from HIPEs, nanoparticles have been placed in the foam walls using the Pickering technique, in which the aqueous phase is stabilized by the same nanoparticles [11, 12]. Recently foam materials with nanoparticles in the cell walls have also been prepared from oil in water emulsions using ice templating techniques and sublimation [13]. The possible applications for these foam-based nanocomposites range from conducting foams, bone scaffold engineering, sensing and catalysis. Moreover, compression of foams containing very high densities of clay platelets in their cell walls could provide nacre-like structures with very high stiffnesses and strengths, comparable with those currently obtained with conventional carbon fibre-reinforced composites.

8.6 Bibliography

[1] P. Podsiadlo, A.K. Kaushik. E.M. Arruda, A.M. Waas, B.S. Shim, J. Xu. H. Nandivada, B.J. Pumplin, J. Lahann, A. Ramamoorthy, N.A. Kotov, *Ultrastrong and stiff layered polymer nanocomposites*. Science **318** (2007) 80

[2] P. Podsiadlo, A.K. Kaushik, B.S. Shim, A. Agarwal, Z. Tang, A.M. Waas, E.M. Arruda, N.A. Kotov, *Can nature's design be improved upon? High strength, transparent nacre-like nanocomposites with double network of sacrificial cross links*. Journ. Phys. Chem. Part B **112** (2008) 14359

[3] V. Mellon, Ph.D. Thesis Université Claude Bernard-Lyon 1 (2009)

[4] J. Faucheux, Ph.D. Thesis INSA Lyon (2008)

[5] J.C. Grunlan, A.R. Mehrabi, M.V. Bannon, J.L. Bahr, *Water-based single walled nanotube filled polymer composite with an exceptionally low percolation threshold.* Adv. Mat. **16** (2004) 150

[6] Z. Zhao, W. Zheng, W. Yu, B. Long, *Electrical conductivity of poly(vinylidene fluoride)/carbon nanotube composites with a spherical substructure.* Carbon **47** (2009) 2112

[7] M. Mu. A.M. Walker, J.M. Torkelson, K.I. Winey, *Cellular structures of carbon nanotubes in a polymer matrix improve properties relative to composites with dispersed structure.* Polymer **49** (2009) 1332

[8] R. Mezzenga, J. Ruokolainen, G.H. Fredrickson, E.J. Kramer, D.Moses, A.J. Heeger, O. Ikkala, *Templating organic semicondictuors via self-assembly of polymer colloids*, Science **299** (2003) 1872

[9] N.R. Cameron, *High internal phase emulsion templating as a route to well defined porous polymer.* Polymer **46** (2005) 1439

[10] C. Zhao, E. Danish, N.R. Cameron, R. Kataky, *Emulsion templated porous materials (polyHIPEs) for selective ion and molecular recognition and transport: application in electrochemical sensing.* Journ. Mat. Chem. **17** (2007) 2446

[11] B. P. Binks, *Macroporous silica from solid stabilized emulsion templates.* Adv. Mat. **14** (202) 1824

[12] P.J. Colver, S.A.F. Bon, *Cellular polymer monoliths made via Pickering high internal phase emulsions.* Chem. Mat. **19** (2007) 1537

[13] C.A.L. Colard, R.A. Cave, N. Grossiord, J.A. Covington, S.A.F. Bon, *Conducting nanocomposite polymer foams from ice-crystal templated assembly of mixtures of colloids.* Adv. Mat. **21** (2009) 2894

Appendix 1

Stress field determination for a single latex particle embedded in an infinite medium.

The analytical calculations of the stress field for a single latex particle embedded in an infinite medium with properties analogous to the composite were carried out using the work of Benveniste et al. for coated fibers [1]. In a 2D simulation the effect of tensile deformation $2\sigma^0$ on a circular particle with a hard shell can be obtained as a superposition of case (a) and (b) of Fig. 1

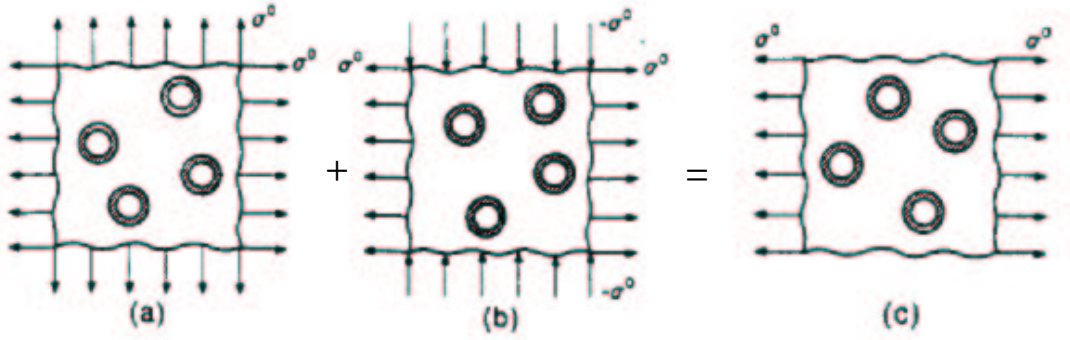

Fig.1 Simple tensile deformation (c) resulting from axisymmetric (a) and transverse shear deformation (b) of coated particle [1].

Let *a* to denote the outer radius of the latex particle and *b* the outer radius of the laponite shell. In what follows cylindrical coordinates (*r, θ*) are chosen because of the problem symmetry. Because the simulations are in 2D all the *z* components are taken equal to zero. The stress in each phase (the matrix *m*, the laponite shell *l* and the composite *c*) considered to be isotropic is expressed in the following way:

$$\sigma_s = \lambda_s (tr\varepsilon_s) + 2\mu_s \varepsilon_s \qquad \text{with } s = m, l, c \qquad \text{A.1}$$

where λ is the Lamé constant and μ is the shear modulus. Their values are calculated for each phase as follows:

$$\lambda_s = \frac{E_s \nu_s}{(1+\nu_s)(1-2\nu_s)} \qquad \mu_s = \frac{E_s}{2(1+\nu_s)} \qquad \text{with } s = m, l, c \qquad \text{A.2}$$

The tensile moduli are respectively E_m = 1.5 GPa, E_l = 14.5 GPa (from Halpin-Tsai in the laponite shell), E_c = 2 GPa. The Poisson's ratios are respectively ν_m = 0.33, ν_l = 0.28, ν_c = 0.31 obtained from a simple rule of mixture.

The two cases of Fig. 1 (a) and (b) will be solved separately in cylindrical coordinates. In the case of axisymmetric deformation (Fig. 1a) the displacements can be written as:

$$u_{m,r} = A_m r \quad , \quad u_{l,r} = A_l r + \frac{B_l}{r} \quad , \quad u_{c,r} = A_c r + \frac{B_c}{r} \qquad \text{A.3}$$

where A_m, A_l, B_l, A_c and B_c are constants to be determined.

The strains components can be written as:

$$\varepsilon_{s,rr} = \frac{\partial u_{s,r}}{\partial r} \quad , \quad \varepsilon_{s,\theta\theta} = \frac{u_{s,r}}{r} \quad , \quad tr\varepsilon_s = \varepsilon_{s,rr} + \varepsilon_{s,\theta\theta} \qquad \text{with } s = m, l, c \qquad \text{A.4}$$

and the stress components from A.1 are

$$\sigma_{s,rr} = \lambda_s tr\varepsilon_s + 2\mu_s \varepsilon_{s,rr} \quad , \quad \sigma_{s,\theta\theta} = \lambda_s tr\varepsilon_s + 2\mu_s \varepsilon_{s,\theta\theta} \qquad \text{with } s = m, l, c \qquad \text{A.5}$$

The above mentioned constants are obtained by imposing the following boundary conditions:

$$u_{m,r}(a) = u_{l,r}(a) \quad , \quad u_{l,r}(b) = u_{c,r}(b) \, , \quad \sigma_{m,rr}(a) = \sigma_{l,rr}(a) \, ,$$

$$, \sigma_{l,rr}(b) = \sigma_{c,rr}(b) \quad , \quad \sigma_{m,rr}(\infty) = \sigma_0 \qquad \text{A.6}$$

The solutions for the case in Fig. 1 (b) are obtained in a similar way. The displacements come from the work of Christensen and Lo [2]:

$$u_{m,r} = \frac{b\sigma_o}{4\mu_m}\left[A_1(\eta_m - 3)\left(\frac{r}{b}\right)^3 + D_1\left(\frac{r}{b}\right)\right]\cos 2\theta$$

$$u_{m,\theta} = \frac{b\sigma_o}{4\mu_m}\left[A_1(\eta_m + 3)\left(\frac{r}{b}\right)^3 - D_1\left(\frac{r}{b}\right)\right]\sin 2\theta$$

$$u_{l,r} = \frac{b\sigma_o}{4\mu_l}\left[A_2(\eta_l - 3)\left(\frac{r}{b}\right)^3 + D_2\left(\frac{r}{b}\right) + C_2(\eta_l + 1)\frac{b}{r} + B_2\left(\frac{b}{r}\right)^3\right]\cos 2\theta \qquad \text{A.7}$$

$$u_{l,\theta} = \frac{b\sigma_o}{4\mu_l}\left[A_2(\eta_l + 3)\left(\frac{r}{b}\right)^3 - D_2\left(\frac{r}{b}\right) - C_2(\eta_l - 1)\frac{b}{r} + B_2\left(\frac{b}{r}\right)^3\right]\sin 2\theta$$

$$u_{c,r} = \frac{b\sigma_o}{4\mu_c}\left[2\left(\frac{r}{b}\right) + A_3(\eta_c + 1)\frac{b}{r} + C_3\left(\frac{b}{r}\right)^3\right]\cos 2\theta$$

$$u_{c,\theta} = \frac{b\sigma_o}{4\mu_c}\left[-2\left(\frac{r}{b}\right) - A_3(\eta_c - 1)\frac{b}{r} + C_3\left(\frac{b}{r}\right)^3\right]\sin 2\theta$$

where A_1, A_2, A_3, B_2, C_2, C_3, D_1, D_2 are constants to be determined and $\eta_s = 3 - 4\nu_s$ with $s = m$, l, c. The strains components are defined as:

$$\varepsilon_{s,rr} = \frac{\partial u_{s,r}}{\partial r} \quad , \quad \varepsilon_{s,\theta\theta} = \frac{1}{r}\frac{\partial u_{s,\theta}}{\partial \theta} + \frac{u_{s,r}}{r} \quad , \quad \varepsilon_{s,r\theta} = \frac{1}{2}\left(\frac{\partial u_{s,\theta}}{\partial r} - \frac{u_{s,\theta}}{r} + \frac{1}{r}\frac{\partial u_{s,r}}{\partial \theta} \right),$$

$$tr\varepsilon_s = \varepsilon_{s,rr} + \varepsilon_{s,\theta\theta} \qquad \text{with } s = m, l, c \qquad \text{A.8}$$

and the stress components are:

$$\sigma_{s,rr} = \lambda_s tr\varepsilon_s + 2\mu_s \varepsilon_{s,rr} \quad , \quad \sigma_{s,\theta\theta} = \lambda_s tr\varepsilon_s + 2\mu_s \varepsilon_{s,\theta\theta} \quad ,$$

$$\sigma_{s,r\theta} = 2\mu_s \varepsilon_{s,r\theta} \qquad \text{with } s = m, l, c \qquad \text{A.9}$$

The above constants are obtained by imposing the following boundary conditions:

$$u_{m,r}(a) = u_{l,r}(a) \quad , \quad u_{m,\theta}(a) = u_{l,\theta}(a) \quad , \quad u_{l,r}(b) = u_{c,r}(b) \quad , \quad u_{l,\theta}(b) = u_{c,\theta}(b) \qquad \text{A.10}$$

$$\sigma_{m,rr}(a) = \sigma_{l,rr}(a) \quad , \quad \sigma_{m,r\theta}(a) = \sigma_{l,r\theta}(a) \quad , \quad \sigma_{l,rr}(b) = \sigma_{c,rr}(b) \quad , \quad \sigma_{l,r\theta}(b) = \sigma_{c,r\theta}(b)$$

The conversion from cylindrical to orthonormal reference system is carried out in both cases with the following transformations:

$$S = \begin{bmatrix} \sigma_{xx} & \sigma_{xy} \\ \sigma_{xy} & \sigma_{yy} \end{bmatrix} \qquad S' = \begin{bmatrix} \sigma_{rr} & \sigma_{r\theta} \\ \sigma_{r\theta} & \sigma_{\theta\theta} \end{bmatrix} \qquad R = \begin{bmatrix} \cos\theta & \sin\theta \\ -\sin\theta & \cos\theta \end{bmatrix} \qquad S = R^T S' R \qquad \text{A.11}$$

The stress components in the same direction are then summed for the cases of Fig. 1 (a) and (b) in order to get the total hydrostatic pressure $P = -(\sigma_{xx} + \sigma_{yy})/3$ as reported in Chapter 7.

Here are reported the results of analytical calculations of the hydrostatic pressure for the axisymmetric deformation (Fig. 2) and for the transverse shear deformation (Fig. 3). They are compared with the results of FE analysis to illustrate good agreement between them. The colour scale is approximatively the same for the images of analytical and FE hydrostatic pressure maps.

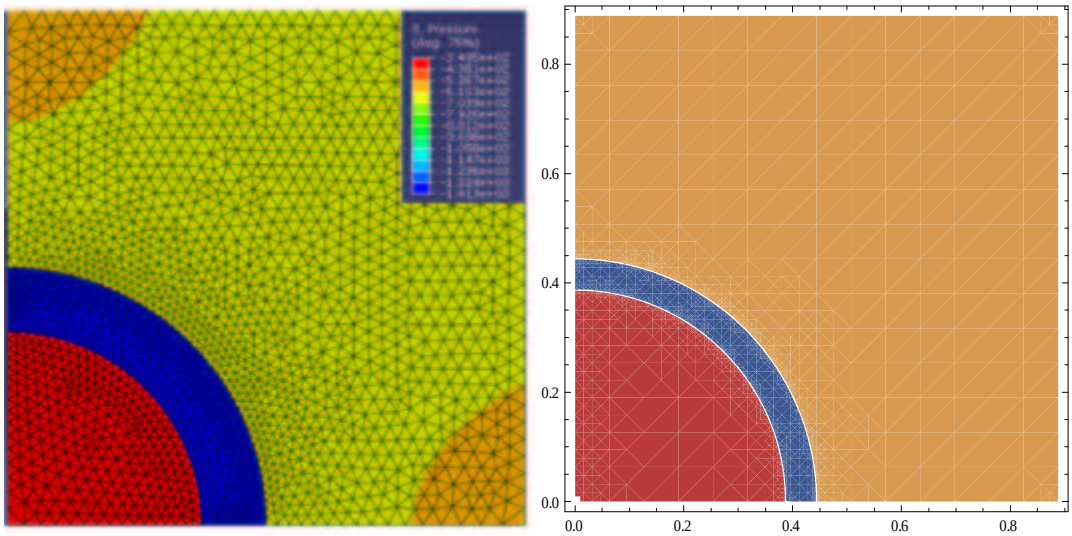

Fig. 2 Hydrostatic pressure for a single latex particle under axisymmetric deformation: FE calculations (left) and analytical calculations (right).

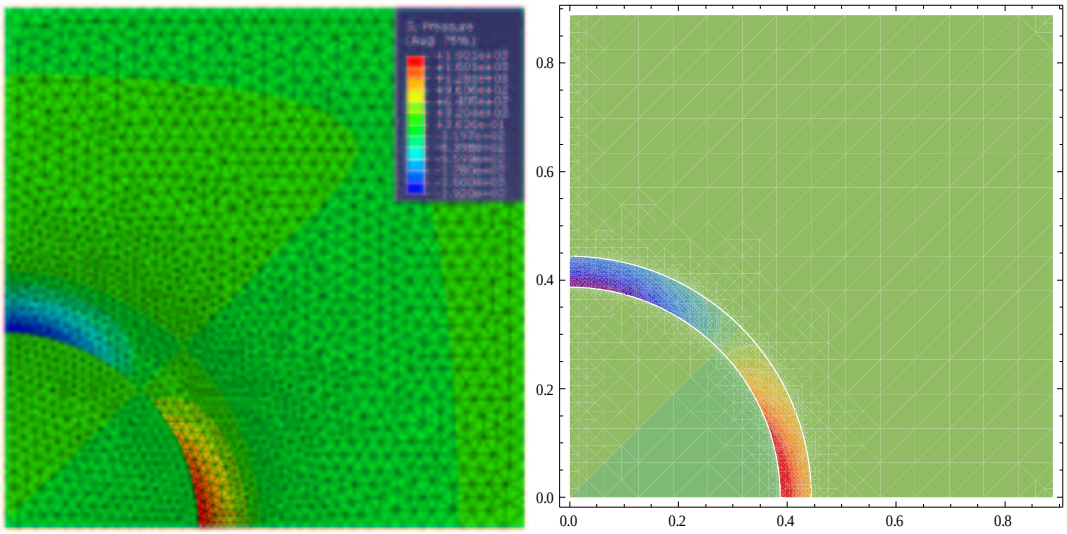

Fig. 3 Hydrostatic pressure for a single latex particle under transverse shear deformation: FE calculations (left) and analytical calculations (right).

[1] Y. Benveniste, G.J. Dvorak, T. Chen, *Stress fields in composites with coated inclusions.* Mech. Mat. **7** (1989) 305

[2] R.M. Christensen, K.H. Lo, *Solutions for effective shear properties in three phase sphere and cylinder models.* Journ. Mech. Phys. Sol. **27** (1979) 315

Appendix 2

Calculation of the number of laponite platelets per latex particle included in section 3.1.1

It is assumed a latex particle of 80 nm in diameter for all laponite contents and the laponite platelets to be discs of 54 nm in diameter and 1 nm in thickness. The density of PS is 1.05 g/cc and the density of laponite is 2.53 g/cc (the same value as montmorillonite).

The real amount of incorporated laponite obtained from ash tests is considered, respectively 4, 6, 8.5, 17, 28 and 44 wt % for L5, L7.5, L10, L20, L30 and L50. The amount of laponite in vol % is then:

$$vol\% = \frac{wt\%/2.53}{wt\%/2.53 + (1-wt\%)/1.05} \qquad \text{A.12}$$

This gives 0.017, 0.026, 0.037 0.078, 0.139 and 0.246 vol % for L5, L7.5, L10, L20, L30 and L50 respectively. The surface area for a single laponite platelet is $\pi(54/2)^2 = 2290$ nm^2 and the surface area of a latex particle is $4\pi(80/2)^2 = 2 * 10^4$ nm^2. The number of platelets that can be accommodated on a latex particle is $2 * 10^4/2290 \sim 9$.

The volume of a latex particle is $4\pi(80/2)^3/3 = 2.67 * 10^5$ nm^3 and the total laponite volume per latex particle is vol% * $2.67 * 10^5$ nm^3, i.e. $4.5 * 10^3$, $6.9 * 10^3$, $9.9 * 10^3$, $2.1 * 10^4$, $3.7 * 10^4$, $6.6 * 10^4$ nm^3 for L5, L7.5, L10, L20, L30 and L50 respectively.

The amount of laponite platelets per latex particle in the films must take into account also the neighbouring particles. This is given by the above results multiplied by a factor 2 and divided by the volume of a single laponite platelet (2290 nm^3). This calculation provides the results reported in section 3.1.1.

Appendix 3

Estimates of the intercalated matrix amount from geometrical calculations and XRD data reported in section 4.1.5.

The calculations are based on Fig.1 describing L50 nanocomposites having fully covered latex particles with a continuous laponite shell:

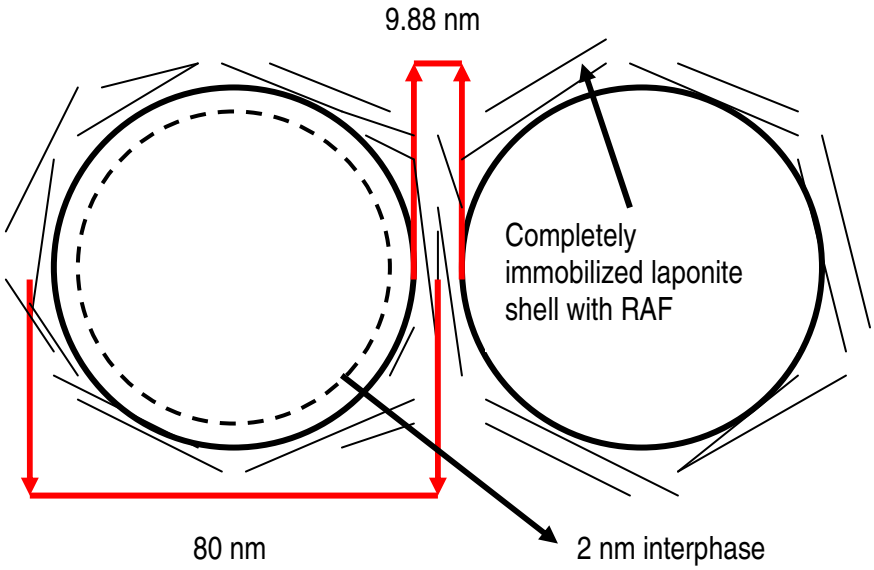

Fig. 1 Two L50 latex particles with the laponite shell.

Considering the latex particle with its laponite shell to have a diameter of 80 nm, the total particle volume is $4\pi(80/2)^3/3 \sim 2.7 * 10^5$ nm^3. Assuming an aggregate thickness of 9.88 nm, the volume occupied by the particle matrix core is $4\pi(80/2 - 9.88/2)^3/3 \sim 1.8. * 10^5$ nm^3. The difference between these two values represents the volume occupied by the laponite shell ~ $8.7 * 10^4$ nm^3.

For the L50 latex particles the volume occupied by the laponite for each particle is $0.24 * 2.7 * 10^5$ nm^3 ~ $6.4 * 10^4$ nm^3. The matrix volume fraction in the laponite rich shell is $8.7 * 10^4 - 6.4 * 10^4$ nm^3 = $2.3 * 10^4$ nm^3 ~ 9 vol % of the entire latex particle volume.

If an interphase of 2 nm is assumed on the aggregate surface (see Fig. 1), the volume of this interphase will be $4\pi/3 *[(80/2 - 9.88/2)^3 – (80/2 - 9.88/2- 2)^3] \sim 2.9 * 10^4$ nm^3, which together with previously found value of $2.3 * 10^4$ nm^3 would double the RAF amount.

From XRD data in Fig. 4.7 (see section 4.1.3), a basal spacing between laponite platelets of about 0.48 nm was found. This is filled by PS matrix in the nanocomposites. Given "*n*" the number of laponite platelets per latex particle as calculated in Appendix 2, the number of intercalated layers per latex particle is about *(n/2)-1* for every laponite content. Considering the laponite aggregates as discs of 54 nm in diameter, the intercalated volume is then *(n/2)-1* * 0.48 * π * $(54/2)^2$, which gives the results reported in section 4.1.5.

Riccardo Ruggerone
Ch. Pré Lébaz 14
1054 Morrens Switzerland
+41 (0) 21 731 37 12
riccardo-ruggerone@libero.it

Born February 21st 1980
Italy

Work experience

2006-to date	**Laboratory of Composite and Polymer Technology,** Swiss Federal Institute of Technology (EPFL), Lausanne, Switzerland Research assistant
2005	**Research Institute CIMAINA**, Milan, Italy Research assistant
2004	**University of Milan-Bicocca,** Milan, Italy Diploma work: "Growth of organic molecular crystals and their optical properties"

Education

2006-to date	**Laboratory of Composite and Polymer Technology,** Swiss Federal Institute of Technology (EPFL), Lausanne, Switzerland Ph.D. Thesis: "Structure-property relationships in polymer nanocomposites films derived from novel nanostructured latexes"
2004	**University of Milan-Bicocca,** Milan, Italy Degree in materials science
1999	**Liceo Scientifico G.Galilei**, Borgomanero, Italy High school diploma

Publications, communications and conferences related to this thesis

- R. Ruggerone, C.J.G. Plummer, N. Negrete Herrera, E. Bourgeat-Lami, J-A.E. Månson, "Highly filled polystyrene/laponite nanocomposites prepared by emulsion polymerization", Eur. Pol. Journ. **45** (2009) 621.

- R. Ruggerone, C.J.G. Plummer, N. Negrete Herrera, E. Bourgeat-Lami, J-A.E. Månson, "Mechanical properties of highly filled latex-based polystyrene/laponite nanocomposites", Sol. State. Phen. **151** (2009) 30.

- R. Ruggerone, C.J.G. Plummer, N. Negrete Herrera, E. Bourgeat-Lami, J-A.E. Månson, "Fracture mechanisms in polystyrene/laponite nanocomposites prepared by emulsion polymerization", Eng. Frac. Mech. (2009), accepted and actually in press.

- C.J.G. Plummer, R. Ruggerone, N. Negrete Herrera, E. Bourgeat-Lami, J-A.E. Månson, " Small strain mechanical properties of latex-based nanocomposite films" (2009) submitted to Macromolecular Symposia.
- 4th SAMPE Swiss Chapter, FHNW Windisch (CH) 24 November 2006, winner of the student chapter, oral presentation.
- 28th SAMPE Europe, Paris 31 March-5 April 2007, oral presentation in the student conference
- JEC Exhibition, Paris 2-5 April 2007, Poster presentation at SAMPE stand.
- Swiss Chemical Society Fall meeting, EPFL Lausanne 12 September 2007, oral presentation
- 5th International Conference on Fracture of Polymers, Composites and Adhesives, Le Diablerets (CH) 7-11 September 2008, oral presentation
- 13th International Conference on Polymeric Materials, 24-26 September 2008 Halle, Germany, communication
- E-MRS fall meeting 2008, Warsaw, 15-19 September 2008, oral presentation
- European Coating Show 2009, Nurnberg, 30 March-1 April 2009, communication

Publications not related to this thesis

-M. Campione, R. Ruggerone, S. Tavazzi, M. Moret, "Growth and characterization of centimeter-sized single crystals of molecular organics materials", Journ. Mat. Chem. **15** (2005) 2437.